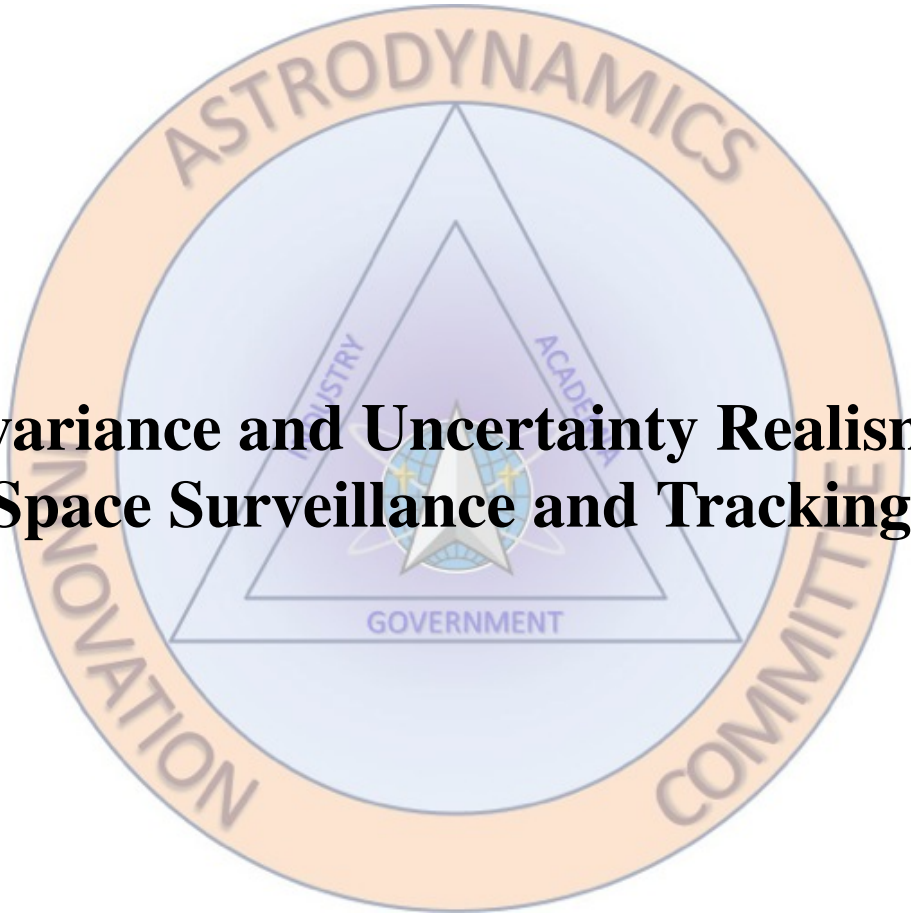

Covariance and Uncertainty Realism in Space Surveillance and Tracking

Date: Monday 27th June, 2016

Working Group on Covariance Realism

Edited By: Aubrey B. Poore, Jeffrey M. Aristoff, and Joshua T. Horwood

E-Mail: {Aubrey.Poore, Jeff.Aristoff, Joshua.Horwood}@Numerica.US

This report was produced under the sponsorship of the Air Force Space Command Astrodynamics Innovation Committee; however, the views in this report represent those of the authors and not the US Government.

REPORT DOCUMENTATION PAGE

Form Approved
OMB No. 0704-0188

PLEASE DO NOT RETURN YOUR FORM TO THE ABOVE ORGANIZATION.

1. REPORT DATE *(DD-MM-YYYY)*	2. REPORT TYPE	3. DATES COVERED *(From - To)*
02-08-2016	Technical Report	Oct 2013 - Aug 2016

4. TITLE AND SUBTITLE

Covariance and Uncertainty Realism in
Space Surveillance and Tracking

5a. CONTRACT NUMBER
N/A

5b. GRANT NUMBER
N/A

5c. PROGRAM ELEMENT NUMBER
N/A

6. AUTHOR(S)
Editors and Contributing Authors:
Aubrey B Poore, Jeffrey M Aristoff, and Joshua T Horwood
Additional Contributing Authors:
Roberto Armellin, William T Cerven, Yang Cheng, Christopher M Cox,
Richard S Erwin, Joseph H Frisbee, Matt D Hejduk, Brandon A Jones,
Pierluigi Di Lizia, Daniel J Scheeres, David A Vallado, Ryan M Weisman

5d. PROJECT NUMBER
N/A

5e. TASK NUMBER
N/A

5f. WORK UNIT NUMBER
N/A

7. PERFORMING ORGANIZATION NAME(S) AND ADDRESS(ES)
Numerica Corporation
5042 Technology Parkway, Suite 100,
Fort Collins, CO 80528

8. PERFORMING ORGANIZATION REPORT NUMBER
N/A

9. SPONSORING/MONITORING AGENCY NAME(S) AND ADDRESS(ES)
Chief Scientist, Air Force Space Command
Director, Astrodynamic Innovation Committee (AIC)
HQ AFSPC/ST
150 Vandenberg St, STE 1105
Peterson AFB CO 80914

10. SPONSOR/MONITOR'S ACRONYM(S)
HQ AFSPC/ST, AIC

11. SPONSOR/MONITOR'S REPORT NUMBER(S)
N/A

12. DISTRIBUTION/AVAILABILITY STATEMENT
Distribution A: Approved for public release, distribution unlimited

13. SUPPLEMENTARY NOTES
This report was produced under the sponsorship of the Air Force Space Command Astrodynamics Innovation Committee; however, the views in this report represent those of the authors and

14. ABSTRACT

The characterization of uncertainty in the estimate of the state of a resident space object is fundamental to many space surveillance tasks including data association, uncorrelated track (UCT) resolution, catalog maintenance, sensor tasking and scheduling as well as space situational awareness (SSA) missions such as conjunction assessments and maneuver detection. The need for and importance of uncertainty quantification is established for each of these problem domains. The following eight generic classes of uncertainty are then identified: structural uncertainty or model bias in the model dynamics, uncertain parameters, sensor level errors, inverse uncertainty quantification, propagation of uncertainty, algorithmic or numerical uncertainty, cross-tag or misassociation uncertainty, hardware and software faults/errors. A state-of-the-art assessment is established for most of these areas through a survey of the existing literature. Research and development recommendations are made for both maturing areas of research such as the propagation of uncertainty and less mature areas such sensor level processing. A final chapter summarizes the recommendations and the "next steps" that promise to improve the overall uncertainty characterization and quantification of resident space objects.

15. SUBJECT TERMS
Uncertainty quantification, covariance realism, uncertainty realism, sensor resource management, anomaly detection, data association, conjunction assessments, structural uncertainty or model bias in the model dynamics, uncertain parameters, sensor level errors, inverse uncertainty quantification, propagation of uncertainty, algorithmic uncertainty, misassociation uncertainty, metrics.

16. SECURITY CLASSIFICATION OF:			17. LIMITATION OF ABSTRACT	18. NUMBER OF PAGES	19a. NAME OF RESPONSIBLE PERSON
a. REPORT	b. ABSTRACT	c. THIS PAGE			Aubrey B Poore
Unclassified	Unclassified	Unclassified	None	159	19b. TELEPHONE NUMBER *(Include area code)* 970 207 2220

INSTRUCTIONS FOR COMPLETING SF 298

1. REPORT DATE. Full publication date, including day, month, if available. Must cite at least the year and be Year 2000 compliant, e.g. 30-06-1998; xx-06-1998; xx-xx-1998.

2. REPORT TYPE. State the type of report, such as final, technical, interim, memorandum, master's thesis, progress, quarterly, research, special, group study, etc.

3. DATES COVERED. Indicate the time during which the work was performed and the report was written, e.g., Jun 1997 - Jun 1998; 1-10 Jun 1996; May - Nov 1998; Nov 1998.

4. TITLE. Enter title and subtitle with volume number and part number, if applicable. On classified documents, enter the title classification in parentheses.

5a. CONTRACT NUMBER. Enter all contract numbers as they appear in the report, e.g. F33615-86-C-5169.

5b. GRANT NUMBER. Enter all grant numbers as they appear in the report, e.g. AFOSR-82-1234.

5c. PROGRAM ELEMENT NUMBER. Enter all program element numbers as they appear in the report, e.g. 61101A.

5d. PROJECT NUMBER. Enter all project numbers as they appear in the report, e.g. 1F665702D1257; ILIR.

5e. TASK NUMBER. Enter all task numbers as they appear in the report, e.g. 05; RF0330201; T4112.

5f. WORK UNIT NUMBER. Enter all work unit numbers as they appear in the report, e.g. 001; AFAPL30480105.

6. AUTHOR(S). Enter name(s) of person(s) responsible for writing the report, performing the research, or credited with the content of the report. The form of entry is the last name, first name, middle initial, and additional qualifiers separated by commas, e.g. Smith, Richard, J, Jr.

7. PERFORMING ORGANIZATION NAME(S) AND ADDRESS(ES). Self-explanatory.

8. PERFORMING ORGANIZATION REPORT NUMBER. Enter all unique alphanumeric report numbers assigned by the performing organization, e.g. BRL-1234; AFWL-TR-85-4017-Vol-21-PT-2.

9. SPONSORING/MONITORING AGENCY NAME(S) AND ADDRESS(ES). Enter the name and address of the organization(s) financially responsible for and monitoring the work.

10. SPONSOR/MONITOR'S ACRONYM(S). Enter, if available, e.g. BRL, ARDEC, NADC.

11. SPONSOR/MONITOR'S REPORT NUMBER(S). Enter report number as assigned by the sponsoring/ monitoring agency, if available, e.g. BRL-TR-829; -215.

12. DISTRIBUTION/AVAILABILITY STATEMENT. Use agency-mandated availability statements to indicate the public availability or distribution limitations of the report. If additional limitations/ restrictions or special markings are indicated, follow agency authorization procedures, e.g. RD/FRD, PROPIN, ITAR, etc. Include copyright information.

13. SUPPLEMENTARY NOTES. Enter information not included elsewhere such as: prepared in cooperation with; translation of; report supersedes; old edition number, etc.

14. ABSTRACT. A brief (approximately 200 words) factual summary of the most significant information.

15. SUBJECT TERMS. Key words or phrases identifying major concepts in the report.

16. SECURITY CLASSIFICATION. Enter security classification in accordance with security classification regulations, e.g. U, C, S, etc. If this form contains classified information, stamp classification level on the top and bottom of this page.

17. LIMITATION OF ABSTRACT. This block must be completed to assign a distribution limitation to the abstract. Enter UU (Unclassified Unlimited) or SAR (Same as Report). An entry in this block is necessary if the abstract is to be limited.

Covariance Realism Working Group

Member	Affiliation	Email Address
Jeffrey M. Aristoff	Numerica Corporation	jeff.aristoff@numerica.us
Christopher M. Cox	Raytheon Corporation	christopher_m_cox@raytheon.com
Nancy Ericson	AFSPC	nancy.ericson@us.af.mil
Joseph H. Frisbee	NASA	joseph.h.frisbee@nasa.gov
Richard W. Ghrist	Northrop Grumman	richard.ghrist@ngc.com
Matt D. Hejduk	Astrorum Consulting	mdhejduk@astrorum.us
Felix R. Hoots	Aerospace Corporation	felix.r.hoots@aero.org
Joshua T. Horwood	Numerica Corporation	joshua.horwood@numerica.us
Moriba K. Jah	University of Arizona	moribajah@email.arizona.edu
Brandon A. Jones	University of Texas	Brandon.Jones@utexas.edu
James Gil Miller	Omitron Inc.	jg.miller@omitron-cos.com
Robert F. Morris	Aerospace Corporation	robert.f.morris@aero.org
Aubrey B. Poore (Chair)	Numerica Corporation	aubrey.poore@numerica.us
Ryan P. Russell	University of Texas	ryan.russell@austin.utexas.edu
Daniel J. Scheeres	University of Colorado	scheeres@colorado.edu
Paul W. Schumacher	AFRL	paul.schumacher@us.af.mil
Carolyn Sheaff	AFRL	carolyn.sheaff@us.af.mil
Daniel Snow	AFSPC	daniel.snow@us.af.mil
William T. Cerven	Aerospace Corporation	william.t.cerven@aero.org
David A. Vallado	CSSI/AGI	dvallado@agi.com
James W. Woodburn	AGI	woodburn@agi.com

Contributing Authors

Author	Affiliation	Email Address	Chapter/Section
Jeffrey M. Aristoff	Numerica Corporation	jeff.aristoff@numerica.us	1, 2, 3.2, 6.1-6.7, 7.1 - 7.10, 8, 9
Roberto Armellin	Universidad de la Rioja (Logrono, Spain)	roberto.armellin@unirioja.es	7.14
William T. Cerven	Aerospace Corporation	william.t.cerven@aero.org	6.8.2
Yang Cheng	Mississippi State University	cheng@ae.msstate.edu	7.12
Christopher M. Cox	Raytheon Corporation	christopher_m_cox@raytheon.com	5
Richard S. Erwin	AFRL	richard.erwin@us.af.mil	3.4
Joseph H. Frisbee	NASA	joseph.h.frisbee@nasa.gov	6.8.1
Matt D. Hejduk	Astrorum Consulting	mdhejduk@astrorum.us	3.1, 8
Joshua T. Horwood	Numerica Corporation	joshua.horwood@numerica.us	1, 2, 3.2, 6.1-6.7, 7.1 - 7.10, 8, 9
Brandon A. Jones	University of Texas	Brandon.Jones@utexas.edu	6.11, 7.11
Pierluigi Di Lizia	Politecnico di Milano (Milan, Italy)	pierluigi.dilizia@polimi.it	7.14
Aubrey B. Poore	Numerica Corporation	aubrey.poore@numerica.us	1, 2, 3.2, 6.1-6.7, 7.1 - 7.10, 8, 9, 10
Daniel J. Scheeres	University of Colorado	scheeres@colorado.edu	3.3
David A. Vallado	CSSI/AGI	dvallado@agi.com	4
Ryan M. Weisman	AFRL	ryan.weisman@us.af.mil	6.9, 7.9, 7.13

Executive Summary

The characterization of uncertainty in the estimate of the state of a resident space object is fundamental to many space surveillance tasks including data association, uncorrelated track (UCT) resolution, catalog maintenance, sensor tasking and scheduling as well as space situational awareness (SSA) missions such as conjunction assessments and maneuver detection. Generally, uncertainties are classified as either *aleatoric, epistemic or a mixture of both*. *Aleatoric uncertainty* is the natural randomness or physical variability present in the system or its environment and is thus statistical in nature. In contrast, *epistemic uncertainty* is uncertainty that is due to limited data or knowledge as discussed in Chapter 2. While aleatoric uncertainty is the focus of this report, epistemic uncertainties certainly deserve more attention by the astrodynamics community.

With respect to some terms, *covariance realism* means that the uncertainty in the state of an object can be represented as a Gaussian random variable and that the estimated mean and covariance of said Gaussian are the true mean and true covariance, respectively. Since the underlying dynamical processes are not always linear nor Gaussian, one may generalize covariance realism to *uncertainty realism* described by a potentially non-Gaussian probability density function. Uncertainty realism requires that all cumulants (beyond a state and covariance) be properly characterized. The relationship between covariance realism and uncertainty realism is that the former is a necessary but not a sufficient condition for achieving the latter. The two definitions coincide if the process is Gaussian. These terms are used throughout the report.

The achievement of covariance or uncertainty realism is a challenging problem due to the complex and numerous sources of uncertainty. To achieve a proper characterization of uncertainty, one must account for the uncertainty sources in the system and roll these up into the uncertainty in the estimate at each needed time. Generic sources of uncertainties for point objects include the following:

1. *Structural uncertainty or model bias* in the model dynamics;
2. *Uncertain parameters* found in the model dynamics (including space environment) and in the measurement equation relating the dynamics to the sensor measurements;
3. *Sensor level errors* including measurement noise and sensor and navigation biases;
4. *Inverse uncertainty quantification* including the statistical orbit determination and bias estimation uncertainty;
5. *Propagation of uncertainty*;
6. *Algorithmic uncertainty* or numerical uncertainty that comes from numerical errors and numerical approximations in a computer model;
7. *Cross-tag or misassociation uncertainty*;
8. *Hardware and software faults/errors*.

Most of these errors for *point objects* are pursued in the subsequent chapters. Additional sources of uncertainty occur for *medium to large objects* called *extended body uncertainties*. For example, an extended body covering several pixels may have an overly optimistic (too small) covariance if the uncertainty of the estimated state only covers the centroid of the body.

The goal of correctly characterizing or quantifying uncertainty is not unique to astrodynamics. Indeed, the currently active field of *uncertainty quantification* deals with the same problem in the many other areas

of engineering and science. Thus, brief comments on the field of *uncertainty quantification* and definitions are provided in Chapter 2.

As stated above, the correct characterization the uncertainty in the state of each object is fundamental to many space surveillance and space situational awareness missions. Four examples are provided in Chapter 3 to demonstrate the importance of *covariance and uncertainty realism*, namely

1. *computation of the probability of collision* for conjunction assessment,
2. *data or track association/correlation*,
3. *maneuver detection*,
4. *sensor tasking and scheduling*.

The primary goal of this Chapter 3 is to explain the impact of having an unrealistic covariance (or, more generally, an unrealistic probability density function) that characterizes the state of a space object.

Chapter 4 presents a macroscopic view of the uncertainties in generic reference systems, time systems, and astrodynamic force models used as a reference for discussing the uncertainties in these models. In addition, an attempt is made to delineate and quantify the structural and parametric uncertainties. Recommendations for reducing and properly characterizing these uncertainties are given in Section 4.3. It is anticipated that a future report on *New Methods of Reentry Modeling* will considerably expand the topic of uncertainty quantification of reentering objects.

The importance of a complete understanding and correct characterization of sensor errors and their temporal behavior is required to achieve covariance and uncertainty realism of a sensor report. This is perhaps one of the most important topics that has received little attention in the literature and yet could offer the biggest payoff to improving uncertainty realism in SSA. This topic is discussed in Chapter 5. First, one has the natural randomness of the intrinsic sensor system in which observations are made. Next, one has to consider a bias model for sensor calibration that includes atmospheric, sensor, and navigation biases. After these are estimated, one must address the uncertainties in the estimates. What is often reported in a sensor report is not an intrinsic observable, but instead a filtered state transformed into yet another coordinate system. Thus, a short burst of measurements over a few seconds or minutes may be highly correlated. The challenge then is to roll up all of these uncertainties into a sensor report or reports and to obtain realistic uncertainties.

Having presented the uncertainties in sensor level processing, dynamical models including atmospheric models, Chapter 6 surveys some of the formulations and methods for the *inverse problem* of extracting a state, e.g., position and velocity, from the sensor reports. In particular, this chapter reviews many of the nonlinear estimation techniques including filtering, smoothing, prediction, and batch estimation that are currently used in the astrodynamics community. The focus is on the estimation techniques that yield the state and its uncertainty at the time of the last measurement, i.e., epoch, as opposed to the propagation of uncertainty after the last sensor report. Included in this chapter is a discussion of the different process noise or stochastic acceleration models often used by the astrodynamics community. Model bias is also treated as a control problem that is discussed in the earlier Section 3.3.

While the previous chapter examined estimation methods through epoch, Chapter 7 addresses the *propagation of uncertainty* in support of the SSA missions discussed in Chapter 3 assuming that the quantification

of uncertainty at epoch is correct. There are several considerations that affect the quality of the representation of uncertainty and the length of time it remains valid. First, the coordinate system in which uncertainty is represented and propagated has a significant impact. Generally this means a Cartesian versus an orbital element space as discussed in Section 7.2. Regardless of which coordinate system is used, each of the aforementioned mission areas may require the representation in a different coordinate system than that in which uncertainty is propagated. Thus, one must address the faithful representation in the needed coordinate system. Research into the topic of "uncertainty propagation" by the astrodynamics community is broad and quite excellent. Thus, the goal of this chapter is to survey most of these methods and to make recommendations on approaches that might be used to evaluate the different methods for different purposes.

The scope of this report is somewhat limited. As indicated above, the uncertainties treated are those of the aleatoric as opposed to epistemic uncertainties. Secondly, no systematic attempt has been made to evaluate any existing or proposed operational system nor make recommendations to improve uncertainty realism for such a system. This was necessary given the Distribution-A requirements on the report; however, we recommend that such a study be undertaken as part of a separate effort. In keeping with this requirement, the intended audience is a general one. While there are some recommendations on specific algorithms throughout the report, no systematic assessment of the different algorithms has been undertaken. Instead of the committee making an assessment of the different algorithms and approaches, the recommendation is to set up an environment whereby one can evaluate the different algorithms. Toward this end, metrics are proposed in Chapter 8 and an initial list of benchmark test cases are proposed in Chapter 9 for a subset of the problems considered in this report.

The concluding Chapter 10 briefly reviews the above chapters from the viewpoint of the aforementioned generic uncertainties and presents recommended "Next steps" in Section 10.5.

Contents

List of Figures

List of Tables

Chapter 1

Introduction

Space situational awareness (SSA) encompasses intelligence, surveillance of all space objects, and the prediction of space events, possible collisions, threats, and activities [1]. Fundamental to SSA are conjunction analysis (probability of collision), sensor tasking and scheduling, data/track association for uncorrelated track (UCT) resolution and catalog maintenance, and anomaly (e.g., maneuver, change) detection. Common amongst these missions is the requirement of a proper characterization of the uncertainty and errors in the estimation of each resident space object (RSO), which is called *covariance* or *uncertainty realism*.

The process of achieving covariance or uncertainty realism lies in the realm of *space surveillance*, which is that component of SSA focused on the detection of space objects and on the use of multi-source data to detect, track, identify and characterize space objects. Space surveillance presents some unique and formidable challenges not found in other tracking environments. In contrast to air, missile, or ground tracking, the space surveillance environment is *data-starved*; however the dynamic models have been and continue to be well developed. Typical resident space object (RSO) tracking problems can require the long term propagation of state probability density functions (PDFs), often on the order of several orbital periods, using high fidelity dynamical models in the absence of measurement or track updates. Even if the uncertainty in the state of an object is characterized as a Gaussian (represented by an ellipsoidal covariance) at some point in time, the state will inevitably become non-Gaussian (non-ellipsoidal) if propagated for a sufficiently long time span under nonlinear dynamics (i.e., gravity, drag, solar radiation, third-body perturbations, etc.). Consequently, the term *covariance realism* used in data-rich tracking environments and referring to the accurate and truthful representation of the errors of an estimate as a Gaussian random variable is only a prerequisite to the more general notion of *uncertainty realism* in which these errors are characterized by a more general probability density function (PDF).

Without the proper representation of uncertainty, false conclusions can arise: non-predicted collisions do occur, RSOs declared to be UCTs do in fact correlate, sensor tasking and scheduling algorithms lead to inefficient use of sensor resources, and maneuvers go undetected. Compounding each of these issues is the expected substantial growth in the number of observed RSOs. With improved sensors such as the newly funded Space Fence (S-Band radar) and improved electro-optical (EO) sensors such as Pan-STARRS, the number of observed RSOs will increase dramatically. Debris fields left by the collision of satellites such as the recent Iridium-Cosmos collision or destruction of satellites as in the Chinese ASAT test is a major

and growing threat to existing satellites. Thus, for space protection and space situational assessment, an *automated system* is needed to track and identify the ever increasing number of objects in space and to support the aforementioned mission areas. Such an automated system will inevitably be statistics-based approach to surveillance. This in turn requires the correct accounting and faithful characterization of the different uncertainties and errors throughout the Space Surveillance Network (SSN), the orbit estimation algorithms in the Command and Control (C2) center and a roll-up of these into that of the state of each RSO.

Thus, the goals of this report are to identify the uncertainties and errors throughout the SSN, to survey some of the associated work in the astrodynamics community for treating these uncertainties, and to make recommendations for improving such or at least to set up a collaborative environment that can lead to such improvements. Not all uncertainties or errors contribute equally to the final rollup, so a subgoal is to identify the more dominant ones. Ideally one would end up with a list of the uncertainties that dominate the final rollup, so they could methodically be reduced.

Generic sources of errors and uncertainty in other surveillance systems have been identified by Drummond [75] and are expanded to the same for space surveillance in Section 1.1. Topics not addressed in this report are outlined in Section 1.2; however, they should be investigated in any future work. Finally, an outline of the report is provided in Section 1.3.

1.1 Generic Sources of Errors and Uncertainty in SSA

Again, uncertainty quantification in SSA deals with the quantification of uncertainty and the achievement of uncertainty realism in the SSN at each stage of the processing with the objective being to roll-up this uncertainty into the state of each resident space object. Motivated by similar uncertainties considered in the field of uncertainty quantification, here are some generic uncertainties for point objects.

1. **Structural uncertainty** is also known as model inadequacy, model bias, or model discrepancy, which comes from the lack of knowledge of the underlying *astrodynamical forces* acting on a RSO as well as that of *maneuvers*.

2. **Uncertain parameters** are found in the model dynamics (including space environment) and in the measurement equation relating the dynamics to the sensor measurements. Included in the latter are the *sensor, navigation, and time biases* as well as the corresponding residual biases and bias drift between sensor calibrations.

3. **Sensor measurement noise**, sometimes called experimental error or observation error, as found in the measurement equation, is generally assumed to be Gaussian and white; however, it can be non-Gaussian and correlated. Sensor measurements can be in the form of the actual or intrinsic measurements of the sensor or pseudo or derived measurements such as sensor tracks. In addition to the random *sensor measurement noise*, one also treats the residual bias noise either by a consider analysis or a Schmidt-Kalman filter.

4. **Inverse uncertainty quantification** includes the statistical orbit determination and bias estimation uncertainty in that both may be considered to be inverse problems. The estimation of the state of

an object and its uncertainty given the sensor reports and astrodynamics models is critical to the propagation of uncertainty. Also included in this subject is the estimation of the sensor, navigation, or time biases given truth objects or fuzzy truth objects (e.g., high accuracy orbits) and the statistical characterization of the uncertainty in these estimates. (An inverse problem is a general framework that is used to convert observed measurements into information about a physical object or system. A bias is a systematic error that does not average out.)

5. **Propagation of uncertainty** refers to the propagation of uncertainty in the state of an object and its uncertainty through nonlinear dynamics or to the transformation through nonlinear functions. Included in this problem is that of predicting space weather into the future.

6. **Algorithmic uncertainty** or numerical uncertainty comes from numerical errors and numerical approximations in a computer model. An example is the truncation *error* in the orbital propagator, which can be mitigated by adjusting the numerical error tolerance so that the magnitude of the numerical error is below that of the uncertainty due to the physics or uncertainty in the state of an object. Another example is that of orbit determination in the presence of ill-conditioning.

7. **Cross-tag or misassociation uncertainty** is discrete in nature and is generally characterized through the computation of the probability of association [166, 205]. Cross-tags can degrade the uncertainty in the state of an object and are especially important for closely spaced objects such as GEO clusters, LEO breakups, and tethered satellites.

8. **Hardware and software faults/errors** are yet another source of uncertainty introduced into the process.

9. While the above sources are valid for *point objects*, there are additional sources of uncertainty for *medium to large objects* called **extended body uncertainties**. For example, an extended body covering several pixels may have an overly optimistic (too small) covariance if the uncertainty of the estimated state only covers the centroid of the body. One must also address the extent of the body, possibly through the use of *feature data* such as multi-band photometry and radiometry. Radar, on the other hand, may receive reflections from multiple point scatterers and the centroided uncertainty may not cover the extent of the body. (We note that the radar cross section (RCS) of an extended object is not well defined. Each point scatterer may have a different RCS. Thus the "object RCS" could be the mean or the maximum of the point scatterers.)

1.2 Focus of the Report and Topics Not Addressed

As indicated above, the uncertainties treated are those of the aleatoric as opposed to epistemic uncertainties. While this report surveys many of the uncertainties in the space surveillance network as well as other contributing sensor inputs in a generic sense, it does not provide a comprehensive review in addressing and identifying the current (or legacy) operational system and its deficiencies with respect to the expected requirements (current or future). This was necessary given the Distribution-A limitations of this report; however, we recommend that such a study be undertaken as part of a separate effort. (Chapter 5 on sensor level

processing does make some generic recommendations along these lines.) In keeping with this requirement, the intended audience is general. While there are some recommendations on specific algorithms throughout the report, no systematic assessment of the different algorithms has been undertaken. Instead of trying to solve the problem, the approach has been to set up an environment where one can evaluate the different algorithms. Toward this end, metrics are proposed in Chapter 8 and an initial list of benchmark test cases proposed in Chapter 9 for a subset of the problems considered in this report.

While this report does address many of the above sources of uncertainty, it does not address all of those listed in Section 1.1. Here is such a list.

- While the subject of *algorithms* is briefly discussed throughout the different sections, there is no in-depth treatment of such algorithms. In particular, there is no comparison between filter/smoothing and batch processing and the corresponding algorithms.
- No attempt is made to address *extended body uncertainties*.
- All of the uncertainties and errors treated in this report are of the aleatoric type.
- No attempt is made to address *cross-tag or misassociation uncertainty*, which is treated to some extent in Drummond [77].
- Metrics and test cases for the estimate of the state and its uncertainties at epoch have not been specifically addressed.
- The report does not provide an estimate of the expected total level of effort in completing the goals and neither addressing potential issues or impact on system interoperability.

1.3 Organization of the Report

The report is organized in the following manner.

- Chapter 2 presents some of the required definitions and some of the salient elements of the related field of uncertainty quantification.
- Chapter 3 presents four mission areas (conjunction assessments, data association, maneuver detection, and sensor tasking and scheduling) that require a proper characterization of errors and uncertainties in the state of a resident space object.
- Chapter 4 surveys some of the structural and parametric uncertainties in the astrodynamics equations of motion including the related space environment.
- Chapter 5 presents an overview of the issues in sensor level processing that results in the sensor reports processed by statistical orbit determination. This chapter also overviews the sensor, navigation, and time biases that are treated as parametric uncertainties in Section 6.2.
- Chapter 6 presents a brief overview of some of the methods used by the astrodynamics community to estimate the state of each object and its uncertainty. In particular, parametric structural uncertainty are discussed in Section 6.2. Structural uncertainty due to model bias or inadequacy is further discussed in Sections 6.6 and 6.7 as well as the earlier Section 3.3

- Chapter 7 surveys some of the different methods being used to propagate uncertainty forward in time in support of the aforementioned mission areas.
- Chapter 8 proposes new metrics to assess the performance of different algorithms, especially for propagating uncertainty.
- Chapter 9 provides some sample test cases that will need to be augmented by the astrodynamics community.
- Chapter 10 provides a summary and some recommendations for the "next steps" as enhancements to this report.

Chapter 2

Uncertainty Quantification

The problem of characterizing uncertainty and errors is an active area of research called *uncertainty quantification (UQ)*, as are the associated subjects of verification, validation, sensitivity analysis, and the quantification of margins and uncertainties (QMU). In particular, there are many fine lectures, articles, and books on this subject. The report by the National Academy of Sciences [54], a popular internet reference 00 [287] and Stanford University's Uncertainty Quantification website [136] provide an assessment of the state-of-art and provide many such references as do the book by Smith [246] and the review article by Owhadi, Scovel, Sullivan, McKerns, and Ortiz [215]. In addition, there are at least two journals that focus entirely on uncertainty quantification, namely, the ASME Journal of Verification, Validation and Uncertainty Quantification and the SIAM/ASA Journal on Uncertainty Quantification. This collection of works provide some guidance about questions being posed, methods being developed, and answers to fundamental questions in quantifying uncertainty in the state of resident space objects. The purpose of this chapter then is to define some of the relevant terms and explain some of the approaches.

2.1 Some Definitions

Following the AAS inspired definitions of uncertainty and errors, the following definitions [136] will be used in the report. "Define *errors* as associated to the translation of a mathematical formulation into a numerical algorithm (and a computational code). Examples are round-off errors, limited convergence of certain iterative algorithms and implementation mistakes (bugs). With this definition of errors, *uncertainties* are naturally associated to the choice of the physical models and to the specification of the input parameters required for performing the analysis."

To properly (or faithfully) characterize the uncertainty in each space object, there are essentially three interrelated processes that one must consider [3, 57, 69].

- **Verification** is the process of determining how accurately the computation solves the underlying equations of the model and other quantities of interest.
- **Validation** is the process of determining the degree to which a model is an accurate representation of the real world for the intended uses of the model.

- **Uncertainty Quantification** is the process of determining the various sources of errors and uncertainties, properly characterizing these errors and uncertainties, and the roll-up of these in the prediction of the quantities of interest.

Sensitivity analysis (SA) [57], on the other hand, investigates the connection between inputs and outputs of a (computational) model; more specifically, it allows one to identify how the variability in an output quantity of interest is connected to an input in the model, and which input sources will dominate the response of the system. On the other hand, uncertainty analysis aims at identifying the overall output uncertainty in a given system. The main difference is that sensitivity analysis does not require input data uncertainty characterization from a real device; it can be conducted purely based on the mathematical form of the model. Large output sensitivities (identified using SA) do not necessarily translate into important uncertainties because the input uncertainty might be very small in a device of interest. SA is often based on the concept of sensitivity derivatives, the gradient of the output of interest with respect to input variables. The overall sensitivity is then evaluated using a Taylor-series expansion, which, to first order, would be equivalent to a linear relationship between inputs and outputs.

An important subfield of UQ is *Quantification of Margins and Uncertainties* (QMU), a methodology that focuses on quantifying the ratio of a system's margin (i.e., the difference between the measured or simulated output of a system and a performance threshold) to its uncertainty (i.e., the variability in the output.) QMU can thus be used to estimate the probability that the true output of the system falls within the performance threshold, and can thus be used for decision making. An application of QMU in SSA might be determining the probability that a detected maneuver is actually a true maneuver, or if it is a false alarm.

Returning to the subject of uncertainty quantification, uncertainties are generally classified as either **aleatoric, epistemic or a mixture of both**. **Aleatoric uncertainty** is the natural randomness or physical variability present in the system or its environment and is thus statistical in nature. For discrete variables, the randomness is parameterized by the probability of each possible value. For continuous variables, the randomness is parameterized by a probability density function. In contrast, **epistemic uncertainty** is uncertainty that is due to limited data or knowledge. Epistemic uncertainty is sometimes referred to as state of knowledge uncertainty, subjective uncertainty, Type B, or reducible uncertainty, meaning that the uncertainty can be reduced through increased understanding (research), or increased and more relevant data.

Aleatoric uncertainties can, by definition, be represented using a statistical approach, such as a covariance matrix or probability density function. In contrast, epistemic uncertainties cannot normally be directly represented by a probability density function. Non-probabilistic approaches include evidence (Dempster-Shafer) theory, possibility theory, fuzzy set theory, and interval analysis. However, since traditional filtering methods, such as Kalman filtering, require the states and parameters to be represented as a probability distribution, it is often necessary to approximate the epistemic uncertainty by adding aleatoric uncertainty to the model.

The term *covariance consistency* [76] is used in other tracking domains in place of the term **covariance realism**, which is the proper characterization of the covariance (statistical uncertainty) in the state of a system. Covariance realism requires that the estimate of the mean be the true mean (i.e., the estimate is unbiased) and the covariance possesses the right size, shape, and orientation (i.e., consistency). Relaxing Gaussian assumptions, **uncertainty realism** is the proper characterization of the uncertainty in that state

using a general (i.e., non-Gaussian) probability density function. Uncertainty realism requires that all cumulants (beyond a state and covariance) be properly characterized. The relationship between covariance realism and uncertainty realism is that the former is a necessary but not a sufficient condition for achieving the latter. The two definitions coincide if the process is Gaussian.

In addition to the two basic types of uncertainties, the two fundamental problems considered in uncertainty quantification are the *forward propagation of uncertainty* and the *inverse assessment of model (e.g., dynamics, space environment, and measurement) uncertainty and parameter uncertainty*.

- The problem of forward propagation of uncertainty is to determine the uncertainties in the state, model, and system parameters at a final time (e.g. after orbital propagation). These uncertainties are usually represented as probability density functions. For astrodynamics, this uncertainty is surveyed in Chapter 7.

- The problem of inverse uncertainty quantification is, given some experimental measurements of a system and some computer simulation results from its mathematical model, to estimate the discrepancy between the true dynamics of the system and the mathematical model (which is called bias correction), and to estimate the values of unknown parameters in the model if there are any (which is called parameter calibration or simply calibration). Generally, it is a much more difficult problem than uncertainty propagation; however, it is of great importance since it is typically implemented in a model updating process.

2.2 Recommendations

The general subject of "uncertainty quantification" is an important area of research and development within the engineering and science community. Many of the objectives in achieving the quantification of errors and uncertainties in this field are directly applicable to those in astrodynamics. While most of the literature on uncertainties in astrodynamics is focused on aleatoric uncertainty, methods and algorithms for epistemic uncertainty quantification should be investigated.

Chapter 3

Survey of Some of the Mission Areas

The improvement or achievement of realistic covariances and more generally a realistic uncertainty realism in the characterization of the errors in the state of a space object is central to at least four areas:

- computation of the probability of collision for conjunction assessment,
- data or track association/correlation,
- maneuver detection,
- sensor tasking and scheduling.

In the following, these four areas are briefly discussed. The primary goal is to explain the impact of having an unrealistic covariance (or, more generally, an unrealistic PDF) that characterizes the state of an object.

3.1 Conjunction Assessment

3.1.1 Role of Covariance in the Calculation of Probability of Collision Parameter

There are two methods typically employed to calculate the probability of collision (P_C), which is the main conjunction analysis and risk assessment parameter between two space objects. The first is used when the duration of the conjunction is extremely short, while the second is used otherwise.

3.1.1.1 Short-Duration Method

When the duration of the conjunction is extremely short, rectilinear motion of the two spacecraft and invariant covariances can be assumed; and it is thus possible to reduce the problem from a 3- to 2-dimensional (or lower) formulation. This is performed as follows:

- The system of both objects is propagated to the time of closest approach (TCA) and projected into a plane orthogonal to the relative velocity vector (Vps and y-axis in this diagram) between the two objects–this is called the conjunction plane,
- The covariances for the primary object (the protected asset) and the secondary object (the conjunctor) are added together to form a combined covariance,

- A coordinate system is created with the position of the secondary object at the origin, the x axis positioned along the relative position vector at TCA (i.e., the primary object is located on the positive x-axis), and the z axis in the conjunction plane and orthogonal to the x axis,
- A Gaussian PDF is created whose center is the origin and whose covariance is the combined covariance, and
- A "region of conjunction" A is created whose center is the position of the primary object and whose radius is large enough to circumscribe both the primary and secondary objects' sizes (this radius is referred to as the "hard-body radius," or HBR).

A diagram of this encounter region (taken from [49]) is given in Figure 3.1.1:

Figure 3.1.1 Conjunction duration as represented in the conjunction plane

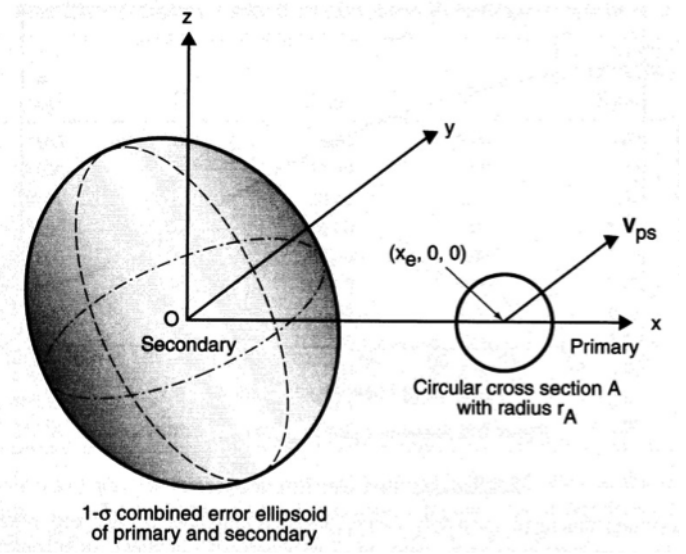

The probability of collision is then the integral of the PDF over the region of conjunction, which can be calculated as follows (this calculation may require a rotation of axes in the conjunction plane to remove undesirable correlation terms; this can be done without loss of generality):

$$P_C = \frac{1}{\sqrt{(2\pi)^2 \left|\mathbf{C}^\star\right|}} \iint_A \exp\left(-\frac{1}{2}\boldsymbol{r}^T \mathbf{C}^{\star -1} \boldsymbol{r}\right) dX dZ \tag{3.1.1}$$

in which $\boldsymbol{r} = [x, z]$ and $\mathbf{C}^\star$ is the two-dimensional covariance matrix that results from projecting the three-dimensional position covariance matrix $\mathbf{C}$ into the conjunction plane. This is the form of simplified evaluation promoted by Foster [90, 91]; other methods that are similar include those by Patera [219], Chan [49], and Alfano [4, 5]. While these approaches may differ in the dimensionality of the solution, all of them hold a similarly prominent role for the combined covariance and its assumed Gaussian behavior. We remark that the rectilinear assumption used in these short-duration methods can be relaxed as described, for example, by Vittaldev and Russell [273].

3.1.1.2 Long-Duration Method

For those situations in which the short-duration assumption does not inhere, some simplified three-dimensional methods (e.g., [200]) or Gaussian mixture models (e.g., [65, 273]) have been proposed; but typical operational procedure is to make use of Monte Carlo techniques. These approaches can be conducted in two ways, the less computationally burdensome of which is as follows:

- Propagate both the primary and secondary states and covariances to TCA,
- Draw Monte Carlo samples from each of these distributions,
- Calculate a new TCA and miss distance* for each pair of draws, and
- Determine whether this miss distance falls within the hard-body radius.

The execution of a large number of such trials will determine a synthetic P_C (number of trials that fall within HBR / total number of trials). This option will address the failure of rectilinear dynamics to represent the actual conjunction situation, but it still relies on a realistic covariance in the region near TCA. The more computationally-intensive but higher-accuracy approach is, instead:

- Draw Monte Carlo samples from the primary and secondary covariances at their epoch times.
- Propagate each of these samples forward to a new TCA and calculate the miss distance, and
- Determine whether the miss distance falls within the hard-body radius.

This approach remediates both shortcomings of rectilinear dynamics in the region of the conjunction and non-linearities in the propagation of the individual objects' covariances to TCA.

3.1.2 Effects of Covariance Irrealism

3.1.2.1 Covariance Size

Figure 3.1.1 shows that the density of the Gaussian PDF in its overlap of the region of conjunction will determine the value of P_C. Since the PDF has support over the entire conjunction plane, there is always overlap with the region of conjunction; the question is whether the overlap occurs in a relatively dense or sparse region of the PDF. One can see that the relative size of the covariance and HBR region, and their relative placement, will affect the P_C calculation. For a fixed miss distance (which is the distance from the center of the PDF to the center of the region of conjunction along the x-axis), we see that:

- If the covariance is very tight (principal axis much smaller than the miss distance), the P_C is low because the conjunction region lies in the tails of the PDF;
- If the covariance is medium size (principal axis approximately equal to the miss distance), the P_C is larger; and,
- If the covariance is very loose (principal axis much larger than the miss distance) the P_C becomes smaller again because the PDF becomes spread out over a larger region, and thus has lower density.

* In point of fact, the miss distance and covariance are themselves linked; so the imposition of a "fixed miss distance" while the covariance is altered is not a realistic decision-support activity in an operational environment. However, it is helpful as an illustrative sensitivity analysis.

Figure 3.1.2, which plots P_C as a function of the ratio of the combined covariance's 1σ value to the miss distance, shows this effect. For simplicity, a spherical covariance (projected into the conjunction plane as a circle) is used here, with a series of contours showing behavior at hard body radii from 1% to 5% of the miss distance. One can observe that the sensitivity of P_C to covariance size can be substantial or relatively minor depending on where on the curve the nominal value happens to fall: in some places the slope is steep; in others rather flat. However, it is clear that there are places on this curve where covariance over- or under-reporting by a factor of 2 or 3 can change the resulting P_C by more than an order of magnitude, the commonly-used rule-of-thumb for considering a change in P_C to be significant.

Figure 3.1.2 P_C as a function of sigma / miss distance ratio, with HBR contours

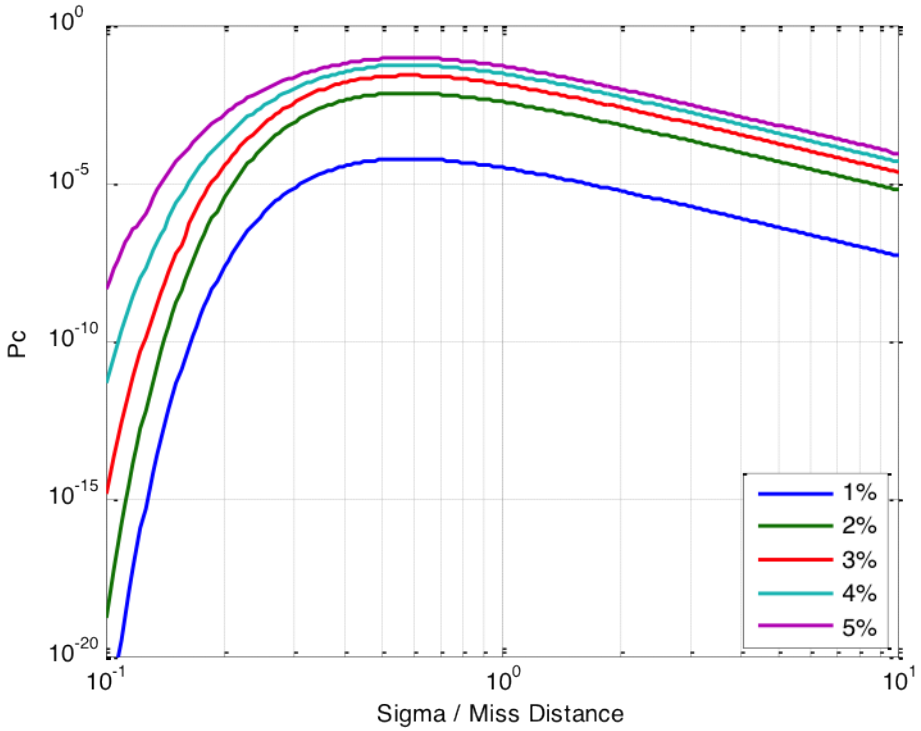

3.1.2.2 Covariance Orientation

The angular orientation of the covariance in the conjunction plane, especially as the covariance moves from circularity to a more oblong ellipse, can have a considerable effect on the P_C. Figure 3.1.3 shows P_C as a function of the "clock angle" in the conjunction plane (angular deviation of the principal axis from the z-axis; a 90° clock angle has the highest P_C because it means that the principal axis is aligned with the x axis) for a variety of covariance oblateness values (minor axis from 10% of principal axis to 100% of principal axis, with 100% indicating a circular covariance; miss distance of unity with covariance principal axis also of unity and HBR of 2% of miss distance).

As one can see, the effect of covariance orientation on P_C can be significant, and the degree of this effect is substantially heightened with increasing covariance oblateness. There are certainly regions in which relatively small changes in orientation can affect the P_C by the order-of-magnitude threshold of significance.

Figure 3.1.3 P_C vs covariance orientation in conjunction plane. Contours show oblateness of covariance.

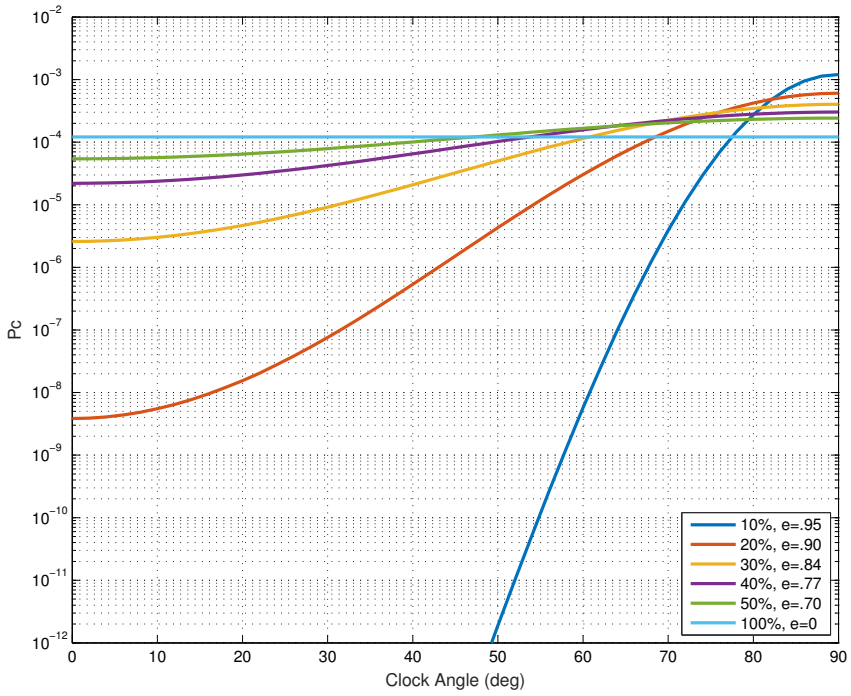

3.1.2.3 Covariance Shape

A number of researchers have demonstrated that even initially Gaussian error volumes, with their familiar ellipsoidal shape, can become non-Gaussian over days or even hours of propagation [64, 122, 149, 158, 218, 231]. This effect is due to the fact that orbit positional evolution (and thus error mapping) is curvilinear in nature and thus not suited to a Cartesian framework. The error manifests itself in Cartesian space as a curved ellipsoid, or "bananoid," as shown by the blue Monte Carlo samples in Figure 3.1.4, as opposed to the red covariance ellipse, which is both incorrect in shape and misaligned with the nominal velocity vector (the object represented here is a near-circular orbit with an altitude of 1400km).

While from the figure the situation may appear severe, one must consider both (1) the fact that in Figure 3.1.4, the Y axis scale is stretched vertically by a factor of 25 relative to the X axis scale to accentuate illustratively the shape differential between the two error regions, and (2) that the two regions do overlap in the area of greatest density. This latter phenomenon was identified by Ghrist and Plakalovic [99], who have shown that this non-Gaussian curvature appears to have little effect on the P_C for high-P_C events (i.e. $P_C > 10^{-4}$, which is the usual threshold for active remediation with conjunction avoidance maneuvers) and that, when it does appear, it can often be addressed by a Monte Carlo evaluation from a post-propagation transformation to equinoctial element space. As such, while it is always desirable to employ the true shape of the error region for the P_C calculation, the issue of a non-ellipsoidal covariance shape is a less urgent issue for conjunction analysis risk assessment than proper sizing and orientation of the ellipsoidal covariance. Nonetheless, while it may be the case that curvilinear bending of the true covariance will often not influence the resultant Pc calculation appreciably, the wholesale under- or over-sizing and mis-orientation of the co-

Figure 3.1.4 "Bananoid" covariance as compared to ellipse from propagated covariance

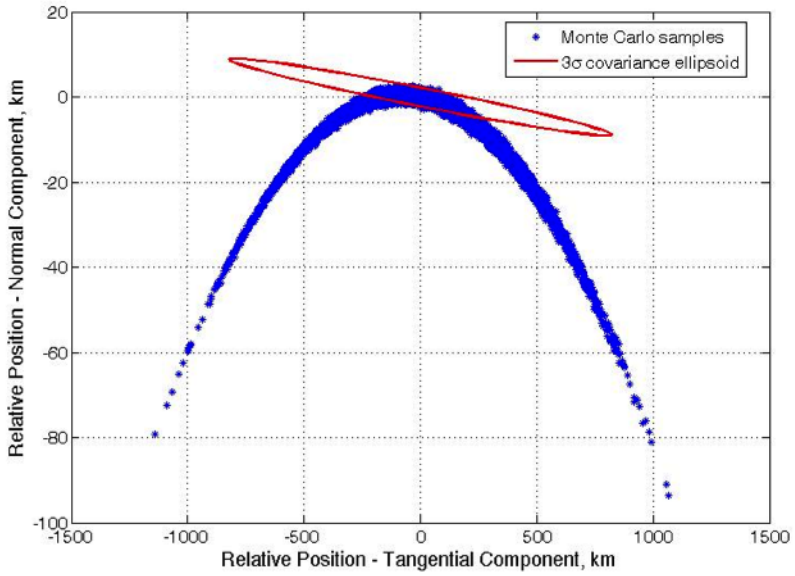

variance, as stated previously, can have a significant effect on the Pc. To this end, it is quite important for the conjunction assessment problem to make all reasonable efforts to obtain realistically sized and oriented covariances.

3.1.3 Conjunction Assessment Covariance Realism Efforts to Date

3.1.3.1 JSpOC Inherent Features

Since the SP catalog maintenance software presently in use at the JSpOC was developed for CA purposes, it includes features that were introduced to improve covariance realism for this particular application. The first of these is the implementation of a consider parameter to improve covariance realism in propagation. Release 14-3 of the SP satellite catalogue software implemented functionality to calculate a dynamic consider parameter that would attempt to compensate for atmospheric density mismodeling and a non-static satellite frontal area. This calculated parameter, the specifics of which are described in more detail below, is added to the ballistic coefficient variance in the unpropagated covariance matrix; and through the pre- and post-multiplication of the state-transition matrix and the ballistic coefficient correlation terms, this increase affects the other covariance elements.

The Dynamic Consider Parameter comprises two components. One component is due to the global error in the atmospheric density forecast. This component will vary for all satellites with changes in the atmospheric density forecast. The other component is due to satellite-specific frontal area variation in the prediction of the ballistic coefficient. This component will change as the frontal area changes over time due to rotation of the satellite. The DCP variance is the sum of the variance of these two components.

The percent RMS error in the atmospheric density forecast is parameterized as a function of height above the surface of the Earth and geomagnetic activity. The main source of atmospheric density prediction errors is due to the sudden short term (less than 3 days) geomagnetic storms, characterized by the geomagnetic

index ap and the disturbance storm time index Dst. The Jacchia-Bowman-HASDM 2009 (JBH09) model uses the ap index for low storm activity and the Dst index during moderate to high storm activity. The percent RMS error in atmospheric density forecast is obtained by comparing the predictions from the JBH09 model with the true densities computed using real temperature corrections from the High Accuracy Satellite Drag Model (HASDM). The frontal area variation is obtained by quantifying the ballistic coefficient error via their histories by satellite, going back in time up to a year. This process includes a preprocessor to handle outliers and regularize the ballistic coefficient histories to even-day values for subsequent reduction of persisted ballistic coefficient error.

The second feature to improve covariance realism in the SP catalog maintenance software is the scaling of the entire covariance by the weighted RMS of the batch differential correction at propagation-time. The covariance that appears in the vector covariance message (VCM) is not scaled this way; but when propagation is conducted by the operational system (and the SP astrodynamics standard), the entire covariance is multiplied by the square of the weighted RMS if it is greater than unity. There are apparently some theoretical arguments for why this is a statistically-sanctioned procedure, but there is no known published explanation that can be cited here.

3.1.3.2 Scale-Factor Computations for JSC ISS Conjunction Assessment

It was recognized early in the history of the ISS protection mission that secondary object covariances were in general undersized and that some sort of covariance scaling approach would be required. JSC performed analyses to compute a single scale factor value for each propagation point of interest; before using the secondary object's covariance in conjunction analysis activities, the entire matrix would be multiplied by this scalar value. The scale factor determination analysis compared, for a select number of satellites, propagated states to reference ephemerides to determine position difference statistics. If these errors are Gaussian in distribution and properly represented by the propagated covariances, then the entire family of such position differences should obey the following relationship:

$$\boldsymbol{r}^T \mathbf{C}^{-1} \boldsymbol{r} = \chi^2_{3dof} \tag{3.1.2}$$

in which r is the vector of position differences between the reference and propagated orbit and $\mathbf{C}$ is the position portion of the combined primary and secondary covariances, propagated to the time of closest approach. The left side of Equation (3.1.2) represents an entire set of points for which this computation has been made, and the right side indicates that it should conform to a chi-squared distribution with three degrees of freedom. The scale factor to be used, therefore, is one that brings the sample distribution as close to a 3-dof chi-squared distribution as possible. The approach used by JSC was to perform visual comparisons of CDF plots and make the determination this way. While some outlier rejection was performed, this is still often a superior approach in the presence of outliers, which tend to derail formal goodness-of-fit tests. Subsequent to their original efforts, JSC has also established a procedure to determine axis-by-axis scale factors (with each set proper to different propagation points). Since their original operational tool could only accept a single scale factor, their current operational practice is to run this tool (with a single factor) and then compare the results to an off-line utility that uses the axis-by-axis scale factors; and anecdotal

evidence does not document a significant deviation between the two approaches (i.e., the resultant values of P_C differ by less than an order of magnitude). The original calculation methodology and results are documented in [92], and an updated methodology and set of scale factors produced after the operational installation of the HASDM functionality is given in [153] and [154].

3.1.3.3 Aerospace Corporation Full-Correction Matrices

The Aerospace Corporation has for several years been pursuing an approach to provide full corrections of the position portion of covariance matrices. Their approach is to develop correction matrices that, when pre- and post-multiplied by an eigenvalue/eigenvector decomposed version of the propagated covariance matrix, will correct all six elements of that matrix to reflect proper scaling in all three axes and proper angular orientation of the covariance axes. State vectors and covariances (from VCMs) are propagated to the epoch times of future VCMs and position comparisons performed; and an elaborate technique, documented in [47] and [48], decomposes the set of matrices to be corrected into their individual components and forms a large linear problem with which to solve for the optimal value for each component of the inner correction matrix. A useful adjunct to this solution is the ability to determine confidence bounds on each correction element; these confidence bounds can be used to produce, say, a 5th percentile corrected covariance and a 95th percentile corrected covariance; these two corrected covariances, along with the nominal corrected covariances, can then be used in three separate P_C calculations to give a 5th, 50th, and 95th percentile P_C value. A confidence-region-enabled P_C calculation would be a very useful addition to conjunction-related risk analysis.

The Aerospace approach has sustained a validation activity, with NASA/GSFC serving as the independent validation agency; the validation report [111] has been completed, but unfortunately is available only to a restricted distribution. These correction matrices, which are calculated for each individual satellite and classes of satellites, all at a series of propagation points, were made available to certain customer sets in the fall of 2014.

3.2 Data Association/Correlation for UCT Resolution and Catalog Maintenance

The data association or correlation problem is that of determining which sensor report goes with which space object. The fusion problem is that of combining information from one or more sensors to improve the state of an object. These two aspects are inseparable parts of the same problem and both impact covariance or uncertainty realism. (Cross-tags degenerate the covariance as discussed in Section 1.1. The probability of association is used to better quantify the likelihood of cross-tags or misassociations.) Likewise, an unrealistic covariance can lead to cross-tags (i.e., misassociations). Before illustrating the sensitivity to unrealistic covariances, a brief review of data association methods is presented.

Data association or correlation methods for multiple target/object tracking divide into two broad classes, namely, single frame methods and multiple frame methods. The single frame methods include nearest neighbor, covariance based track association (CBTA) [6, 114, 116], single hypothesis or global nearest neighbor

based on a two-dimensional assignment problem formulation [38], and joint probabilistic data association (JPDA) (see, e.g. [25] and the extensive references therein). Nearest neighbor works well for widely-spaced objects, but can degenerate significantly as object spacing decreases. Global nearest neighbor extends the validity of nearest neighbor into the regime of closely spaced objects and works well in many track maintenance and low clutter environments. JPDA was developed as an algorithm for track maintenance of a few targets in dense clutter and has been highly successful for such problems. For closely spaced objects in dense clutter environments, JPDA suffers from the coalescence problem [37, 38]. JPDA mitigates misassociations, i.e., cross-tags, by averaging all the measurements within a neighborhood of the projected track. A recent article by Stauch, Baldwin, Jah, Kelecy and Hill [248] demonstrates JPDA for space surveillance. The most successful of the multiple frame methods are multiple hypothesis tracking (MHT) and multiple frame assignment (MFA), which is an optimization based MHT [224]. MHT/MFA methods mitigate misassociation (cross-tags) by providing an opportunity to change past decisions to improve current ones or, equivalently, holding ambiguous association decisions in abeyance until more information is available. MHT/MFA methods work especially well at the system level and in low to moderate clutter environments, but not necessarily in the domain of heavy clutter found at the sensor level. In dense tracking environments such as LEO breakups or GEO clusters with closely-spaced objects, the performance improvements of multiple frame methods over single frame methods are very significant. (The papers by Aristoff, Horwood, Singh, Poore, Sheaff, and Jah [17, 244, 244] demonstrates MHT for space surveillance.) In dense clutter environments where cross-tags are present, JPDA updates to the state covariance are found to improve covariance realism for single and multiple hypothesis tracking [74]. For heavy clutter environments, JPDA methods and those based on finite set statistics (FISST) [187] may be more appropriate.

Each of the above methods makes use of a statistical distance as an association metric whether it be track-to-track or sensor measurement to track, which is in turn based on a probability density function. For example, CBTA [6, 114, 116] uses the Mahalanobis distance (squared). For Gaussian processes, single and multiple hypothesis tracking methods use a negative log of a likelihood ratio, a component of which is a Mahalanobis metric (or distance squared) [224]. To demonstrate the importance of the covariance matrix in data association, consider the case of CBTA in which one measures the statistical distance between two objects using the Mahalanobis metric (see Alfriend [6], [116])

$$M^2 = (\boldsymbol{x}_1 - \boldsymbol{x}_2)^T (\mathbf{P}_1 + \mathbf{P}_2)^{-1} (\boldsymbol{x}_1 - \boldsymbol{x}_2) .$$

In this formulation, we have $M^2 \leq \chi^2_\alpha(6)$.

To demonstrate how sensitive the Mahalanobis distance (squared) can be to the right size and shape of the covariance, suppose $M^2 = \chi^2_{.05}(6)$, then $5M^2 = \chi^2_{0.0002}(6)$. Thus decreasing the size of the covariance by a factor of 5 leads to a change of 3 orders of magnitude in the confidence interval. In general, one would expect a value of 22.5 for a 99.9% confidence interval. However, in one study [116], 22% of the objects had a Mahalonobis distance squared (M^2) value that were greater than 100. This problem can be mitigated by inflating the covariances; however, if the covariance is too large, then for closely spaced objects the associations become ambiguous and cross-tags result. Thus, having a realistic covariance and more general uncertainty is essential for good association. Although this discussion applies to sensor track-to-track association in the presence of no auto or cross correlation, the same is true of associating radar measurements or

EO measurements to system tracks or orbits. Indeed, having realistic covariances is perhaps the single most important need if one is to achieve a superior space surveillance capability.

3.3 Maneuver Detection

Maneuver detection in cataloged space objects and identification of modeling errors for these objects are two sides of the same coin. While each of these usually have distinctive signatures, there is much room for ambiguity between the two. Thus we will treat them similarly in our discussion. The question at hand is what the impact of covariance realism for maneuver detection or model error identification.

Independent of mapping non-linearities or even the non-Gaussian nature of an object's probability distribution function, a key component of orbit determination and prediction is the 2nd moment of an object's uncertainty distribution, or the covariance. While every object has a covariance, it is technically unknowable at any instant and must be predicted from models or inferred from an aggregate of observations of a similar event. This issue is at the heart of covariance realism, and is what makes this problem fundamentally difficult. The most commonly used covariance for an object is the "formal covariance" that arises from a least-squares orbit determination process, in its most simple form just based on the assumed covariance values of the measurements. Such formal covariances are generally optimistic, and for enough measurements will generally over estimate the degree of certainty in an object's state. This holds true even if non-linearities are accounted for in mapping the uncertainty distribution, such as via an unscented transformation [156] or higher-order state transition tensors [218].

An over estimate of certainty, or a too-small covariance, is a core problem when wishing to detect maneuvers or model errors. If the true uncertainty of the object is larger than the predicted covariance, then algorithms that use the predicted covariance to identify statistically rare events as an indication of a maneuver will generate many false alarms, and thus will become untrustworthy. In essence, the maneuver detection algorithm will be detecting statistical variations as an indication of an actual event.

There are two main ways to deal with this problem, and in many cases both can be applied to obtain improved computed covariances. One approach is to better model the uncertainties associated with the known physical forces, measurement biases, and other effects that can influence the dynamics of an object or the measurements of that object. In this approach, sometimes called the "Consider Covariance," the effects of known uncertainties in other parameters that affect the trajectory and measurements of the space object are formally added to the formal covariance which comes out of an orbit determination filter (c.f., [254]). For Gaussian processes, the covariance in the object's state due to these uncertain parameters is just added to the formal covariance of the state due to measurements and mapping alone. Carrying out such an analysis requires exacting models of the dynamics and measurement systems, yet can produce very accurate corrections to the covariance when the physics of these effects and the associated uncertainties in their parameters are well understood. A proper covariance analysis can even be used to determine when certain parameters that would not normally be estimated have sufficient information content in the measurements to be better estimated. This approach to producing improved covariance estimates is widely used in the interplanetary spacecraft navigation community and has been highly refined. When properly defined, a consider covariance-motivated approach can be an effective tool in developing covariances that can be used

for maneuver detection or model improvement.

Despite the development of accurate physical models, the consider covariance approach generally has its limits, and ultimately our ability to model and know all the relevant physical forces acting on an object have a limit. For interplanetary spacecraft, this limit is often only reached for accelerations on the order of 1×10^{-13} km/s^2. For Earth orbiting satellites, however, our ability to gain this level of modeling precision is generally limited due to the atmospheric drag and solar radiation pressure effects. This limitation motivates the other approach that is often used to improve covariance computation.

If the physics of the environment are not well modeled or understood, or if the occurrence of a random event acting on the state is considered to be high, the covariance can be presumed to be acted on by stochastic accelerations as a function of time. Incorporating this into the uncertainty model adds to the formal covariance and causes the overall uncertainty to be higher. This is the approach that has been more commonly applied in the literature and described below.

3.3.1 Previous Work

Typical methods for dealing with uncertain dynamics in the state estimation process include adding process noise to the system, Dynamic Model Compensation (DMC), or appending dynamics parameters to the state vector (citeTaScBo2004,Jazwin1998. Process noise, while effective at preventing divergence due to mismodeling, only masks the problem. It provides no method for estimating the mismodeling, detecting its presence, it does not have a strong physical significance, and the uncertainty it injects in the system limits the accuracy of the state estimates. DMC requires a significant amount of tuning, and the type of dynamics it can replicate are limited by the Gauss-Markov functional form it assumes. Appending dynamics parameters to the state can be an effective method for recovering dynamics, but it requires a known model for those mismodeled dynamics.

Beyond these classical methods, the problems of dynamic mismodeling identification (maneuver detection) and mismodeling estimation (maneuver characterization/reconstruction and natural dynamics estimation) have been addressed for different systems. Generally, algorithms have been developed for highly dynamical systems (e.g. missile tracking and guidance) that are data-rich (i.e. observations taken throughout a maneuver). Methods such as Bar-Shalom and Birmiwal's Variable Dimension Filter [24] and Chan, Hu, and Plant's Input Estimation Method [50] directly append accelerations to the state vector for estimation when a maneuver is detected through residuals, but such methods require observation throughout a continuous maneuver. Patera's space event detection method [220] focuses more on quick events in an astrodynamics context, so it tends to neglect smaller maneuvers and natural dynamics mismodeling as well as being limited in application. Lemmens and Krag [175] addressed maneuver detection for LEO orbits with a Two-Line-Element-based method. Aaron [2] and Folcik, Cefola, and Abbot [89] addressed maneuver detection for Geosynchronous (GEO) orbits with a method based on application of the Extended Semi-analytic Kalman Filter (ESKF). These three methods produce promising maneuver detection results for astrodynamics applications, but they provide no information about the underlying maneuvers. Aside from DMC and appending parameter to the state vector in Kalman filtering, a method for estimating dynamics parameters is provided by Mandankan, Singla, Singh, and Scott [190]. This method relies on polynomial chaos. It provides both state and parameter estimates, but just like other methods it requires a model for mismodeled

perturbations and it does not have maneuver detection properties. Each of the methods described does not fully address the problem of detecting and estimating mismodeled dynamics in data-sparse systems. We seek an algorithm that will fully address the entirety of this problem in as automatic a fashion as possible. To accomplish this, we first must determine a framework that will allow us to approach each aspect of the problem.

The problems of object correlation, maneuver detection, and maneuver characterization in data sparse environments were addressed by Holzinger, Scheeres, and Alfriend [120] with a distance metric approach that is based on optimal control policies. They develop a concept called control distance metrics that measure the integrated control effort that connects two states at different times with a given dynamical model. The distance metric they introduced is an unweighted integral of the scalar quadratic control effort (see Equation (3.3.1)). To generate this metric an optimal control policy ($\boldsymbol{u}(t)$) that perfectly connects the boundary states is calculated and that control policy is integrated as shown in Equation (3.3.1) to yield the associated control distance metric. Control distance metrics discriminate based on how states are connected by control effort rather than state distance. This means if it is much more expensive (from a control standpoint) to move in one direction than another, a control distance metric will reflect this - a state distance metric will not. Singh, Horwood, and Poore [245] adapted the Control Distance Metric approach by using a minimum-fuel cost function, which yields impulsive control policies rather than smooth continuous controls. This makes the method far more numerical than the quadratic control policy approach. This optimal control framework is shown to be quite effective at maneuver detection and characterization in data-sparse systems. Also, it only requires two state estimates at different epoch that may be generated by an independent estimation process, so it does not require cooperative observation. This satisfies all of the requirements of the introduced problem, so it is a good framework from which to approach this problem.

$$d_C = \int_{t_a}^{t_b} \frac{1}{2} \boldsymbol{u}(\tau)^T \boldsymbol{u}(\tau) d\tau \tag{3.3.1}$$

Work with this control distance metric framework has been limited to object correlation, maneuver detection, and characterization.

3.3.2 Approaches to Maneuver Detection

There has been additional recent work on maneuver detection. We call out two specific approaches that take differing philosophies to this problem. One approach develops a generic model for any mis-modeling or thrusting maneuver between measurement epochs, providing a filter with an additional set of parameters that can represent a maneuver over an arbitrary time span and across a wide range of magnitudes and maneuver morphologies. The other approach utilizes the control distance metric defined above to systematically separate non-gravitational modeling errors from what may be maneuvers. Both of these approaches rely on and are aided by the inclusion of realistic covariances. Further, when implemented systematically both of these methods will enable the formal or consider covariances for an object to align more strongly with a realistic covariance.

3.3.2.1 Essential Thrust Coefficients

In an earlier series of research by Hudson and Scheeres [129–131] a particular averaging result regarding the Gauss equations using arbitrary thrusting coefficients was discovered and investigated. That work focused on modeling arbitrary, infinite dimensional control sequences using Fourier Series expansions in different orbital anomalies. It was found that by expanding an arbitrary control as a Fourier Series in Eccentric Anomaly that it could be described by only 14 coefficients, proscribing constant, period 1 or period 2 thrusting in the radial, transverse or normal direction. The Hudson and Scheeres papers [129–131] investigate this representation analytically and numerically to fully confirm this result, to explore the limitations when the control magnitude is large, and to investigate possible applications of this result.

More recently, Ko and Scheeres [164, 165] investigated specific SSA applications of this result. The fundamental idea behind this work is the use of these thrust coefficients to act as a rigorous basis with which unobserved maneuvers performed by a satellite could be represented. Specifically, if a non-zero control distance for a satellite is detected (assuming knowledge of the state at two epochs) it should be possible to represent the unobserved maneuver (or unmodeled forces) in an infinite number of ways using the Thrust Fourier Coefficients, as there are only 6 constraints (if a change in state is detected) but 14 different coefficients to be specified. To investigate this in more detail a systematic study was made to map out the null space in the averaged mapping between Thrust Fourier Coefficients and changes in orbit elements, as this is a linear mapping under standard orbit averaging assumptions. There are a number of obvious singularities between these items, however once those have been removed there are still many possible combinations. It is important to note, however, that 1-1 maps between Thrust Fourier Coefficients and changes in orbit elements can be identified. In [165] there are 6 specific collections of coefficients that are identified as both being 1-1 with arbitrary changes in orbit elements and providing good agreement between averaged predictions and full numerical integrations of these thrust coefficients. Out of this collection we chose one particular set using somewhat arbitrary criterion. This set is notable as it only involves constant and period 1 coefficients, specifically a constant radial coefficient, a constant and period 1 cosine and sine transverse coefficients, and a period 1 cosine and sine out of plane coefficients.

The implication of this result is fundamental: any maneuver performed by a satellite transitioning between two arbitrary sets of orbit elements can be represented on average as an equivalent maneuver involving constant and period 1 Thrust Fourier Coefficients in the radial, transverse and normal direction. The initially derived result was just relevant for orbit elements under an assumption that the thrust magnitude is relatively small. However, this representation can be extended to non-averaged thrusting between Cartesian positions and velocities, indicating a level of universality in these thrust coefficients.

This realization is developed in [165] and a computational algorithm for representing any change in orbit state as an equivalent maneuver using a combination of constant and period 1 thrust laws is given. As such, given a non-ballistic trajectory between two epochs due to a maneuver (or due to mismodeling) it is possible to smoothly interpolate between these states using a unique control law. The procedure developed can be carried out in three basic steps, although the initial steps can sometimes be discarded.

There are several possible applications of this result. In its most basic form, the result provides a unique and rigorous way to interpolate between two non-ballistic states at specified epochs. More recent studies show that it is possible to carry along initial uncertainties (such as covariance matrices) along the interpolated

trajectory [164]. This could enable non-ballistic events along a satellite's trajectory to be automatically incorporated if the start and end orbit states are known, essentially enabling filtering across a maneuver. A significant benefit of this is that it would allow pre and post maneuver tracking to be combined into a single trajectory. It also enables a common representation of maneuver events using these coefficients instead of estimates or guesses of what the actual maneuver was. Once the maneuver is expressed in this basis, it can be further analyzed off-line. As one example of this, mapping a particular set of coefficients into estimates of a series of impulsive maneuvers was investigated by Hudson and Scheeres in [130].

3.3.2.2 Control Distance Metric Decomposition

Previous research has outlined how the control distance metric can be used to identify the abstract distance between two spacecraft states in terms of the optimal control guidance law to connect these states and epoch [120]. An optimal guidance law is unique for the given cost function, however the nature of the guidance laws can vary significantly as a function of the cost function. As a simple example, a minimum norm cost function will generally result in discontinuous maximum thrust segments, whereas a least-squares cost function results in a continuous and smooth thrusting profile that is always on.

More fundamentally, the existence of a non-zero control distance does not mean that a maneuver has occurred, however, as any modeling error in the dynamics or errors in the boundary states would also result in a non-zero control distance between two disparate states. This situation raises a fundamental question regarding the utility of the control distance as a maneuver detection methodology.

Given two states with a non-zero control distance, is it possible to discriminate between modeling errors, state errors or the existence of a maneuver between these state epochs?

A methodology has been developed, based on the control distance theory, to discriminate between these competing possibilities. A detailed study of this method is presented and outlined in [181, 182]. The method is motivated by a few observations regarding optimal guidance laws, mis-modeling and environmental forces. As this method attempts to address questions for which there is insufficient information, there is no definitive answer to the question regarding whether a maneuver has occurred. However, the approach identifies common mis-modeling hypotheses and applies them to determine if control distance discrepancies still exist once gross modeling errors are corrected.

Observations on environmentally mis-modeled forces Environmental forces that act on space objects are generally continuous and smooth. Exceptions occur if an abrupt change in the space object properties occur, however this would nominally be labeled as a maneuver. Furthermore, the nature and magnitude of the forces that act on space objects are quite well known, with some specific exceptions. Thus, the gravity field, 3rd body perturbations, and even upper-atmosphere density errors are either small or can be tracked and calibrated after the fact.

A major exception to this are the non-gravitational parameters that describe how the environmental forces of atmospheric drag and solar radiation pressure act on a space object. Even though the environmental component of these forces can be well characterized or reconstructed, the relevant coefficients can and in general do have significant errors and uncertainties. Due to this, the prime and most common errors in the force models acting on a space object are due to errors in these coefficients. The method described here

directly relies on this fact and focuses on improvement of these coefficients as the prime pathway to model improvement. In the following discussion, and in the theory as outlined in [181, 182], we assume a simple cannonball model for the object in question. We note that this could be replaced with a higher fidelity model if additional information on an object's geometry or attitude is known.

Observations on control distance cost metrics As noted above, the cost metric used in computing the control distance has a fundamental influence on the properties of the resulting optimal guidance law. In a detailed study provided in [182] and summarized in [181], it is found that a least-squares cost metric will mimic un-modeled drag and SRP forces. This is not wholly unexpected, as a least-squares optimal guidance law will be continuous and smooth and will strive to minimize the overall deviation of the control acceleration from zero. Similarly, while natural forces are not in any sense optimal, the motion that ensues from physical forces does satisfy certain optimality constraints. Specifically, the trajectory arising from applied forces will minimize the action integral, which in general will have a quadratic structure in the vicinity of the true trajectory. In contrast, a minimum norm cost metric would mimic natural forces with a finite series of impulses, which is far from their physical realization.

Method for developing modeling updates The above observations motivate the following methodology for identifying and correcting modeling errors that would otherwise be ascribed to state errors or maneuvers. The process given in [181] is as follows:

1. Compute the control distance and associated guidance law for a least-squares cost function
2. Fit atmospheric drag and SRP forces against this guidance law, minimizing the difference between the optimal guidance law and the physics-based force functions by choosing updated coefficients
3. Apply estimated coefficient corrections to existing non-gravitational coefficients
4. Recompute control distance and optimal guidance law with new non-gravitational force terms
5. Repeat until convergence is achieved, represented by zero or minimal updates to non-gravitational coefficients

Following this process, the resulting control distance and optimal guidance law can be subject to further inspection and analysis to determine if any non-zero components are due either to state errors or to the existence of a maneuver. If the non-zero control distance was due entirely to non-gravitational coefficient mis-modeling this process could recover the true model and yield, in the limit, a zero control distance.

This process is separate from a traditional filter estimation in a few ways. First, in the control distance computation part there are no hypotheses on what the non-zero control distance is due to. This ensures that the generated optimal guidance law is purely a function of the current physics and state mis-match. Second, in the update phase, the solution that minimizes the difference between the optimal guidance law and the non-gravitational physics has a simple and immediate solution, requiring no further iteration for the given guidance law. Finally, this process does not try to remove all state offsets by model adjustment, but will only remove those portions that can reasonably be removed through improved non-gravitational

coefficients. References [181, 182] provide significant details and examples of how this methodology can be applied to Earth orbiters, incorporating non-simplistic models for environmental forces.

3.4 Sensor Tasking and Scheduling

The goal of sensor tasking and scheduling for a network of sensors is to allocate resources appropriately in order to gain as much information as possible about a system. A sensor tasker and scheduler must optimize system performance while simultaneously meeting as many, if not all, of the requirements as possible. Sensor tasking and scheduling also entails re-planning those tasks that cannot be completed over a specified time period. While the architectures for planning the assignment of tasks to sensors over a single or multiple time periods may be centralized or distributed/decentralized, the function of scheduling is normally left to the sensor level processing as opposed to the network level.

An excellent summary of the current system used by the United States to perform the detection and tracking functions of SSA, the Space Surveillance Network (SSN), is contained in [202], which includes current methods for tasking the network as well as proposed improvements. Other references documenting sensor management techniques in applications relevant to the SSA mission include Sharma et. al. [240], which discusses the tasking of a space-based space surveillance sensor, and Ben-Asher & Cohen, which covers scheduling of radar resources in the context of a Ballistic Missile Defense (BMD) scenario. [30].

Of specific importance is the distinction between sensor *tasking* and sensor *scheduling*. Sensor tasking involves the generation of a set of tasks that a sensor or sensor network is intended to accomplish, leaving the specifics of accomplishing those tasks (e.g., timing, etc.) to the performing entities. By contrast, sensor scheduling involves not only the assignment of tasks, but also the decisions on the specifics involved in the tasks, to include the timing of when the task must be accomplished.

This distinction is important due to the current state of affairs of the US Space Surveillance Network and the associated commanding and tasking systems, which were designed around a centralized tasking and distributed/decentralized scheduling architecture. Beyond the issues of net-centric command and control infrastructure, there are also further complications in the implementation of centralized scheduling of some of the SSN sensors due to their primary mission as missile warning systems. Given that RSO tracking is a secondary mission for these radars, it is unclear how this constraint would be posed or handled within centralized sensor scheduling approaches. Sensors also have constraints in regards to the number of tracks that can be collected per day as well as their ability to respond to an arbitrary sequence of tasks. These issues complicate algorithms intended to be implemented on the current system.

For the rest of this discussion, we will not make the distinction between tasking and scheduling, but will instead refer to whichever is appropriate via the term *sensor management*, which has been adopted widely in the literature [211, 225]. In general, sensor management has been posed as an optimization problem under uncertainty whether it be a stochastic dynamic programming or deterministic. In the case of acquiring sensor reports or measurements of orbits, one has to optimize the use of space track sensors, radars for low altitude and telescopes for high altitude objects, in the collection of data. In essence, the optimal control problem is to pick an assignment of resources (sensor observation time) against tasks (collection of data on various space objects) that minimizes some cost or utility function, subject to various constraints (e.g.,

line-of-site exists between sensor and target, etc.). The resulting problem is variously known in the literature as Information-theoretic Control/ Active Sensing and Dual Control [93, 104, 109, 119].

It is very well known that stochastic control problems with sensing uncertainty, of which sensor management problems are a special case, can be posed as a Markov Decision Problem (MDP) on the information state, which is usually the conditional filtered PDF of the state [34, 159, 171]. Unfortunately, such problems are notoriously difficult to solve owing to the twin curses of dimensionality and history and have only been solved for small to moderate sized discrete state space problems. A number of approaches have been proposed using simulation-based stochastic search techniques in an attempt to break these computational issues for moderate to large-scale problems [118, 135, 251, 252].

The cost or utility function used in these approaches can vary, but in many cases it will be some function of *information gain*, with information here being the inverse of uncertainty. In this context, information gain is, roughly speaking, the reduction in uncertainty that an decision or sequence of decisions would yield. In the context of SSA, this would translate into the reduction in the uncertainty of the state of the space objects, with state here including not only typical track variables (position/velocity, or some equivalent orbit element set), but also possibly other parameters inferable from observation data such as shape, mass, area, etc.

Many such measures have been proposed, including simple covariance measures [85, 117] as well as more general information divergence measures including Kullback-Leibler [113, 168], Renyi [167, 226], and Cauchy-Schwartz [66]. Regardless of what measure is used, the gain is calculated between the expected uncertainty that would result if a sensor observation was commanded (an expected posterior) and the expected uncertainty if one was not (the prior). The problem is then to find the sensor-object pairings that maximize the aggregate or sum of this information gain over all possible sensor-object pairings. This optimal pairing becomes the optimal management approach, and determines the future observations.

This feedback between the result of the observations and what observations will be collected in the future couples the particulars of the estimation approach used and the management approach used. If the uncertainty in the predicted state is not realistic, some objects will receive un-needed updates that don't significantly reduce our uncertainty, while and others may be lost due to lack of observations that were actually needed. Thus, the need for consistent covariances and more generally realistic uncertainty permeates the management of the sensor resources.

Research into the effects of this coupling has provided a number of interesting results - specifically, that the feedback between the estimation and tasking/scheduling results in cases where improving the estimation method only (and keeping the management method the same) results in less data being required to achieve lower uncertainties [288].

Variations on the general optimization approach discussed above have been examined in the literature. Investigations have been made into how to use sensor management to drive the shape of the uncertainty to desired forms [160] rather than simply reducing the scalar information gain during the optimization process. Other measures beyond information gain have been considered for use in optimizing sensor tasking/scheduling - for example, the use of Lyapunov exponents was considered in [289]. This approach is interesting in that it focuses observations on those objects with dynamics that are the least stable with respect to the modeled dynamics (i.e., the objects hardest to predict accurately). This approach has considerable connections to Orbit Classes used in [202].

Beyond simple metric observations, the SSN system is also tasked within the space community to collect other types of observations that may require operating in a different mode or involve different constraints. Examples of this would be the operation of a sensor in different track modes in order to collect astrometric data (e.g., right ascension & declination measurements) versus photometry (light curve) data. Another example would be the need to operate a sensor in a search mode to search for new, as yet undetected, objects versus a track mode in order to provide additional data on objects that have already been detected. Research has been conducted on the development of methods that can deal with hybrid-state (discrete-valued elements and continuous-valued elements) estimation and sensor management problems that arise in these situations. An example hybrid state would include a quantized element related to how many objects have been detected combined with estimated state variables (position/velocities) for these objects. Random Set Theory and the Finite State Statistics (FISST) approaches provide an elegant and theoretically rigorous approach to such problems, but have the issue of high computational requirements and poor scaling with problem size. Research has been conducted combining the FISST framework with computationally efficient approaches for uncertainty propagation that show some promise to providing a unified framework that can handle hybrid-state estimation and management tasks [79–82, 134, 135]. But the computational complexity of these approaches is still daunting when faced with the thousands of objects that the SSN must track.

In view of the current SSN system, algorithms and methodologies that can deal with the distributed decision making by the individual sensor sites, partial (delayed) information due to the human-driven tasking cycle timing, and uncertain external constraints (such as those represented by the primary missile warning mission) are of high interest. Approaches could include a game-theoretic approach, where the sensor sites that will implement the tasking are independent agents not under the direct control of the centralized planning agent. Such approaches would have to consider all possible actions by the distributed agents in the development of a schedule/tasking plan, not only a single action from each player that is optimal with respect to (for example) an information utility function. The ability to model the response of sensor sites to tasking or scheduling commands would be helpful - even a stochastic response model (e.g., faced with this request, the site will perform the request with such-and-such probability) would be helpful for future efforts. Techniques that can include the ability to handle task dependent constraints (e.g., time required to re-point from last observation taken) and various communications constraints (e.g., space-based systems are not in 24/7 ground contact) would also be relevant. Some theoretical research in distributed optimal filtering under communication constraints has been performed along these lines in the controls community driven by other applications [214, 216].

Chapter 4

Structural and Parametric Uncertainties in the Astrodynamic Force Models

This chapter has three parts. Section 4.1 presents generic reference systems, time systems, and astrodynamic force models used as a reference for discussing the uncertainties in these models. Section 4.2 makes an attempt to delineate and quantify the structural and parametric uncertainties. Recommendations for reducing and properly characterizing these uncertainties are given in Section 4.3.

4.1 Force Models, Time, and Reference Systems

Commonly used reference systems, time systems, and force models for orbit determination, orbit propagation, and other SSA functions are presented in Subsections 4.1.1, 4.1.2, and 4.1.3, respectively. Much of the material is extracted with permission from Vallado [262, Chapters 8 and 9], which was also the basis for Vallado [261] and Gurfil [106].

4.1.1 Reference Systems

The equations of motion are naturally expressed and solved in an inertial frame of reference. For example, one can use the Geocentric Celestial Reference Frame (GCRF) as the inertial reference frame, and the International Terrestrial Reference Frame (ITRF) as the Earth-fixed reference frame. Hence, the coordinate frame rotations include the International Astronautical Union (IAU) 1976 precession, IAU 1980 nutation, IAU 1982 Greenwich Mean Sidereal Time (GMST), and the 1994 equation of equinox*. This is known as the IAU-76/FK5 system and the transformations are detailed in International Earth Rotation and Reference Systems Service (IERS TN-13). Corrections are periodically made with respect to coordinate systems and a series of updates has resulted in the IAU 2010 conventions (IERS 2010) which make use of the non-rotating origin. This is the recommended procedure of the IERS. The 1996 conventions were an intermediate form

*The inertial-to-fixed (and fixed-to-inertial) rotations are used in several places in a tracking system. During orbit propagation, evaluation of the Earth gravity model (Subsection 4.1.3.1) requires these rotations, as do measurement transforms involving right ascension/declination pairs.

that is still sometimes used [223]. More information on these models may be found in the conventions descriptions [207] and [262].

The celestial frame is related to a time-dependent terrestrial frame through an Earth orientation model, calculated by the standard matrix-multiplication sequence of transformational rotations:

$$\boldsymbol{r}_{GCRF} = \mathbf{P}(t)\mathbf{N}(t)\mathbf{R}(t)\mathbf{W}(t)\boldsymbol{r}_{ITRF} \tag{4.1.1}$$

where $\boldsymbol{r}_{GCRF}$ is location with respect to the GCRF, $\mathbf{P}$ and $\mathbf{N}$ are the precession-nutation matrices of date (t), $\mathbf{R}$ is the sidereal-rotation matrix of date (t), $\mathbf{W}$ is the polar-motion matrix of date (t), and $\boldsymbol{r}_{ITRF}$ is location with respect to the ITRF. A combined $\mathbf{PN}$ matrix may be formed as a single operator, depending on the theory adopted. The rotations in equation (4.1.1) are collectively known as reduction formulas (Seidelmann, [236]) or an Earth orientation model. There are two approaches for the reduction formulae: the classical transformation and the Celestial Intermediate Origin (CIO). The latter theory is defined by IAU Resolutions. The IAU-2010/2000 Resolutions were officially released over a period of time (McCarthy and Petit [198], and Kaplan [162]). These resolutions stated that beginning January 1, 2003, the IAU-1976 Precession Model and the IAU-1980 Theory of Nutation were replaced by the IAU-2000A Precession-Nutation theory (accurate to 0.0002”). The IAU-2010 Conventions combined and updated these resolutions (Petit and Luzum [223]) . As of January 1, 2009, the IAU-2000A Precession-nutation theory was separated into the IAU-2000 Nutation theory and the IAU-76 Precession was replaced with the IAU-2006 Precession, also called the P03 model (Capitaine, Wallace and Chapront[45], and Wallace and Capitaine [280]). Before 2003, the recommended reduction to GCRF coordinates was the IAU 1980 Theory of Nutation, plus the corrections ($\delta\Delta\psi_{1980}$, $\delta\Delta\epsilon_{1980}$) given in the Earth Orientation Parameters (EOP) data.

4.1.2 Time Systems

The transformations between the GCRF, ITRF, and intermediate systems are defined by terrestrial time (TT), which can be determined directly from universal time coordinated (UTC), the time system in which measurements are typically provided. Terrestrial time is a dynamical time scale that can be used for precise orbit propagation, and when converting from UTC to TT, leap seconds are taken into account. Time can be expressed in seconds with respect to the J2000 epoch.

Solar time is based on the interval between successive transits of the Sun over a local meridian, which establishes the solar day. This concept has served adequately for ages. The Sun’s apparent motion results from a combination of the Earth’s rotation on its axis and its annual orbital motion about the Sun. UTC is the common time in use today. Sidereal time is the time between successive transits of the stars over a particular meridian. Because the stars are several orders of magnitude more distant than the Sun, their relative locations as seen from Earth don’t change much even during a year. UT1 is the common sidereal time in use. The most commonly used time system is Coordinated Universal Time, UTC, which is derived from an ensemble of atomic clocks. It’s designed to follow UT1 within 0.9s (ΔUT1 = UT1 - UTC). UTC is the basis of civil time systems and is on ordinary clocks. This definition of UTC was introduced in January, 1972, as a convenient approximation of UT1. It’s sometimes called Zulu time, but UTC is more precise. Because UT1 varies irregularly due to variations in the Earth’s rotation, we must periodically insert leap

seconds into UTC to keep the two time scales in close agreement.

A highly accurate time system which is independent of the average rotation of the Earth is based on a highly regular occurrence – International Atomic Time, Temps Atomique International, or TAI, is based on counting the cycles of a high-frequency electrical circuit maintained in resonance with a cesium-133 atomic transition. Terrestrial time, TT, is the theoretical timescale of apparent geocentric ephemerides of bodies in the solar system (Seidelmann [236]). TT is independent of equation of motion theories and uses the SI second as the fundamental interval. It is related to other times as follows:

$$\begin{aligned} UTC &= UT1 - \Delta UT1 \\ TAI &= UTC + \Delta AT \\ TT &= TAI + 32.184s \end{aligned}$$

4.1.3 Force Models

This section discusses the various generic force models including Earth gravity models, third-body perturbations, drag models, solar radiation pressure models, and tide models. Only accelerations on the order of 10^{-11} km/s^2 and above are considered (see Figure 3.1 of [207]).

4.1.3.1 Earth Gravity Models

Modeling Earth gravitation uses a spherical harmonic potential equation in an Earth-centered, Earth-fixed reference frame with the origin at the center of mass of the Earth. The gravitational potential acts on a satellite and is given as:

$$V = \frac{\mu}{r}\left[1 + \sum_{n=2}^{\infty}\sum_{m=0}^{n}\left(\frac{R_\oplus}{r}\right)^n P_{nm}(\sin\varphi_{gcsat})(C_{nm}\cos m\,\lambda_{\text{sat}} + S_{nm}\sin m\,\lambda_{\text{sat}})\right] \tag{4.1.2}$$

where μ is the gravitational parameter, r is the satellite radius magnitude, φ_{gcsat} and λ_{sat} are the geocentric latitude and longitude coordinates of the satellite, respectively, $R_\oplus$ is the earth radius, n and m are the degree and order, respectively, and C_{nm} and S_{nm} are the gravitational coefficients[†]. The acceleration on the satellite is the positive gradient of the potential function, and many approaches exist for evaluating said gradient (as well as different formulations that are singularity-free). The Legendre polynomials are defined by

$$P_n(x) = \frac{1}{2^n n!}\frac{d^n}{dx^n}(x^2-1)^n \text{ and } P_{nm}(x) = (1-x^2)^{m/2}\frac{d^m}{dx^m}P_n(x).$$

The Legendre functions (polynomial or associated function) are called zonal harmonics when $m = 0$, sectoral harmonics when $n = m$, and tesseral harmonics when $n \neq m$.

The first attempts to standardize models of the Earth's gravitational field and the shape of the Earth were begun in 1961. Currently there are several prevailing gravitational models being used within the scientific community for a variety of purposes. These models are determined from a wide range of measurement

[†]For a sufficiently small degree and order, the error in the published gravitational coefficients can be safely neglected for most applications.

types, satellite inclinations and altitudes including surface gravity measurements and satellite altimetry data. An example earth gravity model is the (zero-tide) 2008 Earth Gravity Model [221].

4.1.3.2 Third-Body Perturbations

The presence of third bodies (e.g., Sun, Moon, Venus, Jupiter) perturb the trajectory of Earth-orbiting satellites. The Sun and Moon give rise to gravitational perturbations on the order of 10^{-9} km/s^2, Venus and Jupiter on the order of 10^{-14} km/s^2. Hence Solar and Lunar perturbations are appreciable, whereas perturbations arising from Venus, Jupiter, and the other planets are not relevant in most applications. These are also called n-body perturbations acting on the satellite. The contributions are computed using a point-mass equation. However, the Sun and Moon also include an indirect effect as an interaction between a point-mass perturbing object and an oblate earth. Thus the third-body perturbation includes both direct and in-direct terms of point mass third-body perturbations. Such gravitational perturbations are modeled by considering the acceleration of a satellite by a point mass,

$$\boldsymbol{a}_{3body} = -\frac{G(m_{\oplus} + m_{sat})\boldsymbol{r}_{\oplus\cdot sat}}{r^3_{\oplus\cdot sat}} + Gm_3\left(\frac{\boldsymbol{r}_{sat\cdot 3}}{r^3_{sat\cdot 3}} - \frac{\boldsymbol{r}_{\oplus\cdot 3}}{r^3_{\oplus\cdot 3}}\right) \tag{4.1.3}$$

where G is the gravitational constant, $\boldsymbol{r}_{\oplus\cdot sat}$ and $\boldsymbol{r}_{\oplus\cdot 3}$ are the Earth-centered-inertial position of the satellite and third body, respectively, and $\boldsymbol{r}_{sat\cdot 3}$ is the position of the third body relative to the satellite.

In order to evaluate (4.1.3), one must determine the position of the third body at a given time. A number of analytical models of varying fidelity have been developed for such a purpose [207]. Alternatively, one may utilize high-precision ephemerides from the Jet Propulsion Laboratory via the Horizons Online Ephemeris System, provided that interpolation of sufficient fidelity is used.

4.1.3.3 Aerodynamic Drag Models

Atmospheric density can lead to significant perturbation effects for satellites below about 1000 km altitude, but its effects can be observed at altitudes up to 2500 km. The acceleration due to aerodynamic drag for the often used cannonball model is

$$\boldsymbol{a}_{drag} = -\rho\frac{c_D A}{2m}|\boldsymbol{v}_{rel}|\boldsymbol{v}_{rel} = -\rho\frac{c_D A}{2m}v_{rel}\boldsymbol{v}_{rel}$$

ρ Atmospheric density at LEO altitudes (recently reviewed by Emmert [83]) depends primarily on solar ultraviolet (especially extreme ultraviolet) irradiance, energy from the solar wind and magnetosphere, and dynamical forcing from the lower atmosphere. These influences on density act mainly through changes in temperature and the associated expansion or contraction of the upper atmosphere. The solar and magnetospheric energy inputs are usually represented in models using proxies, most commonly the F10.7 solar radio flux for UV irradiance and a variety of ground-based geomagnetic activity indices for the magnetospheric energy input. The use of proxies itself introduces uncertainty into the modeled density, and the differing choices and applications of these proxies are a source of model-to-model variation. Lower atmospheric influences are currently neglected in operational aerodynamic drag models. Density, which is perhaps the largest contribution to error in LEO orbit determination and

prediction, varies on a broad range of spatial and temporal scales, many of which are not captured (and may never be captured) by models.

c_D The coefficient of drag is related to the shape, as well as the satellite materials, but ultimately it is a difficult parameter to define. Gaposchkin [94] mentions that the c_D is affected by a complex interaction of reflection, molecular content, attitude, etc. It will vary, but typically not very much as the satellite materials usually remain constant. In addition, it depends on the composition and temperature of the atmosphere

A The cross-sectional area changes constantly (unless there is precise attitude control, or the satellite is a sphere). This variable can change by a factor of 10 or more depending on the specific satellite configuration. Macro models are often used for modeling solar pressure accelerations in orbit determination, but seldom if ever, for atmospheric density. There could also be a benefit for applying this technique to atmospheric density for propagation.

m The mass is generally constant, but thrusting, ablation, etc., can change this quantity.

$\boldsymbol{v}_{rel}$ The velocity relative to the rotating atmosphere depends on the accuracy of the *a-priori* estimate, and the results of any differential correction processes. Because it is generally large, and squared, it becomes a very important factor in the calculation of the acceleration. $|\boldsymbol{v}_{rel}| = v_{rel}$ is the magnitude of the vector $\boldsymbol{v}_{rel}$.

The ballistic coefficient ($BC = m/(c_D A)$)) is generally used to combine the mass, area, and coefficient of drag values together. It will vary, and sometimes by a large factor. In orbit determinations, it may not be best to model the combined parameter because it includes several other time-varying parameters that are perhaps better modeled separately. There can also be lift and side force components due to the atmospheric effects. This is especially true for reentering objects. These additional components act in-plane and out-of plane. They are rarely modeled but they do contribute to uncertainty in some situations. In orbit determination applications, it may not be best to model the combined parameter because it includes several other time-varying parameters that are perhaps better modeled separately.

4.1.3.4 Solar Radiation Pressure Models

The force due to solar radiation pressure (SRP) arises when photons from the sun strike a satellite surface and are absorbed (or reflected – specular and diffuse) and thus transfer an impulse to the satellite. Unlike atmospheric drag, the SRP force does not vary with altitude and its main effect is a slight change in the eccentricity and longitude of perigee. The effect of SRP depends on the satellite mass and surface area and is most notable for satellites with large solar panels like communications satellites and Global Positioning Satellites (GPS), or with objects that have High Area to Mass Ratios (HAMR). SRP is often the dominant perturbation for HAMR objects. In cases of geodetic precision orbits, complex models of the exposed satellite surfaces are created often using finite-element computer codes. This is the case with GPS. To find the acceleration due to solar radiation pressure,

$$\boldsymbol{a}_{srp} = -\rho_{SR}\frac{c_R A_{Sun}}{m}\frac{\boldsymbol{r}_{sat-Sun}}{|\boldsymbol{r}_{sat-Sun}|} \tag{4.1.4}$$

ρ_{SR} The incoming solar pressure depends on the time of year, and the intensity of the solar output. Its derived from the incoming solar flux and values of about 1358-1373 W/m^2 are common.

c_R The coefficient of reflectivity indicates the absorptive and reflective properties of the material, and thus the susceptibility of the satellite to the effects of incoming solar radiation. Note that recent research indicates a bi-directional c_R may be more realistic [285].

A_{Sun} The cross-sectional area (with respect to the Sun) changes constantly (unless there is precise attitude control or the satellite is a sphere). This variable can change by a factor of 10 or more depending on the specific satellite configuration. Macro models are often used for geosynchronous satellites. This area is generally not the same as the cross-sectional area for drag. If the satellite attitude is known, the time-varying cross-sectional area may be found at each time, thereby increasing the accuracy of any propagation.

m The mass is generally constant, but thrusting, ablation, etc., can change this quantity.

$\boldsymbol{r}_{sat-Sun}$ The orientation of the force depends on the satellite-Sun vector and is usually different from atmospheric drag.

Similar to atmospheric drag, the solar radiation force is not necessarily exactly along the Sun-satellite vector. In this case, the components are related to the ecliptic plane. There are components orthogonal to this vector, and they can influence the uncertainty.

Accurate modeling of solar radiation pressure is challenging for several reasons. A significant factor is the use of a model to include times when the satellite passes through the Earth's shadow. The model may take several forms, including a simple cylindrical model, to one that models precise umbral and penumbral regions. Models also consider the attenuation effect that the Earth's atmosphere has on the shadow region. Some programs accomplish this with an effective Earth radius that is slightly larger (say 23 km) than the Earth's physical size. Depending on the length of time in the shadow, these options can have a dramatic effect on propagations.

Determining the exact times of entry and exit from the Earth's shadow is important as the satellite will usually cross from sunlight to being in the shadow in the middle of a numerical integration step. This usually requires some type of iteration to obtain the precise entry and exit times.

Using a single value for the incoming solar luminosity, or equivalent flux at 1 AU can also alter the resulting perturbing values. There are seasonal variations in the amount of incoming luminosity that can be included in these values.

Albedo is the radiation pressure emitted from the Earth which causes a small perturbing force on a satellite. Although the effect of SRP is usually far larger, the effects of Earth's albedo can be comparable for certain configurations of orbits (e.g. sun-synchronous). The acceleration due to albedo is generally expressed in terms of a second degree zonal spherical harmonic model, and contributions from various Earth sectors are summed to determine the overall effect.

4.1.3.5 Tide Models

Earth tidal effects on satellites are due to pole tides, ocean tides, and solid earth tides. Most of the data that have resulted in a definitive model have come about within the last couple of decades from Earth observation satellites such as TOPEX and GRACE. As these satellite observations have been processed over the last 20 years, the former rigid Earth model has slowly changed to an elastic Earth model. The basis of the models for pole, solid earth and ocean tide models can be found in the IERS Conventions, with updates in McCarthy and Petit [196–198]. Tidal models do not enjoy the variety of the gravitational and atmospheric models yet, but there are several different approaches. Properly implementing these various models can be a factor if precise comparisons are desired. At this point in time, several models exist, and no clear "leader" has been recognized as the standard approach.

Pole tides define the rotational deformation of the pole due to an elastic Earth. These are modeled by the C21 and S21 coefficients in the Earth's potential. Solid earth tidal contributions are computed as corrections to the spherical harmonics coefficients, as are the ocean tidal contributions.

4.1.3.6 Other Forces

As the accuracy of orbit determination and propagation increases, additional force models are included in analyses. In particular, applications using GPS data often must account for the (primarily) apsidal rotation caused by General Relativity. GPS signals must also be corrected for General Relativity, as well as atomic clock corrections. The effects of General Relativity are very small and only become important where orbit precision below the cm-level is needed. Satellite thrusting can also be a significant perturbing force. Many satellites use maneuvers for mission operation and for orbit maintenance. The forces induced by these motor firings can be large or small. We do not describe these in any detail, but introduce the forces as something needing to be considered in mission planning and precision orbit determination modeling.

4.2 Uncertainties in the Dynamics and Space Environment

Given the above models or any other collection of models, is it possible to characterize the structural and parametric uncertainties? The answer is yes, but there are several considerations that are necessary. Looking at Figure 3.1 in Montenbruck and Gill [207], the force of atmospheric drag is the largest source of uncertainty in the prediction of trajectories of most objects in low Earth orbits, given that uncertainty in the ballistic coefficient can be as high as a few percent. Solar variability is the largest source of error in upper atmospheric density forecasts. In addition to uncertainties in the force models, time and coordinate systems can introduce uncertainty in the solution.

EOP files are necessary for accurate time and coordinate system use in orbit determination and propagation, and sources like CelesTrak consolidate current values. However, not all systems use current EOP files, and the predicted values change continuously, although they are reasonably well-behaved. Bradley, Vallado, Sibois and Axelrad [41] discusses the need to interpolate EOP values in the same way atmospheric drag indices are interpolated (Vallado and Finkleman [264]). To assess the impact of uncertainties in time, consider circular satellites at altitudes of 800 km (LEO) and 35780 km (GEO). Sensitivity tests can be run to

determine the effect of various methods employed, or envisioned in operational systems (see Table 4.2.1). In each case, the same initial state vectors were transformed from Earth fixed (ITRF) to Earth Inertial (GCRF) coordinates, permitting a positional difference determination at the end state.

The first set of options center mainly around the EOP values and how they are used. Much discussion has occurred with leap seconds (Finkleman, Seago and Seidelmann [87]). It is possible that some systems may not use leap seconds, or may not update them. This would lead to errors of 1 or 2 seconds in TAI. Because this is used only as an argument in the transformation, the difference is quite small. If the TT is off by a minute, perhaps because of assumptions or EOP values simply not being used, it is again used as an argument in the transformation.

The EOP files change periodically and are updated daily to include recent observational data. If old EOP files are used, the $\Delta UT1$ value could differ by 0.01 sec. Here one sees additional effects because the UT1 time is affected, along with GMST. If $\Delta UT1$ is not used, the differences become larger in each transformation. If the UTC is off by a second, a clock could be off, or a script error could be present. Since UTC affects all the parameters and arguments, the differences are very large.

Finally, its conceivable that the time tags could be off by a second. This is very different from the previous leap second and EOP errors because the argument is no longer an input into the transformation, but rather a simple offset. The results are significantly larger. Notice that for the case of a 1 sec error affecting the transformation, a vector closer to the earth will move less than a GEO satellite. For the case of a time tag error of 1 sec, the satellites will be off by the orbital velocity over that time interval.

Table 4.2.1 EOP sensitivity tests: several tests were run to examine potential errors and the effect on satellite positions from various EOP discrepancies. The time tag error is not a transformation error and is therefore larger than the UTC time argument error of 1 second.

Test	Possible Cause	LEO	GEO	Notes
TT is off by a min	Not using TT	0.000 m	0.000 m	TT is an argument
ΔAT error of 1 sec	Old EOP file	0.000 02 m	0.000 10 m	Only TAI affected
Correction sources off by 0.0001 ¨	Differences in ΔdX/dY corrections	0.035 m	0.240 m	
ΔUT1 value differs by 0.01 sec ΔUT1	Truncation, old EOP	6.0 m	31.0 m	
Ignoring ΔUT1, assume - 0.25 sec ΔUT1	Not using EOP	145.0 m	800.0 m	
UTC error of 1 sec	Clock off	581.0 m	3075.0 m	UTC is an argument
Time tag is incorrect by 1 sec	Script error	7500.0 m	3075.0 m	Bookkeeping error, (velocity × time)

The force models each contribute uncertainty as they are not perfect, and they all rely on data that has varying degrees of accuracy. Studies generally examine either the perturbation accelerations or an ephemeris accuracy compared to independent reference orbits such as Satellite Laser Ranging derived orbits. Vallado [259] examined the effect of various perturbations on satellite propagation as well as introducing the necessary parameters to align to ensure similar orbit propagations when using multiple propagation techniques or programs. Everything else was kept constant, but the gravity, drag, solar radiation pressure, third body, etc., were changed individually and compared to quantify how much impact each perturbation

had on the resulting ephemeris.

For gravity, the uncertainty has been reduced substantially from the 1960's when different gravity field models would introduce km-level differences in propagation. The fields have grown substantially over the last decade. EGM-96 was 360 x 360, but EGM08 is 2190 x 2190! Thus, gravity fields are often truncated to smaller sizes to afford greater computational speed (36 x 36, 24 x 24 for instance). The increase in size has also driven many new approaches to fast interpolation of the larger field sizes [19, 147, 230].

Atmospheric drag presents many additional challenges, and inserts the largest uncertainty into the solution for low-Earth orbiting satellites. Vallado and Finkleman [264] performed a detailed study of many of the factors contributing to the uncertainty resulting from atmospheric drag. The analysis consisted of two major sections. In the first, low-Earth satellite orbits were propagated with a single atmospheric model and data parameter implementation to form a reference or baseline configuration. Then, numerous variations of atmospheric models and data input parameters were compared to this baseline ephemeris to gauge the influence of each parameter on the propagated orbits. The second analysis used Precision Orbit Ephemerides (POEs) as observations to an Orbit Determination (OD) process. This was an important addition to the simple propagation of the first test because the OD process "corrects" many of the discrepancies in the first test and provides a slightly different and potentially more accurate examination of the influence of various parameters, and atmospheric models. The major error sources found in using atmospheric models are listed below and are a combination from the two analyses performed by Vallado and Finkleman [264].

- Using predicted values of $F_{10.7}$, K_p, a_p for real-time operations
- Lack of satellite attitude in determining the time-varying cross-sectional area
- Using different atmospheric models
- Not using the actual measurement time for the values ($F_{10.7}$ in particular at 2000 UTC)
- Using step functions for the atmospheric parameters vs interpolation
- Using the last 81-day average $F_{10.7}$ vs. the central 81-day average
- Using observed or adjusted space weather parameter values
- Using undocumented differences from the original atmospheric model technical definition
- Not accounting for (possibly) known dynamic effects – changing attitude, molecular interaction with the satellite materials, etc.
- Inherent limitations of the atmospheric models in accurately determining spatial and temporal variations in density
- Use of differing interpolation techniques for the atmospheric parameters
- Using approximations for the satellite altitude, solar position, etc. (this can be appreciable but is difficult to address without attitude data and knowledge of the shape and material properties)
- Using a_p or K_p and converting between these values
- Use of $E_{10.7}$ vs $F_{10.7}$ in the atmospheric models (this is not well characterized yet)

Solar radiation pressure also inserts uncertainty to the solution and can be significant for GEO and HAMR objects. Accurate modeling of solar radiation pressure is challenging for several reasons. The major error sources are:

- Use of macro models/attitude – this is perhaps the largest difference between programs
- Use of differing shadow models (umbral / penumbral regions, cylindrical, none, etc.)
- Using a single value for the incoming solar luminosity, or equivalent flux at 1 AU
- Use of an effective Earth radius for shadow calculations (23 km additional altitude is common) – this approximates the effect of attenuation from the atmosphere
- Using different methods to account for seasonal variations in the solar pressure
- Not integrating to the exact points of arrival and departure at the shadow boundary
- Use of simplified treatment for the light-time travel from the Sun to the satellite (instantaneous (true), light delay to central body accounted for (app to true), light delay to satellite (default))

Although not as large an effect as atmospheric drag, the general effect can be several hundred meters to a few kilometers.

There is also a lack of academic treatment of the exact causes of the uncertainty in atmospheric drag models themselves. There are a few studies that have begun to address the problem, e.g., papers by Anderson, Born, and Forbes [9], Emmert, Byers, Warren, and Segerman [84], and Lenard, Forbes, and Born [176].

4.3 Recommendations

Recall that covariance realism implies that the estimated state be the true state, and that the estimated covariance be the true covariance. Thus, while the committee strongly supports the continued development of improved models for producing more accurate state estimates, this alone is not sufficient to achieve covariance realism. *A proper characterization of the uncertainty in each model is needed so that the uncertainty may be treated in a statistical fashion.* For example, can we model the error in the acceleration vector due to mismodeled dynamics at a given point in space at a given time? If done correctly, then any two models will produce solutions that agree to within the level of the uncertainty, and it is not necessary that the two models have the exact implementation, or even be of the same fidelity. Approaches for accounting for the uncertainties in the models are given in Section 6.2. A recommendation would be to apply these approaches to particular astrodynamic models.

Alternatively or in addition, by examination of the structural and parametric uncertainties, one can strive to enable multiple organizations to arrive at propagated ephemerides that compare to some level of positional accuracy. We have shown that there is uncertainty at each step of process, from the time and coordinate systems, and force models, to the data input parameters that drive the force models. To achieve perfect alignment requires a very large set of interface controls that may be beyond a specific organization's needs. Thus, the recommendations are grouped into a somewhat descending order of importance in each category of time and coordinate systems, force models, data input parameters, and parameter uncertainty treatment.

Time and coordinate systems have become complex. The latest IAU-2010 conventions stipulate a precise method of converting vectors between Earth fixed and inertial locations, but the full implementation consists of literally thousands of mathematical operations. Unfortunately, most users still use a variant of the older IAU-76/FK5 (which by itself has a few hundred operations), or an approximation of an intermediate form of these systems. Any variation can lead to potentially large uncertainties. Thus, strict adherence,

use, and documentation of exactly which coordinate system is used is imperative for any mutual operation. Likewise, time systems present many different approaches to measuring epochs. While UTC and GPS offer common systems that are reasonably well understood, organizations have been known to make assumptions where, for their particular operation, some parameters may not be included. This presents the potential for step discontinuities and large positional differences. Message formats with insignificant precision insert additional ambiguity into measurements and observations. Again, the solution is to document and understand what the limitations of any particular time system will insert into the operation, and convey that to any other participating organization.

For the force models themselves, it is imperative that the exact technical implementation is known either through detailed documentation of the equations and approach, or through the availability of well-documented computer code. Implicit is the understanding of any and all assumptions that are used in the development and implementation of each force model. Although gravity is by far the most dominant perturbing force, it is well modeled and understood and is often not a major contributor to uncertainty. The force model uncertainty effects for LEO satellites are

- Atmospheric drag,
- Solar Radiation Pressure,
- Earth Albedo,
- Ocean and Solid Tides.

For higher altitude satellites, atmospheric drag is not present and therefore drops off the list. The data input parameters also can introduce uncertainty into the ephemeris generation process. Several of these were detailed in the Section 4.2.

The single greatest improvement in atmospheric drag and solar radiation pressure would be to improve the accuracy of the predicted indices/flux values. A close second would be to model the dynamic attitude of the satellite so that the individual cross sectional areas could be computed and used with the acceleration models. The remainder of the items listed in the discussion represent second tier effects that are important, but have a much smaller effect on the uncertainty.

While the different uncertainties have been listed in this section with respect to size, the impact of each of these on the propagated uncertainty remains an open question, i.e., the relative contribution to the propagated state still needs to be investigated.

Chapter 5

Measurement Errors and Sensor Level Processing

5.1 Introduction

Complete understanding of sensor error characteristics and their temporal behavior is required for covariance and uncertainty realism. Observation noise and biases contribute to the final covariance in different ways. Failure to accurately reflect sensor noise and biases correctly will result in erroneous covariance predictions, regardless of the quality of the basic covariance propagation. Correct assessment and modeling requires understanding of the intrinsic sensor system observables and the noise and bias behavior in that reference system. The relative contribution of the data errors and force modeling errors to orbit covariance is a strong function of the sensor performance, the object's ballistic coefficients, and the altitude of the object. It is difficult to make generalisms - it is best to do a full analysis on a case-by-case basis.

In the past, sensor performance limitations and mission accuracy requirements allowed a lot of approximations and short cuts to be taken in the sensor data processing. As new, more accurate, sensors come online these approximations can be a significant source of error in the orbit determination processing at the JSpOC. This transition is similar to the experience in the precision geodetic community as the second and third generation laser tracking systems and GPS came online.

This chapter of the report is intended to provide a generic background on the intrinsic observables and sensor level processing that occurs in the data reported to the JSpOC and used in the catalog maintenance. It is hoped that this will enable a more detailed assessment of the data. While some of this material appears basic to those who work at the sensor level, for many working at the JSpOC catalog processing, and general orbit determination applications, the processing that occurs at the sensor is not fully understood and is treated as a blackbox.

This chapter covers phased array radars, dish radars, hybrid radars, and optical tracking systems. Each sensor type section describes the processing of the observations *before* they are sent to the JSpOC. For each of those sensor types the intrinsic observables, generic sources of measurement biases and noise in those observables, sensor level processing effects, and sensor level calibration are explained. Because of overlap in functionality, the JSpOC level calibration processes are also described.

We also summarize the results of the assessment, drawing on team experience, and make recommendations. Short-term recommendations will focus on improvements at the JSpOC with currently available data. It is expected that sensor side improvements cannot be made in the short term. Mid-term recommendations focus on gaining better insight into the actual sensor performance to assess the use of the actual sensor detection data. Long-term recommendations focus on changes to future system requirements and algorithms to drive future upgrades and new systems in the net-centric environment.

5.2 Overview

Sensor noise and bias phenomenology varies remarkably between the sensor types. From a modeling perspective, the noise and biases can be a function of the sensor intrinsic variables, the local topocentric frame, or celestial coordinates. Further, noise and biases can behave differently at different time scales: detection-to-detection, track-to-track, and long-term or constant behavior, depending on the sensor type. Computation of correct covariances ideally needs to reflect these time frames.

The data are registered to basic reference frames. Radar data is referenced to the Earth fixed system, through the radar boresite, and the rotation to the local topocentric frame. Optical data is typically measured with respect to the stellar background, and referenced to a celestial frame. The angular errors in this kind of optical data are very small compared to radar data. Some newer small optical sensors are going to use Azimuth/Elevation mounts and the observations will be reference to the local topocentric earth fixed frame. Errors in modeling the transformation between the earth fixed and celestial frames can result in a bias between the optical data and radar data.

Within the SSN, observations are reported as metric observation in the "B3" format. The B3 format supports several different types of observations. For radars, the reported data consist of a range, azimuth, elevation and range-rate at an indicated time. These are generally produced at rates depending on the sensor and conditions. Right ascension and declination are usually used for optical systems. While the B3 format simplifies data exchange, the limited options for data representation can further complicate observation processing. The intrinsic observables are *not* typically reported. Instead, synthetic observations, often computed based on track filters, are reported. This can have a significant effect on the data errors, statistical behavior, data analysis, and modeling. This is explained in more detail in following sections.

Most of the sensors perform routine internal calibration. For phased array radars, precision reference ephemeris information from the JSpOC, or other sources, is used to calibrate the observed range and angle information generated by radar. This calibration data is the stored in the system to correct future observations. This process occurs at a schedule that is not aligned with the JSpOC calibration processes. An intense calibration process is performed prior to system IOC or after major refits. Maintenance, equipment degradation, or environmental effects can cause the calibrations to drift, triggering a recalibration process. As a result the biases for individual sensor can change during the calibration period used by the JSpOC for the entire network. This change in the bias from the computed value can result in additional unaccounted for error in the JSpOC's orbit determination and prediction, reducing covariance accuracy.

Initial orbit determination is performed at most sites, but is not usually reported to the JSpOC. In order for the radar systems to track uncued objects, they run a track filter to determine where the next track beam

needs to be pointed (they do not raster scan the entire sky). This track filter computes position and velocity information commensurate with an IOD solution. In some cases this is reported to various customers. For example, the Early Warning systems report the tracks for missile warning and defense applications. The IOD reflects the best estimate of the correlation of observations within a track (i.e. it is a track of a unique object). This information is used to generate and tag each of the metric observations for the track. The metric observations are sent into the JSpOC as individual observations, losing the information that all the observations within the track are strongly correlated to a single object.

As sensor and catalog processing quality improves, the subject of sensor precision vs accuracy will become ever more important. Some of the current optical systems, and some of the radar sensors that may be used in the future provide very high quality observations. In general, the level of noise in the data, which often drives precision, is decreasing. This makes handling of biases, which can limit accuracy, ever more important.

5.3 Phased Array Radars

5.3.1 Intrinsic Observables

Phased array radars typically measure Range, U, and V direction cosines (hereafter abbreviated RUV) [179]. These are usually computed for every detection in the signal processing. The U/V direction cosines are referenced to the grid of array transmit/receive elements within the array aperture. The U and V reference directions lie in the plane of the aperture and are orthogonal. Thus a detection at U=0, V=0 is directly on the line normal to the aperture, which is referred to as the boresite. Range-rate is not an actual observable for most systems, but some of the newer radar systems include Doppler waveforms that permit measurement of velocity. Some of the phased array tracking sites have multiple apertures (sometimes referred to as faces). An example of such is the Upgraded Early Warning Radar in Fylingdales, England. In this case, the RUV data is referenced to the actual aperture making the detection.

Provided with a suitably accurate cue, phased array radars can directly track an object based on the predicted ephemeris. If the object is uncued, for example a UCT, the track is maintained by using a sequential track filter to predict the location of the target at the next pulse transmit time. Tracks are usually updated every few seconds to keep the track filter estimates accurate.

Within the SSN, the data is typically corrected at the detection level for system biases, tropospheric and ionospheric refraction before being used in the track filters. Since the RUV data is registered to the aperture boresite, array phase center and aperture rotation around the boresite vector, the data is tied to the terrestrial reference frame.

Biases

Phased array radar biases are caused by three major classes of problems: environmental, electronic, and pointing. These biases have different signatures in the intrinsic observable measurement space and also range, azimuth, elevation (RAE). The environmental errors are typically dependent on RAE, and do not map 1:1 into the RUV coordinates of the radar. If the boresite is pointed at the horizon, elevation will align

with one of the direction cosine reference axes in the middle of the FOV, but will cross the axes further off boresite. The electronic errors are strong functions of RUV. Operationally, pointing errors tend to small and can be aligned with RAE or RUV coordinates. Therefore calibration of radar data biases needs to account for corrections in at least RAE and RUV, and in some cases need to account for the bore site orientation. Biases in the intrinsic observables are usually corrected at the detection level before being used in the sensor level processing.

Troposphere and Ionosphere Refraction Errors For phased array apertures oriented with the boresite pointed near the horizon, a primary source of error is refraction. Corrections are typically made for the troposphere; however, the model accuracy is limited to approximately 10% [26, 27, 53, 203]. Residual errors can result in a measurement accuracy floor at low elevations.

Tropospheric refraction models represent a long term mean for the wet and dry components of the atmosphere. Most models assume that the correction is uniform in azimuth. Local weather, such as fronts and storms, along the line of sight can vary significantly from the model and induce errors in both elevation and azimuth [26]. Figures 5.3.1 and 5.3.2 show typical tropospheric refraction errors in the elevation and range directions before and after correction. Below approximately 20° elevation the tropospheric refraction errors are significant. The accuracy of the correction depends on the model, and the averaging period for the local weather data used in the correction.

Figure 5.3.1 Elevation angle error due to tropospheric refraction. Vehicle height is 200 km. Maximum remaining error after correction is based upon exponential troposphere ray-tracing. Results are applicable to most tracking sites and, in particular, those near Miami, FL; Flagstaff, AZ; Brownsville, TX; Washington, DC; Fresno, CA; Bismarck, ND; and Hamilton, Bermuda. Source: Schmid [234].

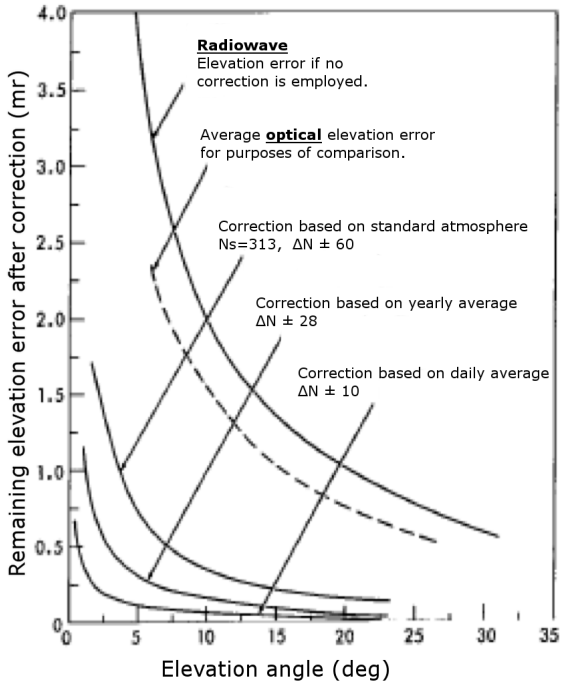

Ionospheric refraction affects longer wavelengths more strongly. Figures 5.3.3 and 5.3.4 show typical ionospheric refraction errors. The effects are significant at VHF/UHF, less so at L band, and relatively minor

Figure 5.3.2 Tropospheric range error remaining after correction versus elevation angle. The error remaining after correction represents the difference between ray-traces at $N_s = 377$ and $N_s = 313$ (standard atmosphere). Source: Schmid [234].

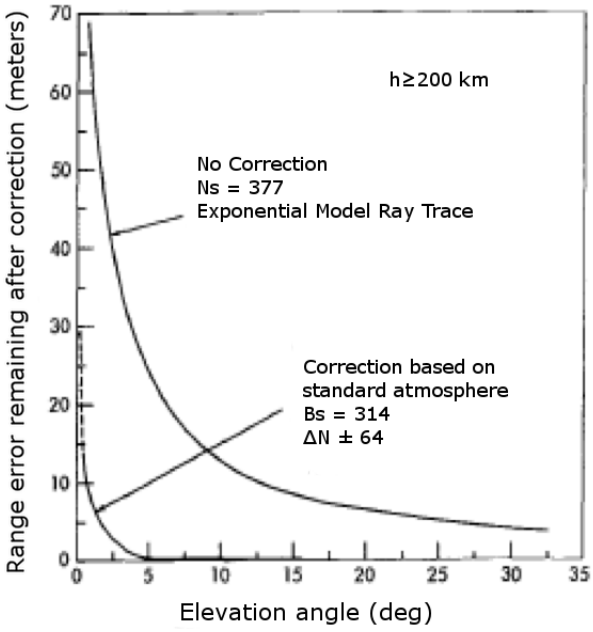

at X band. There is a time of day dependence, and a strong dependence on site latitude, with stronger effects seen at equatorial sites. (In both Figures 5.3.3 and 5.3.4, the ordinate "Mc" stands for mega cycles, i.e., megahertz "MHz.")

Tropospheric and ionospheric errors can vary over a long track. If the object is tracked horizon to horizon, the errors will have the same sign at the beginning of the track and the end of the track. Very strong local weather, such as large thunderstorms, can result in significant changes in the tropospheric errors through a track. A scale correction to the model can often correct the errors for a given track or time period.

Electronic Biases. Electronic biases are the result of errors in the knowledge of the electronic performance parameters in the radar. In some cases these are errors in the knowledge of the parameters, and in some cases limits in the stability of the parameters. There are simple constant biases, for example a constant phase error in a phase-phase steered system that results in a U or V bias. There are also scan-dependent biases that can result from thermal effects on the array, causing an error in the knowledge of the element spacing, as well as phase dependent errors. Thermal effects cause scale errors of the form $E_U = xU$ and $E_V = xV$, where E_U and E_V are the errors in the U and V components respectively. If the array is large enough there could be temperature gradients across the array, complicating the form of the bias. For arrays pointed at or near the horizon, residual tropospheric effects on a given short track (not passing point of closest approach) can generate errors that look like scale errors if constant biases are also computed. These biases can vary from track to track depending on the design of the system. For IOD purposes they look like a pure bias, however for multipass orbit determination using multiple days of data, some of these biases look like a long period structured noise.

Figure 5.3.3 Ionospheric maximum elevation angle error for 5° elevation. Error decreases as elevation angle increases above 5°. Source: Schmid [234].

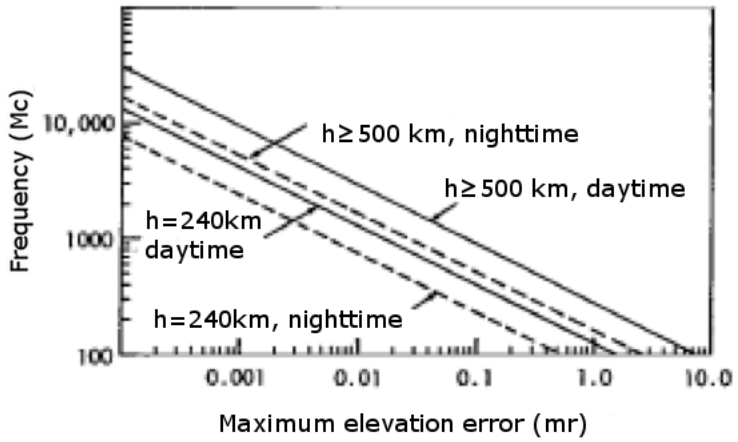

Figure 5.3.4 Ionospheric maximum range error for 5° elevation. Error decreases as elevation angle increases above 5°. Source: Schmid [234].

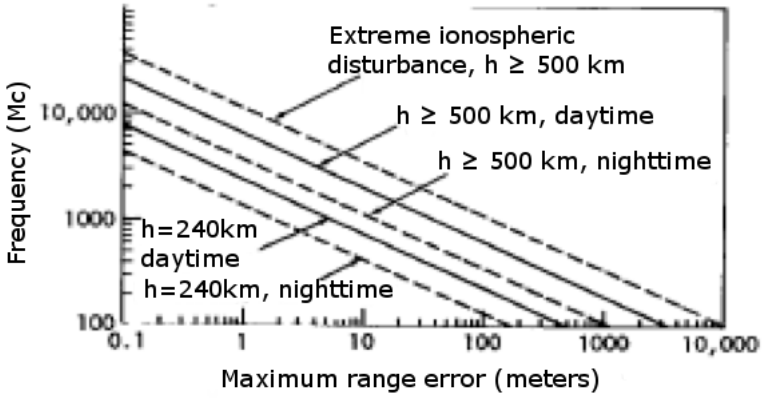

Pointing Biases. Pointing biases are the error in the knowledge of the array pointing and affect the U and V direction cosines. Usually these are computed based on survey results. With newer more accurate tracking systems coming online, these errors may be observable. The correction requires knowing the direction of the boresight, which can be expressed in azimuth and elevation, as well as the rotation about the boresight. The direction of the boresight may be absorbed by other biases estimates in calibration, but the rotation about the boresight will not.

Noise

U and V direction cosine noise on a radar is driven by the wavelength, beam width and waveform processing. In general the noise will decrease as the aperture size increases. Beam broadening with the angle off of boresight will increase the noise by a factor of $\sec(\theta)$, where θ is the angle off boresight. Range noise is a function of the resolution set by the waveform used for each detection. At 60° off boresite, the phased array angle data is twice as noisy as it is at boresite.

Figure 5.3.5 Nominal noise profile as a function of detection SNR. This curve assumes a nominal 20:1 BSR at infinite SNR. This curve is generally descriptive for angle and range. Noise values are normalized against the noise floor, hence unitless, and do not represent any actual system.

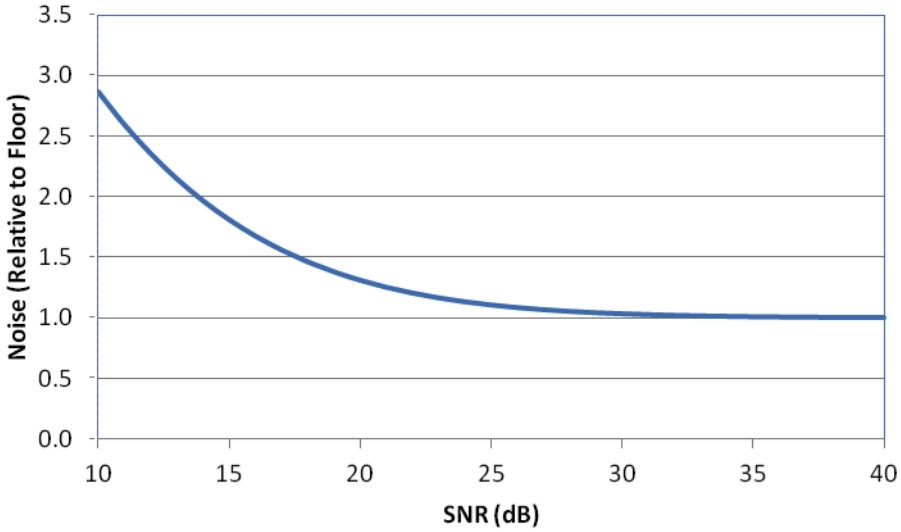

RUV noise variation is also driven by signal to noise ratio (SNR) dependent noise. In general noise decreases as SNR increases, asymptotically approaching a noise floor [Figure 5.3.5]. The noise floor itself can vary sensor by sensor, even in a family of sensors. The ratio of this noise floor to the beam width is referenced to as the beam split ratio (BSR) at infinite SNR. These values can differ for range, U and V. Typical BSR values are 10 or 20:1.

In general, the detection data noise varies over a track. SNR and the angle off boresight are not constant along a track. Likewise, waveforms typically vary over a track. The details of this variation are driven by the sensor track design and the way the system accounts for radar cross-section (RCS) fluctuation. Some systems put more power (i.e. use a higher SNR) at the start of the track to settle the track filter. Later in the track a lower SNR or update rate is used to preserve system capacity. If the SNR is reported for each detection, the noise floor is known, and the correct RCS is used (peak vs average), then the noise variance for a given detection can be accurately computed.

Provided that sensor has sufficient capacity, the quality of the data will not depend on the number of objects in track. However, as the sensor capacity is saturated, for example in a breakup, less capacity may be allocated for each track. This behavior will be very dependent on the details of the design and implementation of each sensor.

5.3.2 Sensor Level Processing

Phased array radars are capable of processing thousands of detections a second. In the past, data was compressed into the metric observations required by the JSpOC. This compression of the tracking data to a smaller set of data points that theoretically carry the same information is a common practice in orbit determination environments. This is done for spacecraft mission navigation, and high precision geodetic

applications. However, in the case of the SSN, the metric observations reported do not reflect the actual detection data. For the SSN, the phased array radar detections are transformed from their natural coordinate system (RUV) to the range, azimuth, elevation and range-rate information reported in the metric observations. Range-rate is produced, even if there was not intrinsic range rate observable.

Metric Observation Processing

Some phased arrays lack the angle resolution in a single detection to meet metric observation accuracy requirements. The detection data is filtered to reduce the noise, and compress the data. In legacy systems the metric observation data is computed on the basis of the track filter state. Once the covariance in the filter has reached the required level, the metric observations are computed at a periodic interval as necessary to satisfy the system tasking. These filtered values are currently reported in the B3 Metric observation message, however the uncertainty data is not.

A phased array radar track filter is intended to keep the comparatively wide radar beams on target. A simplified model is used to propagate the state vector and covariance in the centered rotating frame, and state updates are done in the radar RUV coordinates. Initialization of the track filter state depends on whether the target was cued. If cued, the cue can be used to start the filter. If uncued, the initialization parameters are computed from the initial detections, and the rate terms by differing the values. While this track filtering process works well for pointing the beams, it can potentially introduce errors into the metric observations.

Depending on the track filter tuning, the errors in the initial state can be carried through the entire track. In some cases the bias errors in the initial points could be noise, or tropsospheric/ionospheric errors, or differences in processing of detect, verify, initial track maintenance, or track waveforms. Use of the track filter state to compute the metric observations produces observations that have reduced noise, however, the observations are correlated to each other across the track, and are not of uniform weighting. Further, the B3 metric observation format lacks any mechanism to report the observation uncertainties from the sensor.

Accurate range data computation requires computation of a Range-Doppler coupling constant for correction of the range data. This requires an accurate estimate of the range-rate. Track filter errors in range-rate will cross over into the range. This can lead to an error in range that is variable across the track. Ideally this correction needs to be recomputed once the track is complete.

Use of the metric observations to produce a calibrated covariance will be subject to a number of limitations: 1) the distribution of the observations over a track does not match the detection data, 2) the metric observation Azimuth and Elevation does not map directly into the intrinsic U/V direction cosine space used by the radar, 3) unless the radar includes a Doppler waveform, the range rate information is not a real measurement; using it as such will bias the covariance.

Sensor Level Calibration

Calibration of the large phased array radars is done at multiple levels. The phase delays and related biases in the array are calibrated using a mix of Fourier gages (known signal feeds) as well as subarray calibration on satellites, and metric data calibration. Correction factors are applied at many levels within the system, as dictated by the hardware design. These calibrations are done infrequently, generally on an as needed basis.

Of primary importance for this report is the metric calibration.

.

Most of the radars calibrate against targets with known ephemerides to determine Range, U, V corrections. Generally these are treated as constant biases across the FOV, but it is possible to compute higher order corrections. This is limited in practice by correlation between environmental phenomena, such as tropospheric refraction modeling errors, and higher order terms, such as U or V scale biases for sensors pointed near the horizon.

The current operational practices favor using high SNR observations for calibration. For some of the existing systems this is possible only near boresight (due to beam steering losses). The result is that the sensor is not necessarily calibrated over the full FOV; instead, the results may be dominated by bias features specific to the area near boresight.

One aspect of the Russian Space Surveillance System that is different from the US is the radar tracking of objects in LEO and the reporting of observations. Rather than report a set of observations as we do they report the object state at one time and the diagonal part of the covariance. The state reported is the range, azimuth and elevation and the three rates. Azimuth is measured in the radar frame, not from North as is usually done. In this frame the covariance is mostly diagonal so only the diagonal is transmitted and this reduces the amount of date transmitted for each object tracked.

5.3.3 Initial Orbit Determination

All the phased arrays generate a state vector in the track filter for all cases where a track is successful. This estimate includes the covariance, which represents the covariance of a Kalman filter tuned for track maintenance. If the sensor is a multi-mission sensor (e.g. providing missile warning and space surveillance support) the IOD state vector and covariance are reported to some customers. However, the track state vector and covariance data is not reported to the JSpOC. Sometimes the elsets are sent to the JSpOC, but the current format does not include the covariance.

It is possible for the JSpOC to perform IOD from the metric observations. The track filter based computation of metric observations represents a “lossy” data compression technique, like JPEG. It is “lossy” because the effective track arc length is reduced. This is particularly true of the start of the track where the filter is converging. The result is that IOD based on the metric observations can have degraded performance, especially for short UCT tracks.

5.4 Other Radar Types

5.4.1 Mechanical Radars

The primary difference between dish radars and phased arrays for purposes of catalog maintenance is the effect of the mount type. The mechanical mount will drive the biases in the pointing due to biases in measurement of the orientation, sag, misalignment etc. If the mount is an az-el type mount, estimating the corrections in that frame is best. Noise for the angle data will still be driven by the aperture size and SNR. Beam broadening will not be a factor in the noise. There can be a small component of noise added by the

transducers that measure the mount location.

5.4.2 Hybrid Radars

Hybrid radars, having a phased array mounted on a mechanical mount share characteristics of both mechanical and phased array radars. The mechanical mount will add biases in the pointing due to biases in measurement of the orientation, sag, misalignment etc. This will apply on top of the phased array biases in the RUVD coordinate system. If the mount is an az-el type mount, it may be necessary to estimate corrections in the RAE and RUV frames simultaneously. Noise for the angle data will be driven by the aperture size, SNR, and beam broadening. There can be a small component of noise added by the transducers that measure the mount location.

5.5 Optical Tracking

Optical tracking data provides angle accuracies that are much better than radar data, with correspondingly low noise. The lack of range data complicates IOD. Being referenced to the celestial frame, and expressed in Right Ascension and Declination, there is no need to account for refraction corrections and biases, mount issues, etc., like phased array radars. Some future optical sensors are using RAE mounts and reporting in the RAE frame. This will be subject to differences between Earth Center Fixed and Celestial reference frames, just like the phased array radars.

Optical tracking systems use large telescopes equipped with charge-coupled devices (CCDs) to detect photons from the target. The mount types and orientation vary based on the telescope and platform. Since CCDs work by integrating the incident light energy striking a given cell, the motion of the source over the CCD array can strongly affect the sensitivity and quality of the track. Most systems operate in one of two basic tracking modes: scan while track, deep stare, or both depending on the tasking. If the object is tumbling during the track, the signal can vary over the track as well. Newer processing techniques for track before detect are being researched, and could be added to future systems.

5.5.1 Intrinsic Observables

The image scanned from the CCD forms the basic set of observable data. Tracks and features are scanned in the CCD image, and compared to a stellar background. This registers the image to the celestial background and celestial reference frame. After registration to the stellar catalog, the tracks can be identified (the specific star catalog varies from site to site). The photometric flux of the object can be computed based on the intensity of the signal at the CCD. This flux value can then used to compute a visual magnitude.

In a deep stare mode, the sensor is pointed at a fixed point in the inertial sky. Returns from space objects form tracks on the CCD, while stars show as dots. These tracks are scanned for in the image and identified. In scan while track mode, the telescope is programmed to follow a specified track that is intended to match the motion of the target. The stellar background may appear as streaks, while the intended (or hoped for) target will be a bright dot. Velocity errors in the anticipated track will result in image smearing. This method allows for longer integration time on the track, allowing fainter objects to be tracked.

Biases

Biases can arise from multiple sources: stars in field of view, sensor resolution (telescope size), CCD quality, and track smearing.

Noise

Noise is driven by: target brightness, Sensor Resolution (telescope size), CCD quality, etc. Track smearing and atmospheric blurring can also affect noise.

5.5.2 Sensor Level Processing

Metric Observation Processing

Optical angle measurements are registered to stellar background. Removal of the background signal allows tracks to be identified. The track data is filtered to determine the track end points and observation rates. These form the basis of the metric observations.

Biases can arise from the presence of stars on or near the track, and the selection of stellar catalog and reference stars in the imaged field. A star in near a track can result in a bias in the computed track end point position. The signature of the star and the target are close enough to form one elongated blob, which corrupts pixel centering algorithms. A weak geometry or mismatch in the selection of reference stars can result in a poor computation of the location of the track. The reference catalogs vary between the systems and JSpOC processing, potentially introducing biases between systems. An additional source of bias is sensor location errors.

Noise in the metric observations is driven by the data noise, as well as the accuracy of the track fit. In addition, the B3 message format lacks sufficient significant figures for the measurements, introducing an accuracy floor in the observations for some orbital regimes.

Sensor Level Calibration

Internal calibration of the sensor is performed to calibrate the visual magnitude accuracy as well as the telescope boresight to support mission operations. Since the data itself is registered to the stellar background, the biases applied internal to the sensor for pointing are not a factor in the data returned to the JSpOC.

5.5.3 IOD

Angles-only IOD from short tracks is subject to large orbit uncertainties, if it is even possible due to the short tracks involved. The assumption of some of the orbit parameters, such as semimajor axis or eccentricity, is required depending on the theory being used. The IOD results can be used for short term planning, and are not generally reported to the JSpOC.

5.6 Current JSpOC Calibration

JSpOC currently calibrates the sensors used in the catalog on a periodic basis. An independent set of high precision orbit ephemeris data is used to process observations of a limited number of targets to assess the standard deviation and biases in the data. The standard deviation of and biases of RAE residuals are computed for radar sites, and right ascension/declination residuals for optical sties. The results represent an average over many passes. These values are then applied to the catalog processing.

This approach does not take into account the variability in formal uncertainty for the radar sites as a function of angle off the boresight. The elevation noise and bias will capture most refraction modeling errors. However, the radar noise and biases do not map linearly into azimuth. Consequently the computed azimuth noise will not accurately reflect track accuracy throughout the field of view. For upward looking sensors, such as the now decommissioned VHF fence and possibly the future S band fence, the singularity in the RAE frame that occurs directly overhead of the sensor, coupled with non uniform data distributions, can lead to a calibration computation that does not reflect the actual system behavior.

5.7 Summary

Correct modeling and assessment of sensor noise and bias performance is necessary for correct covariance estimation. The corrections and models that are required to be used for optimal assessment differ remarkably between sensor types. Radar systems require correction for refraction effects, as well as other system biases in order to accurately determine an orbit from the data. The optical data is registered to the stellar background, eliminating the need for refraction correction models. However, optical sensors do not provide range. Overall the radar and optical sensors are complementary, but correct modeling is required to ensure they produce orbits in the same effective reference frame.

The reported metric observations for phased array radars do not match the intrinsic measurements. Phased array radars work in the RUV frame, as opposed to the Time, Elevation, Range and Range-rate (TEARRR) form used in the B3 data. Most of the radars do not intrinsically measure range-rate. Generation of the metric observations from the track filter can be an added source of error in the data, and results in correlation between the observations that is not reflected in the JSpOC calibration.

Phased array radar noise performance is strongly determined by the angle off boresight and the track SNR. The distribution of the detections along the track is also not uniform. This results in a variable weighting of the track depending on location in the FOV. However, the current B3 format does not allow reporting of the per observation uncertainties. Radar bias performance is also a strong function of the RUV frame. By comparison the JSpOC calibration of noise and biases works in the RAE frame.

In general, in the angular components, the optical data is much more accurate than the radar data. The data is registered to a given celestial frame via comparison of the image to the stellar background. However, different star catalogs are used at different systems, potentially causing biases between optical sensors, and the optical and radar data sets. As with the radar data, observation uncertainties are nor reportable in the B3 metric observation format. In addition, the B3 format lacks the precision to fully exploit the accuracy potential of the optical data in all regimes.

5.8 Recommendations

Significant improvement in measurement covariances from the SSN sensors can be achieved by making changes at the sensors as well as at the JSpOC. The current sensor and JSpOC architecture is rigid. Nonetheless there is still the possibility of some short and mid-term actions to improve uncertainty realism. A future JSpOC Mission System improvement will provide a significant step forward in terms of opportunity for improvement, but additional improvements to the network will still be required. The capability to fully and accurately exploit the sensor data for uncertainty realism will need to come in later developments.

5.8.1 Short-Term

In the short term, it may be possible to realize some operational improvement by development and use of an empirical error model for weighting of the sensor data at the JSpOC. This would have to use the existing B3 Metric observation format data. Error models would need to be developed for classes of sensors and applied to individual sensors. These models would still provide range and bias correction estimates; however, they would make use of basic sensor uncertainty characteristics to develop more accurate bias and noise estimates. This should be coupled with corresponding changes in the orbit determination software. Without that change, the improved estimates may simply be wasted.

Example phased array bias corrections should include the following terms as a core:

Boresight Azimuth Elevation and Clock Angle (rotation around the boresight): These are needed to properly transform the measurements from the Metric Observation RAE to an intrinsic observable RUV frame. Most of the existing arrays are symmetrical, so the U/V designation is arbitrary, but should be consistently handled. However, not all arrays for radars that may be used are symmetrical, so care should be taken to accurately reflect the orientation.

Simple bias by intrinsic observable type: Where possible when using detection data, this should reflect the waveform type used, as jumps can occur between waveforms. When metric observations are used, this is unnecessary. It may be necessary to break this bias up over time, as some biases fluctuate at intervals of hours to weeks.

Scale bias for each intrinsic observable type: This will handle array spacing and thermal correction errors on phased arrays. Scale errors can affect range, and Doppler as well. As with the simple biases, it may be necessary to break these parameters over time periods to account for drift in some of the driving factors For example, thermal expansion/contraction in the array will cause scale errors in the U/V measurements.

For a typical radar, this will require that approximately nine parameters be estimated. Note that range-rate biases should not be included unless the radar actually measures Doppler shifts via a pulse-Doppler waveform. However, it may be useful for characterization of metric observation performance.

The error model development would start with calibration residuals for a few radars on a per metric observation bias over a 90-day period. The initial step would be to plot the errors as a function of azimuth, elevation, range, off-boresight angles, local time, etc. Statistical analysis would be performed to identify dominant relationships as a function of track geometry. The statistical analysis should be backed up by covariance analysis to fully understand the empirical results. Covariance analysis can be used to map force model errors and observation modeling biases to the orbit determination and prediction accuracy, allowing

the top contributors to be identified. This will require tools capable of computing the contribution of the force model errors and data biases to the orbit determination covariance, as well as the effect of the error on the prediction. Such covariance analysis tools exist (e.g., NASA's ORAN [110, 199] or ODEAS [256]); alternatively Monte Carlo analyses can be performed.

Knowledge of the top modeling error contributions to the covariance can be used to develop a model for a given class of sensor to apply in testing. The modified software including the error model can be evaluated against the baseline software and assessed using the precision ephemeris data. The realism of estimated noise-only error at the end of the OD arc and at a nominal prediction time can be assessed. If significant and meaningful improvements are achieved, then modification of the operational software can be explored.

5.8.2 Mid-Term

As sensors are upgraded, there will be the opportunity to expose and use the actual detection data directly. A study should be performed to assess the practical noise characteristics for each sensor, using the actual sensor detection data. The results of this study can be used to guide development planning and prioritization. Sensors for which the detection data will provide the most improvement in accuracy and uncertainty realism can be prioritized for upgrade first.

The detection data will need to be collected from the sensor systems as it is not reported currently. This goes a step further than the short term recommendation by looking at the actual intrinsic measurement quality and characteristics, along with the reported (or computable) noise variances. This will allow the impact of the sensor level processing (metric observation via the track filter), the detection distribution through a track, and the per detection noise variations to be assessed.

A mid-term operational enhancement that may be practical is to have the sensors report the uncertainties in the metric observations to the JSpOC via the current messaging architecture. This can be accomplished by reporting the uncertainties in the same B3 format, but with a flag to indicate that they are the uncertainties in the observations. This will require relatively little modification to each sensor, but will take time for all the sensors to be upgraded. JMS Increment 2 should be able to make use of this data however.

5.8.3 Long-Term

Long-term developments of JSpOC processing, net-centric interfaces and sensor backends will provide the opportunity for enhanced sensor data exploitation and uncertainty realism. Some of these efforts will by necessity take years to put in place. Future JSpOC Mission System updates should provide an opportunity for improvement in the modeling and application of sensor noise statistics that should improve uncertainty realism.

The following recommendations are meant to provide guidance for research and development, prototyping, and new systems and upgrades requirements development:

1. Where possible, intrinsic observables from sensors should be used. Track filter derived metric observations should not be used. This will allow correct calibration correction and weighting of the data in the catalog orbit solutions. The ability to model and calibrate the sensor boresight pointing is recommended for best results.

2. Detection data should be made available, which in turn enhances the flexibility in data processing. There will be a 10x increase in the number of observations. If the volume of data from the modern radars exceeds catalog processing limits, then a "normal point" process can be used to compress the data. This technique, used by the International Laser Ranging Service [222], compresses the data by using a remove-restore algorithm to filter high rate laser observations over a given time window to filter high rate laser observation over a given time window (e.g., the Herstmonceux algorithm [243]). The remove-restore does not produce residual error artifacts like a track filter does, and has been demonstrated to support 1 cm orbit precision.

3. Sensor noise should be supplied for each observation. This will permit modeling of the degraded Phased Array performance off boresight and improve radar calibration and improve the accuracy of the orbit solution covariances. In the full implementation, the radar should report the observation variance (noise) for each point. In the interim, it is possible to develop models for the variation in noise across the radar FOV, however this will not account for SNR variation.

4. Best practices from the wider astrodynamics community for reporting of detection data and corrections are highly recommended. The precision radar altimetry community has successfully employed a process for over 20 years where the raw measurement and all corrections are reported in each data record. This allows for consistent processing of data from multiple sensors, leading to more accurate products, and error estimates. Examples of information that should be included for SSN data include:

   - Raw measurements
   - Local Weather (Pressure, Temperature, Humidity, Total Electron Count, etc)
   - Troposphere refraction corrections
   - Ionosphere refraction corrections
   - Range-Doppler coupling factor, correction, aberration, and Doppler source
   - Other applied bias corrections and bias correction uncertainties, by correction
   - Reference star catalog or Reference boresight direction (as appropriate for the sensor)
   - Observation variances (noise)
   - Observation SNR for radar

   These corrections should be reported for the actual detection data, as well as any compressed data reported to the JSpOC.

5. Calibration of sensor data should be performed in the natural coordinate system of the reported intrinsic observables. This will improve the accuracy of the orbit product covariance.

6. IOD state vector products should be routinely provided. This should include the covariance as well to support correlation and planning product generation. While this data may not use these in routine processing, these products are very useful for first tracks of UCTs and new launches/releases. Publishing the data will enable more flexible mission operations under JSpOC policy management. It should be noted that the sensor provided covariance accuracy may be of limited by the sensor processing.

7. Availability of detection data through a track, as well as the uncertainties, will allow the JSpOC to tailor their processing of the tracks as needed. This may render many of the existing tasking codes obsolete, and simplify tasking. This aspect should be investigated and reviewed.

8. The Star Catalog used to process the optical tracking data needs to be coordinated across the SSN. This catalog should be kept up to date, so the sensor data can be registered to commonly used reference frames in the wider astrodynamics community. At this point a Hipparcos mission derived Star Catalog, or later, should be considered. Either the star catalog needs to be standardized for all reported observations from all sensors, or the catalog used at the sensor needs to be indicated in the data records.

9. The latest International Astronomical Union reference frames, including the Celestial Intermediate Origin (CIO) based system used for the Hipparcos Star Catalog data, should be used. This will improve co-registration of the optical and radar data, as well as make the resulting space catalog products more interoperable with the wider astrodynamics community. Future enhancements are expected to provide a significant improvement in this area.

10. Another alternative that would reduce the amount of data transmitted would be to use the Russian approach, but report the complete track covariance.

Chapter 6

The Inverse Problem: A Brief Review of Estimation Formulations Used in Space Surveillance

Having presented the uncertainties in sensor level processing, dynamical models including atmospheric models, this chapter surveys some of the formulations and methods for the *inverse problem* of extracting a state, e.g., position and velocity, from the sensor reports. The general subject of linear and nonlinear estimation is presented in the extensive literature of articles, texts, and reference books, some classical and some of more recent vintage. In particular, many of the problem formulations and methods in this chapter can be found in the books by Escobal [86], Jazwinski [139], Anderson and Moore [8], Gelb [96], Bar-Shalom, Li, and Kirubarajan [25], Crassidis and Junkins [55], and Särkkä [233]. A more recent handbook on nonlinear filtering is that of Crisan and Rozovskii [56]. Thus, the objective in this chapter is to briefly survey some of the formulations and methods for nonlinear estimation including filtering, smoothing, prediction, and batch estimation that are currently used in the astrodynamics community. In particular, a goal is to estimate the state and its uncertainty at the time of a sensor report. The next chapter surveys some of the methods used in predicting this uncertainty forward in time.

6.1 The Measurement and Dynamic Equations

The problem of estimating the dynamic state of an object assumes a stochastic differential equation and a sequence of measurements $\boldsymbol{Z}_k = \{\boldsymbol{z}_1, \ldots, \boldsymbol{z}_k\}$ at the respective times $\{t_1, \ldots, t_k\}$. The measurement equation is normally written as

$$\boldsymbol{z}_k = \boldsymbol{h}_k(\boldsymbol{x}(t_k)) + \boldsymbol{\nu}_k \ (k \geq 1) \tag{6.1.1}$$

wherein the noise sequence $\{\boldsymbol{\nu}_i\}_{i=1}^k$ is generally modeled as independent zero mean Gaussian random variables with covariance $\mathbf{R}_i$. (More generally, the noise sequence can be modeled by a the corresponding sequence of independent probability density functions, say $\{p_{\boldsymbol{\nu}_i}(\boldsymbol{\nu}_i)\}_{i=1}^k$). $\boldsymbol{h}_k(\boldsymbol{x})$ represents the transformation of the state $\boldsymbol{x}$ of an object to the space of the measurement $\boldsymbol{z}$ at time t_k. (Parameters that may be present in the measurement equation have been suppressed.)

The astrodynamic equations of motion define a second order system of equations in position which can then be converted to a dynamic state $\boldsymbol{x}(t)$ of position and velocity at time t. The corresponding equations with process noise or stochastic acceleration can be formulated as a continuous-time model of first-order stochastic differential equation of the form

$$\frac{d\boldsymbol{x}(t)}{dt} = \boldsymbol{f}(\boldsymbol{x}(t), \boldsymbol{\alpha}, t) + \mathbf{G}(\boldsymbol{x}(t), t)\, \boldsymbol{n}(t), \tag{6.1.2}$$

where $\boldsymbol{f} : \mathbb{R}^n \times \mathbb{R}^p \times \mathbb{R} \to \mathbb{R}^n$, $\mathbf{G} : \mathbb{R}^n \times \mathbb{R} \to \mathbb{R}^{n \times m}$, $\boldsymbol{\alpha} \in \mathbb{R}^p$ is a vector of the system parameters, and $\boldsymbol{n}(t)$ is an m-dimensional representation of the stochastic acceleration or process noise. The function $\boldsymbol{f}$ encodes the deterministic force components of the dynamics (e.g., gravity, drag, solar radiation pressure, etc.) and parameters $\boldsymbol{\alpha}$. The term $\mathbf{G}(\boldsymbol{x}(t), t)\, \boldsymbol{n}(t)$ should encode the uncertainty in the dynamic models and space environment. Several examples of stochastic acceleration are presented in the Section 6.1.1. In each case the dynamics and process noises are reduced to the form in equation 6.1.2 in which $\boldsymbol{n(t)}$ is a white zero mean Gaussian process. In addition, $\boldsymbol{x(t_0)}$, $\boldsymbol{n}(t)$, and $\{\nu_k\}$ are assumed to be independent.

While the astrodynamic equations of motion are formulated naturally as a stochastic differential equation (6.1.2) with the discrete measurement or sequence report sequence (6.1.1), many of the methods of estimation are developed for the discrete problem

$$\boldsymbol{x}_k = \boldsymbol{f}_{k-1}(\boldsymbol{x}_{k-1}, \boldsymbol{\alpha}, \boldsymbol{\omega}_{k-1}) \ (k \geq 1) \tag{6.1.3}$$

$$\boldsymbol{z}_k = \boldsymbol{h}_k(\boldsymbol{x}_k, \boldsymbol{\nu}_k) \ (k \geq 1) \tag{6.1.4}$$

where $\boldsymbol{x}_k = \boldsymbol{x}(t_k)$, $\boldsymbol{f}_k : \mathbb{R}^n \times \mathbb{R}^p \times \mathbb{R}^m \to \mathbb{R}^n$, $\{\boldsymbol{w}_k\}$ and $\{\boldsymbol{\nu}_k\}$ are independent noise sequences that are also independent of $\boldsymbol{x}_0$. Often the further specializations are made to their being zero mean and $\mathrm{E}[\boldsymbol{w}_k\, \boldsymbol{w}_j^T] = \mathbf{Q}_k\, \delta_{kj}$ and $\mathrm{E}[\boldsymbol{\nu}_k\, \boldsymbol{\nu}_j^T] = \mathbf{R}_k\, \delta_{kj}$. In addition, $\boldsymbol{x}_0 \sim N(\bar{\boldsymbol{x}}_0, \mathbf{P}_0)$. Both $\boldsymbol{f}_k$ and $\boldsymbol{h}_k$ may additionally contain parameters. There are at least four different cases in which one can use the discrete formulation (6.1.3) as a substitute or approximation for the continuous version (6.1.2).

1. The continuous equations of motion are linear and the process noise term $\mathbf{G}(\boldsymbol{x}(t), t)\, \boldsymbol{n}(t)$ does not depend on the state $\boldsymbol{x}$.

2. The stochastic acceleration term $\mathbf{G}(\boldsymbol{x}(t), t)\, \boldsymbol{n}(t) = 0$, but the dynamics are otherwise nonlinear.

3. The continuous stochastic differential equation is approximated by the discrete version in the case of *small* process noise.

4. The stochastic differential equation is approximated by a numerical scheme [163].

6.1.1 Examples of Process Noise for Continuous Dynamics

Process noise or stochastic acceleration is often used by the astrodynamics community to mitigate modeling errors as well as sensor biases. Four different examples are provided below for the scalar case; however, there are analogous developments for the multidimensional case. Each can be included in the dynamics and converted to a stochastic differential equation of the form (6.1.2).

White Noise

The basic noise process $n(t)$ in the stochastic differential equation (SDE) (6.1.2) is zero-mean white noise,

$$n(t) = w(t), \mathrm{E}[n(t)] = \mathrm{E}[w(t)] = 0$$

defined by the autocovariance function

$$\mathbf{\Psi}(t,s) = \mathrm{E}[(w(t) - \mathrm{E}[w(t)])\,(w(s) - \mathrm{E}[w(s)])^T] = \mathbf{Q}(t)\,\delta(t-s)$$

The choice of the covariance matrix $\mathbf{Q}(t)$ is part of the design problem. Bar-Shalom, Li, and Kirubarajan [25] discuss this design for a nearly constant velocity model based on the need to accommodate accelerations of a pre-specified strength.

The Ornstein Uhlenbeck Process

The Ornstein Uhlenbeck process is one specified by the stochastic differential equation

$$dn(t) = \rho(\mu - n(t))\,dt + \sigma\,dW(t)$$

where $\rho > 0$, μ and $\sigma > 0$ are parameters and $W(t)$ denotes the Wiener process. In physical sciences, the Ornstein-Uhlenbeck process is rewritten as the Langevin equation

$$\frac{dn(t)}{dt} = \rho(\mu - n(t)) + \sigma w(t),$$

where $w(t)$ is zero mean white Gaussian noise with $\mathrm{E}[w(t)w(s)] = \delta(t-s)$. Furthermore, one can make the long term mean μ stochastic to another stochastic differential equation (SDE) in what is sometimes called a cointelation SDE. In finance, the Ornstein Uhlenbeck process is called the Vasicek model for governing the evolution of interest rates.

One can solve for $n(t)$ to obtain

$$n(t) = \exp\left(-\rho(t-t_0)\right)n(t_0) + \mu(1 - \exp\left(-\rho(t-t_0)\right)) + \int_{t_0}^{t} \exp\left(-\rho(t-s)\right)\sigma dW(s)$$

The typical parameters μ, ρ, and σ, together with the initial condition $n(0)$, completely characterize the dynamics, which can be characterized as follows.

i. μ represents the "long term mean." All future trajectories of n will evolve around a mean level μ in the long term.

ii. $\rho > 0$ denotes the "speed of reversion," i.e., it characterizes the rate at which trajectories will approach or decay onto μ in time;

iii. σ is the "instantaneous volatility" and measures the amplitude of randomness entering the system. Higher σ implies more randomness.

iv. The quantity $\sigma^2/2\rho$ denotes the long term variance. All future trajectories of $r(t)$ will regroup around the long term mean with this variance after a long time.

Note that ρ and σ tend to oppose each other: increasing σ increases the amount of randomness entering the system, but at the same time increasing ρ amounts to increasing the speed at which the system will stabilize statistically around the long term mean μ with a corridor of variance determined also by ρ. This is clear when looking at the long term variance, $\sigma^2/2\rho$ which increases with σ but decreases with ρ.

One can compute the following for the Ornstein Uhlenbeck process

$$\begin{aligned}
\mathrm{E}[n(t)] &= \exp\left(-\rho(t-t_0)\right)n(t_0) + \mu(1-\exp\left(-\rho(t-t_0)\right)) \\
\mathrm{Cov}[n(s),n(t)] &= \mathrm{E}[(n(s)-\mathrm{E}[n(s)])(n(t)-\mathrm{E}[n(t)])] \\
&= \frac{\sigma^2}{2\rho}\exp(-\rho(s+t))(\exp(2\rho\mathrm{min}(s,t)-1) \\
&= \frac{\sigma^2}{2\rho}(\exp(-\rho(t-s)) - \exp(-\rho(t+s))) \text{ provided } s<t.
\end{aligned}$$

The Ornstein Uhlenbeck process fits within the general framework above by state augmentation. To see this, consider the combined system

$$\begin{aligned}
\boldsymbol{x}'(t) &= \boldsymbol{f}(\boldsymbol{x}(t),t) + \mathbf{G}(\boldsymbol{x}(t),t)\,n(t), \\
n'(t) &= \rho(\mu - n(t)) + \sigma\, w(t).
\end{aligned}$$

Now define the augmented state variable $\boldsymbol{y} = (\boldsymbol{x}, n)$. Then,

$$\begin{aligned}
\boldsymbol{y}'(t) &= \begin{bmatrix}\boldsymbol{x}'(t)\\ n'(t)\end{bmatrix} = \begin{bmatrix}\boldsymbol{f}(\boldsymbol{x}(t),t) + \mathbf{G}(\boldsymbol{x}(t),t)\,n(t)\\ \rho(\mu-n(t))\end{bmatrix} + \begin{bmatrix}0\\ \sigma w(t)\end{bmatrix} \\
&\equiv \tilde{\boldsymbol{f}}(\boldsymbol{y}(t),t) + \tilde{\mathbf{G}}\,\tilde{\boldsymbol{n}}(t).
\end{aligned}$$

Therefore, in the SDE governing the augmented state $\boldsymbol{y}(t)$, the noise process is white. Finally, we note this process is also used for a maneuvering target model in the general field of multiple target tracking as described in the survey by Li and Jilkov [178].

First-Order Gauss-Markov Process

The first-order Gaussian-Markov process (GMP1) is a special case of the Ornstein Uhlenbeck process ($\mu = 0$) and is defined by the stochastic differential equation

$$dn(t) = -\rho n(t)\,dt + \sigma\,dW(t)$$

where $\rho > 0$ and $\sigma > 0$ are parameters and $W(t)$ denotes the Wiener process. Again, the solution is provided by

$$n(t) = \exp\left(-\rho(t-t_0)\right)n(t_0) + \int_{t_0}^{t}\exp\left(-\rho(t-s)\right)\sigma\,dW(t)$$

In this formulation $\sigma > 0$ and $\rho \geq 0$. The parameters ρ and σ, together with the initial condition $n(0)$, completely characterize the dynamics, and can be quickly characterized as follows.

i. ρ characterizes the velocity at which such trajectories will converge to zero;

ii. σ measures the amplitude of randomness entering the system. Higher σ implies more randomness.

iii. $\sigma^2/2\rho$ is the long term variance.

We note that

$$\mathrm{E}[n(t)] = \exp\left(-\rho(t-t_0)\right)n(t_0)$$

$$\Psi(t,s) = \mathrm{Cov}[n(s),n(t)] = \mathrm{E}[(n(s)-\mathrm{E}[n(s)])(n(t)-\mathrm{E}[n(t)])] = \frac{\sigma^2}{2\rho}\exp(-\rho(s+t))(\exp(2\rho\mathrm{min}(s,t)-1)$$

$$= \frac{\sigma^2}{2\rho}(\exp(-\rho(t-s)) - \exp(-\rho(t+s))) \text{ provided } s < t.$$

For large ρ, this process approximates zero-mean Gaussian white noise with covariance $\sigma^2/2\rho$ [139]. This model is sometimes called the Singer model in the general area of multiple target tracking [38, 178]. Also, this stochastic process can be included in the system dynamics within the framework described by equation (6.1.2) with white noise.

Second-Order Gauss-Markov Process

Leonard, Nievinski, and Born [177] suggest that stochastic accelerations in the perturbed two-body problem of orbital mechanics can be modeled as *second-order* Gauss-Markov processes (GMP2). Following Leonard *et al.*, a scalar GMP2 process is defined by

$$\frac{d^2n(t)}{dt^2} = -2\zeta\omega\,\frac{n(t)}{dt} - \omega^2 n(t) + \sigma w(t),$$

where $\omega > 0$, $\delta > 0$, $0 < \zeta < 1$, $w(t)$ is zero-mean Gaussian white noise with unit variance, and $n(t_0)$, $\frac{dn(t_0)}{dt}$, and $w(t)$ are mutually independent. Defining $\beta = \omega\sqrt{1-\zeta^2}$, the autocovariance function for $n(t)$ is found to be

$$\Psi(t,s) = \mathrm{E}[(n(t)-\mathrm{E}[n(t)])\,(n(s)-\mathrm{E}[n(s)])^T] = \frac{\sigma^2}{4\omega^3\zeta}\,\mathrm{e}^{-\zeta\omega|t-s|}\left[\cos\beta|t-s| + \frac{\zeta\omega}{\beta}\,\sin\beta|t-s|\right].$$

By reduction of the second-order SDE for $n(t)$ to first-order form and by state augmentation, the nonlinear SDE with a GMP2 noise process can be reduced to one (6.1.2) in which the noise process is white.

6.2 Structural and Parameter Uncertainty

6.2.1 Structural Uncertainty

The term "structural uncertainty" refers to the uncertainty in the force model or models discussed in Chapter 4 and Section 3.3. Mathematically, "structural uncertainty" refers to $\delta \boldsymbol{f}(\boldsymbol{x}(t), \boldsymbol{\alpha}, t)$ in the equation

$$\frac{d\boldsymbol{x}(t)}{dt} = \boldsymbol{f}(\boldsymbol{x}(t), \boldsymbol{\alpha}, t) + \delta \boldsymbol{f}(\boldsymbol{x}(t), \boldsymbol{\alpha}, t) \tag{6.2.1}$$

wherein one actually uses the model (6.1.2) instead of the true model (6.2.1). In this case, the term $\boldsymbol{f}(\boldsymbol{x}(t), \boldsymbol{\alpha}, t) + \delta \boldsymbol{f}(\boldsymbol{x}(t), \boldsymbol{\alpha}, t)$ represents the true forces acting on the RSO. Thus the problem is to estimate $\delta \boldsymbol{f}(\boldsymbol{x}(t), \boldsymbol{\alpha}, t)$ or to account for the uncertainty by a stochastic acceleration such as that modeled as $\mathbf{G}(\boldsymbol{x}(t), t)\, \boldsymbol{n}(t)$ in (6.1.2). Here, one approach is to make use of the Uhlenbeck-Ornstein model described in Section 6.1.1 or Vasicek process. The parameter in the Uhlenbeck-Ornstein model could be estimated or the parameter could be subjugated to a second stochastic differential equation. A second approach to this problem is to estimate the unmodeled dynamics using optimal control theory as discussed in Sections 3.3, 6.6, and 6.7. Structural uncertainties are usually related to the force model accelerations, and the particular force model formulation. While many of the force models have become very robust, the specific use of each model can sometimes be complicated by the fact that little or no information regarding the actual use is available to an outside user. For example, the EGM-08 gravitational model is extremely accurate. Yet, if one uses a 12×12 field and another uses a 70×70 field, they will get very different answers. Even greater differences would arise if simulations used a WGS-72 gravitational model while another used the EGM-08 model.

In addition to the force model itself, the input data parameters (gravitational coefficients, solar flux, etc) can be equally important to the results of a propagation. Consider the solar flux parameters that are required for most atmospheric models. Is the solar flux observed or adjusted to the Earth's average position from the Sun? Is the 81-day average found from the previous 81 days for which there is measured data, or from 40 or 80 days in the future when half or more of the data is predicted, and therefore much less reliable? What are the sources and accuracy of the predicted data? Answers to all these questions have never been collected into a standards document.

Several standards organizations attempt to provide a means for users to exchange information (ISO, CCSDS, etc). While there is rudimentary information in many of these standards to permit a user to accurately reproduce an ephemeris from the given state vector, there is still a need to encapsulate "enough" information so a user can reproduce an ephemeris from the given state information within a specified level of accuracy throughout the ephemeris. Vallado [259] investigated some of the requirements needed to ensure a consistent orbital propagation between two organizations. The conclusions suggested that numerous additional parameters and information were needed beyond a simple list of force models. An example is the Conjunction Data Message (CDM). While basic force model information is included, there's really no way to accurately propagate the given states because one barely knows which force model (EGM-08, MSIS-00, etc) is used, let alone how the data input parameters are used (interpolation, last average, etc). There is also no information about how to propagate the covariance.

6.2.2 Parameter Uncertainty in the Equations of Motion

Parametric uncertainties in the measurement equations and dynamic model ((6.1.1) and (6.1.2) or (6.1.4) and (6.1.3)) can be addressed in several ways depending on observability. The vector of parameters $\boldsymbol{\alpha} \in \mathbb{R}^p$ may be certain or uncertain. Here are some options for treating these parameters.

a. If a parameter is certain or known significantly below the remaining uncertainties in the system, then the parameter may be considered as fixed.

b. If a parameter is included in the orbit determination procedure and is observable, then its estimate and the uncertainty in the estimate is available at epoch. One can then include the parameter $\boldsymbol{\alpha}$ in the dynamical system as $\frac{d\boldsymbol{\alpha}}{dt} = 0$ and propagate its uncertainty through the differential equation to some future time. One might also consider in this treatment, the Schmidt-Kalman filter [235], which addresses the statistical cross correlation between the uncertain parameters and the state.

c. The case in which some of the system parameters are not observable is more complex. One possibility is to use batch estimation combined and the singular value decomposition [112] to determine those parameters or roll-ups that are observable and those that are not. If a parameter is observable, then it can be estimated and treated as above. In case a parameter is not observable, it is often treated probabilistically by assuming a uniform probability density function on an interval of a parameter and approximating the uniform distribution with a Gaussian sum [61], by polynomial chaos (see Section 7.11), or deterministically as a systemic uncertainty by sampling techniques [204, 229].

d. It is sometimes possible to construct an analytical model to approximate the effect of the uncertainty in a set of parameters. This can be important when the number of uncertain parameters is very large and often weakly or non-observable such as an uncertain gravitational field which may contain thousands of coefficients. While inclusion of the uncertain parameters in the state is computationally prohibitive, it is possible to obtain a tractable approximation to the associated growth in orbit uncertainty [292].

6.2.3 Parameter Uncertainty in the Measurement Equation

Parameters in the measurement equations are generally called sensor biases, navigation errors, and time biases, and are estimated using truth or fuzzy truth objects as training data. The different biases are addressed more specifically in Chapter 5. The determination of these parameters is normally part of sensor calibration. Some of these parameters may be observable or unobservable while rollups may be observable or unobservable. Again, this can be determined using the singular value decomposition [112].

6.3 The Filtering Problem for Continuous and Discrete Dynamics

Given an initial probability density function (PDF) describing the uncertainty in the state of an object, say, $p = p(\boldsymbol{x}, t_{k-1}|\boldsymbol{Z}_{k-1})$, the PDF at a future time $p = p(\boldsymbol{x}, t|\boldsymbol{Z}_{k-1})$ for $t > t_{k-1}$ is governed by the *Fokker-Planck-Kolmogorov equation (FPKE)* [139].

$$\frac{\partial p}{\partial t} = -\nabla_{\boldsymbol{x}}^T(p\boldsymbol{f}) + \frac{1}{2}\,\mathrm{tr}\big[\nabla_{\boldsymbol{x}}\nabla_{\boldsymbol{x}}^T(p\mathbf{G}\mathbf{Q}\mathbf{G}^T)\big], \tag{6.3.1}$$

where $\nabla_{\boldsymbol{x}}$ is the gradient with respect to $\boldsymbol{x}$ viewed as a column operator and $n(t)$ is assumed to be white noise with power spectral density $\mathbf{Q}$. This is sometimes called the *prediction step or time update*. Given a new sensor report/measurement z_k at time t_k, the *measurement update* is obtained from Bayes' rule using the measurement density $p(\boldsymbol{z}_k|\boldsymbol{x}_k)$ and the predicted density via

$$p(\boldsymbol{x}(t_k), t_k \mid \boldsymbol{Z}_k) = \frac{p(\boldsymbol{z}_k \mid \boldsymbol{x}(t_k))\, p(\boldsymbol{x}(t_k) \mid \boldsymbol{Z}_{k-1})}{\int p(\boldsymbol{z}_k \mid \boldsymbol{x}(t_k))\, p(\boldsymbol{x}(t_k) \mid \boldsymbol{Z}_{k-1})\, d\boldsymbol{x}(t_k)}. \tag{6.3.2}$$

Analytical solutions to the FPKE and to the prediction and correction equations in Figure 6.3.1 are generally intractable and are only known in a few restrictive cases. Conventional approaches for the numerical solution of this equation suffer from the "curse of dimensionality"; however, sparse grid methods for solving the FPKE show promise for a real time solution and are still very much a research problem [161].

For nonlinear and non-Gaussian models, approximate or suboptimal algorithms are utilized for the Bayesian state estimator. The most often used approximate algorithms are based on the extended Kalman filter (EKF), unscented Kalman filter (UKF), and perhaps the second order extended Kalman filters. These, however, represent the propagation of the mean and covariance and do not directly address the propagation of non-Gaussian processes encountered in astrodynamics. Due to the need to propagate uncertainties over extended periods of time in the absence of measurement updates, higher-order cumulants (e.g., skewness, excess kurtosis) can become non-negligible and must be accounted for in order to achieve uncertainty consistency.

In a recursive filtering approach for discrete dynamics (3), measurement data is processed *sequentially*, rather than as a batch. Given the initial density of the state $p(\boldsymbol{x}_0) \equiv p(\boldsymbol{x}_0|\boldsymbol{Z}_0)$, the PDF $p(\boldsymbol{x}_k|\boldsymbol{Z}_k)$ is obtained recursively in two stages, namely prediction and correction, as illustrated in the flowchart of Figure 6.3.1. The former is obtained from the transitional density $p(\boldsymbol{x}_k|\boldsymbol{x}_{k-1})$ in conjunction with the *Chapman-Kolmogorov equation* defined in the prediction step box of Figure 6.3.1.

Figure 6.3.1 Predictor-corrector step for the recursive Bayesian state estimator

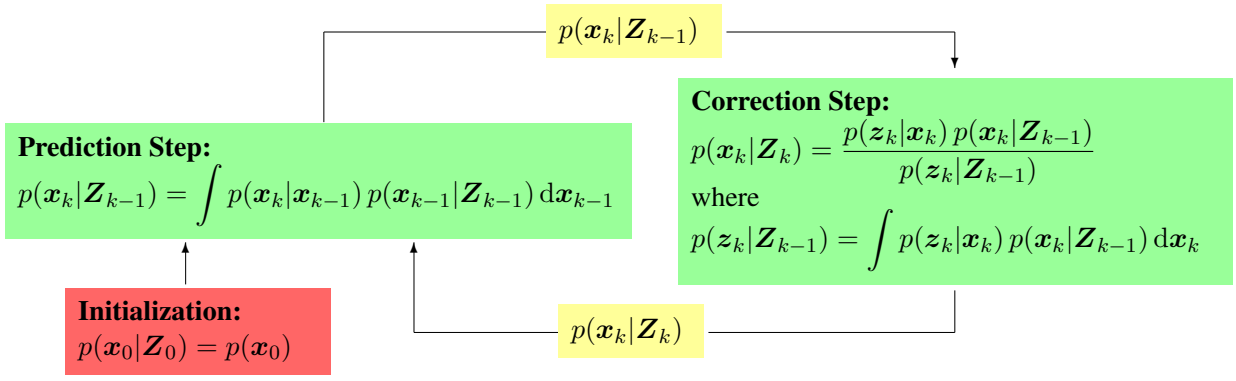

The term $p(\boldsymbol{z}_k|\boldsymbol{Z}_{k-1})$ in the denominator of the correction step is called the *prediction error* and appears in the likelihood ratios for scoring an assignment of a report (i.e., $\boldsymbol{z}_k$) to a track (see, for example, Poore [224]). Thus, its accurate evaluation is critical for correct data/track association (correlation).

6.4 Filter-Smoother and the Relationship to Batch Estimation

There are several filter-smoothing algorithms (e.g., fixed-interval, fixed point, and fixed lag) in which one determines the probability density function $p(\boldsymbol{x}(t_k) \mid \boldsymbol{Z}_N)$ wherein in $N > k$. A discussion of these filter-smoother algorithms can be found in the books by, for example, Gelb [96], Särkkä [233], Crassidis and Junkins [55] and Tapley, Schutz, and Born [254]. The relationship between the extended Kalman filter/smoother and batch estimation (with or without process noise) has been established in the literature starting with the work of Bell and Cathey [29], Bell [28], Bertsekas [33] and summarized in the 2012 review paper by Humpherys, Redd, and West [132]. Essentially, a Gauss-Newton step is equivalent to a filter-smoother pass as shown in this review paper [132] and the paper by Bell [28].

The astrodynamics surveillance community makes extensive use of batch estimation and filter-smoothers. Batch estimation is often solved by a sequence of Gauss-Newton steps; however, most nonlinear least squares algorithms add a globalization method such as a line search or a trust region method to assist with convergence.

For the filter/smoother solution, the *McReynolds test* [293] was developed to test the consistency between the filter and smoother. This in a way helps ensure a consistent performance. The filter-smoother consistency test is applied by testing that the difference between the filtered state (X_f) and smoother state (X_s) is normally distributed in n dimensions (assuming n is the size of the state-difference vector) with a covariance equal to the filter covariance subtracted from the smoother covariance [201]. The test may be applied to the entire estimation state or any subset thereof. In practice the filter-smoother consistency test is often applied to individual components of a state, which often provides more focused diagnostic information. Due to correlations between the filtered and smoothed solutions, it is also common practice to plot this metric as a function of time evaluated against confidence bounds which depend on the dimension of the sub-state involved in the computation of the metric as opposed to applying formal distribution tests. For example, filter-smoother consistency is generally claimed for the single state case when this metric stays within $pm3\sigma$ over the fit interval.

Significant excursion of the test metric $\left(\text{Consistency} = \frac{X_f - X_s}{\sqrt{\sigma_f^2 - \sigma_s^2}}\right)$ outside expected bounds is typically the result of an incorrect dynamical model, incorrect measurement statistics or the processing improper measurements. Typical examples of problems are incorrect ballistic or solar pressure coefficient characterizations, un-modeled out-gassing or momentum dumps, tracking data from an improperly configured ground station and mis-tagged observations.

As an aside, given the relationship between Gauss Newton steps in batch estimation and the above consistency test for the filter-smoother, it would be interesting to investigate the relationship between this consistency test, the Gauss Newton steps and the use of a globalization method for nonlinear least squares such as a line search.

6.5 The Consider or Schmidt-Kalman Filter

The Schmidt-Kalman filter is a modification of the Kalman filter that addresses a state and parameters in the dynamics and measurement equations wherein the parameters are assumed to be Gaussian distributed

with known means and covariances. Rather than estimating these parameters as part of a Kalman filter, the Schmidt-Kalman filter builds the statistics of the parameters into the state of the object and its statistics. Here is an example. Assume that the system parameters in both the dynamics and the measurement equations have been estimated with the resulting estimates being Gaussian random variables. The Schmidt-Kalman filter then accounts for the cross-correlation of between estimated parameters and the state thereby modifying the covariance of the state. The primary advantage of utilizing the Schmidt-Kalman filter instead of increasing the dimensionality of the state space is the reduction in computational complexity. This can enable the use of filtering in real-time systems. Another usage of Schmidt-Kalman occurs when residual biases are unobservable; that is, the effect of the bias cannot be separated out from the measurement. .

The Schmidt-Kalman filter [235] is also presented in the book by Jazwinski [139] and more recent articles by Zanetti and Ď Souza [297]. Stauch and Jah [249] combine the unscented Kalman filter with the Schmidt-Kalman filter into a unscented Schmidt-Kalman filter. A different approach to a consider filter can be found in the book by Tapley, Schutz, and Born [254].

6.6 Batch Estimation with Process Noise in the Continuous Case

A formulation of the estimation problem in the case of continuous dynamics with process noise can be found in the book by Jazwinski [139]. When the measurement noise sequence is white zero mean Gaussian with $\boldsymbol{\nu}_k \sim N(0, \mathbf{R}_k)$ and the process noise is white zero mean Gaussian $\boldsymbol{w}(t) \sim N(0, \mathbf{Q}(t))$, $\boldsymbol{x}_0 \sim N(\bar{\boldsymbol{x}}_0, \mathbf{P}_0)$, and these are independent, then the following is often used:

$$\begin{aligned} \text{Minimize}_{(\boldsymbol{x},\boldsymbol{w})} J(\boldsymbol{x},\boldsymbol{w}) = & \frac{1}{2}\big(\boldsymbol{x}_0 - \bar{\boldsymbol{x}}_0\big)^T \mathbf{P}_0^{-1}\big(\boldsymbol{x}_0 - \bar{\boldsymbol{x}}_0\big) \\ & + \frac{1}{2}\sum_{k=1}^{N}\big(\boldsymbol{z}_k - \boldsymbol{h}_k(\boldsymbol{x}(t_k))\big)\mathbf{R}_k^{-1}\big(\boldsymbol{z}_k - \boldsymbol{h}_k(\boldsymbol{x}(t_k))\big) \\ & + \frac{1}{2}\int_{t_0}^{t_N} \boldsymbol{w}(\tau)^T \mathbf{Q}^{-1}(\tau)\boldsymbol{w}(\tau)d\tau \end{aligned} \tag{6.6.1}$$

$$\text{Subject To: } d\boldsymbol{x} = \boldsymbol{f}(\boldsymbol{x}, \boldsymbol{\alpha}, \boldsymbol{w}(t), t)dt, \quad t_0 \le t \le t_N \tag{6.6.2}$$

to characterize the state and its uncertainty. (The case of $N = 1$ corresponds to sequential processing.) Note that any of the process noises in Section 6.1.1 can be treated in this way via state augmentation. If one thinks of this formulation from a controls viewpoint, a feature is that the term $\boldsymbol{f}(\boldsymbol{x}, \boldsymbol{\alpha}, \boldsymbol{w}(t), t) - \boldsymbol{f}(\boldsymbol{x}, \boldsymbol{\alpha}, 0, t)$ might now be interpreted as the *model bias or model inadequacy* in the model dynamics $\boldsymbol{f}(\boldsymbol{x}, \boldsymbol{\alpha}, 0, t)$ discussed in Section 6.2.1. A difference in the treatment of $\boldsymbol{w}$ as a control instead of noise is that w is determined a posteriori as part of the solution rather being specified a priori in the case of process noise. This optimal control approach could also assist with the design of the process noise discussed in Section 6.1.1. Here are two observations. In both cases, the choice of the covariance matrix $\mathbf{Q}(t)$ is the nontrivial part of the design problem and can significantly impact the results. The data association is assumed to be correct; otherwise, erroneous conclusions can follow from a choice of a control that allows one to "connect" measurements that emanate from different objects. Finally, another discussion of control approaches is also contained in Section 3.3.

The corresponding problem without process noise or control w is

$$\text{Minimize } J(\boldsymbol{x}_0) = \frac{1}{2}\big(\boldsymbol{x}_0 - \bar{\boldsymbol{x}}_0\big)^T \mathbf{P}_0^{-1}\big(\boldsymbol{x}_0 - \bar{\boldsymbol{x}}_0\big) + \frac{1}{2}\sum_{k=1}^{N}\big(\boldsymbol{z}_k - \boldsymbol{h}_k(\boldsymbol{x}(t_k))\big)\mathbf{R}_k^{-1}\big(\boldsymbol{z}_k - \boldsymbol{h}_k(\boldsymbol{x}(t_k))\big) \tag{6.6.3}$$

$$\text{Subject To: } \frac{d\boldsymbol{x}}{dt} = \boldsymbol{f}(\boldsymbol{x}, \boldsymbol{\alpha}, t),\ t_0 \le t \le t_N,\ \boldsymbol{x}(t_0) = \boldsymbol{x}_0 \tag{6.6.4}$$

wherein the only independent variable is $\boldsymbol{x}_0$. For initial orbit determination, the first term is generally absent. In the astrodynamics community, the solution method for this problem is called *differential corrections*. When process noise is absent, the covariance of the state can "collapse;" however, this difficulty is often mitigated with the use of a fading memory process.

6.7 Batch Estimation with Process Noise in the Discrete Case

Given the discrete dynamical system (6.1.3) and measurements (6.1.4), the objective of initial orbit determination (IOD) and batch estimation is to obtain a representation of the (joint) posterior PDF $p(\boldsymbol{x}_0, \ldots, \boldsymbol{x}_N | \boldsymbol{Z}_N)$, where $\boldsymbol{x}_k$ denotes the dynamical state of the system at time t_k, and to extract meaningful statistics (e.g., mean, covariance) from it in a consistent manner. It is assumed that the state evolves according to the discrete-time model

$$\boldsymbol{x}_k = \boldsymbol{f}_{k-1}(\boldsymbol{x}_{k-1}, \boldsymbol{w}_{k-1}) = \boldsymbol{f}_{k-1}(\boldsymbol{x}_{k-1}) + \boldsymbol{w}_{k-1},\ (k \ge 1) \tag{6.7.1}$$

instead of the representation (3). Appealing to Bayes' rule and the above assumptions, the joint posterior PDF is derived in Jazwinski [139, §5.3] and is found to be

$$p(\boldsymbol{x}_0, \ldots, \boldsymbol{x}_N | \boldsymbol{Z}_m) = c\, p_0(\boldsymbol{x}_0) \prod_{k=1}^{N} p_{w_k}(\boldsymbol{x}_k - \boldsymbol{f}_{k-1}(\boldsymbol{x}_{k-1})) \prod_{k=1}^{N} p_{v_k}(\boldsymbol{z}_k - \boldsymbol{h}_k(\boldsymbol{x}_k)), \tag{6.7.2}$$

where c is a normalizing constant, and p_0 is the prior PDF of the state $\boldsymbol{x}_0$ at time t_0. Further, in (6.7.2), the p_{w_k} and p_{v_k}, for $k = 1, \ldots, N$, are the respective PDFs of the process and measurement noise processes. In practice, they are often assumed to be Gaussian with zero mean and covariances of $\mathbf{Q}_k$ and $\mathbf{R}_k$, respectively.

The posterior PDF (6.7.2) *is* the complete description of the uncertainty of the state at each of the measurement times. In practice, a finite dimensional representation of the uncertainty is sought. Thus, the emphasis of the batch estimation problem is on how statistical information can be extracted from (6.7.2) consistently and accurately. Nonlinear optimization theory provides a framework for computing the *modal trajectory* or *maximum a posteriori (MAP)* estimate of (6.7.2). For a Gaussian prior with $\boldsymbol{x}_0 \sim N(\bar{\boldsymbol{x}}_0, \bar{\mathbf{P}}_0)$ and Gaussian noise processes as described above, the modal trajectory is obtained by solving the least

squares or batch problem

$$\begin{aligned}(\hat{\boldsymbol{x}}_0,\ldots,\hat{\boldsymbol{x}}_N)^{MAP} &= \underset{\boldsymbol{x}_0,\ldots,\boldsymbol{x}_N}{\arg\max}\; p(\boldsymbol{x}_0,\ldots,\boldsymbol{x}_N|\boldsymbol{Z}_N)\\ &= \underset{\boldsymbol{x}_0,\ldots,\boldsymbol{x}_N}{\arg\min}\; \frac{1}{2}\|\boldsymbol{x}_0-\bar{\boldsymbol{x}}_0\|^2_{\bar{\mathbf{P}}_0^{-1}} + \frac{1}{2}\sum_{k=1}^{m}\|\boldsymbol{x}_k-\boldsymbol{f}_{k-1}(\boldsymbol{x}_{k-1})\|^2_{\mathbf{Q}_{k-1}^{-1}} + \frac{1}{2}\sum_{k=1}^{N}\|\boldsymbol{z}_k-\boldsymbol{h}_k(\boldsymbol{x}_k)\|^2_{\mathbf{R}_k^{-1}}.\end{aligned} \tag{6.7.3}$$

If the matrix Q_{k-1} depends on x_{k-1}, then one needs to add the term $\sum_{k=1}^{N}\ln\det\big(2\pi\mathbf{Q}_{k-1}(\boldsymbol{x}_{k-1})\big)$.

Methods for solving nonlinear least squares problems, such as Gauss-Newton, full Newton, and quasi-Newton updates, along with globalization methods such as line search and trust region methods including Levenberg-Marquardt [88], are efficient and mature and will not be discussed further here. In the astrodynamics community, such solution techniques are called *differential correction* methods. In any nonlinear least squares problem such as (6.7.3), one must provide the solver a starting guess in order to initiate the differential correction method. This is the *initial orbit determination (IOD)* problem. In the case of measurement data from a single radar or EO sensor, a first estimate can be obtained using the classical methods of Lambert or Gauss (see, for example, [260]). Additionally, for angle-only observations, a recent algorithm due to Gooding [103] has shown promise for IOD scenarios involving both ground-based and space-based EO sensors [263]. An improvement can be found in the recent work of Casotto [46]. Finally, it is important to stress that batch estimation is generally employed using a sliding window rather than using all measurements over all time.

Finally, one can also consider this discrete formulation within the context of a discrete optimal control approach discussed in Section 6.6.

6.8 The Use of Empirical Covariance Matrices

The above discrete least squares formulations for IOD or OD in equations (6.6.3) for continuous dynamics and no process noise or discrete dynamics (6.7.3) with or without process noise can all be formulated abstractly as solving for $\boldsymbol{x}$ from the equation

$$\boldsymbol{f}(\boldsymbol{x}) = 0 + \epsilon$$

wherein $\epsilon \sim N(0,\mathbf{W})$, i.e., is a zero mean Gaussian with covariance $\mathbf{W}$, $\boldsymbol{f} : \mathbb{R}^m \to \mathbb{R}^n$ is a smooth function and $\mathbf{W} \in \mathbb{R}^{m\times m}$ is a symmetric positive definite matrix. The unknown $\boldsymbol{x} = \boldsymbol{x}_0$ for the formulation (6.6.3) or $\boldsymbol{x} = (\boldsymbol{x}_0,\boldsymbol{x}_1,\ldots,\boldsymbol{x}_N)$ for the discrete problem 6.7.3 with process noise. These problems are normally formulated as

$$\text{Minimize}_{\boldsymbol{x}}\|\boldsymbol{f}(\boldsymbol{x})\|^2_{\mathbf{W}^{-1}} \tag{6.8.1}$$

Given a minimizer $\boldsymbol{x}$, one generally writes the maximum likelihood estimate of the covariance matrix as

$$\mathbf{P} = \big(\mathbf{J}(\boldsymbol{x})^T\mathbf{W}^{-1}\mathbf{J}(\boldsymbol{x})\big)^{-1}$$

where $\mathbf{J}(\boldsymbol{x}) = D_{\boldsymbol{x}}\boldsymbol{f}(\boldsymbol{x})$ is the Jacobian matrix of $\boldsymbol{f}(\boldsymbol{x})$.

6.8.1 An Empirical Covariance Matrix for Batch Processing

An empirical covariance has been derived by Frisbee [155]. In view of the equivalence between batch and the filter/smoother, Frisbee's empirical covariance applies both to the filter/soother as well as the batch processing. Extensions to the iterated EKF and other filters may also be possible.

Here is a synopsis of this work [155]. Matrices originating through the usual estimation techniques (batch, sequential) are theoretical state error covariance matrices representing only the effect of assumed measurement uncertainties. Techniques exist in both batch and sequential methods for adding a so-called process noise. (Notwithstanding the following description, process noise actually has a more simple explanation.) Typically such noise is determined empirically through prior analysis of the performance of any specific estimation process. Any process noise added is intended to represent the historical averaged effect of unmodeled error sources. The effectiveness of process noise is dependent upon the consistency of the noise sources. This consistency should be both within the analysis leading to the determination of the process noise as well as between the future solutions to which it as applied and the past history from which it is derived. With regards to the state error covariance matrix, classical process noise has no ability to adequately account for within solution model or measurement noise variations. Neither can the classical process noise account for spontaneous changes in the measurement noise or dynamic model.

An alternative is the empirical state error covariance matrix which is created in such a way as to include all errors reflected in the measurement residuals. The empirical state error covariance matrix includes, without regard to whether the source might be known and anticipated or unknown and spontaneous, all errors existing over the estimation fit interval and reflected in the measurement residuals. The empirical error covariance matrix also represents each solution uniquely and individually. That is if a condition existed temporarily and in such a way so as to only affect a satellite or some group of satellites during a short interval of time (fit interval, day, hour, observation) the empirical error covariance matrix has the ability to reflect the changes that occurred. This is true even if the effects are not recognized to have occurred at the time.

The batch estimation empirical state error covariance matrix, as presented by Frisbee [155], is just the final part of the standard sample data problem. That problem gives rise to various statistics such as: the average (estimate of the population mean), empirical covariance (estimate of the population covariance), and empirical covariance of the average (estimate of the uncertainty of the average with respect to the population mean). Traditionally, estimation has only addressed the estimate of the mean and the theoretical value of the covariance of the average with respect to the mean. Batch estimation is a simple application of a standard sample data problem in frequentist statistics. All of the usual rules of that discipline apply. As an example, the state error covariance matrix is a sample covariance and thus is inherently uncertain. However there are specific paths within statistics to address such uncertainty. It might be argued that the current theoretical error covariance matrices are not uncertain. That is correct. However, those matrices are just simply wrong because they leave out all error sources except the assumed measurement uncertainties, which could themselves be wrong.

6.8.2 Use of an Empirical Covariance for Propagation

One of the challenges in using empirical covariances in estimating the uncertainty in orbit determination is that the data is usually sparse. Dense tracking data situations, such as that possible from GPS receivers in a LEO orbit or continually telemetered GEO communication satellites, while increasing in commonality, are still the exception rather than the rule, as most objects in space are inactive, and of those that are active, data is usually restricted to owner-operators. The time scale required to collect enough data for a traditional empirical covariance would likely span multiple orbit revolutions, if not multiple days, over which short-periodic or transient effects could be lost in the estimate. As noted in the previous section, the standard covariance calculations are based on a-priori knowledge of measurement error (reflected in the measurement weighting matrix) and modeling error (most often modeled in the form of some flavor of process noise), which are rarely a precise description of the error in the orbit. However, they do include most of the dominant sources of error, and their propagation includes many of the short periods and transients that might be lost if one were averaging over a sparse data environment. Thus, there is a benefit to simply correcting error in existing covariance using empirical methods rather than using empirical methods alone.

The development by Cerven [47, 48] analyzes the error in the covariance through normalization of the data by the a-priori covariance. Let the true covariance $\mathbf{P}_t$ of $x \in \mathbb{R}^n$ be defined relative to the predicted covariance $\mathbf{P}_p$ via a normalized covariance $\mathbf{P}_n$ such that

$$\mathbf{P}_t = \big(\mathbf{V}_p\mathbf{D}_p\big)\mathbf{P}_n\big(\mathbf{V}_p\mathbf{D}_p\big)^T,$$

where $\mathbf{D}_p$ and $\mathbf{V}_p$ are the matrices of eigenvalues and eigenvectors, respectively, of the predicted covariance $\mathbf{P}_p$. This normalized covariance then encapsulates the error in the predicted covariance. To solve this problem, let us compare predicted states $\boldsymbol{x}_p$ and covariances $\mathbf{P}_p$ against measurements $\boldsymbol{y}_m \in \mathbb{R}^m$ with covariance $\mathbf{P}_m$, where measurement space is mapped to state space such that $\boldsymbol{y} = \boldsymbol{f}(\boldsymbol{x})$ (with linearization $\mathbf{H}(\boldsymbol{x}) = D_{\boldsymbol{x}}\boldsymbol{f}(\boldsymbol{x})$). The difference in the measurement to the mapped predicted state is $\Delta\boldsymbol{y}$ with a covariance $\mathbf{P}_d$ such that

$$\begin{aligned} \Delta\boldsymbol{y} &= \boldsymbol{f}(\boldsymbol{x}) - \boldsymbol{y}_m, \\ \mathbf{P}_d &= \boldsymbol{\Psi}\mathbf{P}_n\boldsymbol{\Psi}^T + \mathbf{P}_m \quad \big(\boldsymbol{\Psi} = \mathbf{H}\mathbf{V}_p\mathbf{D}_p\big), \\ \mathbf{P}_{t\boldsymbol{y}} &= \boldsymbol{\Psi}\mathbf{P}_n\boldsymbol{\Psi}^T = \mathbf{P}_d - \mathbf{P}_m, \end{aligned} \tag{6.8.2}$$

where $\mathbf{P}_{t\boldsymbol{y}}$ is the mapping of $\mathbf{P}_t$ to the measurement space and can be sampled by a single $\Delta\boldsymbol{y}$ such that

$$\hat{\mathbf{P}}_{t\boldsymbol{y}} = \Delta\boldsymbol{y}\Delta\boldsymbol{y}^T - \mathbf{P}_m$$

Letting $\boldsymbol{p}_{t\boldsymbol{y}}$ and $\boldsymbol{p}_n$ be vector representations of the upper-triangular matrices of $\mathbf{P}_{t\boldsymbol{y}}$ and $\mathbf{P}_n$, respectively, one can use creative algebra to turn equation (6.8.2) into the following linear equation.

$$\boldsymbol{p}_{t\boldsymbol{y}} = \boldsymbol{\Theta}(\boldsymbol{\Psi})\boldsymbol{p}_n$$

which, through sufficient sampling of the measurement data with the assumption that the matrix $\mathbf{P}_n$ is effectively constant across the time spanned by the measurements in question, can be solved by a simple linear least squares method. Furthermore, this can be mapped directly to the traditional sample covariance calculation when measurements are full rank.

As this estimate of the normalized matrix $\mathbf{P}_n$ is based on sampling, confidence bounds on the errors in this matrix can be estimated using sample distribution theory as well, which can be calculated in terms of the errors on the variances and correlation factors of this matrix. The sampling distribution of the variance takes the form of a gamma distribution dependent on the actual standard deviation of the distribution and the number of samples, while the sample distribution of the bivariate correlation coefficients follows Pearson's r-distribution and can be mapped to an (approximately) Gaussian distribution via the Fisher transformation.

The sensitivity of the probability of collision to these confidence bounds can be found by finding the minimums and maximums over the range of variances and correlation factors, a basic parameter optimization problem.

6.9 Particle Filters

Particle filters are sequential Monte Carlo methods based on based on the representation of an arbitrary PDF by a set of independent and identically distributed random samples, which can be applied to any state-space model, and which generalize the traditional Kalman filtering methods to nonlinear and non-Gaussian problems [21, 73, 228]. These methods are used in space object tracking, e.g., [174, 194, 241].

6.10 Nonlinear Filtering Using Sparse Grid Methods

Conventional approaches for the numerical solution of the Fokker-Planck-Equation suffer from the curse of dimensionality and are therefore not applicable in higher dimensions. Sparse grid methods for solving the Fokker-Planck-Equation show promise for a real time solution and are still very much a research problem [161].

6.11 FISST Based Methods

Multi-target filters based on FInite Set STatistics (FISST) provide a method for estimating a multi-target state when given a set of observations [187, 188]. As described in Section 3.2, data association based on MHT/MFA or JPDA provides a means for updating a single-target state when given a method for data association. Instead, FISST-based algorithms include the data association process as a fundamental part of a given multi-target filter. Such methods leverage Random Finite Sets (RFS) to estimate the probability density function (PDF) of the multi-target state, which provides an estimate (with uncertainty) in the number of objects and their states. FISST provides the mathematical tools for characterizing and analyzing uncertainty in the estimated multi-target state, which is consistent with standard probability theory [276].

In the RFS approach, the multi-target state X_k and observation Z_k at time t_k are represented by the finite

sets

$$X_k = \{x_1, x_2, \ldots, x_n\} \subset \mathbb{X} \tag{6.11.1}$$

$$Z_k = \{z_1, z_2, \ldots, z_m\} \subset \mathbb{Z} \tag{6.11.2}$$

where $\mathbb{X}$ and $\mathbb{Z}$ denote the single-target state and measurement spaces, respectively. For example, if there are two targets with states x_1 and x_2, then $X_k = \{x_1, x_2\}$ and the estimated number of objects is the number of elements in X_k. For a single sensor scan, such as a single CCD image, there may be multiple measurement vectors $z_1, \ldots, z_m$. The measurement Z_k is then the set of these observation vectors at time t_k. Note that the $|X_k| = n$ does not necessarily equal $|Z_k| = m$ due to missed detections and clutter. Each single-target state x is assumed to be a random vector with realization $x_i \in \mathbb{X}$. The Bayes multi-target filter is then an analog of the single-target Bayes filter (see 6.3) to estimate X_k when given a measurement Z_k. Such filters includes a framework to model target birth (analogous to IOD in astrodynamics), target survival probability, spawning of new objects, and probability of detection. Such models will vary with application and required fidelity.

Several forms of the FISST-based filter exist to satisfy variations in system requirements and computation considerations. The FISST filter provides a full PDF of the multi-target state, but is intractable for a large number of targets [187] . This motivated the development of principled approximations of the FISST filter. The most well studied of these include the Probability Hypothesis Density (PHD) filter [185, 275, 276], the Cardinalized Probability Hypothesis Density (CPHD) filter [186, 279], and various forms of the multi-Bernoulli filter (e.g., see [227, 277, 278]). The PHD filter estimates the density of objects in the single-target space, but does not include knowledge of target identity. To improve stability in the PHD filter, the CPHD filter augments the density function with an estimated cardinality distribution, i.e., a probability mass function describing the number of targets. Alternatively, the multi-Bernoulli filters estimate X_k based on a parameterization $\{(r_i, p_i(x))\}_{i=1}^{N}$ where r_i is the probability of existence for the i-th target and $p_i(x)$ is the state PDF. Such a parameterization allows for estimating information on specific targets instead of a more general target density function [278]. A general description of finite set statistics and the various FISST-based filters may be found in [187] and [188].

Applications of RFS-based multi-target filters for tracking orbital debris have been demonstrated in recent literature. This includes the FISST filter for at most three targets [133, 133, 134], the PHD/CPHD filter for up to hundreds of objects [51, 95, 150, 195], and the labeled Multi-Bernoulli filter (LMB) [152]. The fundamental forms of the PHD-based filters maintain no identifying information, e.g., a catalog number. The LMB filter described in [227] and applied to tracking orbital debris in [152] provides a means for maintaining knowledge of target identity in the context of the FISST-based filters.

6.12 Recommendations

Many of the estimation methods are surveyed above. Virtually all of the current estimation techniques are being used to estimate the state and uncertainty of resident space objects. Here are some final comments and recommendations.

1. A set of benchmark test cases similar to those proposed in Chapter 9 for assessing covariance/uncertainty realism during propagation should be developed for assessing uncertainty/covariance realism at epoch.

2. In addition to state estimation, the *uncertain parameters* in the dynamics and *sensor biases, navigation errors, and time biases* in the measurement equation should all be considered and potentially estimated if observable. The latter are generally determined as part of the calibration process and the former as part of the orbit determination process. Finally, a consider filter might be used to improve the estimation of uncertainty due to statistical cross correlation between the uncertain parameters in the dynamics and measurement equations.

3. The astrodynamics community is divided on the use of process noise or stochastic acceleration; however, process noise is one technique that can account for model mismatch and parameter uncertainty, especially if its design is physics-based. The four models in Section 6.1.1 remain applicable to helping characterize the uncertainty in the state of an object. The use of process noise such as these four models does not replace the goal of developing good physical models, but should be viewed as an approach to account for the uncertainties in the models.

4. Sections 6.6 and 6.7 present batch formulations of the continuous and discrete problems, respectively. Of particular note is that these can be treated in a controls formulation in which the noise is viewed as a control that is determined as part of the solution (state and control). This approach as noted in Section 3.3 presents a method for treating *structural uncertainty*. A comparison of the controls and noise approaches should be investigated and compared.

5. The use of empirical covariances described in the work of Frisbee [155] and Cerven [47, 48] and briefly summarized in Section 6.8 appears to be promising and should be further studied to see if it could lead to improvements in the representation of uncertainty in the state of a space object.

6. While batch estimation formulations are quite classical (e.g., Jazwinski [139] and Escobal [86]), the development of robust numerical methods is more recent. A recommendation is to make use of a globalization technique such as a line search or trust region method to improve the convergence of the methods to solutions whose errors are substantially below those in the measurements and astrodynamic models. Also, one finds that many of the nonlinear least squares problems arising in astrodynamics often have multiple optima, so some care is needed in selecting the correct solution.

7. The measurements from a short arc of sensor reports are frequently, if not most often, correlated while the above estimation techniques assume they are uncorrelated. Thus, attention to the correlation is needed to improve performance and achieve covariance realism during orbit determination.

8. Algorithms that are capable of representing the entire PDF or at least higher moments should be considered for propagating uncertainty.

Chapter 7

Propagation of Uncertainty

7.1 Introduction to the Propagation of Uncertainty

The *propagation of uncertainty* from epoch, i.e., at the time of the last measurement update, is required to support the mission areas of conjunction analysis, data association, anomaly detection, and sensor tasking and scheduling. These uncertainties fall into two broad classes, namely aleatoric and epistemic uncertainties. The former are generally treated within a probabilistic framework and the latter, by other methods such as fuzzy logic and evidence theory (Dempster-Shafer theory) [253, 258]. The methods addressed in this chapter are of the aleatoric type. What is generally assumed is that the uncertainty is represented by a Gaussian random variable at epoch; however, this is not necessary. Regardless of the representation, the probability density function (PDF) must be propagated through the nonlinear dynamical system (6.1.2).

In addition to the methods for propagating uncertainty, there are several considerations that affect the quality of the representation of uncertainty and the length of time it remains valid. First, the coordinate system in which uncertainty is represented and propagated has a significant impact. Generally this means a Cartesian versus an orbital element space as discussed in Section 7.2. Regardless of which coordinate system is used, each of the aforementioned mission areas may require the representation in a different coordinate system than that of the propagated uncertainty. Thus, one must address the faithful representation in the needed coordinate system. Other variables in testing the different approaches include the following: a) inclusion/exclusion of model mismatch (i.e., the difference between the ”truth” model and the hypothesized model), b) inclusion/exclusion of process noise or stochastic acceleration, c) the size of the initial uncertainty, e.g., the size of the semi-major axis variance, and d) computational complexity.

Research into the topic of “propagation of uncertainty” by the astrodynamics community is broad and quite excellent. Thus, the goal of this chapter is to survey most of these methods and to make recommendations on approaches that might be used to evaluate the different methods for different purposes. No doubt, different methods may be required for different applications. The framework for the astrodynamic equations of motion is presented in Section 4.1 and Chapter 6 and will not be repeated here.

7.2 Coordinate Systems for Representing Uncertainty in SSA

Under Gaussian assumptions, the coordinates used to represent the state space can impact how long one can propagate the uncertainty under a non-linear dynamical system; a Gaussian random vector will not be mapped to a Gaussian under a non-linear transformation, but can remain nearly Gaussian for some time depending on the coordinate system. The representation of a space object's kinematic state in *orbital element coordinates* [207], rather than Cartesian Earth-Centered-Inertial (ECI) position-velocity coordinates, is well-suited to the space surveillance tracking problem since such coordinates "absorb" the most dominant terms in the non-linear gravitational potential leading to "less non-linear" propagations. Thus, these special coordinates can mitigate the departure from "Gaussianity" under the non-linear propagation of an initial Gaussian state PDF with respect to orbital elements [231].

For example, the *Keplerian orbital elements* $(a, e, i, \Omega, \omega, M)$ define a system of curvilinear coordinates with respect to six-dimensional position-velocity space and encompass the geometric and physical properties of unperturbed two-body dynamics. As noted above, by absorbing the most dominant non-linear term in the equations of motion (i.e., the $1/r^2$ term), propagation is less non-linear in orbital elements, thereby more closely preserving any Gaussian and linear approximations. Such orbital elements are, however, singular at zero eccentricity and inclination [207]. Thus, one turns to the nonsingular equinoctial elements, which are in wide use for propagating uncertainty. Based on the merits of the equinoctial elements for representing the PDF of a space object's orbital state, one can ask if further improvements are possible by incorporating higher-order gravity perturbations beyond the $1/r^2$ contribution. Indeed, following the work of Brouwer [42] and Lyddane [183], one can define a new system of orbital elements, called the J_2 *equinoctial orbital elements*, that effectively absorb the J_2 zonal correction (i.e., the most dominant term in the geopotential expansion that accounts for the Earth's oblateness) [10]. Like the traditional equinoctial elements discussed above, the J_2 equinoctial elements also possess the desirable property of being non-singular for orbits with zero eccentricity or zero inclination [14]. The use of these different orbital element spaces to represent uncertainty and then the transformation of the uncertainty to a Cartesian space to support, for example, conjunction assessments is discussed in Section 7.9.

7.3 The Fokker-Planck-Kolmogorov Equation for Continuous Dynamics

For continuous time dynamics, the dynamical model of the form (6.1.2) governs the astrodynamics. Given an initial probability density function describing the uncertainty in the state of an object, say, $p = p(\boldsymbol{x}, t_{k-1}|\boldsymbol{Z}_{k-1})$, the pdf at a future time $p = p(\boldsymbol{x}, t|\boldsymbol{Z}_{k-1})$ for $t > t_{k-1}$ is governed by the *Fokker-Planck-Kolmogorov equation (FPKE)* [139]

$$\frac{\partial p}{\partial t} = -\nabla_{\boldsymbol{x}}^T(p\boldsymbol{f}) + \frac{1}{2}\,\mathrm{tr}\big[\nabla_{\boldsymbol{x}}\nabla_{\boldsymbol{x}}^T(p\mathbf{G}\mathbf{Q}\mathbf{G}^T)\big], \tag{7.3.1}$$

where $\nabla_{\boldsymbol{x}}$ is the gradient with respect to $\boldsymbol{x}$ viewed as a column operator. In addition FPKE, there is a corresponding backward equation [139, p. 130] that can be used for smoothing. Additional details are given in Section 6.3.

Analytical solutions to the FPKE are generally intractable and are only known in a few restrictive cases. A sparse grid method [161] is one possible approach to solving the FPKE numerically; otherwise, one turns

to approximate methods discussed in subsequent sections.

7.4 Extended Kalman Filter

General nonlinear state estimation problems are generally not solved exactly. The most widely used approximate solution is the extended Kalman filter (EKF), which applies the standard linear Kalman filter algorithm with linearization of the nonlinear system. This algorithm requires that the process (stochastic acceleration), observation noises, and the initial random variable $\boldsymbol{x}(t_0)$ be independent white Gaussian processes. In this setting, given a Gaussian, say $N(\boldsymbol{\mu}_0, \mathbf{P}_0)$, the mean $\boldsymbol{\mu}_0$ and covariance $\mathbf{P}_0$ are propagated via the noiseless dynamics and Ricatti equation dynamics

$$\frac{d\boldsymbol{x}(t)}{dt} = \boldsymbol{f}(\boldsymbol{x}(t), \boldsymbol{\alpha}, t), \quad \boldsymbol{x}(t_0) = \boldsymbol{\mu}_0 \tag{7.4.1}$$

$$\frac{d\mathbf{P}(t)}{dt} = \mathbf{F}(\boldsymbol{x}(t), \boldsymbol{\alpha}, t)\mathbf{P} + \mathbf{P}^T\mathbf{F}^T(\boldsymbol{x}(t), \boldsymbol{\alpha}, t) + \mathbf{G}(\boldsymbol{x}(t), t)\mathbf{Q}(t)\mathbf{G}^T(\boldsymbol{x}(t), t), \quad \mathbf{P}(t_0) = \mathbf{P}_0, \tag{7.4.2}$$

respectively, where $\mathbf{F}(\boldsymbol{x}(t), \boldsymbol{\alpha}, t) = D_{\boldsymbol{x}}\boldsymbol{f}(\boldsymbol{x}(t), \boldsymbol{\alpha}, t)$. In case $\mathbf{Q}(t) = 0$, i.e., the noiseless case,

$$\mathbf{P}(t) = \boldsymbol{\Phi}(t)\mathbf{P}_0\boldsymbol{\Phi}(t)^T \tag{7.4.3}$$

where

$$\frac{d\boldsymbol{\Phi}(t)}{dt} = \mathbf{F}(\boldsymbol{x}(t), \boldsymbol{\alpha}, t)\boldsymbol{\Phi}(t), \quad \boldsymbol{\Phi}(t_0) = \mathbf{I}. \tag{7.4.4}$$

A summary of the EKF can be found in the book edited by Gelb [96], the book by Jazwinski [139], or in almost any book on Kalman filtering.

Advantages and disadvantages of the extended Kalman filter are discussed extensively in the vast literature. Vallado [262, pp 799-800] specifically discusses these for astrodynamics, so a review of this literature will not be undertaken here. Here are some brief comments. A Gaussian random variable is propagated analytically through the first-order linearization of a nonlinear system. As such, the EKF can be viewed as providing "first-order" approximations to the optimal probability density function. These approximations, however, can introduce large errors in the true posterior mean and covariance of the transformed (Gaussian) random variable, which may lead to sub-optimal performance and sometimes divergence of the filter. When propagation times are longer or the initial uncertainties are large, the propagated covariances become unrealistic sooner than other methods to follow and cannot capture the higher order moments. Also, covariances become overly optimistic when process noise is omitted. Proper accounting of dynamical model deficiencies through the use of stochastic model parameters and/or process noise is required to maintain a realistic covariance.

7.5 Second Order EKFs

The second order extended Kalman filter (SOEKF) [139] is based on a second order Taylor expansion of a nonlinear system, in contrast to the more common (first order) extended Kalman filter (EKF). Despite a solid theoretical ground for its approximation, it is seldom used in applications, where the EKF and

the unscented Kalman filter (UKF) are the standard algorithms. One reason might be the requirement for analytical Jacobian and Hessian of the system equations, e.g., the gravity model, and the high complexity that scales with the state order. An exception is the work of Park and Scheeres [218] and Vittaldev, Russell, Arora, and Gaylor [274] in astrodynamics.

7.6 Covariance Propagation using the Unscented Kalman Filter

The unscented Kalman filter (UKF) uses the unscented transform for both the discrete state and measurement equations, i.e., Equations (6.1.3) and (6.1.4), respectively. It provides a minimum-mean-squared error (MMSE) estimate of the state. The UKF was first introduced by Julier, Uhlmann, and Durant-Whyte [157] in 2000 and can also be viewed as a central difference filter [212]. A novel feature of the UKF is its "derivative-free" nature. (Such a feature mitigates some of the complexity in trying to take higher order derivatives of the gravity model.) Within the filter prediction step, the propagated state estimate and covariance are reconstructed from a deterministically chosen set of "sigma points" propagated through the full non-linear dynamics. The equivalence between this reconstruction or "unscented transform" and Gauss-Hermite (GH) quadrature has been established [125, 138]. Variations and extensions of the UKF, including a more numerically stable "square-root version" and the higher-order GH filters, have also been formulated [138, 269]. A detailed description of the algorithm for the UKF as it applies to the discrete system in Equations (6.1.3) and (6.1.4), including process noise, can be found in the paper by Wan and Merwe [281] and in Section 3.2.3 of the thesis by Merwe [268]. A more recent description is that of Stauch and Jah [249] who combine the unscented Kalman filter with the Schmidt-Kalman filter into a unscented Schmidt-Kalman filter.

At a high level, covariance propagation using the unscented transform (or, equivalently, Gauss-Hermite quadrature [138]) works as follows. The initial uncertainty is assumed to be Gaussian with respect to some state coordinates, for example, Cartesian ECI position-velocity coordinates or (equinoctial) orbital elements. For the former, one first deterministically selects a sequence of sigma points (i.e., Gauss-Hermite quadrature nodes) and weights from the initial Gaussian in ECI space. Each of these sigma points is then propagated to a future epoch. Lastly, the state and covariance at the final epoch are reconstructed using the weights and propagated sigma points. For the case in which the initial Gaussian is represented in a space other than Cartesian ECI coordinates (say equinoctial elements for sake of example), one proceeds similarly by first selecting the sigma points and weights in equinoctial space. Each sigma point is then transformed to Cartesian space and then propagated to a future epoch* (as in the previous case). Finally, each propagated sigma point is transformed back to the equinoctial space and the Gaussian at the final epoch is recovered using the weights and propagated (equinoctial) sigma points. The transformation of covariance and mean back to orbital elements may require Gaussian sums as discussed in the paper [16]. Some additional comments on covariance propagation using the UKF are provided below.

1. The unscented transform used in the UKF is equivalent to a third-order GH quadrature rule [138]. Such a third-order rule can be obtained with $2n + 1$ sigma points (nodes) where n is the dimension of the state space.

*The reason for this transformation is that the dynamics modeled by the ODEs in (6.1.2) are commonly defined in ECI space.

2. In practice, negligible differences are observed between the propagated state and covariance obtained using the traditional unscented transform (i.e., a third-order GH rule) and a higher-order GH rule [121]. This suggests that the standard UKF resolves the correct mean and covariance of the propagated uncertainty; i.e., it achieves covariance realism.

3. One can choose any numerical method for propagating the sigma points such as explicit or implicit Runge-Kutta, Adams-Bashforth-Moulton, or Gauss-Jackson. No matter what propagator is used, the sigma points can be propagated in parallel. A finer level of parallelization is also possible using implicit Runge-Kutta methods, wherein each force-model evaluation can be parallelized. Implicit Runge-Kutta are also well-suited for sigma-point propagations since recent developments [12, 14] have demonstrated that the sigma points can be propagated *collectively*, rather than *individually*, leading to improved computational efficiency even in a serial computing environment. Further, as remarked in the comments on the EKF, the numerical truncation error committed by the orbital propagator should be significantly below the uncertainty in the model or physics [15].

4. If continuous-time process noise is modeled in the dynamics through a stochastic differential equation, one can instead numerically integrate an analogous Riccati equation for the covariance following the work of Särkkä [232]. Alternatively, one can replace the underlying stochastic differential equation by an approximate discrete-time formulation of the dynamics (with discrete-time process noise) thereby allowing one to use the unscented transform as described above in conjunction with a standard orbital propagator.

5. If observable, uncertain parameters in the dynamics can be treated using state augmentation or via an extension of the Schmidt-Kalman filter [139].

6. The computed "state estimate" from the unscented transform (GH quadrature) is the mean of the propagated probability distribution function, which can be different from the mode of the true PDF (see, for example, Figure 7.10.1 discussed in Subsection 7.10.2).

Here is a list of some advantages of the UKF.

- The UKF is derivative free, i.e., no explicit calculation of Jacobians or Hessians are necessary to implement the algorithm.

- The overall number of computations are higher than that of the EKF; however, if one propagates the sigma points collectively, the computations can be reduced to about the same as the EKF (see Section 7.15 and [15, 123]).

- The UKF when combined with an orbital element space in which the uncertainty is represented can considerably extend the life of a faithful representation of the uncertainty longer than the EKF in a Cartesian space.

Some disadvantages of the UKF are as follows.

- The sigma points must be computed with sufficient accuracy to allow for a meaningful reconstruction of the mean and covariance of the transformed sigma points.

- The UKF still breaks down as do all of the approximate filters; however, Gaussian sums and the GVM filter in the next sections can extend the life of the UKF.
- The UKF's range of validity is more limited than that of a particle filter; however, the computational cost is substantially less.

7.7 Uncertainty Propagation using the Gauss von Mises Filter

Because uncertainty propagation using the UKF only captures the first two cumulants (i.e., mean, covariance) of the (possibly non-Gaussian) state PDF, higher-order cumulants (e.g., skewness, kurtosis) can become non-negligible in scenarios involving propagations over extended time intervals in the absence of measurement updates. In such cases, what is needed to achieve uncertainty realism is a representation of the state PDF beyond a simple Gaussian, such as the newly proposed Gauss von Mises (GVM) distribution [126, 127], which is designed to work in orbital element space and not a Cartesian space. Some of the salient features of GVM distribution are presented in this section; the detailed explanations can be found in [127].

The random variables[†] $(\boldsymbol{x}, \theta) \in \mathbb{R}^n \times \mathbb{S}$ are said to be jointly distributed as a *Gauss von Mises (GVM) distribution* if and only if their joint probability density function has the form

$$p(\boldsymbol{x}, \theta) = \mathcal{GVM}(\boldsymbol{x}, \theta; \boldsymbol{\mu}, \mathbf{P}, \alpha, \boldsymbol{\beta}, \boldsymbol{\Gamma}, \kappa) \equiv \mathcal{N}(\boldsymbol{x}; \boldsymbol{\mu}, \mathbf{P})\, \mathcal{VM}(\theta; \Theta(\boldsymbol{x}), \kappa),$$

where

$$\mathcal{N}(\boldsymbol{x}; \boldsymbol{\mu}, \mathbf{P}) = \frac{1}{\sqrt{\det(2\pi\mathbf{P})}} \exp\left[-\frac{1}{2}(\boldsymbol{x}-\boldsymbol{\mu})^T \mathbf{P}^{-1}(\boldsymbol{x}-\boldsymbol{\mu})\right],$$
$$\mathcal{VM}(\theta; \Theta(\boldsymbol{x}), \kappa) = \frac{1}{2\pi \mathrm{e}^{-\kappa} I_0(\kappa)} \exp\left[-2\kappa \sin^2 \frac{1}{2}\big(\theta - \Theta(\boldsymbol{x})\big)\right],$$

and

$$\Theta(\boldsymbol{x}) = \alpha + \boldsymbol{\beta}^T \boldsymbol{z} + \tfrac{1}{2}\boldsymbol{z}^T \boldsymbol{\Gamma} \boldsymbol{z}, \quad \boldsymbol{z} = \mathbf{A}^{-1}(\boldsymbol{x} - \boldsymbol{\mu}), \quad \mathbf{P} = \mathbf{A}\mathbf{A}^T.$$

The parameter set $(\boldsymbol{\mu}, \mathbf{P}, \alpha, \boldsymbol{\beta}, \boldsymbol{\Gamma}, \kappa)$ is subject to the following constraints: $\boldsymbol{\mu} \in \mathbb{R}^n$, $\mathbf{P}$ is an $n \times n$ symmetric positive-definite matrix, $\alpha \in \mathbb{R}$, $\boldsymbol{\beta} \in \mathbb{R}^n$, $\boldsymbol{\Gamma}$ is an $n \times n$ symmetric matrix, and $\kappa \geqslant 0$. The matrix $\mathbf{A}$ in the definition of the normalized variable $\boldsymbol{z}$ is the lower-triangular Cholesky factor [102] of the parameter matrix $\mathbf{P}$. Some key properties of the GVM distribution are listed below.

1. The GVM distribution is a PDF defined on the cylindrical manifold $\mathbb{R}^n \times \mathbb{S}$ that satisfies the *periodicity property* $p(\boldsymbol{x}, \theta) = p(\boldsymbol{x}, \theta + 2\pi k)$, for any integer k. The GVM filter treats the variable θ as a bona fide angular coordinate, within the framework of direction statistics [192], rather than an unbounded Cartesian coordinate. Space object orbital states in (traditional or J_2 [10]) equinoctial orbital elements can be represented rigorously using the GVM distribution in which the variable $\boldsymbol{x}$ is identified with the first five elements (a, h, k, p, q) and the angular variable θ is identified with the mean longitude coordinate ℓ.

[†]The notation $\mathbb{R}^n$ denotes n-dimensional (flat) Euclidean space. The notation $\mathbb{S}$ denotes the one-dimensional manifold $\{(x, y) \in \mathbb{R}^2 \mid x^2 + y^2 = 1\}$; i.e., the circle. Thus, $\mathbb{R}^n \times \mathbb{S}$ denotes the $(n+1)$-dimensional cylindrical manifold.

2. The GVM distribution is *unimodal* on $\mathbb{R}^n \times \mathbb{S}$ with

$$(\boldsymbol{\mu}, \alpha) = \text{argmax}_{\boldsymbol{x},\theta}\, \mathcal{GVM}(\boldsymbol{x}, \theta; \boldsymbol{\mu}, \mathbf{P}, \alpha, \boldsymbol{\beta}, \boldsymbol{\Gamma}, \kappa).$$

3. The parameters $\boldsymbol{\beta}$ and $\boldsymbol{\Gamma}$ in the GVM distribution model correlation between $\boldsymbol{x}$ and θ. In particular, the parameter matrix $\boldsymbol{\Gamma}$ can be tuned to give the level sets of the GVM distribution their distinctive banana or boomerang shape (see, for example, Figure 7.10.1), thereby allowing one to model higher-order cumulants.

4. The GVM distribution reduces to a Gaussian distribution in the limit as $\boldsymbol{\Gamma} \to 0$ and $\kappa \to \infty$.

5. It follows that [127] the scalar

$$\mathcal{U}(\boldsymbol{x}, \theta; \boldsymbol{\mu}, \mathbf{P}, \alpha, \boldsymbol{\beta}, \boldsymbol{\Gamma}, \kappa) \equiv (\boldsymbol{x} - \boldsymbol{\mu})^T \mathbf{P}^{-1} (\boldsymbol{x} - \boldsymbol{\mu}) + 4\kappa \sin^2 \tfrac{1}{2}\big(\theta - \Theta(\boldsymbol{x})\big), \tag{7.7.1}$$

possesses the distribution $\chi^2(n+1)$ in the limit as $\kappa \to \infty$. This is precisely the uncertainty realism metric proposed in the companion paper [124] that generalizes the Mahalanobis distance of a Gaussian random vector $\boldsymbol{x}$ with mean $\boldsymbol{\mu}$ and covariance $\mathbf{P}$.

We now give a high-level description of uncertainty propagation using the GVM filter will full details provided in Horwood and Poore [127]. The initial uncertainty is assumed to be a GVM distribution with respect to some system of orbital element coordinates (e.g., equinoctial). If the initial distribution is a Gaussian, it can be converted to a GVM distribution as described in reference [127]. By analogy to the unscented transform, one begins by deterministically selecting a sequence of sigma points and weights from the initial GVM distribution. Note that the prescription for choosing such sigma points and weights differs from that used in the unscented transform or Gauss-Hermite quadrature. Each sigma point is then transformed to Cartesian space and then propagated to a future epoch (with dynamics governed, for example, by the ODEs (6.1.2)). Finally, each propagated sigma point is transformed back to the underlying orbital element space and the parameter set $(\boldsymbol{\mu}, \mathbf{P}, \alpha, \boldsymbol{\beta}, \boldsymbol{\Gamma}, \kappa)$ of the GVM distribution at the final epoch is recovered using the weights and propagated (orbital element) sigma points. Some additional comments on uncertainty propagation using the GVM distribution are provided below.

1. Uncertainty propagation using the (third-order) GVM filter only requires the propagation of 13 sigma points (for a 6D equinoctial orbital element state); *hence it has approximately the same computational cost as the UKF.* Higher-order versions of the GVM filter are also possible. Higher order versions of the GVM filter are possible such as the third-order version of the GVM filter and a fifth-order GVM filter with the latter requiring 73 sigma points [124].

2. In practice, we observe that the GVM filter effectively "extends the life of the UKF," by maintaining uncertainty realism longer than the UKF, up to 7 times in many examples. Evidence is provided in references [126, 127].

3. Like the UKF, the GVM filter is compatible with standard orbital propagators as well as implicit Runge-Kutta methods that exploit collective propagation of the sigma points for improved computational efficiency [12, 14].

In summary, the GVM provides improved covariance and uncertainty realism at no additional computational cost compared to traditional methods for uncertainty propagation. In particular, some *advantages* of the GVM filter are as follows:

1. Operates on a new family of multivariate PDFs that provide a statistically rigorous treatment of uncertainty in orbital element space.
2. Provides both covariance and uncertainty realism by modeling higher-order cumulants (e.g., skewness and kurtosis) beyond a state and covariance.
3. Reduces to a Gaussian for a subset of the parameter space.
4. Has the same computational cost as the traditional UKF (i.e., only 13 "sigma points" or particles need to be propagated for uncertainty propagation of a 6D orbital state).
5. Admits a natural extension of the classical Mahalanobis distance that is useful in estimation and tracking applications.
6. Can be extended to a mixture filter, to provide improved accuracy in extreme cases at over a 95 reduced cost compared to Gaussian mixtures.

Disadvantages of the GVM filter are similar to those of the UKF. Other disadvantages are as follows.

- The sigma points must be computed with sufficient accuracy to allow for a meaningful reconstruction of the mean and covariance of the transformed sigma points.
- The GVM still breaks down as do all of the approximate filters; however, mixture versions of the GVM filter can extend the life of the GVM.
- The GVM's range of validity is more limited than that of a particle filter; however, the computational cost is substantially less.
- The GVM represents uncertainty in an element space. Thus, in applications requiring a Cartesian representation of the uncertainty, the GVM distribution (in element space) must be transformed to a Cartesian space using, for example, a Gaussian sum as described in Section 7.9.

7.8 Gaussian Sum Filters

A Gaussian sum is a mixture density of the form

$$p(\boldsymbol{x}) = \sum_{\alpha=1}^{N} w_\alpha \mathcal{N}(\boldsymbol{x}; \boldsymbol{\mu}_\alpha, \mathbf{P}_\alpha),$$

where the weights w_α are non-negative scalars which sum to unity and $\mathcal{N}(\boldsymbol{x}; \boldsymbol{\mu}, \mathbf{P})$ denotes the Gaussian PDF with mean $\boldsymbol{\mu}$ and covariance $\mathbf{P}$; i.e.,

$$\mathcal{N}(\boldsymbol{x}; \boldsymbol{\mu}, \mathbf{P}) = \frac{1}{\sqrt{\det(2\pi\mathbf{P})}} \exp\left[-\frac{1}{2}(\boldsymbol{x}-\boldsymbol{\mu})^T \mathbf{P}^{-1}(\boldsymbol{x}-\boldsymbol{\mu})\right]. \tag{7.8.1}$$

The Gaussian sum filter (GSF) is based on a fundamental result of Alspach and Sorenson [7] which states that any PDF can be approximated arbitrarily close (in the L^1 sense) by a weighted sum (mixture) of Gaussian PDFs henceforth called a Gaussian sum. Thus, Gaussian sums provide a mechanism for modeling non-Gaussian densities and for more accurately approximating the solution of the FPKE. Computationally, the GSF has the added advantage of being *parallelizable* since filters such as the EKF or UKF act *independently* on each component Gaussian in the prediction and correction steps. With regards to the weights, means, and covariances in the Gaussian sum approximation, there are two key problems. The *first* is to select these via the L^1 theory to represent the given probability density function. The *second* is to adapt these as the true probability density function changes due to its being propagated forward in time or is transformed through a coordinate system change, e.g., equinoctial orbital elements to a Cartesian system.

A method for the first problem is discussed in in the paper by Horwood, Aragon, and Poore [122] in which a covariance or Gaussian sum is represented in equinoctial orbital element space with component means, covariances, and weights initially selected (by solving an L^2 optimization problem offline) such that the (square-root version of the) UKF [269], when acting in parallel on each component, accurately approximates the solution of the Fokker-Planck-Kolmogorov equation (FPKE). The number of Gaussian components required to achieve an accurate approximation is chosen *adaptively* based on the length of the propagation time and the initial error (standard deviation) along the radial direction (semi-major axis coordinate). Consequently, by representing the PDF in the equinoctial elements, the algorithm achieves superior computational efficiency because it only requires a Gaussian sum along *one dimension*. The refinement methodology is illustrated in Figure 7.8.1. Under a nonlinear transformation, a Gaussian (represented by the thick black ellipse) need not be mapped to a Gaussian (e.g., the level surfaces of the transformed distribution could look crescent-shaped).

Figure 7.8.1 Depiction of a single Gaussian and its Gaussian sum approximation undergoing a nonlinear transformation.

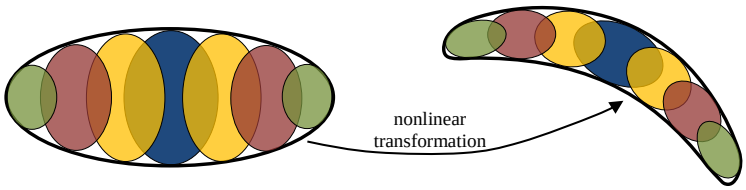

However, in a sufficiently small neighborhood, any (smooth) nonlinear map will be approximately linear. Consequently, Gaussians with smaller covariances (represented by the colored elliptic disks) remain more Gaussian than those with larger covariances under the nonlinear mapping. Therefore, a Gaussian sum refined by approximating each constituent Gaussian by a finer Gaussian sum will exhibit better behavior through nonlinear transformations. It suffices to optimally refine the unit one-dimensional Gaussian $\mathcal{N}(x, 0, 1)$; refinement of a multivariate Gaussian with an arbitrary covariance is obtained by a series of linear transformations detailed in the paper by Horwood, Aragon, and Poore [122]. A metric for ranking directions according to their nonlinearity and only splitting along the necessary directions can be found in the work of Vittaldev and Russell [273].

For the second problem, several have proposed methods for adapting the weights based on various *online* L^2 optimization criteria [62, 100, 255, 271, 272]. As we note, the weights are chosen or adapted using an

L^2 optimization criteria which is different from the basic theory in L^1. A method for this is to solve the L^2 optimization problem and then verify the accuracy in L^1 as has been done in the paper by Horwood, Aragon, and Poore [122].

Some advantages of the Gaussian sum representation of uncertainty include.

- The weights, means, and covariances in a Gaussian sum PDF can represent an arbitrary PDF in the L^1 sense according to the theory of Alspach and Sorenson [7] .
- With either the EKF or UKF, the propagation is parallelizable.
- A brute force method such as Monte Carlo methods using massive parallelization on GPUs may make the computations tractable in some cases [20].

Disadvantages of the Gaussian sum filters include the following.

- The optimization problem that one often solves is that in L^2 instead of L^1 .
- The computational complexity of a Gaussian sum filter generally indicates that they are for special purposes such as propagating a Gaussian over a long time period.

7.9 Transformation of Uncertainty from an Element Space to ECI

The paper by Aristoff, Horwood, Singh, and Poore [16] demonstrates how uncertainty in orbital elements can be faithfully (and efficiently) transformed to Cartesian space using Gaussian mixtures. Thus, this paper brings to a completion the initial representation in an element space, the propagation forward in time, the representation again in element space, and the final transformation back to a Cartesian space. For example, given the Gaussian sum representation in a Cartesian space, one can use the representation in the work of DeMars, Cheng, and Jah [65] or Vittaldev and Russell [272, 273] to compute the probability of collision.

In other work, Weisman et al. [282–284] demonstrate probability density function mapping between measurement space and state-spaces of interest (Cartesian, Keplerian, Gim-Alfriend, and mean Keplerian) as well as the impact of initial orbit determination processes on the state distribution utilizing the transformation of variables [217]. This mapping produces exact knowledge of the system likelihood distribution to allow for a better idea of the combination of system states which generated the measurement. Since the likelihood distribution is exactly mapped between domains, Bayesian estimation can easily be carried out if the prior distribution is appropriately characterized. The posterior probability density function computed by Bayes' Theorem allows for all statistical moments to be assessed, not just the mean and covariance as with conventional filtering techniques. Availability of the state probability density function given a single measurement set can allow for automation of the covariance initialization required by conventional filtering, thereby decreasing the amount of tuning needed to ensure proper filter operation. The method requires an analytic form of the starting probability density function to be given as well as the mapping equations between the starting space and the desired space of interest, additionally the number of states in the desired space must be equal to or less than the number of states in the starting space. With regard to propagation of probability density functions, Majji, Weisman, and Alfriend [189] were able to demonstrate that if an initial

probability density function was analytically available then the propagation of uncertainty for Two-Body motion in Keplerian variables without any perturbations was able to be effectively carried out through use of the technique. It was shown that the solution flow of the Keplerian variables inherently satisfied Liouville's Equation, the Fokker-Planck-Kolmogorov equation without diffusion, due to the linear time update for the mean anomaly.

7.10 Some Computational Comparisons

In this section, an example is presented to demonstrate the performance of some of the above approaches to propagating uncertainty. The example is a scenario in low Earth orbit (LEO) which compares the GVM filter prediction step with that of the extended Kalman filter (EKF) [139], the unscented Kalman filter (UKF) [157], a Gaussian sum filter (GSF) [122], and a particle filter [228]. The accuracy of the GVM uncertainty propagation algorithm is also validated using a metric based on the L_2 error. For the specific LEO scenario, it is shown that the GVM filter prediction step properly characterizes the actual uncertainty of a space object's orbital state while simple less sophisticated methods which make Gaussian assumptions (such as the EKF and UKF) do not. Specifically, under the non-linear propagation of two-body dynamics, the new algorithm properly characterizes the uncertainty for up to eight times as long as the standard UKF all at no additional computational cost to the UKF. In what follows, the particulars of the simulation scenario are defined in Subsection 7.10.1 and the results are discussed in Subsection 7.10.2.

7.10.1 Scenario Description

This subsection describes the specific input to the uncertainty propagation algorithm in Sections 7.4-7.8, how the output is visualized, and how the accuracy of the output is validated.

7.10.1.1 Input

The initial GVM distribution of the space object's orbital state is defined with respect to equinoctial orbital elements $(a, h, k, p, q, \ell) \in \mathbb{R}^5 \times \mathbb{S}$ with parameter set $(\boldsymbol{\mu}, \mathbf{P}, \alpha, \boldsymbol{\beta}, \boldsymbol{\Gamma}, \kappa)$ given by

$$\boldsymbol{\mu} = (7136.635\,\text{km}, 0, 0, 0, 0)^T, \quad \mathbf{P} = \text{diag}\big((20\,\text{km})^2, 10^{-6}, 10^{-6}, 10^{-6}, 10^{-6}\big),$$
$$\alpha = 0, \quad \boldsymbol{\beta} = \mathbf{0}, \quad \boldsymbol{\Gamma} = \mathbf{0}, \quad \kappa = 3.282806 \times 10^7.$$

The mode of this distribution describes a circular, non-inclined orbit in LEO with a semi-major axis of 7136.635 km. This choice of semi-major axis is made so that the instantaneous orbital period of the object is 100 minutes. In all subsequent discussions, a time unit of one orbital period is equal to 100 minutes. It is noted that the GVM distribution with the above parameter set is approximately Gaussian (since $\boldsymbol{\Gamma} = \mathbf{0}$ and $\kappa \gg 1$). In particular, the standard deviation in the mean longitude coordinate ℓ is $\sigma_\ell = 1/\sqrt{\kappa} = 0.01^\circ = 36''$. Finally, it is acknowledged that the initial parameter set defined above is representative of the uncertainty of a short radar track segment that has yet to be correlated to an existing object in the space catalog. Due to the sensitivity of releasing any real data acquired by the authors, this "sanitized example", motivated from the real data, is used instead.

The input parameters are the epoch time t_0 of the input, the final epoch time t, and the specific forces used to model the perturbations. In all simulations, t_0 is the J2000 epoch (1 Jan 2000, 12:00 UTC) and $t - t_0$ is varied from 0.5 to 8 orbital periods. The EGM96 gravity model of degree and order 70 is used to model the perturbations. Though one can include additional non-conservative forces such as atmospheric drag, the non-linearities induced by the gravity alone (especially in LEO) are sufficiently strong to stress the algorithm. Finally, the numerical integration of the ordinary differential equations is performed using a Gauss-Jackson method.

7.10.1.2 Visualization

The output of the uncertainty propagation algorithm in Section 7.7 is a GVM distribution characterizing the uncertainty of the space object's orbital state at a specified future epoch. In order to visualize this six-dimensional probability density function (PDF), the level curves (i.e., curves of equal likelihood) of the two-dimensional (2D) marginal PDF in the semi-major axis a and mean longitude ℓ coordinates are plotted. In each subfigure, the a and ℓ coordinates are rotated so that the principal axes of the EKF Gaussian are aligned with the horizontal and vertical. (Any such rotation or rescaling does not exaggerate any non-Gaussian effects or the extremity of the boomerang shape because all cumulants of order three and higher are invariant under an affine transformation.) This choice is made because it is along this particular 2D slice where the greatest departure from "Gaussianity" and the most extreme "banana" or "boomerang" shaped level curves are observed.

In the panels of Figure 7.10.1, the $n\sigma$ level curves (of the marginal PDF in the a and ℓ coordinates) are plotted in half-sigma increments starting at $n = \frac{1}{2}$ to $n = 3$ for various final epoch times t. In order to visualize these marginal PDFs which are defined on a cylinder, the cylinder is cut at $\tilde{\alpha} - \pi$ (where $\tilde{\alpha}$ is the α parameter of the propagated GVM distribution) and rolled out to form a 2D plane. This plane is then rotated so that the semi-major and semi-minor axes of the osculating Gaussian covariance are aligned with the horizontal and vertical and then compressed. (Any such rotation or rescaling does not exaggerate any non-Gaussian effects or the extremity of the boomerang shape because all cumulants of order three and higher are invariant under an affine transformation.) These level curves are shown in shades of orange and red, as indicated. Where appropriate, overlays of the level curves generated from the EKF and UKF are shown in green and grey, respectively. Additionally, blue crosses represent particles generated from a Monte-Carlo-based uncertainty propagator. If the represented PDF properly characterizes the actual uncertainty, then approximately 98.9% of the particles should be contained within the respective 3σ level curve.

7.10.1.3 Validation

An inspection of the panels in Figure 7.10.1 provides a simple visual means to assess whether the represented uncertainty properly characterizes the actual uncertainty of the space object's orbital state; "most" of the particles (blue crosses) should be contained within the level curves. To quantify uncertainty realism more rigorously and hence validate the prediction steps of the different filters under consideration, the normalized L_2 error [63] is studied.

For functions $f, g : \mathcal{M} \to \mathbb{R}$, the *normalized L_2 error* between f and g is the scalar

$$\bar{L}_2(f, g) = \frac{\|f - g\|_{L_2}^2}{\|f\|_{L_2}^2 + \|g\|_{L_2}^2},$$

where $\|\cdot\|_{L_2}$ is the L_2 norm:

$$\|f\|_{L_2}^2 = \int_{\mathcal{M}} f(\boldsymbol{x})^2 \, \mathrm{d}\boldsymbol{x}.$$

By non-negativity of the L_2 norm, $\bar{L}_2 \geqslant 0$ with equality if and only if $f = g$ in the L_2 sense. By the triangle inequality, $\bar{L}_2 \leqslant 1$ with equality if and only if f and g are orthogonal in the L_2 sense.

The validation tests shown in Figure 7.10.2 generate a time history of the normalized L_2 error

$$\bar{L}_2\big(p_{\text{approx}}(\cdot, t), p_{\text{baseline}}(\cdot, t)\big),$$

where t is the final epoch time. Further, $p_{\text{approx}}(\boldsymbol{u}, t)$ represents an approximation to the PDF of a space object's orbital state at time t ($\boldsymbol{u}$ represents equinoctial orbital elements) as computed by the prediction step of the GVM filter, EKF, UKF, or a Gaussian sum filter. Moreover, $p_{\text{baseline}}(\boldsymbol{u}, t)$ is a high-fidelity approximation to the exact state PDF which serves as a baseline for comparison. This baseline is computed using a high-fidelity Gaussian sum using the GSF of Horwood *et al.* [122]. Thus, p_{approx} is a good approximation to the actual state PDF if the normalized L_2 error between it and the baseline p_{baseline} is zero or "close to zero" for all time.

7.10.2 Discussions

As described in Subsection 7.10.1.2, the panels in Figure 7.10.1 show the evolution of a space object's orbital uncertainty (with initial conditions defined in Subsection 7.10.1.1) computed using the prediction steps of the EKF, UKF, GVM filter, and a particle filter. Each of the six panels shows the respective level curves in the plane of the semi-major axis and mean longitude coordinates at the epochs $t - t_0 = 0, 0.5, 1, 2, 4, 8$ orbital periods. In each of the six epochs, the level curves produced by the GVM filter prediction step (shown in shades of orange and red) correctly capture the actual uncertainty depicted by the particle ensemble. Each set of level curves is deduced from the propagation of only 13 sigma points (corresponding to a third-order GVM quadrature rule); the computational cost is the same as that of the UKF. For the UKF, its covariance (depicted by the grey ellipsoidal level curves) is indeed consistent (realistic) in the sense that it agrees with that computed from the definition of the covariance. Thus, in this scenario, the UKF provides "covariance realism" but clearly does not support "uncertainty realism" since the covariance does not represent the actual banana-shaped uncertainty of the exact PDF. Further, the state estimate produced from the UKF coincides with the mean of the true PDF; however the mean is displaced from the mode. Consequently, the probability that the object is within a small neighborhood centered at the UKF state estimate (mean) is essentially zero. The EKF, on the other hand, provides a state estimate coinciding closely with the mode, but the covariance tends to collapse making inflation necessary to begin to cover the uncertainty. In neither the EKF nor UKF case does the covariance actually model the uncertainty. In summary, *the GVM filter prediction step maintains a proper characterization of the uncertainty; the EKF and UKF do not.*

Figure 7.10.1 The uncertainty of a space object's orbital state at different epochs $t - t_0$ computed from the prediction steps of the EKF, UKF, GVM filter, and a particle filter. Shown are the respective level curves in the plane of the semi-major axis and mean longitude coordinates.

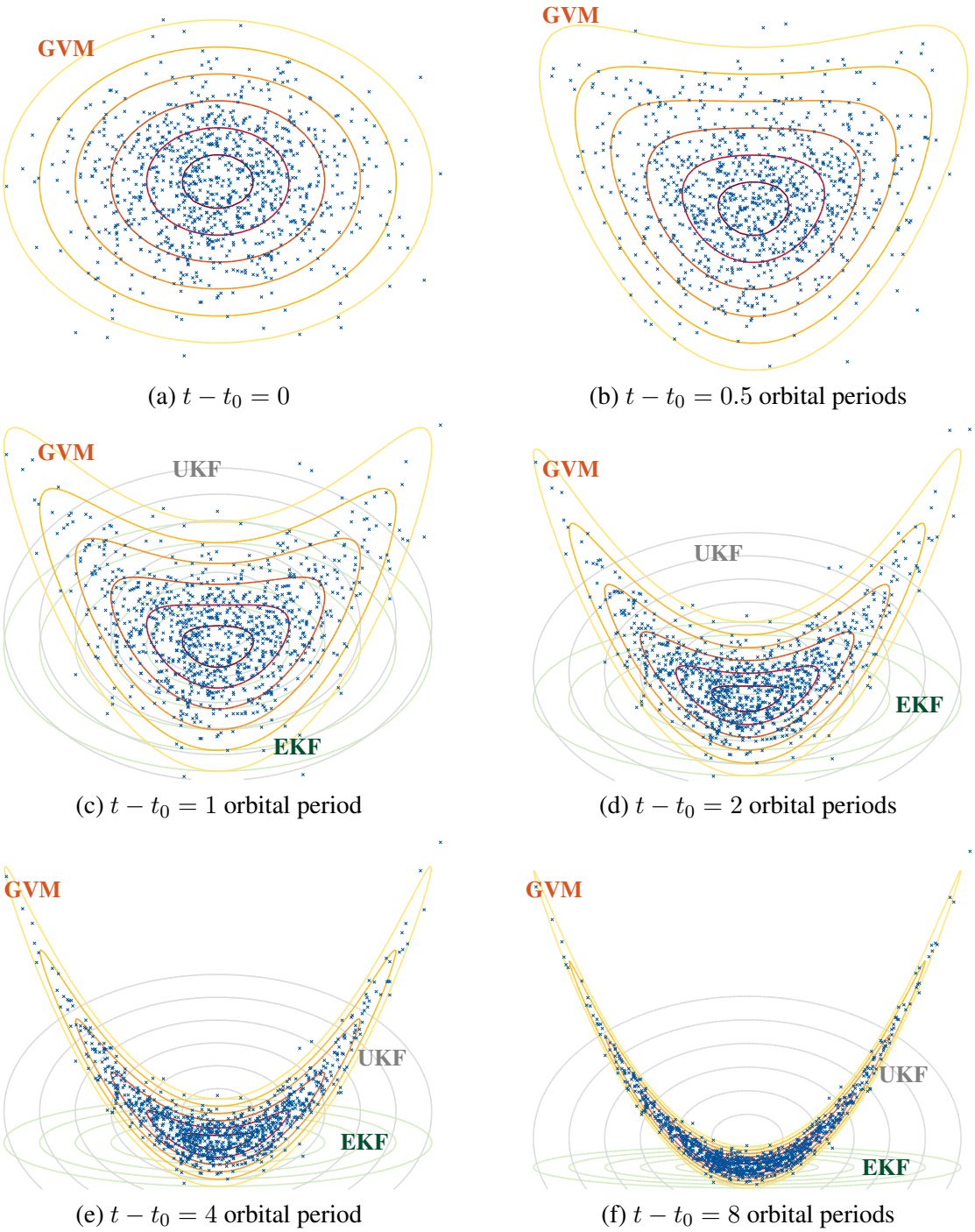

(a) $t - t_0 = 0$

(b) $t - t_0 = 0.5$ orbital periods

(c) $t - t_0 = 1$ orbital period

(d) $t - t_0 = 2$ orbital periods

(e) $t - t_0 = 4$ orbital period

(f) $t - t_0 = 8$ orbital periods

Figure 7.10.2 Plots of the normalized L_2 error using different methods for uncertainty propagation.

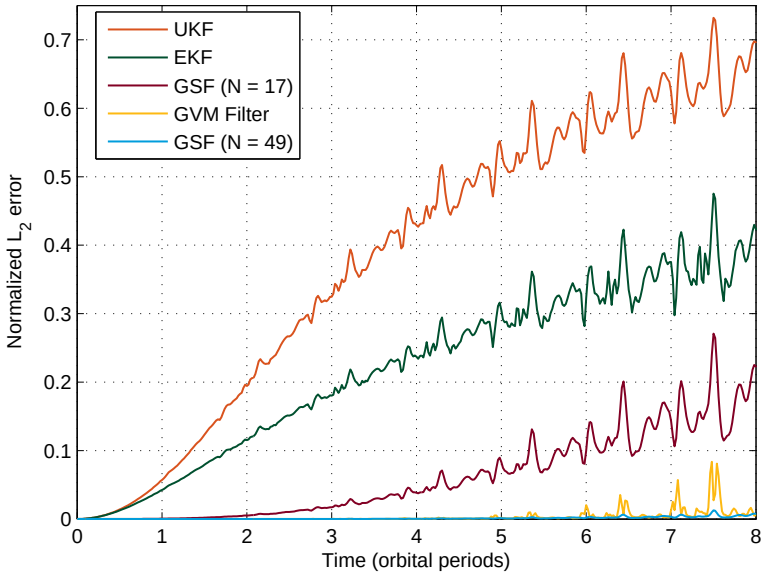

Figure 7.10.2 shows the evolution of the normalized L_2 error, as defined in Subsection 7.10.1.3, computed from the (prediction steps of the) UKF, EKF, the Gaussian sum filter (GSF) of Horwood *et al.* [122] with $N = 17$ and $N = 49$ components, and the GVM filter. Uncertainty propagation using the UKF and EKF quickly break down, but accuracy can be improved by increasing the fidelity of the Gaussian sum. The normalized L_2 errors produced from the GVM filter prediction step lie between those produced from the 17 and 49-term Gaussian sum. It is noted that the 17-term Gaussian sum requires the propagation of $17 \times 13 = 221$ sigma points; the GVM distribution only requires 13. If one deems a normalized L_2 error of $\bar{L}_2 = 0.05$ to signal a breakdown in accuracy, then the UKF and EKF prediction steps first hit this threshold after about one orbital period. By examining when the normalized L_2 error first crosses 0.05 for the GVM filter prediction, it is seen that *the GVM filter prediction step can faithfully propagate the uncertainty for about 8 times longer than when using an EKF or UKF.*

These results also suggest what could be achieved if the orbital state uncertainty is represented as a *mixture* of GVM distributions, in analogy to the Gaussian sum (mixture). As a single GVM distribution achieves accuracy (in the L_2 sense) between the 17 and 49-term Gaussian mixture, it is hypothesized that a GVM mixture would require about 95% fewer components than a Gaussian mixture to achieve comparable accuracy and uncertainty realism. Thus, one can extend the validity over which the uncertainty is propagated without the ballooning cost of doing so. Extending the work of this paper to GVM mixtures is future research.

7.11 Polynomial Chaos

Polynomial chaos (PC) approximates the solution of a stochastic differential equation by projecting it onto a basis of orthogonal polynomials. The work in [286] first proposed this type of approximation, with methods based on Hermite polynomial chaos more recently established in [97, 98], among other works, and general-

ized to other types of orthogonal polynomials [295]. We note that the term "polynomial chaos" was adopted before the modern definition of chaos (implying a sensitive dependence on initial conditions). In the context of PC, chaos refers to *random*.

Propagation of orbit state uncertainty using polynomial chaos leverages a stochastic ordinary differential equation (SODE) description of the dynamics, i.e., it considers one or more inputs to the propagator as a random variable with some *a priori* knowledge of its distribution. The PC-based approximation of this SODE, known as a polynomial chaos expansion (PCE), describes the propagated solution as a function of its random inputs $\boldsymbol{\xi}$. These random inputs correspond to, for example, initial position, velocity, and force model parameters. Using a PCE to quantify uncertainty differs from methods directly propagating a probability density function (PDF) in that the polynomial surrogate describes the sensitivity of the solution to the stochastic inputs. Information on the PDF may then be determined via analytic analysis or random evaluations of the PCE solution. Polynomial chaos is an active area of research in the applied mathematics community, with demonstrated uses for uncertainty quantification in fluid dynamics [173, 295], solid mechanics [97, 98], and many other applications. In the context of astrodynamics, PCE-based propagation of uncertainty has been demonstrated for orbit uncertainty propagation given a probabilistic description of the initial state [149], to estimate the probability of collision between two spacecraft [148, 151], and for characterizing the sensitivity of atmospheric density to the model inputs [270].

Figure 7.11.1 Outline of non-intrusive solution generation process for a PCE

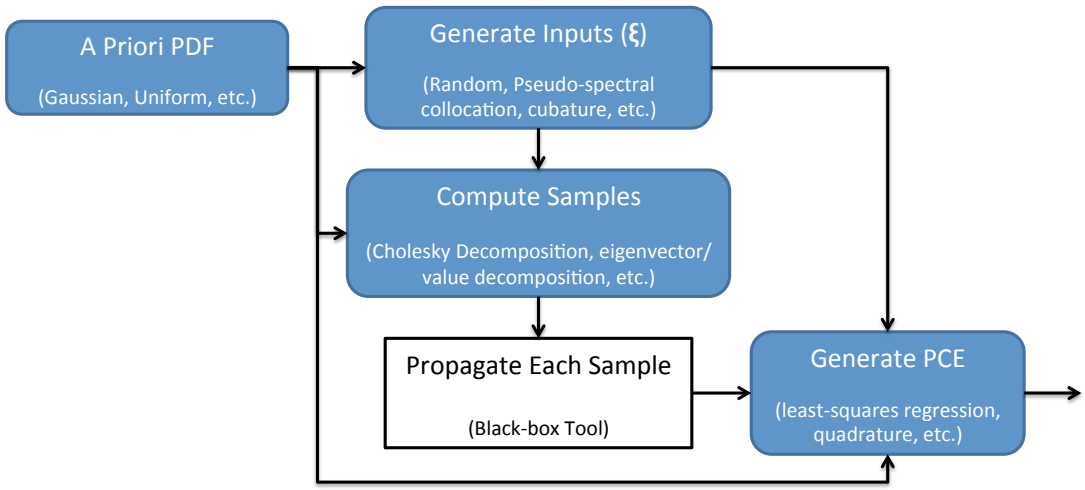

In the context of stochastic differential equations, a solution of interest $\boldsymbol{X}(t, \boldsymbol{r}, \boldsymbol{\xi})$ is a function of the random inputs $\boldsymbol{\xi} \in \mathbb{R}^d$ and can be a function of time t and/or position $\boldsymbol{r}$. The PCE solution is then

$$\boldsymbol{X}(t, \boldsymbol{r}, \boldsymbol{\xi}) = \sum_{\boldsymbol{\alpha} \in \mathbb{N}_0^d} \boldsymbol{c}_{\boldsymbol{\alpha}}(t, \boldsymbol{r}) \psi_{\boldsymbol{\alpha}}(\boldsymbol{\xi}), \tag{7.11.1}$$

where $\mathbb{N}_0^d := \{(\alpha_1, \cdots, \alpha_d) : \alpha_i \in \mathbb{N} \cup \{0\}\}$ is the set of multi-indices of size d defined on non-negative integers. The basis functions $\{\psi_{\boldsymbol{\alpha}}(\boldsymbol{\xi})\}$ are multi-dimensional spectral polynomials of maximum degree p, referred to as the "polynomial chaos," that are orthogonal with respect to the joint probability measure of $\boldsymbol{\xi}$.

Details on the selection of the polynomial basis may be found in the literature (e.g., see [295]). The exact vector of generalized Fourier coefficients $\boldsymbol{c}_{\boldsymbol{\alpha}}(t, \boldsymbol{r})$ in Equation (7.11.1), referred to as the PC coefficients, are computed by the projection of $\boldsymbol{X}(t, \boldsymbol{r}, \boldsymbol{\xi})$ onto each basis function $\psi_{\boldsymbol{\alpha}}(\boldsymbol{\xi})$, and may be approximated by sampling an existing solver as a black-box [98, 172, 294]. The PCE solution is then the best linear approximation of $\boldsymbol{X}(t, \boldsymbol{r}, \boldsymbol{\xi})$ in a finite dimensional space spanned by multi-dimensional polynomials in $\boldsymbol{\xi}$. This general process, dubbed a *non-intrusive* method since it treats a given propagator as a black box, is outlined in Figure 7.11.1. Example non-intrusive methods of generating a PCE approximation include, but are not limited to: least squares regression [128], pseudo-spectral collocation [172, 294], Monte Carlo sampling [172], and compressive sampling [71]. For the case of orbit state uncertainty propagation, the equations of motion are described by a SODE and the output (often position and velocity) state $\boldsymbol{X}(t, \boldsymbol{\xi})$. Hence, for orbit state uncertainty propagation, the PCE approximation is

$$\widehat{\boldsymbol{X}}(t, \boldsymbol{\xi}) = \sum_{\boldsymbol{\alpha} \in \Lambda_{p,d}} \widehat{\boldsymbol{c}}_{\boldsymbol{\alpha}}(t) \psi_{\boldsymbol{\alpha}}(\boldsymbol{\xi}), \tag{7.11.2}$$

where

$$\Lambda_{p,d} = \left\{ \boldsymbol{\alpha} \in \mathbb{N}_0^d : \sum_{i=1}^{d} \alpha_i \leqslant p, \ \|\boldsymbol{\alpha}\|_0 \leqslant d \right\}, \tag{7.11.3}$$

and $\|\boldsymbol{\alpha}\|_0$ denotes the number of non-zero elements in $\boldsymbol{\alpha}$. The maximum polynomial degree p is selected based on accuracy requirements, computation time limitations, etc., and (along with d) determines the number of elements in Equation 7.11.2.

As an example of the use of PC, consider the function

$$f(\xi) = \xi^2 + \xi - 1 \tag{7.11.4}$$

where the input ξ is a random variable with zero mean and unit variance. Since there is only one random input, then $d = 1$. Although not depicted here, the PDF describing f is non-Gaussian. When using regression to generate a PCE approximation of this function with a maximum polynomial degree $p = 2$, we instead express Equation (7.11.2) as the linear system

$$f(\xi) = \begin{bmatrix} \psi_0(\xi) & \psi_1(\xi) & \psi_2(\xi) \end{bmatrix} \begin{bmatrix} c_0 \\ c_1 \\ c_2 \end{bmatrix}. \tag{7.11.5}$$

Since the random input ξ has a standard normal distribution, then the basis functions ψ_α are Hermite polynomials each with degree α [295]. In this example, we will generate a solution for the coefficients c_0, c_1, and c_2 using least-squares regression. Given $M \geqslant 3$ random realizations of ξ, we have

$$\begin{bmatrix} \psi_0(\xi_1) & \psi_1(\xi_1) & \psi_2(\xi_1) \\ \psi_0(\xi_2) & \psi_1(\xi_2) & \psi_2(\xi_2) \\ \vdots & \vdots & \vdots \\ \psi_0(\xi_M) & \psi_1(\xi_M) & \psi_2(\xi_M) \end{bmatrix} \begin{bmatrix} c_0 \\ c_1 \\ c_2 \end{bmatrix} = \begin{bmatrix} f(\xi_1) \\ f(\xi_2) \\ \vdots \\ f(\xi_M) \end{bmatrix}, \tag{7.11.6}$$

which may be solved using the normal equation solution of the least squares estimator. Given $M \gg 3$, this yields a reasonable approximation of the true solution

$$c_0 = 0, \qquad c_1 = 1, \qquad c_2 = 1. \tag{7.11.7}$$

In the context of Figure 7.11.1, the inputs ξ are generated from a given pseudo-random number generator (pRNG), the propagation of the sample is the evaluation of Equation (7.11.4) for a given ξ_i, and the generation of the PCE is the estimation of the coefficients using least squares. In this case, conversion of the pRNG output to samples based on the a priori PDF is not required, but it would be necessary when given an initial orbit state PDF and an orbit propagator.

The key advantages of these PC-based techniques are:

- fast, up to exponential, mean-squares convergence of the expansion with respect to the order of the polynomial basis even when $u(t, \boldsymbol{r}, \boldsymbol{\xi})$ is highly non-Gaussian,
- construction of an explicit functional representation (i.e., response surface) of the solution of interest with respect to the random inputs $\boldsymbol{\xi}$, and
- the combination of random inputs $\boldsymbol{\xi}$ each described by different PDF's (i.e., Generalized Polynomial Chaos).

Disadvantages include:

- the curse of dimensionality that causes problems for most methods of uncertainty quantification, and
- some applications require some post-processing to analyze the *a posteriori* PDF.

It is noted that the effects of the curse of dimensionality may be mitigated through various means (e.g., separated representations and compressive sampling), which constitutes an active area of research (e.g., see [70–72, 213, 296] and the references therein). However, the use of such methods remains somewhat problem dependent, but generating a PCE using compressive sampling has already been demonstrated for propagating uncertainty after a spacecraft maneuver [151]. Additionally, [23] used separated representations (similar to a PCE) to propagate orbit state uncertainty, but some work remains to demonstrate its efficacy for mitigating the curse of dimensionality for such a problem. PC and Gaussian mixtures models have also been combined showing benefits that neither alone can provide [271].

7.12 Sparse Grid Quadrature Approach to Orbit Uncertainty Propagation

Sparse grid quadrature is a deterministic numerical approach to computing the moments of the orbit state, for example, mean, covariance, skewness, and kurtosis. The sparse grid quadrature approach is applicable to the orbit uncertainty propagation problem in which the orbit dynamics can be written as $\boldsymbol{x}_t = \boldsymbol{\phi}(t; \boldsymbol{x}_0, \boldsymbol{\alpha})$, where t denotes time, $\boldsymbol{x}_t$ and $\boldsymbol{x}_0$ denote the state at time t and initial time t_0, respectively, $\boldsymbol{\alpha}$ denotes the model parameter vector, and $\boldsymbol{\phi}$ denotes the nonlinear mapping from t_0 to t [210, 257]. The orbit state can be either position and velocity or orbital elements. In coupled attitude/orbit uncertainty propagation,

the state may include attitude and angular velocity as well [257]. The state and model parameters can be either Gaussian or non-Gaussian. The approach treats the mapping $\boldsymbol{\phi}$ as a "black box" and can therefore be used with any force model. Applications of this approach to orbit uncertainty propagation can be found in [210, 257].

The sparse grid quadrature approach to orbit uncertainty propagation is based on the fact that moments of the orbit state are mathematical expectations of nonlinear transformations of the initial orbit state and model parameters and therefore can be computed using a quadrature (or cubature) method. For example, the state mean $\hat{\boldsymbol{x}}_t = E[\boldsymbol{\phi}(t, \boldsymbol{x}_0, \boldsymbol{\alpha})] \approx \sum_{i=1}^{N} w_i \, \boldsymbol{\phi}(t, \boldsymbol{x}_0^{(i)}, \boldsymbol{\alpha}^{(i)})$, where the expectation is taken with respect to the joint probability density function of $\boldsymbol{x}_0$ and $\boldsymbol{\alpha}$, $[\boldsymbol{x}_0^{(i)T}, \boldsymbol{\alpha}^{(i)T}]^T$ are quadrature points in the joint space of $\boldsymbol{x}_0$ and $\boldsymbol{\alpha}$, w_i are the associated weights, and N is the number of quadrature points [210, 257]. The superscript T denotes transpose. Higher moments can be computed in a similar manner. An n-dimensional sparse grid quadrature is constructed from linear combinations of tensor products of one-dimensional quadratures by using Symolyak rule. The one-dimensional quadratures are usually from the family of Gaussian quadratures, for example, Gaussian-Hermite quadrature for Gaussian distributions and Gaussian-Legendre quadrature for uniform distributions [210]. Moment matching can also be used to determine the points and weights of one-dimensional quadratures [142]. A sparse grid quadrature can be anisotropic, which means that more quadrature points are located along certain directions than along other directions [141]. The sparse grid quadrature differs from other quadratures only in the quadrature points and weights.

If the mapping $\boldsymbol{\phi}(t; \boldsymbol{x}_0, \boldsymbol{\alpha})$ is polynomial in $\boldsymbol{x}_0$ and $\boldsymbol{\alpha}$, the sparse grid quadrature with sufficient number of quadrature points can compute *any moments* of $\boldsymbol{x}_t$ *exactly* [210]. This makes the sparse grid quadrature approach very appealing to moment computation for polynomial-like systems. The computational complexity of the sparse grid quadrature is proportional to the number of quadrature points N, a polynomial function of the dimension of the joint vector of $\boldsymbol{x}_0$ and $\boldsymbol{\alpha}$ [210]. The widely used unscented transform of the unscented Kalman filter or sigma-point filter can be viewed as a low-accuracy sparse grid quadrature [140, 142]. In addition to orbit uncertainty propagation, nonlinear filters based on sparse grid quadrature have been developed and shown to be more accurate and have better convergence properties than the extended Kalman filter or the unscented Kalman filter in the presence of large initial uncertainty [140–142]. The cubature Kalman filter [143] is also closely related to the sparse grid quadrature filter [144]. The sparse grid method can take into consideration the discrete-time process noise by a linear transformation of the quadrature points [52].

Advantages The sparse grid method is an efficient and easy-to-implement method for computing the moments of the orbit state. It only requires forward orbit propagation and the number of orbit propagations is polynomial (instead of exponential) in the dimension of the state and model parameters. It can be used for a large class of orbit uncertainty propagation problems, where the uncertainty can be Gaussian or non-Gaussian and the state can be Cartesian coordinates or orbital elements. The accuracy of the sparse grid method is high when the nonlinear mapping is polynomial like. One such example is the mean and covariance propagation of an LEO object for 15 orbital periods [210].

Disadvantages: The sparse grid method itself cannot provide a parametric model of the probability density function. The accuracy of the sparse grid method depends on whether the nonlinear mapping is polynomial-like. When the mapping is significantly dissimilar to a polynomial function, the accuracy of

the sparse grid method degrades and is no better than the Monte Carlo or quasi Monte Carlo method [210]. (Moments computed using state transition tensors, generalized polynomial chaos, and conjugate unscented transform have similar accuracy degradation when the polynomial approximation of the nonlinear mapping is invalid.) The sparse grid method cannot guarantee that all the weights are positive. This is no problem when the nonlinear mapping is polynomial or polynomial-like, but when the mapping is far from polynomial, that is, when the applicability of the sparse grid method is questionable, the computed variance or other even moments may be negative [210].

7.13 Particle Filters

Particle filters are sequential Monte Carlo methods based on the representation of an arbitrary PDF by a set of independent and identically distributed random samples. They can be applied to any nonlinear and/or non-Gaussian state space model; however, they are computationally intensive. Particle filters were extensively developed in the nineties [21, 228] and remain a applicable approach to propagating uncertainty in astrodynamics [174, 193, 194]. Although computationally expensive, a key advantage is the representation of general PDFs. In addition, particle filters are easily parallelized [20, 242].

Particle filters utilize Monte Carlo sampling to approximate the posterior PDF via random samples with appropriately chosen weights. Monte Carlo simulation is applied in conjunction with importance sampling to allow for state estimation using weights computed from a sampled posterior density. Importance sampling computes the weights of generated samples and is deemed necessary because it is not possible, in general, to effectively sample the posterior distribution due to its multivariate, nonstandard, and only known up to a certain order nature. Importance sampling requires the user to define the analytic character of the posterior state PDF, known as the importance or proposed density [228]. The filter designer proposes the importance density and the number of particles to be utilized by the filter to produce an accurate and consistent estimate while balancing computational burden. One of the over-looked requirements for implementation of particle filtering is that the density of instantaneously unobserved variables must be dictated. For example, if only position level measurements are available, the velocity distribution must be given so that the filter can compute samples. If an incorrect form is given for instantaneous unobserved state variables, degeneracy will arise faster and more resampling steps are required. If the posterior PDF is not known exactly, as is common in most problems, a posterior approximation must be used rendering the PF suboptimal. Commonly, the importance density is selected to fit the assumption that state variable uncertainties are of Gaussian character with a given mean and covariance. The Gaussian assumption for the importance density produces a suboptimal filter for nonlinear problems, even if the Gaussian assumption is valid for a certain state variable, it may not be valid for others. Using the Gaussian distribution assumption, the importance density becomes equivalent to the prior. If the posterior PDF is relatively well known, the number of samples must be rather large so that the importance density approaches the true posterior PDF.

If the chosen importance density is not exactly the posterior distribution, the variance of the importance weights has been shown to increase as the number of recursive steps increases leading to only one particle possessing a nonzero weight. This is known as degeneracy and resampling is carried out to combat this problem [228]. The resampling step eliminates samples with low importance and increases the number of

samples with high importance to avoid excessive computational resources for near zero weights. However, resampling requires a measure of degeneracy, such as the inverse of the sum of the square weights, and a user-defined threshold for triggering the resampling procedure. Accordingly, appropriate selection of the importance density is crucial to particle filter operation since incorrect selection can result in divergence or excessive degeneracy. Refinement methods have been introduced to increase the accuracy of the importance density in various ways: (a) using intermediate densities between time steps to re-weight the particles which are resampled, (b) using the measurement at time K to refine the particles at time $K-1$ before propagation, or (c) applying an EKF or UKF to generate a Gaussian approximation for the importance density [228].

Sample diversity is an important concern since degeneracy is inherent to sequential importance sampling particle filters and resampling can cause diversity loss among particles. Other methods such as regularization or the Markov Chain Monte Carlo (MCMC) move step have been implemented to maintain diversity, which can be hard to accomplish especially for systems with little or no process noise. The regularized PF combats loss of diversity by jittering the particles selected from the importance density by a proposed kernel density. Since particle jittering can cause divergence from the true posterior, addition of a MCMC move step, utilizing the Metropolis-Hastings acceptance probability dictating jittering acceptance, can improve operation. If the propagation process equations have little to no process noise, this will result in significant resampling because the sampled a posteriori density particles will not span enough of the space to maintain diversity for long compared with a propagation process that is augmented with process noise.

7.14 Differential Algebra

The basic idea behind differential algebra (DA) is to bring the treatment of functions and the operations on them to a computer environment in a similar manner as the treatment of real numbers [35, pp 82-96]. Referring to Figure 7.14.1, consider two real numbers a and b. Their transformation into the floating-point (FP) representation, $\bar{a}$ and $\bar{b}$, respectively, is performed to operate on them in a computer environment. Then, given any operation $*$ in the set of real numbers, an adjoint operation $\circledast$ is defined in the set of FP numbers so that the diagram in Figure 7.14.1 commutes. (The diagram commutes approximately in practice due to truncation errors.) Consequently, transforming the real numbers a and b into their FP representation and operating on them in the set of FP numbers returns the same result as carrying out the operation in the set of real numbers and then transforming the achieved result in its FP representation. In a similar way, given two k-differentiable functions, f and g, in n variables, DA operates on them using their kth-order Taylor expansions, F and G, respectively. Therefore, the transformation of real numbers in their FP representation is now replaced by the extraction of the kth-order Taylor expansions of f and g in the computer environment. For each operation in the space of k-differentiable functions, an adjoint operation in the space of Taylor polynomials is defined, so that the corresponding diagram commutes; that is, extracting the Taylor expansions of f and g and operating on them in the space of Taylor polynomials using DA returns the same result as operating on f and g in the original space and then extracting the Taylor expansion of the resulting function. The proper implementation of DA in a computer allows the user to efficiently compute the Taylor coefficients of any coded function up to a specified order k.

The availability of such high order expansions can be exploited when uncertainties are propagated

Figure 7.14.1 Floating-point representation of real numbers (left) and algebra of Taylor polynomials (right).

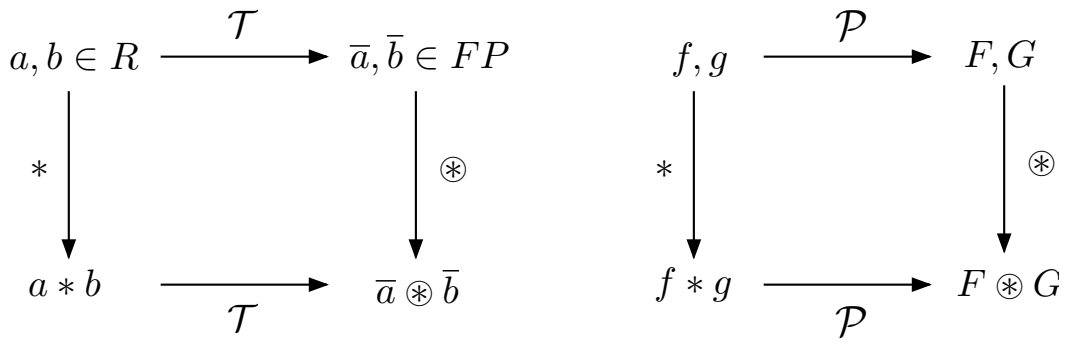

through nonlinear functions or dynamical models. Without loss of generality, consider the initial value problem

$$\frac{d\boldsymbol{x}(t)}{dt} = \boldsymbol{f}(\boldsymbol{x}(t), \boldsymbol{\alpha}, t), x(t_0) = x_0, \tag{7.14.1}$$

where $\boldsymbol{x}$ is the state vector and $\boldsymbol{\alpha}$ is the model parameter vector. The associated flow is denoted by $\boldsymbol{\phi}(t; \boldsymbol{x}_0, \alpha)$. The kth-order Taylor expansion of the flow at any time t with respect to initial conditions and model parameters can be obtained by initializing $\boldsymbol{x}_0$ and $\boldsymbol{\alpha}$ as DA variables, and carrying out all the operations of an integration algorithm in the DA framework. The resulting polynomial is a kth-order map linking the domain of initial conditions and model parameters to the manifold of attainable states at time t.

The polynomial map can be used to efficiently propagate uncertainties through different methods. A first method consists of running Monte Carlo simulations on the map rather than on the original flow. In this way, it is possible to substitute thousands of point-wise numerical integrations required for classical Monte Carlo simulations with an equal number of map evaluations (i.e., fast polynomial evaluations). Applications of this method to the analysis of asteroid close encounters with Earth and to impact probability computation between Earth-orbiting objects can be found in [18, 208, 209]. Secondly, DA can be exploited to compute the moments of the transformed probability density function (e.g., mean, covariance, skewness, and kurtosis) by applying the expectation operation to the polynomial maps [266, 267], or to analytically map the probability density function by computing the expansion of the determinant of the Jacobian of the transformation [290]. Lastly, polynomial bounders can be applied on the polynomial map to estimate the maximum size of the propagated uncertainty set along each coordinate [180].

Advantages

Differential algebra is an automatic procedure that allows the expansion of the flow of ODE at arbitrary order. Thus, the approach is suitable for dealing with highly nonlinear dynamics, where linearized approaches fail to deliver an accurate description of the evolution of the uncertainty set. In addition, as the flow expansion is obtained with an algebra of Taylor polynomials, DA method does not involve the integration of variational equations and its implementation is essentially problem independent. DA can be implemented very efficiently in a computer environment, thus it is possible to obtain high order expansions of the flow in

a limited amount of time. As an example, a sixth order expansion of the flow of a restricted n-body problem takes on average only 10 times more than a simple point-wise integration. This shows that a DA-based Monte Carlo simulation can be orders of magnitude faster than a classical one, when a significant number of particles need to be propagated. The DA approach for uncertainty propagation is also independent from the initial statistics. In case different initial statistics need to be analyzed, the same polynomial map (obtained with a single DA integration) can be used. The same consideration applies to model parameters. Finally, as the flow expansion is analytical, an analytic framework is delivered. The use of tools for inverting and composing polynomials, as well as integrating and differentiating them, allows the user to build algorithms to solve complex problems that may also involve constraint satisfaction.

Disadvantages

DA approach is based on Taylor expansions. Thus, the problem to be dealt with must be well behaved. Discontinuous dynamical models (e.g., eclipses or, in general, if statements) are a major limitation for the method, and complicated ad hoc procedures are needed to deal with these conditions (when possible). In addition, the accuracy of the method tends to decrease drastically when the uncertainty domain becomes too stretched in one or more directions. This can be due to one or a combination of the following causes: high nonlinearity of the dynamics, large initial uncertainty sets, and long term propagations. Thus, it is necessary to estimate the convergence radius of the Taylor expansion in order to guarantee the fulfillment of the accuracy requirements. In order to address this problem, a method referred to as automatic domain splitting has been recently proposed. The underlying idea is to split the initial domain into manageable subdomains over which the Taylor expansion shows good convergence properties [291]. This results in the need of managing multiple Taylor expansions, which can be an issue when many splits occur.

7.15 Numerical Integrators for Orbit State and Uncertainty Propagation

The subject of the numerical integration of ordinary differential equations has an extensive history and rich development from which one can draw for the specialization of methods and the development of new ones for propagating astrodynamic states and their associated uncertainty. One can use virtually any of these well developed methods for the purposes of orbit propagation. Thus, one might ask "Why is there a need for further development?" The answer lies in the current and future needs given the large number of space objects expected in the future and the need to propagate orbits and their uncertainty as efficiently as possible. One of the requirements is that whatever method is used, the numerical error, i.e., the discretization and truncation errors, in the orbital propagators should remain significantly below the uncertainty in the dynamical model. There are several new orbital propagators that respond to this need, many of which are briefly reviewed here. Recent developments have focused on the efficient use of gravity models, highly-efficient integrators for specific orbit types, error estimation and stepsize control to automate the propagation of any orbit type, parallelization to reduce computational costs, large step sizes, e.g., half an orbit or more, allowed by many of the newer propagators, and the propagation of an ensemble of orbits to support particle- and sigma-point-based approaches to the propagation of uncertainty.

Many numerical integration methods have been specialized for propagating orbits, as surveyed in Montenbruck [206], Montenbruck and Gill [207], and Jones and Anderson [146]. Current state-of-the-art numerical integrators used for orbit propagation include Dormand-Prince 8(7) (DP8), Runge-Kutta-Nystrom 12(10) (RKN12), Adams-Bashforth-Moulton (ABM), and Gauss-Jackson (GJ). Both DP8 and RKN12 are high-order explicit Runge-Kutta methods that use variable-stepsize error control (Iserles [137], Butcher [44], Hairer, Norsett and G. Wanner [107]). However, RKN12 is an integration method that cannot handle velocity-dependent forces, and so its use for general orbit propagation is limited. ABM and GJ are predictor-corrector methods that utilize an explicit method for the prediction and an implicit method for the correction. Fixed-step implementations of GJ (using judiciously chosen Sundman regularizations for propagating highly-elliptic orbits) are widely used in numerical integration problems for astrodynamics and dynamical astronomy. For example, an eighth-order GJ algorithm has been used for space surveillance since the 1960s (Berry and Healy [32]). It is worth noting that although GJ will reduce its step size (typically by factors of two) to ensure convergence of a given time step; however, this does not imply that GJ is a variable-step integration method as discussed below. JPL uses a variable-step, variable-order multi-step propagator due to Keogh [169, 170] which is reported to have better stability characteristics than the aforementioned ABM method.

More recently, Bradley, Jones, Beylkin, and Axelrad [39] studied the use of fixed-step implicit Runge-Kutta (IRK) methods for orbit propagation based on Gauss-Legendre quadrature. Bai and Junkins [22] investigated a related scheme based on Gauss-Chebyshev-Lobatto quadrature and fixed-point iteration, which they coined modified Chebyshev-Picard iteration (MCPI). Gauss-Legendre IRK (GL-IRK) and Gauss-Chebyshev IRK methods are of particular interest because, unlike the above explicit methods, they are parallelizable, thus amenable to high-performance computing, and A-stable at all orders, thus allowing for larger (and fewer) time steps to be taken without sacrificing stability (Iserles [137], Butcher [44], Hairer and Wanner [108][‡]. The caveat is that a nonlinear system of equations must be solved via iterative methods at each time step. While this is a clear disadvantage for implicit methods in general, for the perturbed perturbed two-body problem, one may use approximate analytical solutions to warm-start the iterations, leading to faster convergence.

By tuning the number of time steps, the number of stages (nodes) per time step, and the convergence criteria (iteration tolerance for a given time step), these authors demonstrated that IRK methods can be made both precise and efficient, at least for nearly-circular orbits, based on the number of force-model evaluations required to propagate the orbit[§] in a serial computing environment. In Bai and Junkins' study [22], zonal harmonics in the Earth's gravity up to degree five were considered; higher-fidelity gravitational force models were considered by Beylkin and Sandberg [36] and Bradley, Jones, Beylkin, Sandberg and Axelrad [39, 40], specifically, zonal, tesseral, and sectorial harmonics up to degree and order 70.

Variable-step methods, on the other hand, estimate the numerical truncation error and control it by adapting the stepsize. In addition to rejecting or accepting the current stepsize based on meeting the prescribed

[‡]Recent work by Beylkin, Sandberg, Bradley, Jones and Axelrad [36, 40] suggests that band-limited collocation-based IRK methods are more efficient (for a large number of nodes) than their Gauss-Legendre and Gauss-Chebyshev counterparts, while also being parallelizable and "numerically" A-stable.

[§]In the perturbed two-body problem, evaluation of the force models (the Earth gravity model in particular) is the dominant cost of orbit propagation. The number of force-model evaluations can thus be used as a crude measure of propagator performance.

error tolerance and convergence of the nonlinear equations, these methods also predict the stepsize for the next time step. This is different from adjusting the stepsize to achieve convergence of the above nonlinear equations in the implicit methods. While there is a computational price for maintaining control over the truncation error, these variable-step methods with error-stepsize control generally lead to a more efficient method suitable for all regimes of space without modification [15]. Variable-step GL-IRK-based orbital propagators, such as those developed by Jones [145], and Aristoff, Horwood, and Poore [11, 14, 15], on the other hand, can be considered self-tuning. The user selects an acceptable level of numerical truncation error (per step) in the state of the object, and the method then estimates and controls the error by adjusting the step size so that the error is close to but does not exceed the specified error tolerance. As a result, the work devoted to each step and the accuracy achieved in the step are balanced for overall efficiency (Butcher [44] and Shampine [237, 238]). Note that fixed-step propagators do not reject steps because there is no accuracy requirement.

For an object in highly-elliptic orbit, a variable-step propagator will take smaller steps near perigee and larger steps near apogee, thereby solving the IVP in an efficient manner. Conversely, fixed-step propagators take larger steps near perigee and smaller steps near apogee. As a result, they are forced to take extremely small time steps throughout the entire propagation in order to achieve the same accuracy as that of a variable-step method of the same order. For this reason, the equations of motion are typically transformed (e.g., using the Sundman or generalized Sundman transform [31]) so that fixed steps can be taken in an orbital anomaly (e.g., eccentric anomaly or true anomaly), rather than in time, in an effort to distribute the numerical truncation error evenly across the steps.

As previously mentioned, precise uncertainty propagation, in addition to precise orbit propagation, is needed to support numerous methods for advanced SSA. A large class of methods for propagating the uncertainty in an object's state (i.e., its probability density function) requires finding high-order numerical solutions to ensembles of IVPs. Uncertainty propagation via the unscented Kalman filter (UKF) [156], for example, requires $2n + 1$ trajectory (orbit) propagations, where n is the dimension of the state[¶]. The variable-step implementation of GL-IRK developed by Aristoff, Horwood, and Poore [11, 14, 15] exploits the proximity of the particles or states and enables them to be propagated collectively, rather than individually. Specifically, once the first state in the ensemble is propagated, the remaining states can be propagated at a fraction of the cost by reusing the (near) optimal step sizes taken during propagation of the first state, and by using the solution to the first IVP itself to warm-start the iterations for the Runge-Kutta equations arising when solving the remaining IVPs. For the perturbed two-body problem of orbital mechanics, this approach was found to significantly reduce the computational cost of uncertainty propagation, measured by the number of force-model evaluations for a given accuracy [11, 13, 14].

7.16 Recommendations

Many of the methods for uncertainty propagation are surveyed above. Here are some final comments and recommendations.

1. While one cannot compare all the methods presented above, the computational results in Section 7.10

[¶]The $2n + 1$ states arising within the UKF are often referred to as sigma points.

indicate the performance advantage of the representation of uncertainty in orbital element space and the performance of the UKF, GVM filter, and Gaussian sums in element space. A more detailed study that uses a common set of metrics and test cases, such as those described in Section 9.1, and applies them to the uncertainty propagation methods reviewed in this chapter should be undertaken in the future.

2. The above outline of methods currently being researched by the astrodynamics community demonstrates that virtually every nonlinear filtering method that could be investigated is being investigated to propagate uncertainties. We find this maturing area of research to be of very high quality with each method having its own merits. To better understand the strengths (and weaknesses) of the above methods, one needs a set of test problems, a set of performance metrics, and a list of test cases that can help evaluate these strengths and weaknesses. Given the performance metrics discussed in Chapter 8 and the test cases outlined in Chapter 9, here is a list of potential comparisons:

   - an assessment of the *range of validity* for each method for propagating uncertainty as a function of the initial uncertainty,
   - performance with and without process noise or stochastic acceleration,
   - performance with and without model mismatch,
   - computational complexity and runtime,
   - performance in different regimes of space.

   In addition to propagation of uncertainty forward in time, the transformation of uncertainty from one coordinate system to another should be considered.

3. With respect to orbital propagation, the use of one that can control the error relative to the model dynamics is highly recommended so that the error in the propagated state is guaranteed to be substantially below the uncertainties in the dynamics including initial conditions. The newer orbital propagators based on implicit Runge-Kutta methods or modified Picard iteration as presented in Section 7.15 should be considered due to their numerical stability properties, efficiency due to large step sizes, adaptability to high performance computing and parallelization, and the ability to propagate an ensemble of orbits needed in the unscented Kalman filter, Gauss-Hermite filters, Gauss von Mises filter, or particle filters.

4. While the methods of this chapter address covariance and uncertainty realism during propagation, the sensitivity of each of the four mission areas presented in Chapter 3 to degraded covariance/uncertainty realism should be investigated in conjunction with the above metrics. Such an understanding might help set some of the metric parameters and be useful in decision making processes.

Chapter 8

Metrics

8.1 Introduction

This chapter addresses metrics for covariance and uncertainty realism for *aleatoric uncertainties* in the propagated state of an object. Central to this type of uncertainty are the properties of a point estimator which uses sample data to calculate a single value or statistic. Two desirable properties of a point estimator are that it be *unbiased* and *consistent*. The estimator is unbiased if the difference between the expected value and the true value of the parameter being estimated is zero. It is consistent if the expected value of the estimator converges in probability to the true value of the parameter being estimated as the sample size increases. Under Gaussian assumptions, *covariance realism*[*] is the proper characterization of the covariance (statistical uncertainty) in the state of a system - that is, the rigorous estimation of both its mean and covariance. Covariance realism thus requires that the estimate of the mean be the true mean (i.e., the estimate is unbiased) and the covariance possesses the right size, shape, and orientation (i.e., consistency). Relaxing Gaussian assumptions, *uncertainty realism* is the proper characterization of the uncertainty in that state using a general (i.e., non-Gaussian) probability density function. Uncertainty realism requires that all cumulants (beyond the state and covariance) be properly characterized. The relationship between *covariance realism* and *uncertainty realism* is that the former is the necessary but not the sufficient condition for achieving the latter. The two definitions coincide if the process is Gaussian. In future systems wherein the number of objects may increase tenfold, the number of sensor reports for each space object may necessarily decrease, even for objects in the space catalog, nonlinearity may have an increasing impact on the uncertainty. Also, for UCTs, which generally have larger covariances than those in the space catalog or for cases where longer-term prediction is needed, such as for conjunction assessments, non-Gaussian representations of uncertainty, such as those described in Chapter 7, may be necessary to characterize the actual uncertainty in the state of the space objects. We thus consider metrics for assessing both covariance realism and uncertainty realism.

Metrics for evaluating covariance realism have been in use in astrodynamics community for some time. These can be found in the paper by Vallado and Seago [265], references therein, and the report [105]. One of these metrics is based on the averaged Mahalanobis distance metric and has been used by several groups [16, 68, 115, 231] in assessing covariance realism. Specifically, this metric assesses, for a particular

[*]The term *covariance consistency* [76] is used in other tracking domains in place of the term "covariance realism."

object, the mean normalized chi-squared statistic of the track (orbit) assigned to that object. This metric is defined using the square of the Mahalanobis distance [184] and is necessary for covariance realism, but is not sufficient. More robust and general metrics are needed for both covariance realism and uncertainty realism. Specifically, the following attributes of a metric are desirable.

1. Metrics should be computationally tractable and statistically based.
2. Metrics should be sufficiently powerful to detect breakdown of covariance and more generally uncertainty realism.
3. Metrics should be compatible with any choice of coordinate system used to represent uncertainty (i.e., they should not be restricted to Cartesian representations of the covariance matrix or more generally uncertainty).
4. Metrics should address both covariance and uncertainty realism, i.e., non-Gaussian realism.
5. Metrics should be non-intrusive to avoid the need to share proprietary algorithms, models, and software.

To achieve these objectives, we present and discuss several potential metrics. In order to propose metrics that enable the assessment of uncertainty realism for more general probability density functions, e.g., a Gaussian sum, it is necessary to generalize the Mahalanobis distance to one that that tests the proper characterization of the probability density function of the state, i.e., uncertainty realism. Under weak assumptions as explained in Section 8.3, this new *uncertainty realism metric* is also a chi-squared random variable. As such, analogous tests for covariance realism (both in off-line simulations with multiple Monte-Carlo trials and online with real data) can be extended to use the uncertainty realism metric, some of which are reviewed in this report, such as Pearson's chi-squared goodness-of-fit test [247] and the Cramér-von Mises goodness-of-fit test [59, 78, 250]. We acknowledge that the uncertainty realism metric and the corresponding tests for uncertainty realism proposed in this report only address *aleatoric* uncertainties (which fit naturally in a probabilistic framework) and not *epistemic* uncertainties (which are generally treated by non-probabilistic methods).

The remainder of this chapter is as follows. The classical Mahalanobis distance and its use for testing covariance realism is reviewed in Section 8.2. Since distributions other than Gaussians arise, we then discuss how the Mahalanobis distance can be generalized to non-Gaussian probability density functions (PDFs) in Section 8.3, thereby defining a metric for uncertainty realism. An *averaged uncertainty realism metric* is then presented in Section 8.4. The more powerful distribution matching tests and examples are presented in Section 8.5 and a summary of the recommendations in Section 8.6.

8.2 Mahalanobis Distance

The track (orbit) covariance realism metric evaluates the consistency of the uncertainty corresponding to the orbit state estimate against some known truth state. The uncertainty in the state of an object is often

represented by a Gaussian. Recall that the random vector $\boldsymbol{x} \in \mathbb{R}^n$ is jointly distributed as a Gaussian distribution if and only if its joint PDF has the form

$$p_x(\boldsymbol{x}; \boldsymbol{\mu}, \mathbf{P}) = \mathcal{N}(\boldsymbol{x}; \boldsymbol{\mu}, \mathbf{P}) \equiv \frac{1}{\sqrt{\det(2\pi\mathbf{P})}} \exp\left[-\frac{1}{2}(\boldsymbol{x}-\boldsymbol{\mu})^T\mathbf{P}^{-1}(\boldsymbol{x}-\boldsymbol{\mu})\right]. \tag{8.2.1}$$

In this definition, $\boldsymbol{\mu} \in \mathbb{R}^n$ denotes the mean (which also coincides with the mode) and $\mathbf{P}$ is an $n \times n$ symmetric positive-definite matrix called the covariance. Under these Gaussian assumptions, the covariance realism metric is defined using the square of the Mahalanobis distance. Let $\boldsymbol{x}$ be a given (Gaussian) orbital state estimate at a certain time t and let $\mathbf{P}$ be its corresponding estimated covariance. Further denote $\boldsymbol{x}_{truth}$ as the truth state of the target at time t. The *squared Mahalanobis distance* between the estimated orbit state and truth target state is defined as

$$\mathcal{M}(\boldsymbol{x}; \boldsymbol{x}_{truth}, \mathbf{P}) = (\boldsymbol{x}-\boldsymbol{x}_{truth})^T\mathbf{P}^{-1}(\boldsymbol{x}-\boldsymbol{x}_{truth}). \tag{8.2.2}$$

The expected value of $\mathcal{M}$ is n, where n is the dimension of the state vector $\boldsymbol{x}$. Moreover, it follows that $\mathcal{M} \sim \chi^2(n)$; i.e., $\mathcal{M}$ is chi-squared distributed with n degrees of freedom.

Given a significance level α (typically 0.01 or 0.001), one can derive a two-sided $100(1-\alpha)\%$ confidence interval for the distribution $\chi^2(n)/n$ given by $[\chi^2(n;\alpha/2)/n, \chi^2(n;1-\alpha/2)/n]$, where $\chi^2(n;\beta)$ is the $100\beta\%$ quantile of the distribution $\chi^2(n)$. One rejects the null hypothesis that the covariance $\mathbf{P}$ centered at the estimate $\boldsymbol{x}$ is realistic given the truth $\boldsymbol{x}_{truth}$ if $\mathcal{M}(\boldsymbol{x}; \boldsymbol{x}_{truth}, \mathbf{P})/n$ falls outside this two-sided confidence interval. For example, if $\alpha = 0.001$ and $n = 6$, the two-sided 99.9% confidence interval for this test is $[0.0499, 4.017]$.

We remark that (8.2.2) can be modified to accommodate the case in which the truth state $\boldsymbol{x}_{truth}$ is imprecise or "fuzzy." If the uncertainty in $\boldsymbol{x}_{truth}$ is provided as a covariance matrix $\mathbf{P}_{truth}$ then, in place of (8.2.2), one can use

$$\mathcal{M}(\boldsymbol{x}; \boldsymbol{x}_{truth}, \mathbf{P}_{truth}, \mathbf{P}) = (\boldsymbol{x}-\boldsymbol{x}_{truth})^T(\mathbf{P}+\mathbf{P}_{truth})^{-1}(\boldsymbol{x}-\boldsymbol{x}_{truth}). \tag{8.2.3}$$

The use of a covariance for the truth is discussed more generally in the report by Frisbee [155].

The covariance realism metric based on the squared Mahalanobis distance (8.2.2) or (8.2.3) has many applications both at the sensor- and system-level. One example of its use for validating covariance realism during uncertainty propagation is the following. First, we make the following basic assumptions: (i) the orbital state uncertainty is identically Gaussian and is realistic[†] at some initial epoch t_0, and (ii) the truth state $\boldsymbol{x}_{truth}$ is available at some future time $t > t_0$. With these assumptions, we propagate the Gaussian at epoch t_0 to time t, approximate the propagated uncertainty by a Gaussian with state (mean) $\boldsymbol{x}$ and covariance $\mathbf{P}$, and evaluate the metric (8.2.2). The application of this metric is only valid if the propagated uncertainty is represented by a Gaussian distribution. A generalization of the covariance realism metric to an uncertainty realism metric that relaxes the assumptions that the initial or propagated uncertainty be Gaussian is described next.

[†] In this example, we will not be concerned about how this initial Gaussian covariance is generated and if it is indeed realistic.

8.3 Generalization of the Mahalanobis Distance

In order to treat probability density functions other than a Gaussian, it is necessary to generalize the Mahalanobis distance. Let $p_x(\boldsymbol{x};\boldsymbol{\Theta})$ denote a general PDF in the n-dimensional orbit state $\boldsymbol{x}$ with some parameter set $\boldsymbol{\Theta}$. The proposed generalization of the squared Mahalanobis distance which serves as a metric for *uncertainty realism* is defined by

$$\mathcal{U}(\boldsymbol{x};\boldsymbol{\Theta}) = -2\ln\left[\frac{p_x(\boldsymbol{x};\boldsymbol{\Theta})}{p_x(\hat{\boldsymbol{x}};\boldsymbol{\Theta})}\right], \tag{8.3.1}$$

where $\hat{\boldsymbol{x}}$ is the mode of $\boldsymbol{x}$:

$$\hat{\boldsymbol{x}} = \text{argmax}_{\boldsymbol{x}}\, p_x(\boldsymbol{x};\boldsymbol{\Theta}).$$

We remark that for a Gaussian PDF, as defined in (8.2.1), the parameter set $\boldsymbol{\Theta}$ encapsulates the mean $\boldsymbol{\mu}$ and covariance $\mathbf{P}$. Further, in such a case, the uncertainty realism metric (8.3.1) reduces to

$$\mathcal{U}(\boldsymbol{x};\boldsymbol{\Theta}) = \mathcal{U}(\boldsymbol{x};\boldsymbol{\mu},\mathbf{P}) = (\boldsymbol{x}-\boldsymbol{\mu})^T\mathbf{P}^{-1}(\boldsymbol{x}-\boldsymbol{\mu}),$$

which is precisely the squared Mahalanobis distance (8.2.2) defined earlier. The uncertainty realism metric (8.3.1) is chi-squared distributed or approximately so under the following scenarios.

Suppose again that $p_x(\boldsymbol{x};\boldsymbol{\Theta}) = \mathcal{N}(\boldsymbol{x};\boldsymbol{\mu},\mathbf{P})$, and let $\boldsymbol{x} = \boldsymbol{\Phi}(\boldsymbol{y})$ where $\boldsymbol{\Phi}$ is a volume-preserving transformation[‡] (i.e., the determinant of its Jacobian is unity). By the change of variables theorem, it follows that $p_y(\boldsymbol{y};\boldsymbol{\Theta}) = \mathcal{N}(\boldsymbol{\Phi}(y);\boldsymbol{\mu},\mathbf{P})$ and, from the definition of the uncertainty realism metric (8.3.1), $\mathcal{U}(\boldsymbol{y};\boldsymbol{\Theta}) = \mathcal{M}(\boldsymbol{\Phi}(y);\boldsymbol{\mu},\mathbf{P})$. Thus, quite remarkably, the uncertainty realism metric for any (possibly non-linear) volume-preserving transformation of a Gaussian random vector also possesses the chi-squared property.

The property presented above is significant with regards to uncertainty propagation of a space object's orbital state under perturbed two-body dynamics and no process noise. Since the dynamics are dominated by conservative forces (i.e., gravity), any initial Gaussian distribution that is propagated under said dynamics will have the form $\det(\partial\boldsymbol{\Phi}/\partial\boldsymbol{y})\,\mathcal{N}(\boldsymbol{\Phi}(y);\boldsymbol{\mu},\mathbf{P})$, where $\det(\partial\boldsymbol{\Phi}/\partial\boldsymbol{y}) \approx 1$. This is a consequence of Liouville's theorem [101] in Hamiltonian mechanics. Thus, the uncertainty realism metric (8.3.1) applied to this distribution will be (approximately) chi-squared distributed.

Another example is that of Gaussian mixtures, which are used by many authors [67, 122, 125, 138, 255] to represent a general probability density function. If the Gaussian mixture well approximates[§] the actual distribution $\det(\partial\boldsymbol{\Phi}/\partial\boldsymbol{y})\,\mathcal{N}(\boldsymbol{\Phi}(y);\boldsymbol{\mu},\mathbf{P})$, then one can apply the definition (8.3.1) directly to the Gaussian mixture knowing that the resulting test statistic is (approximately) chi-squared distributed.

Finally, a Gauss von Mises distribution [123, 126, 127] is a new distribution for representing uncertainty in orbital element space. It has been shown to have superior properties under nonlinear uncertainty propagation compared to a Gaussian when propagated using the (prediction steps of) the UKF or EKF. Under weak conditions, $\mathcal{U}(\boldsymbol{x};\boldsymbol{\Theta})$ is also chi-squared distributed with n degrees of freedom [127]. Thus, in analogy to

[‡] One example of a volume-preserving transformation is the solution flow of a *conservative* dynamical system (without process noise) that propagates some initial state x_0 at time t_0 to a state $\boldsymbol{x}$ at time t.

[§] In principle, any PDF can be approximated by a Gaussian mixture to within any desired accuracy (in the L^1 sense) due to a result of Alspach and Sorenson [7].

Figure 8.3.1 Setup for the statistical significance tests. The yellow shaded regions are those regions in which the null hypothesis is rejected. Dependence on the parameter set $\boldsymbol{\Theta}$ in $f(\boldsymbol{x};\boldsymbol{\Theta})$ is omitted in the figure.

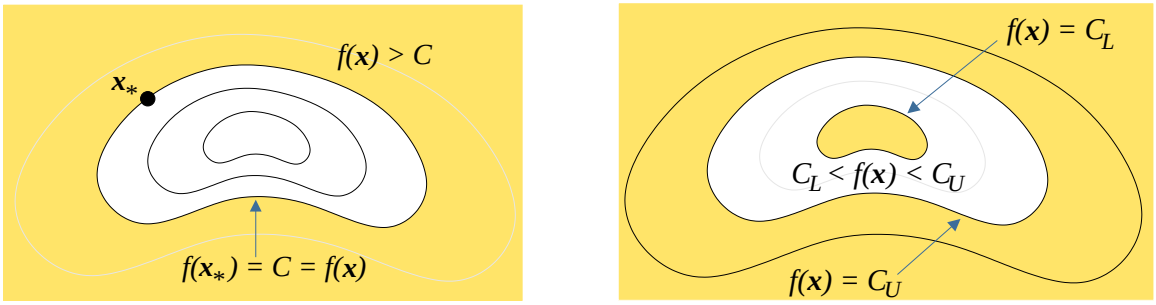

(a) One-sided test

(b) Two-sided test

the statistical test for covariance realism described at the end of Subsection 8.2, the metric (8.3.1) provides a test for uncertainty realism.

8.3.1 Statistical Interpretation

The statistical interpretation of the Mahalanobis distance metric (8.2.2) and its generalization, given by (8.3.1), can be understood by considering the general setting of a multivariate random vector $\boldsymbol{x}$ with support on a differentiable manifold $\mathfrak{M}$. We express its PDF in the form $p_x(\boldsymbol{x};\boldsymbol{\Theta}) = \mathrm{e}^{-f(\boldsymbol{x};\boldsymbol{\Theta})/2} \Leftrightarrow f(\boldsymbol{x};\boldsymbol{\Theta}) = -2\ln p_x(\boldsymbol{x};\boldsymbol{\Theta})$. Suppose now that a point $\boldsymbol{x}_* \in \mathfrak{M}$ is given and one wishes to test the null hypothesis H_0 that $\boldsymbol{x}_*$ is not a statistically significant realization of the random vector $\boldsymbol{x}$ (i.e., $\boldsymbol{x}_*$ is a representative draw from $\boldsymbol{x}$). The p-value for a one-sided test is

$$p = \Pr[\boldsymbol{x} \in \Omega_*] = \int_{\Omega_*} \mathrm{e}^{-f(\boldsymbol{x};\boldsymbol{\Theta})/2}\,\mathrm{d}\boldsymbol{x}, \tag{8.3.2}$$

where $\Omega_* = \{\boldsymbol{x} \mid f(\boldsymbol{x};\boldsymbol{\Theta}) > f(\boldsymbol{x}_*;\boldsymbol{\Theta}) \equiv C\}$. Smaller p-values imply that the realization $\boldsymbol{x}_*$ lies farther out on the tails of the PDF (see Figure 8.3.1(a)). The null hypothesis H_0 is rejected at the significance level α (e.g., 0.01) if $p < \alpha$. Figure 8.3.1(b) shows the setup for the analogous two-sided hypothesis test. For a given significance level α, one determines the contours C_L and C_U such that

$$\int_{\Omega_L} \mathrm{e}^{-f(\boldsymbol{x};\boldsymbol{\Theta})/2}\,\mathrm{d}\boldsymbol{x} = \int_{\Omega_U} \mathrm{e}^{-f(\boldsymbol{x};\boldsymbol{\Theta})/2}\,\mathrm{d}\boldsymbol{x} = \frac{1}{2}\alpha,$$

where $\Omega_L = \{\boldsymbol{x} \mid f(\boldsymbol{x};\boldsymbol{\Theta}) < C_L\}$ and $\Omega_U = \{\boldsymbol{x} \mid f(\boldsymbol{x};\boldsymbol{\Theta}) > C_U\}$. (Note that the yellow shaded region in Figure 8.3.1(b) has probability α.) A two-sided test with significance level α rejects the null hypothesis H_0 if $f(\boldsymbol{x}_*;\boldsymbol{\Theta}) < C_L$ or $f(\boldsymbol{x}_*;\boldsymbol{\Theta}) > C_U$.

8.3.2 Examples

Suppose $p_x(\boldsymbol{x};\boldsymbol{\Theta}) = \mathcal{N}(\boldsymbol{x};\boldsymbol{\mu},\mathbf{P})$ (i.e., $\boldsymbol{x}$ is Gaussian) and a realization $\boldsymbol{x}_* \in \mathbb{R}^n$ is given, then

$$f(\boldsymbol{x};\boldsymbol{\Theta}) = -2\ln\mathcal{N}(\boldsymbol{x};\boldsymbol{\mu},\mathbf{P}) = \mathcal{M}(\boldsymbol{x};\boldsymbol{\mu},\mathbf{P}) + \ln\det(2\pi\mathbf{P}),$$

where $\mathcal{M}$ is the Mahalanobis distance (8.2.2). The integration region Ω_* in (8.3.2) is

$$\Omega_* = \{\boldsymbol{x} \in \mathbb{R}^n \mid f(\boldsymbol{x}; \boldsymbol{\Theta}) > f(\boldsymbol{x}_*; \boldsymbol{\Theta})\} = \{\boldsymbol{x} \in \mathbb{R}^n \mid \mathcal{M}(\boldsymbol{x}; \boldsymbol{\mu}, \mathbf{P}) > \mathcal{M}(\boldsymbol{x}_*; \boldsymbol{\mu}, \mathbf{P})\}.$$

Substituting this information into (8.3.2) yields

$$p = \Pr[\boldsymbol{x} \in \Omega_*] = \Pr[\mathcal{M}(\boldsymbol{x}; \boldsymbol{\mu}, \mathbf{P}) > \mathcal{M}(\boldsymbol{x}_*; \boldsymbol{\mu}, \mathbf{P})] = \Pr[\chi^2(n) > \mathcal{M}(\boldsymbol{x}_*; \boldsymbol{\mu}, \mathbf{P})].$$

Thus, the resulting p-value can be computed by evaluating the complementary cumulative distribution function (i.e., tail distribution) of $\chi^2(n)$ at the Mahalanobis distance (8.2.2) evaluated at the realization $\boldsymbol{x}_*$.

The uncertainty realism metric (8.3.1) can also be applied in analogy to the example discussed in Subsection 8.2 on uncertainty propagation. We make the analogous basic assumptions that (i) the orbital state uncertainty is represented by some general PDF (that need not be Gaussian) and is realistic at some initial epoch t_0, and (ii) the truth state $\boldsymbol{x}_{truth}$ is available at some future time $t > t_0$. With these assumptions, we propagate the initial PDF at epoch t_0 to time t yielding the PDF $p_x(\boldsymbol{x}; \boldsymbol{\Theta})$, and evaluate the uncertainty realism metric $\mathcal{U}(\boldsymbol{x}_{truth}; \boldsymbol{\Theta})$ from the definition (8.3.1). Based on some confidence interval of the underlying chi-squared distribution, we might reject the null hypothesis that the propagated PDF "captures the truth"; i.e., $\boldsymbol{x}_{truth}$ is a representative draw from $p_x(\boldsymbol{x}; \boldsymbol{\Theta})$.

8.3.3 Important Remarks

It is important to understand that covariance realism does not always imply uncertainty realism. Said in another way, if one has properly characterized the first two cumulants (i.e., mean and covariance) of the state PDF, then it does not necessarily imply that those two cumulants alone are sufficient for characterizing the full PDF. Consequently, while our proposed tests for uncertainty realism can detect a breakdown in uncertainty realism, such a breakdown does not say anything about the realism of the covariance[¶]. This is a moot point; one needs to strive for uncertainty realism. Henceforth, we will use the terms "uncertainty realism metric" and "uncertainty realism test" exclusively.

8.4 Averaged Uncertainty Realism Metric

As an uncertainty realism metric, one can consider the value of $\mathcal{U}$ (or $\mathcal{M}$ in the Gaussian case), averaged over all orbits or at each time instance (averaged over one or many Monte-Carlo trials, or with real data), together with upper and lower bounds for a particular confidence interval. Specifically, let $\mathcal{U}^{(i)}$ be the uncertainty realism metric (8.3.1) computed in the i-th Monte-Carlo trial. Let k be the total number of independent trials. Then,

$$\bar{\mathcal{U}} \equiv \frac{1}{nk} \sum_{i=1}^{k} \mathcal{U}^{(i)} \sim \frac{1}{nk} \chi^2(nk). \tag{8.4.1}$$

[¶]If one is only interested in testing covariance realism without regard to uncertainty realism, some options are provided by Vallado and Seago [265].

One can test the null hypothesis that the (normalized) average of the samples $\mathcal{U}^{(i)}$, given by $\bar{\mathcal{U}}$, is consistent with the mean of the distribution $\chi^2(nk)/(nk)$. For example, if $n = 6$ and $k = 100$, a two-sided 99.9% confidence interval for the distribution (8.4.1) is $[0.8209, 1.2010]$. Note that this is a necessary (but not sufficient) test of uncertainty realism, and that $\mathbb{E}[\bar{\mathcal{U}}] = 1$. Moreover, $\mathrm{Var}[\bar{\mathcal{U}}] \to 0$, as $k \to \infty$ (i.e., the confidence interval becomes infinitesimally small).

As motivated in Section 8.5, a stronger test for uncertainty realism (in an off-line setting with multiple Monte-Carlo trials) would be to consider the distribution of the Monte-Carlo samples $\mathcal{U}^{(i)}$ and perform a distribution matching or goodness-of-fit test [247]. This test would indirectly consider the consistency of the sample with both the mean and higher-order cumulants of the matching chi-squared distribution. The example below highlights some of the differences between the averaged uncertainty realism metric and metrics based on distribution matching and motivates the need for the latter more powerful tests.

8.4.1 Averaged Uncertainty Realism Metric for the Propagation of Uncertainty

An off-line simulation with multiple Monte-Carlo trials that applies the metric (8.4.1) for assessing uncertainty realism during uncertainty propagation is the following. First, we make the basic assumption that the orbital state uncertainty is identically Gaussian and is realistic at some initial epoch t_0. With this assumption, we perform the following operations:

1. Propagate the Gaussian at epoch t_0 to time t and approximate the propagated uncertainty by a Gaussian with state (mean) $\boldsymbol{\mu}$ and covariance $\mathbf{P}$.
2. Sample random particle states[‖] $\boldsymbol{x}^{(i)}(t_0)$, $i = 1, \ldots, k$, from the initial Gaussian distribution at epoch t_0.
3. Propagate each particle state $\boldsymbol{x}^{(i)}(t_0)$ from time t_0 to time t yielding a propagated particle state $\boldsymbol{x}^{(i)}(t)$.
4. For $i = 1, \ldots, k$, compute $\mathcal{U}^{(i)} = \mathcal{M}\big(\boldsymbol{x}^{(i)}(t); \boldsymbol{\mu}, \mathbf{P}\big)$.
5. Compute the averaged uncertainty realism metric $\bar{\mathcal{U}}$ from (8.4.1) in conjunction with the metrics $\mathcal{U}^{(i)}$ computed in the previous step[**].
6. Perform the hypothesis test described in the text following Equation (8.4.1).

Figure 8.4.1 illustrates the differences between the conclusions one might make when applying the averaged uncertainty realism metric described here and a distribution matching test. If one were to plot a histogram of the Monte-Carlo samples $\mathcal{U}^{(i)}$, it could look like the one shown in the figure. In this example, computing the average of the $\mathcal{U}^{(i)}$ would yield a value of n, in agreement with the expectation of the $\chi^2(n)$ distribution. Consequently, one would be tempted to assert that one has uncertainty realism since the test statistic (i.e., $\bar{\mathcal{U}}$) would lie in the center of any confidence interval. Indeed, consistency of the sample mean

[‖] A random draw $\boldsymbol{x}$ from a multivariate Gaussian with mean $\boldsymbol{\mu}$ and covariance $\mathbf{P}$ can be obtained as follows. Let $\boldsymbol{z}$ be a vector where each component is an independent random draw from the standardized Gaussian (i.e., the Gaussian with mean 0 and variance 1); this functionality is provided in most programming languages and scientific and statistical software. Then, the required $\boldsymbol{x}$ is the vector $\boldsymbol{\mu} + \mathbf{A}\boldsymbol{z}$, where $\mathbf{A}$ is the lower-triangular Cholesky factor [102] of the covariance $\mathbf{P}$ such that $\mathbf{P} = \mathbf{A}\mathbf{A}^T$.

[**] Alternatively or in addition to Steps 5 and 6, one can compute the normalized Pearson test statistic or the Cramér-von Mises test statistic from the $\mathcal{U}^{(i)}$, and perform the corresponding hypothesis tests described in Subsection 8.5.

Figure 8.4.1 Depiction of a distribution matching test. Shown is a histogram of Monte-Carlo trials with the expected $\chi^2(n)$ matching distribution. In this example, the sample mean (e.g., as would be computed from the uncertainty realism test described in Subsection 8.4) is consistent with the expected value of the matching distribution; the sample variance (and higher-order moments) would not be consistent. Thus, a distribution matching test would correctly reject the null hypothesis that the samples come from a $\chi^2(n)$ distribution; a first-order moment (mean) matching test would not.

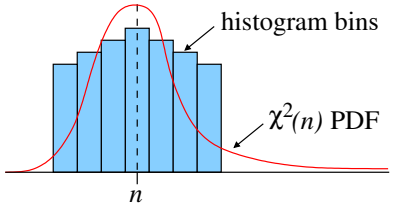

with the expected value of the matching distribution is only a necessary condition for uncertainty realism. Clearly, as the figure shows, the variance (as well as the higher-order moments) of the $\mathcal{U}^{(i)}$ do not match those of the target chi-squared distribution; the histogram is a poor fit. Therefore, a distribution matching test, such as one based on Pearson's test or the Cramér-von Mises test described in the next subsection, is a better test for uncertainty realism in this case.

8.4.2 Averaged Uncertainty Realism Metric and Orbit Determination

The above sections on metrics have focused on the application to the propagation of a Gaussian (covariance realism) and a general probability density function (uncertainty realism). These metrics are often used in several different contexts.

- For a single orbit and real data with fuzzy truth, one can compute the (squared) generalized Mahalanobis distance $\mathcal{U}^{(i)}$ in Equation (8.3.1) for a sequence of orbit updates, i.e., at the times of the sensor report updates, and then apply the average, generalized Mahalanobis distance test 8.4.1.
- Again for a single orbit but in a simulation environment, we can use multiple Monte Carlo runs with different draws of the sensor reports (at the same times) and then proceed as in the previous example.
- Given an ensemble of orbits and truth, one can compute the (squared) generalized Mahalanobis distance $\mathcal{U}^{(i)}$ in Equation (8.3.1) and used the generalized Mahalanobis 8.4.1 for the ensemble.

8.5 Distribution Matching Tests

It is helpful to keep in mind that the purpose of the multivariate PDF is to represent the statistical distribution of the actual state errors. Durable testing of the adequacy of this PDF, therefore, must be an exercise in distribution matching. Said another way, it must be a determination of whether the statistical distribution of a set of state errors, usually calculated by the comparison of state estimates to an externally-determined precision reference orbit, matches to a reasonable degree the distribution represented by the hypothesized multivariate PDF. Testing approaches that do less than this, such as distribution-matching of only a single component of the state error or the testing only for a matching of distribution mean values (as in the averaged

uncertainty realism metric described in Subsection 8.4), render results that can be of some use; but they will not allow a definitive assessment of the realism of the uncertainty. It is thus important to discuss fully-formed methods of uncertainty realism and the particular virtues that they possess so that the advantages and drawbacks of more abbreviated methods can be thrown into relief.

Most multivariate distribution matching approaches proceed by calculating test statistics (e.g., a Mahalanobis distance) that can then be evaluated for conformity to a canonical univariate distribution (e.g., a χ^2 distribution) and thus employ standard goodness-of-fit (GOF) techniques. GOF approaches comprise both specialty tests for a specific distribution type (a number of these, for example, exist for the Gaussian distribution) and more general tests that are capable of evaluating conformity to a number of different distributions. Because covariance realism evaluation usually requires the evaluation of conformity to both the Gaussian and the chi-squared distribution, and because uncertainty realism evaluation can involve testing for conformity to a variety of different distributions (including potentially distributions that have no analytic representation), one should focus on these more fungible techniques, principal among them the traditional chi-squared distribution matching test and the family of empirical distribution function (EDF) tests. An example of the former, Pearson's chi-squared GOF test, is discussed in Subsection 8.5.1, while examples of the latter, including the Kolmogorov-Smirnov, Cramér-von Mises, and Anderson-Darling tests, are described in Subsection 8.5.2. Other possible GOF and EDF tests and our reasons for not using them to assess covariance and uncertainty realism in space surveillance applications are briefly discussed in Subsection 8.5.3.

8.5.1 Pearson's Chi-Squared Goodness-of-Fit Test

Pearson's chi-squared distribution matching test can be considered the most ecumenical in that it can be deployed as a test of conformity to any distribution and can be used for discrete as well as continuous distributions. Further, as a staple of most introductory statistics courses, it has the additional advantage of familiarity to most scientists and engineers. When testing a random sample to see if it can be considered to belong to a hypothesized parent distribution, the basic procedure is to (i) divide up the possible range of values of the random sample into a set of m discrete cells; (ii) determine the number of values that actually fall into each cell and the number that should have fallen into each under the assumed parent distribution; and (iii) compute the chi-squared test statistic (defined below) and compare it to a critical value from the χ^2 distribution. It what follows, we describe these steps in more detail.

Specifically, let $x^{(i)}$, $i = 1, \ldots, k$, denote the observed sample trials. We wish to test the null hypothesis that these observations belong to a particular matching distribution. Suppose the observations $x^{(i)}$ are grouped into m cells or bins where o_j is the number of observations contained in the j-th bin. The *normalized Pearson test statistic* is defined by

$$P_\chi = \frac{1}{m-1-p} \sum_{j=1}^{m} \frac{(o_j - e_j)^2}{e_j}, \tag{8.5.1}$$

where e_j is the expected number of observations contained in j-th bin as determined from the definition of the j-th bin and the properties of the matching distribution. The normalized Pearson test statistic P_χ in (8.5.1) asymptotically approaches the distribution $\chi^2(m-1-p)/(m-1-p)$ where the integer p is the

number of co-variates used in fitting the matching distribution. For example, if the matching distribution is fixed (e.g., to a $\chi^2(6)$ distribution), then $p = 0$. The approximation of P_χ by a chi-squared distribution breaks down if the expected frequencies e_j are too low. One way to ensure that the e_j are sufficiently large (so that the asymptotic property of the Pearson statistic holds) is to choose m "equiprobable" bins so that $e_j = k/m$ for all j. In other words, the bins are of variable width all having the same expected probabilities. One prescription for choosing the number of bins is

$$m = \max(5, \min(100, 0.01k)).$$

We now specialize the framework of this goodness-of-fit test to the case when the observed samples $x^{(i)}$ are $\mathcal{U}^{(i)}$ corresponding to the uncertainty realism metric (8.3.1) of the i-th trial. (Recall that Subsection 8.4.1 provides an example of how the $x^{(i)}$ are generated in an uncertainty propagation scenario.) In both cases, the target matching distribution is $\chi^2(n)$, where n is the dimension of the orbital state space. For sake of example, we take $n = 6$. We define the m bins so that the expected number of observations e_j is k/m for all j. Let $b^{(i)} \in \{1, \ldots, m\}$ denote the bin number in which each observation $x^{(i)}$ belongs. By virtue of the choice of the expected frequencies e_j, these bin numbers can be determined from the cumulative distribution function (CDF) of the matching distribution. For a $\chi^2(6)$ matching distribution, its CDF enjoys a particularly simple form:

$$F(x) = \begin{cases} 1 - \frac{1}{8}\mathrm{e}^{-x/2}(x^2 + 4x + 8), & x > 0, \\ 0, & \text{otherwise.} \end{cases} \tag{8.5.2}$$

It follows that

$$b^{(i)} = \lceil mF(x^{(i)}) \rceil,$$

for $i = 1, \ldots, k$. The number of observations contained in each bin can be readily determined as follows: (i) initialize $o_j = 0$, for $j = 1, \ldots, m$, and (ii) for $i = 1, \ldots, k$, do $o_{b^{(i)}} \leftarrow o_{b^{(i)}} + 1$. Finally, we compute the normalized Pearson test statistic:

$$P_\chi = \frac{1}{m-1} \sum_{j=1}^{m} \frac{(o_j - e_j)^2}{e_j} = \frac{1}{m-1} \sum_{j=1}^{m} \frac{(o_j - k/m)^2}{k/m}.$$

Given a significance level α (typically 0.01 or 0.001), we can derive a one-sided $100(1-\alpha)\%$ confidence interval for the distribution $\chi^2(m-1)/(m-1)$ given by $[0, \chi^2(m-1; 1-\alpha)/(m-1)]$, where $\chi^2(m-1; \beta)$ is the $100\beta\%$ quantile of the distribution $\chi^2(m-1)$. One rejects the null hypothesis that the observed samples $x^{(i)}$ belong to a $\chi^2(6)$ distribution if the normalized Pearson test statistic P_χ computed above falls outside this confidence interval.

8.5.2 Empirical Distribution Function (EDF) Tests

The simplicity and flexibility of the Pearson GOF test make it quite appealing, but it unfortunately harbors considerable disadvantages as well. The first is a relative lack of power when used to test against continuous distributions. Discretizing a continuous distribution by dividing it up into individual cells eliminates some of

Figure 8.5.1 Depiction of the Kolmogorov-Smirnov test. The test statistic, up to a normalization in the sample size k, is the largest deviation between the hypothesized CDF $F(x)$ and the empirical CDF $F_k(x)$, as indicated by the black arrow.

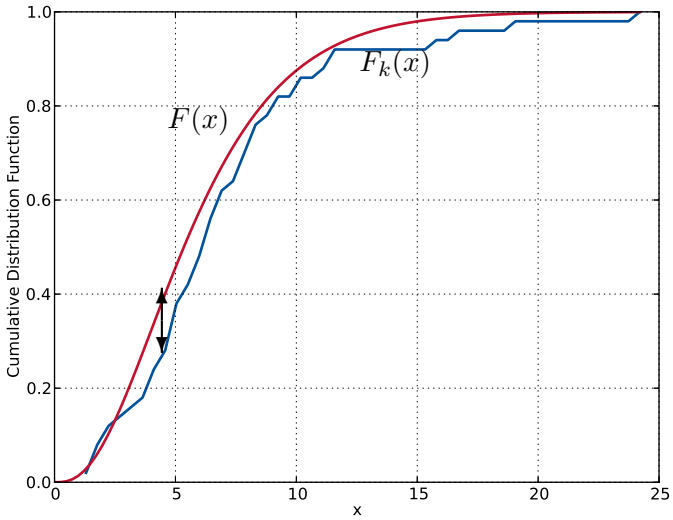

[

the distribution's information; techniques that can preserve continuity will generally render more powerful results. The second is an inherent arbitrariness introduced by the number of cells selected. Certain studies have shown that the test is more powerful when performed with cells sized so as to be equiprobable (as detailed in Subsection 8.5.1), and cell quantities optimized for the use of the test against a hypothesized Gaussian distribution can be recommended [191]. However, there is no set of such recommendations for the general case, with both the test outcomes and the resulting statistical inference affected by different bin quantities and sizes. Given these problems, it is typically best to select other GOF approaches unless one is performing tests against a hypothesized distribution that is natively discrete.

The leading alternative candidate for this type of GOF testing is the family of tests based on the *empirical distribution function (EDF)* of the sample data and the hypothesized distribution. The basic idea here is to (i) calculate the differences between a cumulative distribution function (CDF) for the hypothesized distribution and an empirical CDF (ECDF) for the sample distribution; (ii) encapsulate these differences in terms of a GOF test statistic; and (iii) determine the likelihood, by the use of published p-value tables, that the sample actually could have the hypothesized distribution as a parent. Constructing the CDF for the hypothesized distribution and the ECDF for the sample distribution is straightforward enough; plotting them on the same graph can reveal the differences visually. At this point, there are two different approaches to determining the overall amount of deviation. The supremum approach is to catalog the largest deviation between the hypothesized and empirical result and examine the p-value associated with this large a deviation; this approach is the basis of the *Kolmogorov-Smirnov* test.

In Figure 8.5.2, the hypothesized distribution's CDF $F(x)$ is given in red and the ECDF $F_k(x)$ for the sample is shown in blue. The x-axis is the actual function value, and the y-axis is the cumulative probability. The largest deviation between the hypothesized and empirical CDF is indicated by the arrow. In applying

the Kolmogorov-Smirnov test, one computes this deviation and adjusts it for the sample size k:

$$D_k = \sqrt{k} \sup_x |F_k(x) - F(x)|.$$

One then compares the Kolmogorov-Smirnov test statistic D_k to a table of p-values in order to determine the likelihood that the sample set could have originated from the hypothesized distribution. The formulation of the hypothesis test here is somewhat unusual; the null hypothesis is that the two distributions (hypothesized and sample) are the same. The null hypothesis is rejected for low p-values. This approach is called "weak-hypothesis testing" and is occasionally criticized for being too permissive. Note that it must be remembered that the purpose here is not to identify the true underlying distribution, only to determine whether the hypothesized distribution is a reasonable candidate for a parent distribution of the sample. P-values from 0.1–1% are typically used as the rejection threshold in GOF testing. It is the authors' experience that at this significance level, mismatched distributions are clearly rejected, even with small sample sizes.

The second strain of EDF GOF test approaches are the *quadratic statistics*. These approaches sum up all of the deviations and use this sum as the test statistic. The canonical summation equation is the following:

$$Q_k = k \int_{-\infty}^{\infty} \big[F_k(x) - F(x)\big]^2 \psi(F(x))\, \mathrm{d}F(x). \tag{8.5.3}$$

The weighting factor $\psi(F(x))$ is typically either set to unity to produce the *Cramér-von Mises statistic* or to a function that will give more weight to the tails, such as $\psi(F(x)) = 1/[F(x)(1 - F(x))]$, to produce the *Anderson-Darling statistic*. Testing proceeds in the same way as that described for the Kolgomorov-Smirnov test. The test statistic Q_k is calculated, and tables of p-values are consulted to determine the significance level for the test statistic indicated. A good source for these tables is the monograph of D'Agostino and Stephens [59] on this subject. Tables exist for all of the major distributions (e.g., normal, gamma, chi-squared, von Mises), both as fully-specified distributions ("Case 0") and as distributions in which distribution parameters are represented by estimators ("Cases 1-3").

With regards to assessing uncertainty realism using an EDF test in the context of the example of Subsection 8.4.1, we recommend using a GOF test based on a quadratic statistic rather than the Kolmogorov-Smirnov test. The latter is generally considered less powerful than quadratic tests because it considers only one value (i.e., the largest deviation). Of the two quadratic tests reviewed here, we recommend the Cramér-von Mises test over the Anderson-Darling test because the latter, though usually considered more powerful, is more fragile due to sensitivity of the test on the tails. Specializing (8.5.3) to $\psi(F(x)) = 1$, the resulting Cramér-von Mises test statistic is[††]

$$Q_k = \frac{1}{12k} + \sum_{i=1}^{k} \left[\frac{2i-1}{2k} - F(x^{(i)})\right]^2, \tag{8.5.4}$$

where the $x^{(i)}$, $i = 1, \ldots, k$, are the observed samples in increasing order.

[††] A detailed explanation of the derivation of (8.5.4) from (8.5.3) can be found in the monograph of Darling [60].

8.5.3 Other Distribution Matching Tests

There are a number of additional GOF testing approaches that are common in modern engineering practice that were not pursued here for reasons of both suitability and convenience. The Akaike Information Criterion [43] is an entropy-based approach that has achieved currency for model adequacy assessment. While in some ways it is more powerful than traditional hypothesis testing, its chief drawback is that it can serve only as a comparative test to evaluate the relative performance of two or more models; it cannot give an absolute evaluation, in a p-value sense, of the conformity of the data to any single hypothesized distribution. Regression/correlation GOF tests, such as the well-known Shapiro-Wilk test [239], and moment-based tests, such as the combination third-fourth moment test [58], are very much legitimate GOF tests that often can confer substantial power. However, the ability to deploy them requires certain *a priori* products: for regression tests, it is a set of data weighting coefficients appropriate to the hypothesized distribution; and for moment-based tests, it is the null distributions of those moments for the hypothesized distribution. The present authors were not able to locate published sources for these *a priori* products for the chi-squared distribution, which is one of the principal hypothesized distributions to be tested for the present application. While it may be possible to establish these *a priori* products through private Monte-Carlo studies, this was seen as unnecessary labor when other GOF tests – equally powerful – already exist with the deployment products necessary for the testing of all of the hypothesized distributions presently considered. For this reason, the present collection of GOF test was limited to the traditional Pearson test and the mainstream EDF tests (Kolmogorov-Smirnov, Cramér-von Mises, and Anderson-Darling).

8.5.4 An Example for Orbit Propagation

We now provide an example that tests uncertainty realism in the context of the uncertainty propagation scenario described in Section 8.4.1 and examines the power and effectiveness of the averaged uncertainty realism test, the Pearson goodness-of-fit (GOF) test, and the Cramér-von Mises test. The high-level setup for these tests is as follows [123]. The initial orbital state at epoch describes a high accuracy low Earth orbit (LEO) object; its uncertainty is taken to be Gaussian in the osculating equinoctial orbital element coordinate system. The LEO object state and covariance are propagated using the prediction step of the unscented Kalman filter [157] (UKF); individual sigma points in the UKF are propagated using an implicit Runge-Kutta-based method [12, 13] in conjunction with a 32×32 gravity model and lunar-solar perturbations. A total of 1000 Monte-Carlo trials are used; 10 (equiprobable) bins are defined when applying the Pearson test. Three variations of the scenario are considered which differ only by the choice of coordinate system used to the represent the state and covariance. These coordinate systems are (i) osculating equinoctial orbital elements, (ii) Cartesian position-velocity coordinates, and (iii) J_2 equinoctial orbital elements [10]. For scenarios that use the latter two coordinate systems, the initial state and covariance (defined in the osculating elements as described above) are converted to (and approximated by) a Gaussian in the target coordinate system using the unscented transform*.

*The initial state uncertainty is well-approximated by a single Gaussian in all three coordinate systems, as evidenced in Figure 8.5.4, since the averaged uncertainty realism metric, Pearson test statistic, and Cramér-von Mises test statistic are (approximately) equal at the initial epoch and well within their respective 99.9% confidence intervals.

Figure 8.5.2 Application of the (a) averaged uncertainty realism test, (b) Pearson goodness-of-fit test, and (c) Cramér-von Mises test to an uncertainty propagation scenario in space surveillance. The coordinate system in which the state and covariance are represented is Cartesian position-velocity coordinates **(red)**, osculating equinoctial orbital elements **(green)**, or J_2 equinoctial orbital elements **(blue)**. The 99.9% confidence region is shown in the shaded area. The less-powerful tests in (a) and (b) suggest that uncertainty realism does not break down in osculating element space **(green)** over the entire duration of propagation, whereas the more-powerful Cramér-von Mises test (c) indicates a breakdown after about 90 orbital periods of propagation.

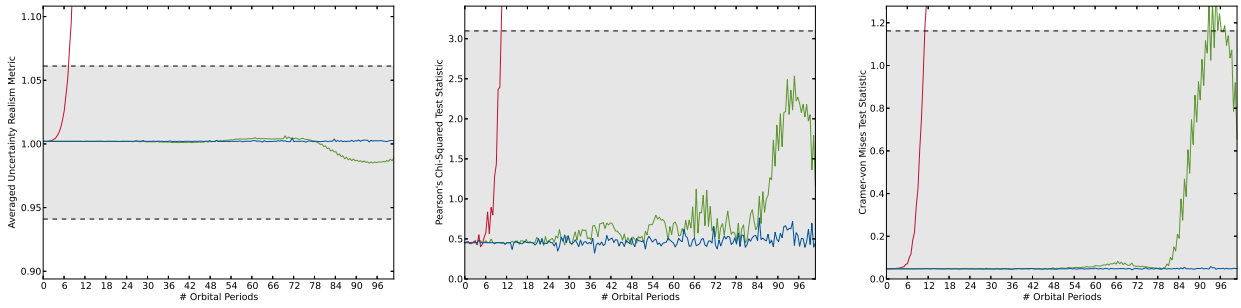

(a) Averaged uncertainty realism test (b) Pearson goodness-of-fit test (c) Cramér-von Mises test

Figure 8.5.4 presents the results of the uncertainty realism tests outlined above. All tests show that uncertainty realism breaks down the fastest when the uncertainty is represented in Cartesian coordinates (see the red curves). This is not surprising since the non-linearity in the dynamics is the greatest in these coordinates, and non-linearity implies that the initial Gaussian density quickly becomes non-Gaussian. In contrast, the osculating equinoctial orbital elements absorb the most dominant term in the non-linear dynamics (i.e., the $1/r^2$ term in the gravity) while, in addition, the J_2 equinoctial elements absorb the J_2 perturbation in the gravity [123]. As such, representing uncertainty in one of these orbital element systems mitigates the departure from "Gaussianity," "extends the life" of the UKF, and preserves uncertainty realism longer. The results inferred from the averaged uncertainty realism metric in Figure 8.5.4(a) are deceptive for the osculating equinoctial case (green curve) and suggest that uncertainty realism is maintained over the entire duration of propagation (since the test statistic fails to pierce the 99.9% confidence interval). The application of the Pearson GOF test in Figure 8.5.4(b), a more powerful test for uncertainty realism, suggests that a breakdown is imminent (in the osculating element case), though the Pearson test statistic is still within the 99.9% confidence interval. On the other hand, the Cramér-von Mises test statistic, plotted in Figure 8.5.4(c), confirms a potential breakdown in uncertainty realism after about 90 orbital periods. By using the J_2 variant of the equinoctial elements to represent uncertainty (blue curve), the Cramér-von Mises test statistic is nearly constant over the entire duration of propagation which strongly suggests that the uncertainty remains Gaussian in such coordinates and its uncertainty (and covariance) realism does not degrade. We also remark that the Cramér-von Mises test tends to produce a smoother (less noisy) test statistic when comparing panels (b) and (c) of Figure 8.5.4 due in part to the test's power, robustness, and the fact that it is "bin agnostic." Clearly, this example shows that first-moment tests such as the averaged uncertainty realism test are not recommended since they have very little determinative power. Pearson's test statistic is an improvement, but it is not to be preferred over the more fungible and powerful Cramér-von Mises test.

A more thorough study of the test described above using a broader range of initial conditions is provided in the paper [123]. Additional methods for non-linear filtering are also evaluated, namely, the prediction

steps of the extended Kalman and Gauss von Mises filters [123, 126, 127], as are different coordinate systems for representing uncertainty.

8.5.5 Distribution Matching Tests for Orbit Determination

The above sections on metrics have focused on the application to the propagation of a Gaussian (covariance realism) and a general probability density function (uncertainty realism). These metrics are often used in several different contexts.

- For a single orbit and real data with fuzzy truth, one can compute the (squared) generalized Mahalanobis distance $\mathcal{U}^{(i)}$ in Equation (8.3.1) for a sequence of orbit updates, i.e., at the time of the sensor report update, and then the Cramér-von Mises test statistic (8.5.3).
- Again for a single orbit but in a simulation environment, we can use multiple Monte Carlo runs with different draws of the sensor reports and then proceed as in the previous example.
- Given an ensemble of orbits, one can compute the (squared) generalized Mahalanobis distance $\mathcal{U}^{(i)}$ in Equation (8.3.1) and use the Cramér-von Mises test statistic (8.5.3) for the ensemble.

8.6 Recommendations

This chapter has defined a number of metrics and statistical tests to assess covariance realism (and more general uncertainty realism) for the propagation of space object state uncertainty as well as orbit determination that additionally enable quantitative comparisons between different approaches. In addition to the use of the squared Mahalanobis distance (8.2.2) and the corresponding "fuzzy truth" version (8.2.3), we have presented a generalized Mahalanobis distance metric (8.3.1) for use with more general probability density functions. These can be used for the *averaged uncertainty realism metric* in Section 8.4 and the *empirical distribution matching metric* for uncertainty realism presented in Section 8.5.2. These metrics are intended for the *aleatoric* uncertainties that can be described in a probabilistic sense. We have not addressed *epistemic uncertainties*. Here are the recommendations.

1. When the orbit determination or uncertainty propagation method produces a Gaussian representation of the state of an object, we recommend the averaged Mahalanobis test, possibly using fuzzy truth, and the Cramér-von Mises test (8.5.3). For more general probability density functions, we recommend the averaged, generalized Mahalanobis test (8.4.1) and the Cramér-von Mises test statistic (8.5.3). Here are some examples of their use.
    - In uncertainty propagation scenarios involving real data with truth on a single object (e.g., a high accuracy orbit) or in off-line simulations with only a few Monte-Carlo trials (between 1 and 10) in which there are insufficient number of samples to perform a more powerful goodness-of-fit (GOF) or distribution matching test, we recommend using the averaged uncertainty realism metric. The use of such a metric provides a necessary condition for uncertainty realism based on the chi-squared property of the computed test statistic.

- In uncertainty propagation scenarios involving real data with truth on multiple objects or in off-line simulations amenable to a large number of Monte-Carlo trials (at least 10), the use of first-moment tests (such as the one based on the averaged uncertainty realism metric) are not recommended due to their limited determinative power. In fact, the application of such tests can lead to deceptive results as demonstrated in Section 8.5.4. Instead, the Cramér-von Mises test is recommended over the Pearson GOF test or the related Anderson-Darling test because the former tends to be more robust and less sensitive to outliers in the tails of the distribution and the number of samples used in the test.
- For a single orbit and real data with possibly fuzzy truth, one can compute the (squared) generalized Mahalanobis distance $\mathcal{U}^{(i)}$ in Equation (8.3.1) for a sequence of orbit updates, i.e., at the time of each sensor report update, and then use the average uncertainty realism test (8.4.1) and the Cramér-von Mises test statistic (8.5.3).
- In a simulation environment wherein one can make multiple Monte Carlo runs with different draws of the sensor reports, one can compute the (squared) generalized Mahalanobis distance $\mathcal{U}^{(i)}$ in Equation (8.3.1) for a sequence of orbit updates, i.e., at the time of each sensor report update, and then use the average uncertainty realism test (8.4.1) and the Cramér-von Mises test statistic (8.5.3) after each sensor report update to the orbit.
- Given an ensemble of orbits, one can compute the (squared) generalized Mahalanobis distance $\mathcal{U}^{(i)}$ in Equation (8.3.1) and use the average uncertainty realism metric (8.4.1) and the Cramér-von Mises test statistic (8.5.3) for the ensemble. In case of real data, a covariance measuring the accuracy of the data is needed.

2. Metrics for *epistemic uncertainties* should be developed.

3. While the metrics proposed in this chapter are applicable for assessing covariance and uncertainty realism during propagation, the sensitivity of each of the four mission areas presented in Chapter 3 to a degraded covariance/uncertainty realism should be investigated. Such an understanding might help set some of the metric parameters and be useful in decision making processes.

Chapter 9

Test Cases

9.1 Propagation of Uncertainty

The purpose of this section is to define an initial hierarchy of test cases, from easy to challenging, that allow one to validate the performance of a particular uncertainty propagation method. In doing so, we propose a variety of states and covariances representative of space objects in different orbital regimes that are used to initialize an uncertainty propagation method under consideration. Following Horwood, Aristoff, Singh, and Poore [123], the actual testing is an off-line process conducted using multiple Monte-Carlo trials and the uncertainty realism metric described in Chapter 8. The uncertainty realism metric evaluations collected over multiple Monte-Carlo trials are then tested for goodness-of-fit using the averaged uncertainty realism test or the Cramér-von Mises criterion, both of which are defined in Chapter 8. Ultimately, the testing allows to one to identify the first instance in time at which uncertainty realism breaks down during uncertainty propagation given a particular set of initial conditions, filter configuration, and choice of coordinate system for representing uncertainty. Full details of this testing procedure are described below.

1. Define an initial state and covariance at time t_0 by selecting one of the scenarios listed in Table 9.1.1.

2. Select a coordinate system in which to represent the uncertainty, such as Cartesian ECI or equinoctial orbital elements (EqOE). If the state and covariance in Step 1 are not in this coordinate system, convert it to the targeted coordinate system using, for example, the unscented transform*.

3. Select an uncertainty propagation method such as the (prediction step of the) EKF, UKF, or GVM filter. (If the GVM filter is selected, then the Gaussian in Step 1 must be converted to a GVM distribution.)

4. Select a particular (deterministic) dynamical model in the form of a system of ODEs (6.1.2) governing two-body dynamics.

5. Select propagation times $t_1, \ldots, t_M$. The final time t_M should be sufficiently large so as to see a breakdown in uncertainty realism. The number of time points M must be sufficiently large so as to

*Even for the low accuracy initial covariances in Table 9.1.2, this transformation does not result in loss of information, as demonstrated in the results of [123].

resolve the time-evolution of the filter performance. A suggested value for the scenarios in Table 9.1.1 is $M = 200$. Note that sampling only at multiples of the orbital period is discouraged.

6. Sample random particle states, $\boldsymbol{x}^{(i)}(t_0)$, $i = 1, \ldots, k$, from the initial PDF defined in Step 1. To provide repeatability, use the same random seed for each test.)

7. For each initial particle state $\boldsymbol{x}^{(i)}(t_0)$, $i = 1, \ldots, k$, use an orbital propagator to generate an ephemeris $\boldsymbol{x}^{(i)}(t_j) = \boldsymbol{\phi}(t_j; \boldsymbol{x}^{(i)}(t_0), t_0)$, for $j = 1, \ldots, M$, where $\boldsymbol{\phi}$ is the solution flow of the dynamical model selected in Step 4.

8. For $j = 1, \ldots, M$:

   (a) Propagate the PDF in Step 1 from time t_0 to t_j using the method selected in Step 3 in conjunction with the dynamical model specified in Step 4.

   (b) For $i = 1, \ldots, k$, evaluate the uncertainty realism metric $\mathcal{U}_j^{(i)}$ as follows.

   - If the propagated PDF in Step 8(a) is represented as a Gaussian, the uncertainty realism metric is the Mahalanobis distance

   $$\mathcal{U}_j^{(i)} = \big(\boldsymbol{x}^{(i)}(t_j) - \boldsymbol{\mu}_j\big)^T \mathbf{P}_j^{-1} \big(\boldsymbol{x}^{(i)}(t_j) - \boldsymbol{\mu}_j\big),$$

   where $\boldsymbol{x}^{(i)}(t_j)$ is obtained from the ephemeris computed in Step 7 and $(\boldsymbol{\mu}_j, \mathbf{P}_j)$ is the mean-covariance pair of the propagated Gaussian obtained from Step 8(a).

   - If the propagated PDF in Step 8(a) is represented as a GVM distribution, the uncertainty realism metric is computed from Equation (7.7.1) where '$(\boldsymbol{x}, \theta)$' is given by $\boldsymbol{x}^{(i)}(t_j)$ (note that θ is the last component in this ephemeris vector) and '$(\boldsymbol{\mu}, \mathbf{P}, \alpha, \boldsymbol{\beta}, \boldsymbol{\Gamma}, \kappa)$' is the parameter set of the propagated GVM distribution obtained from Step 8(a).
   - If the propagated PDF in Step 8(a) is neither a Gaussian nor a GVM distribution, evaluate the general uncertainty realism metric specified by Equation (4) in Chapter 8 where '$\boldsymbol{x}$' is given by $\boldsymbol{x}^{(i)}(t_j)$ and '$\boldsymbol{\Theta}$' is the parameter set of the propagated distribution obtained from Step 8(a).

   (c) Using the samples $\mathcal{U}_j^{(i)}$ computed in Step 8(b), compute the averaged uncertainty realism metric

   $$\bar{\mathcal{U}}_j = \frac{1}{nk} \sum_{i=1}^{k} \mathcal{U}_j^{(i)}$$

   and the Cramér-von Mises test statistic. The definition of the latter is specified by Equation (8.5.3) in Chapter 8.

9. For visualization purposes, plot the averaged uncertainty realism metric $\bar{\mathcal{U}}_j$ and the Cramér-von Mises test statistic versus time t_j.

10. Determine the time when the averaged uncertainty realism metric $\bar{\mathcal{U}}_j$ and the Cramér-von Mises test statistic first pierce a 99.9% confidence interval (or some other confidence interval) and declare that

the uncertainty propagation method has broken down. Construction of the confidence intervals used in these tests are provided Chapter 8.

Table 9.1.1 Initial orbital states, with respect to (osculating) Keplerian orbital elements, used in the uncertainty propagation testing. The state covariances corresponding to the low, medium, and high accuracy cases are listed in Table 9.1.2. Depending on the scenario, the orbit and its uncertainty are propagated for 1, 7, or 30 days, beginning on 1 January 2008.

Scenario	Orbit Type	Orbit Accuracy	a (km)	e	i (°)	Ω (°)	ω (°)	M (°)	Timespan (days)
1	LEO	Low	7136.6	0.00949	72.9	116.0	57.7	105.5	1
2	LEO	Low	7136.6	0.0	0.0	0.0	0.0	0.0	1
3	LEO	High	7136.6	0.00949	72.9	116.0	57.7	105.5	7
4	GEO	Medium	42164.1	0.0	0.0	0.0	0.0	250.0	30
5	HEO	Medium	26628.1	0.742	63.4	120.0	0.0	144.0	7

This testing framework is agnostic to the choice of perturbations in the dynamical model; however, we recommend a model of sufficient fidelity be used in the testing. For each, in the paper [123], the authors used the following forces. For the LEO objects, a degree and order 32 Earth gravity model was used, together with lunar-solar perturbations. For the GEO object, a degree and order 8 Earth gravity model was used, together with lunar-solar perturbations and a nominal solar radiation pressure ballistic coefficient (SRPBC) of 0.1 m^2/kg. For the HEO object, a degree and order 32 Earth gravity model was used, together with lunar-solar perturbations and a nominal SRPBC of 0.1 m^2/kg.

We remark that the testing framework presented here could be augmented by providing an additional metric that assesses the computational requirements of a particular configuration. Although all of the filter, coordinate system, and initial condition combinations considered in the study in Section 7.10 break down at some future time, in principle, one could achieve perfect uncertainty realism indefinitely using, for example, a particle filter or Gaussian sum filter of sufficiently high fidelity. Quantifying the computational demands in terms of runtime would not be preferable due to dependencies on computing architectures or programming languages. Instead, for sigma-point- or particle-based filters such as the UKF, GVM, and mixture filters thereof, we would recommend quantifying the computational performance by the number of particles (or sigma points) required in a single propagation step[†]. This would allow the user to evaluate the merit of a method in its ability to maintain uncertainty realism while at the same time quantifying the computational cost required to do so.

Table 9.1.2 Parameters of the initial covariances used in the uncertainty propagation testing. The orbital state initial conditions are listed in Table 9.1.1. A covariance matrix $\mathbf{P}$ with respect to equinoctial orbital elements is constructed from a row in the table according to $\mathbf{P} = \mathbf{A}\mathbf{A}^T$, where $\mathbf{A} = \mathrm{diag}(\sigma_a, \sigma_h, \sigma_k, \sigma_p, \sigma_q, \sigma_\ell)$. Note that $1'' \doteq 4.848 \cdot 10^{-6}$ radians.

Orbit Accuracy	σ_a (m)	σ_h	σ_k	σ_p	σ_q	σ_ℓ
Low	20000	10^{-3}	10^{-3}	10^{-3}	10^{-3}	$36''$
Medium	2000	10^{-4}	10^{-4}	10^{-4}	10^{-4}	$28''$
High	50	10^{-5}	10^{-5}	10^{-5}	10^{-5}	$20''$

[†]This recommendation is based on the assumption that orbit propagation is the dominant cost in uncertainty propagation. Note that for the EKF prediction step, the dominant cost is due to propagating the mean state vector and the state transition matrix.

9.2 Recommendations

The test cases presented in this chapter are but an initial list and are focused on the propagation of uncertainty. Thus, the recommendations are as follows.

1. A list of test cases should be developed to assist in the evaluation of each of the recommendations in Section 7.16. Presumably this will come from the astrodynamics community and, initially, from the many publications on the propagation of uncertainty.

2. Similarly, a set of test cases for testing the correct uncertainty at epoch should be developed.

Chapter 10

Conclusions

10.1 The Problem Addressed

The purpose of this report has been to delineate the many, but not all, issues that must be addressed if one is to achieve a correct characterization of the uncertainty in the estimated state (e.g., position and velocity) of a space object. As stressed in Chapter 3, this characterization is fundamental to achieving robust SSA functions such as conjunction assessments, data association, maneuver detections, and sensor resource management in the anticipated space environment of the future wherein the automation of these processes will be required. While this report surveys many candidate algorithms for achieving this characterization, the ranking of these algorithms has been specifically avoided in preference for a set of benchmark test cases and metrics to evaluate such algorithms. Only in this way, can a reasonably unbiased conclusion be made.

10.2 Generic Uncertainties

Covariance and uncertainty realism is the proper characterization of the "uncertainty" in the state of an object. Uncertainty realism as defined in Section 2.1 is limited to aleatoric anchorites and is that of having a correct probability density function (PDF) that characterizes the "uncertainty" and "errors" in the state of an object. As such, it generalizes covariance uncertainty which only requires the correct mean and covariance matrix, but not necessarily the higher order moments. In the remainder of this chapter, the term *uncertainty realism* will be used to include both cases of a general PDF and a Gaussian PDF.

The general subject of uncertainty realism is one that is currently an active area of research in the field of "uncertainty quantification" in many areas of science and engineering and one that is briefly outlined in Chapter 2 with references to some of the extensive literature. A *recommendation* (Section 2.2) then is to keep abreast of the developments in this field. The two types of uncertainties treated in this field are called aleatoric and epistemic uncertainties. This report addresses aleatoric uncertainties, i.e., those that can be characterized probabilistically. Thus, a *recommendation* is to investigate the use of epistemic or a mixture of both aleatoric and epistemic in treating uncertainties in astrodynamics.

The general goal of uncertainty realism for space surveillance is that of assessing and rolling up the different "uncertainties" and "errors" into the state of an object at epoch, i.e., the time of the last measurement,

and then propagating this uncertainty to some future time in support of SSA missions, e.g., conjunction assessments, data association, maneuver detection, and sensor resource management discussed in Chapter 5. Such an effort starts with a characterization the parametric and structural uncertainties in the astrodynamics equations of motion in Chapter 4 including the uncertainties in the space environment. Next, sensor level processing produces the sensor reports used in initial or orbit determination. The estimation of the state in the presence of possibly unrealistic uncertainties in the sensor reports is the next step, followed by a propagation of the state and its uncertainty to a future time as required by some SSA missions.

The specific recommendations in the report are contained in the Sections 2.2, 4.3, 5.8, 6.12, 7.16, 8.6, and 9.2. Rather than repeating these recommendations in the chapter-by-chapter order, it may be instructive to briefly re-examine these recommendations from the viewpoint of the generic sources of uncertainty presented in Section 1.1.

10.2.1 Structural Uncertainties

There are two basic approaches to the treatment of *structural uncertainty* in the astrodynamics equations of motion, namely the use of process noise model such as those presented in Section 6.1.1 and an optimal control approach presented in Sections 3.3, 6.2, 6.6, and 6.7. (The use of a controls approach assumes that the data association is correct; otherwise, one might fit the dynamics to two different objects.) These appear to be a fruitful approaches, especially if the two views can augment each other. Astrodynamics models and an enumerated list of uncertainties associated with the equations of motion are presented in Chapter 4 with the recommendations in Section 4.3.

10.2.2 Uncertain Parameters

Parameters are present in the dynamics and measurement equations. Many of the parameters in the dynamics are reviewed in Chapter 4 and methods for treating them within the obit determination process are presented in Section 6.2.2. (The most dominant uncertainties are those of solar radiation pressure and atmospheric drag; a more complete list can be found in Section 4.3.) Some parameters may be estimated, but others may not due to observability issues. In the former case, the parameters are estimated as part of the orbit determination procedure, and the uncertainty in the estimate is incorporated as a consider parameter. In the latter case, one generally should consider the methods of epistemic uncertainties to represent the uncertainty, but aleatoric methods are frequently used as discussed in Section 6.2.2. In addition, there are parameters in the predicted atmospheric density due to a dynamic space weather environment that are required for predicting the state and its uncertainty into the future from the last sensor report, i.e., epoch. (While extensive efforts have been extended to the development of algorithms for propagating structural, parametric, and initial state uncertainties forward in time, having a statistically realistic model for the predicted impacts of space weather is essential to achieving realistic uncertainties in the predicted state for near-earth objects.) The objective in dealing with uncertain parameters is their estimation and ranking of the uncertainties so that at least the most dominant ones are treated. There is much outstanding research in the treatment of these topics including the use of a consider or Schmidt-Kalman filter to better account for the statistical cross correlation between the state and the uncertain parameters, thereby improving the uncertainty in the state.

In the measurement equation that relates the state to the sensor report, the uncertain parameters are generally delineated as sensor biases, navigation errors, and time biases. These are normally treated as part of the calibration process as discussed in the next subsection and more extensively in Chapter 5.

10.2.3 Sensor Measurement Noise

The process of generating sensor reports is a complicated one that could not be fully investigated in this report due to both time and the availability of documents at the Distro-A level; however, improved characterizations of the sensor reports and their uncertainty may well be the biggest contributor to improved covariance and uncertainty realism. For example, a radar may generate reports in the following way. A space object may be detected in the natural intrinsics of the radar, e.g. (r, u, v) measurements, which are then filtered. The filtered state (and hopefully its covariance) is then transformed to a different measurement space such as range, azimuth, and elevation. Such sensor reports are thus highly correlated and the covariances unrealistic. Compounding this problem is that of the different biases including atmospheric, sensor, navigation, and time which can vary with time. Ideally, one would report the different biases, their uncertainties, the sensor measurement and its uncertainties in the intrinsic measurement space. This would potentially offer the best opportunity for treating uncertainty at the sensor level. *Thus, a recommendation is to undertake a program to investigate the potential improvement in the achievement of covariance/uncertainty realism at the sensor level by better processing.* Much more extensive justification for this recommendation can be found in Chapter 5 and, in particular, the short-term to long-term recommendations in Section 5.8.

10.2.4 Inverse Uncertainty Quantification

The inverse problem includes the statistical orbit determination and bias estimation. The estimation of the state of an object and its uncertainty given the sensor reports and astrodynamics models is critical to the propagation of uncertainty. Also included in this subject is the estimation of the sensor, navigation, or time biases given truth objects or fuzzy truth objects (e.g., high accuracy orbits) and the statistical characterization of the uncertainty in these estimates. (An inverse problem is a general framework that is used to convert observed measurements into information about a physical object or system. A bias is a systematic error that does not average out.) A brief synopsis of the estimation techniques used in astrodynamics was presented in Chapter 6 and includes the estimation of the state of an object as well as the sensor, navigation, time, and atmospheric biases in sensor level processing. Of particular note, is the use of empirical covariances as opposed to the theoretical covariances as described in the recommendations in Chapter 6.

10.2.5 Propagation of uncertainty

The propagation of uncertainty in state of an object and its uncertainty through nonlinear dynamics or to transformation through nonlinear functions changes the form of the uncertainty characterization. For example, initially characterized as a Gaussian will become non-Gaussian. Included in this problem is that of predicting the space weather environment in the future.

Coordinate systems discussed briefly in 7.2 are particularly important in the length of time uncertainty can be maintained by a particular filtering method. For example, element spaces absorb the dominant term

in the gravity and thereby make the representation of the dynamics less nonlinear. At least one complete set of algorithms have been developed that start with uncertainty represented in either Cartesian space or element space, represents the uncertainty in element space, propagates sigma points or particles in the inertial Cartesian space, and then transforms the sigma points (or particles) back to element space wherein the uncertainty can be recovered. Next if the uncertainty is required in another coordinate system, a Gaussian sum representation of the uncertainty can be used to transform the uncertainty 7.9. Alternately, one can simply transform the uncertainty in a Cartesian space using an adaptive Gaussian sum representation.

As noted in Chapter 7 this area of uncertainty quantification has been extensively developed with virtually all methods of estimation applied to this problem in astrodynamics. One can consider this as a maturing subject. What is missing are papers on the comparison of the different methods.

While this report does not compare all the methods presented above, the computational results in Section 7.10 indicate the performance advantage of the representation of uncertainty in orbital element space and the performance of the UKF, GVM filter, and Gaussian sums in element space. A more detailed study that uses a common set of metrics and test cases, such as those described in Section 9.1, and applies them to the uncertainty propagation methods reviewed in this chapter should be undertaken in the future. Such comparisons need to be extended to the vast number of methods presented in Chapter 7. To better understand the strengths (and weaknesses) of the above methods, one needs a set of test problems, a set of performance metrics, and a list of test cases that can help evaluate these strengths and weaknesses. While performance metrics are discussed in the next section, here is a list of potential comparisons.

- An assessment of the *range of validity* for each method for propagating uncertainty,
- Time the representation stays within a specified confidence region,
- Performance with and without process noise or stochastic acceleration,
- Performance with and without model mismatch,
- Performance as a function of the size of the initial uncertainty,
- Computational complexity,
- Dependence on the different regimes of space.

In addition to propagation of uncertainty forward in time, the transformation of uncertainty from one coordinate system to another should be considered.

The newer orbital propagators based on implicit Runge-Kutta methods or modified Picard iteration as presented in Section 7.15 are recommended due to their numerical stability properties, efficiency due to large step sizes, adaptability to high performance computing and parallelization, and the ability to propagate an ensemble of orbits needed in the unscented Kalman filter, Gauss-Hermite filters, Gauss von Mises filter, or particle filters.

10.2.6 Algorithmic Uncertainty

Algorithmic or numerical uncertainty comes from numerical errors and numerical approximations in a computer model. An example is the truncation *error* in the orbital propagator, which can be mitigated by adjusting the numerical error tolerance so that the magnitude of the numerical error to ensure that it is below

that of the uncertainty due to the physics or uncertainty in the state of an object. Another example is that of orbit determination in the presence of ill-conditioning.

10.2.7 Cross-tag or Misassociation Uncertainty

Misassociation uncertainty is discrete in nature and is generally characterized through the computation of the probability of association [166, 205]. Cross-tags can degrade the uncertainty in the state of an object and is especially important for closely spaced objects such as GEO clusters, LEO breakups, and tethered satellites.

10.2.8 Hardware and Software Faults/Srrors

These non-algorithm errors are yet another source of uncertainty introduced into the process, but are not addressed in this report.

10.2.9 Extended Body Uncertainties

Extended body uncertainties represent an additional source of uncertainty for *medium to large objects*. For example, an extended body covering several pixels may have an overly optimistic (too small) covariance if the uncertainty of the estimated state only covers the centroid of the body. One must also address the extent of the body, possibly through the use of *feature data* such as multi-band photometry and radiometry. Radar, on the other hand, may receive reflections from multiple point scatterers and the centroided uncertainty may not cover the extent of the body. (We note that the radar cross section (RCS) of an extended object is not well defined. Each point scatterer may have a different RCS. Thus the "object RCS" could be the mean or the maximum of the point scatterers.)

10.3 Metrics

Tests or metrics for evaluating covariance and uncertainty realism are an essential part of evaluating the different methods for generating uncertainty of the propagated state or uncertainty at epoch. The focus of the metrics in this report has been that of the propagated state and should be extended to that of the uncertainty at epoch. In general, when the orbit determination or uncertainty propagation method produces a Gaussian representation of the state of an object, we recommend the averaged Mahalanobis test, possibly using fuzzy truth, and the Cramér-von Mises test (8.5.3). For more general probability density functions, we recommend the averaged, generalized Mahalanobis test (8.4.1) test and the Cramér-von Mises test statistic (8.5.3) as discussed in Chapter 8.

In future work, metrics for evaluating uncertainty at epoch will be required. Furthermore, metrics for *epistemic uncertainties* should be developed. While the above addresses uncertainty realism, the sensitivity of each of the four mission areas presented in Chapter 3 to a degraded uncertainty realism should be investigated in conjunction with the above metrics.. Such an understanding might help set some of the metrics parameters and be useful in decision making processes.

Metrics for evaluating uncertainty at epoch, i.e., the time of the last sensor report should be undertaken; however, this development is probably best made in conjunction with improving uncertainty realism in the sensor reports.

10.4 Some Specific Topics Not Addressed

While this report addresses many of the above sources of uncertainty, it does not address all of those sources listed listed in Section 1.1. Here is such a list plus additional metrics.

- While the subject of *algorithms* is briefly discussed throughout the different sections, there is no in-depth treatment of such algorithms. In particular, there is no comparison between filter/smoothing and batch processing and the corresponding algorithms.
- No attempt is made to address *extended body uncertainties*.
- All of the uncertainties and errors treated in this report are of the aleatoric type. The subject of epistemic and mixtures of epistemic and aleatoric uncertainties should be investigated and addressed in future work. In addition, metrics for epistemic uncertainties will be needed.
- No attempt is made to address *cross-tag or misassociation uncertainty*, which is treated to some extent in Drummond [77].
- Metrics and test cases for the estimate of the state and its uncertainties at epoch have not been specifically addressed, but should be in future work.
- Most of the recommendations require further investigations, tests and evaluations for potential optional approaches. In addition, the report does not provide an estimate of the expected total level of effort in completing the goals and neither addressing potential issues or impact on system interoperability.

10.5 Next Steps

The report offered an analytical survey on covariance and uncertainty realism in space surveillance and a list of recommendations in each technical area for further evaluation of various approaches. It does not give a comprehensive review in addressing and identifying the current (or legacy) operational system and its deficiencies with respect to the expected requirements (current or future) to justify the R&D recommendations listed in the report. This is due in part to the Distro-A requirement. In keeping with this requirement, the audience for this report is a general one.

The recommendations at the end of each chapter are focused on the specific topics in that chapter. Some areas, such as the propagation of uncertainty discussed in Chapter 7, have received much attention in the astrodynamics community and is now maturing, while other fundamentally important areas such as error characterization of the sensor reports in Chapter 5 have received little attention. Hence, this final section is designed to outline what the next steps might be.

A. The first recommended "next step" is that a companion study be undertaken to examine existing system capabilities and known deficiencies in order to establish the basis for undertaking a research and development program and analysis effort. Recommendations coming out of this study should then be made for short, medium, and long term improvements.

B. As noted in Chapter 5, one of the most critical difficulties for operational SSA and space surveillance is that the input sensor reports can be of very limited quantity, quality, and poor distribution. In addition, there can be huge uncertainties in the weather forecast at near-earth altitudes. Yet, there are few publications on these topics. Without key improvements in the error characterization of input data and weather forecasting, most of the research into other aspects of uncertainty quantification in SSA (e.g., propagation of uncertainty) may not give the implied improvement in the overall operational system. An extensive set of recommendation is provided in Section 5.8 for sensor level processing. From a research and development viewpoint, attention to improvements in sensor level processing and space weather prediction models is needed before one can take full advantage of the ongoing research in uncertainty quantification of the orbits.

C. The Committee recommends the development of a repository of benchmark test problems, metrics to evaluate performance, and test results so that the community can make assessments of the developed or proposed algorithms. Since the topic of propagation of uncertainty appears to be maturing, one could start with this topic assuming the covariance or PDF at epoch is realistic.

D. This report has proposed new metrics for the evaluation of uncertainty realism in the propagated state of an object, however, the real test should be that of degraded performance in the aforementioned mission areas in Chapter 3. While some of the sensitivity of these mission to unrealistic covariances has been examined in the literature, the focus of metrics must eventually be that of the impact on the mission areas. Likewise, the sensitivity to unrealistic input data should be undertaken.

E. The development of improved dynamic models is one method of reducing uncertainty in the state of an object and such improvements are certainly to be continued. The emphasis on the use of methods of "uncertainty quantification" represents a shift in the approach to estimating the state and its uncertainty in a given model. The goal here then is to take a given model, to quantify its uncertainty, and to use the uncertainty in support of the mission areas discussed in Chapter 3. The use of optimal control and process noise still offer an opportunity to account for model mismatch and has not yet been fully exploited.

F. Chapter 4 orders the different parameters in the dynamics and space weather in order of their uncertainties. A more extensive survey of the literature should be undertaken with recommended directions of development. It is anticipated that a future report on *New Methods of Reentry Modeling* will considerably expand the topic of uncertainty quantification of reentering objects.

G. A conference or special session in one of the astrodynamics conferences should be scheduled to discuss the pressing problem of achieving uncertainty realism in SSA.

Acknowledgements

This paper was produced under the sponsorship of the Air Force Space Command Astrodynamics Innovation Committee; however, the views in this paper represent those of the authors and not of the US Government. We wish to thank the following authors for their contributions to the report: William Cerven (Section 6.8.2), Yang Cheng (Section 7.12), Christopher Cox (Chapter 5), Richard Erwin (Section 3.4), Joseph Frisbee (Section 6.8.1), Matt Hejduk (Section 3.1 and Chapter 8), Brandon Jones (Sections 7.11 and 6.11), Daniel Scheeres and Dan Lubey (Section 3.3), David Vallado (Chapter 4), and Ryan Weisman (Sections 6.9, 7.9, 7.13). Aubrey Poore, Jeffrey Aristoff, and Joshua Horwood (Chapters 1, 2, 8, 9 and Sections 3.2, 6.1-6.7, 6.12, 7.1 - 7.10, 7.16) wrote and edited the remainder of the report and accept responsibility for its content. The Committee also wishes to thank six referees for their considerable input, which we believe considerably improved the report.

Symbols, Abbreviations, and Acronyms

The following provides a glossary for symbols, abbreviations, and acronyms.

AFRL Air Force Research Laboratory

ASAT anti-satellite

CBTA covariance based track association

CCD charge-coupled device

CDF cumulative distribution function

CIO celestial intermediate origin

DA differential algebra

DC differential correction

DCP dynamic consider parameter

DMC dynamic model compensation

ECDF empirical cumulative distribution function

ECI Earth centered inertial

EDF empirical distribution function

EKF extended Kalman filter

EO electro-optical

EOP Earth orientation parameters

EUV extreme ultraviolet

FISST finite set statistics

FPKE Fokker-Planck-Kolmogorov equation

GCRF geocentric celestial reference frame

GEO geostationary orbit

GOF goodness of fit

GMST Greenwich mean sidereal time

GVM Gauss von Mises

HASDM high accuracy satellite drag model

HBR hard body radius

HEO highly elliptical orbit

IAU International Astronautical Union

IERS International Earth Rotation and Reference Systems Service

ITRF International terrestrial reference frame

IOD initial orbit determination

IMM interacting multiple model

JPDA joint probabilistic data association

JSC Johnson Space Center

JSpOC Joint Space Operations Center

LEO low Earth orbit

MAP maximum a posteriori

MEO medium Earth orbit

MFA Multiple Frame Assignments

MHT Multiple Hypothesis Tracking

ML maximum likelihood

MMSE Minimum Mean Squared Error

NASA National Aeronautics and Space Administration

NASA/GSFC NASA Goddard Space Flight Center

OD orbit determination

PC polynomial chaos

$\mathbf{P_C}$ probability of collision

PDF Probability Density Function

PMF Probability Mass Function

$\mathbf{R}_\oplus$ radius of the Earth

RSO resident space object

RMS root mean square

SDE stochastic differential equation

SOEKF second order extended Kalman filter

SP Special Perturbations

SSA space situational awareness The requisite current and predictive knowledge of the space environment and the operational environment upon which space operations depend as well as all factors, activities, and events of friendly and adversary space forces across the spectrum of conflict.

SRP solar radiation pressure

SSN space surveillance network

STSS space tracking surveillance system

UKF unscented Kalman filter

QMU quantification of margins and uncertainties

TAI temps atomique international (international atomic time)

TCA time of closest approach

TT terrestrial time

UQ uncertainty quantification

UTC universal time coordinated

V&V verification and validation

Bibliography

[1] Joint publication 3-14: Space operations. http://www.dtic.mil/doctrine/new_pubs/jp3_14.pdf, May 2013.

[2] B. S. Aaron. *Geosynchronous Satellite Maneuver Detection and Orbit Recovery Using Ground Based Optical Tracking*. PhD thesis, Department of Aerospace Engineering, Massachusetts Institute of Technology, Cambridge, MA, 2006.

[3] AIAA. Guide for the verification and validation of computational fluid dynamics simulations. Technical report, American Institute for Aeronautics and Astronautics, Reston, VA, 1998. Paper AIAA G-077-1998e.

[4] S. Alfano. A numerical implementation of spherical object collision probability. *Journal of the Astronautical Sciences*, 53:103–109, 2005.

[5] Salvatore Alfano. Relating position uncertainty to maximum conjunction probability. *The Journal of the Astronautical Sciences*, 53(2):193–205, April-June 2005.

[6] K. T. Alfriend. A dynamic algorithm for UCT processing. In *Proceedings of the AAS/AIAA Astrodynamics Specialist Conference*, Sun Valley, ID, 1997. Paper AAS 97-607.

[7] D. Alspach and H. Sorenson. Nonlinear Bayesian estimation using Gaussian sum approximations. *IEEE Transactions on Automatic Control*, 17(4):439–448, 1972.

[8] B. D. O. Anderson and S. B. Moore. *Optimal Filtering*. Prentice Hall, 1979.

[9] R. L. Anderson, G. H. Born, and J. M. Forbes. Sensitivity of orbit predictions to density variability. *J. Spacecraft and Rockets*, 46:1214–1230, 2009.

[10] J. M. Aristoff, J. T. Horwood, and K. T. Alfriend. On a set of j_2 equinoctial orbital elements. in preparation, 2016.

[11] J. M. Aristoff, J. T. Horwood, and A. B. Poore. Implicit Runge-Kutta methods for uncertainty propagation. In *Proceedings of the 2012 Advanced Maui Optical and Space Surveillance Technologies Conference*, Wailea, HI, September 2012.

[12] J. M. Aristoff, J. T. Horwood, and A. B. Poore. Orbit and uncertainty propagation: a comparison of Gauss-Legendre-, Dormand-Prince-, and Chebyshev-Picard-based approaches. *Celestial Mechanics and Dynamical Astronomy*, 118:13–28, 2014.

[13] J. M. Aristoff, J. T. Horwood, and A. B. Poore. Realistic state and measurement error uncertainty

computation. AFOSR Final Scientific and Technical Report FA9550-12-C-0034, Numerica Corporation, February 2014.

[14] J. M. Aristoff, J. T. Horwood, and A. B. Poore. Implicit Runge-Kutta-based methods for fast, precise, and scalable uncertainty propagation. *Celestial Mechanics and Dynamical Astronomy*, 122:169–182, 2015.

[15] J. M. Aristoff, J. T. Horwood, N. Singh, and A. B. Poore. Error estimation and control for efficient and reliable orbit (and uncertainty) propagation. In *Proceedings of the 24th AAS/AIAA Space Flight Mechanics Meeting*, Santa Fe, NM, January 2014. Paper AAS 14-346.

[16] J. M. Aristoff, J. T. Horwood, N. Singh, and A. B. Poore. Non-linear uncertainty propagation in orbital elements and transformation to Cartesian space without loss of realism. In *Proceedings of the 2014 AAS/AIAA Astrodynamics Specialist Conference*, San Diego, CA, August 2014.

[17] J. M. Aristoff, J. T. Horwood, N. Singh, A. B. Poore, C. Sheaff, and M. K. Jah. Multiple hypothesis tracking (MHT) for space surveillance: theoretical framework. In *Proceedings of the 2013 AAS/AIAA Astrodynamics Specialist Conference*, Hilton Head, SC, August 2013. Paper AAS 13-705.

[18] R. Armellin, P. Di Lizia, F. Bernelli-Zazzera, and M. Berz. Asteroid close encounters characterization using differential algebra: the case of apophis. *Celestial Mechanics and Dynamical Astronomy*, 107:451–470, 2010.

[19] N. Arora and R. P. Russell. Efficient interpolation of high-fidelity geopotentials. *Journal of Guidance, Control, and Dynamics*, 2015. (To Appear).

[20] N. Arora, V. Vittaldev, and R. P. Russell. Parallel computation of multiple space trajectories using gpus and interpolated gravity models. *Journal of Guidance, Control, and Dynamics*, 2015.

[21] M. S. Arulampalam, S. Maskell, N. Gordon, and T. Clapp. A tutorial on particle filters for online nonlinear/non-Gaussian Bayesian tracking. *IEEE Transactions on Signal Processing*, 50(2):174–185, February 2002.

[22] X. Bai and J. L. Junkins. Modified Chebyshev-Picard iteration methods for orbit propagation. *Journal of Astronautical Sciences*, 3:1–27, 2011.

[23] M. Balducci, B. A. Jones, and A. Doostan. Orbit uncertainty propagation with separated representations. In *Proceedings of the 2013 AAS/AIAA Astrodynamics Specialist Conference*, Hilton Head, SC, August 2013. Paper AAS 13-870.

[24] Y. Bar-Shalom and K. Birmiwal. Variable dimension filter for maneuvering target tracking. *Aerospace and Electronic Systems*, 18(5):621–629, 1982.

[25] Y. Bar-Shalom, X. R. Li, and T. Kirubarajan. *Estimation with Applications to Tracking and Navigation*. John Wiley & Sons, New York, 2001.

[26] D. K. Barton and H. R. Ward. *Handbook of Radar Measurement*. Prentice Hall, Englewood Cliffs, NJ, December 1969.

[27] B. R. Bean and E. J. Dutton. Radio meteorology. Technical Report Monograph 92, National Bureau

of Standards, March 1966.

[28] B. M. Bell. The iterated Kalman smoother as a Gauss-Newton method. *SIAM Journal of Optimization*, 4(3):626–636, 1994.

[29] B. M. Bell and F. W. Cathey. The iterated Kalman filter update as a Gauss-Newton method. *IEEE Transactions on Automatic Control*, 38:294–297, 1993.

[30] J. Z. Ben-Asher and D. Cohen. Allocation of radar tracking resources by direct optimization. *Journal of Aerospace Computing, Information, and Communication*, 6:523–539, September 2002.

[31] M. Berry and L. Healy. The generalized Sundman transformation for propagation of high-eccentricity elliptical orbits. In *Proceedings of the 12th AAS/AIAA Space Flight Mechanics Meeting*, San Antonio, TX, January 2002. Paper AAS-02-109.

[32] M. M. Berry and L. M. Healy. Implementation of Gauss-Jackson integration for orbit propagation. *Journal of the Astronautical Sciences*, 52(3):331–357, 2004.

[33] D. P. Bertsekas. Incremental least squares methods and the extended Kalman filter. *SIAM Journal of Optimization*, 6:807–822, 1996.

[34] D. P. Bertsekas. *Dynamic Programming and Optimal Control*. Athena Scientific, Belmont, MA, 2000.

[35] M. Berz. *Modern Map Methods in Particle Beam Physics*. Academic Press, 1999.

[36] G. Beylkin and K. Sandberg. ODE solvers using bandlimited approximations. *Journal of Computational Physics*, 265:156–171, 2014.

[37] S. Blackman. Multiple hypothesis tracking for multiple target tracking. *IEEE A&E Systems Magazine*, 19(1):5–18, January 2004.

[38] S. Blackman and R. Popoli. *Design and Analysis of Modern Tracking Systems*. Artech House, Boston, 1999.

[39] B. K. Bradley, B. A. Jones, G. Beylkin, and P. Axelrad. A new numerical integration technique in astrodynamics. In *Proceedings of the 22nd Annual AAS/AIAA Spaceflight Mechanics Meeting*, Charleston, SC, January 2012. Paper AAS-12-216.

[40] B. K. Bradley, B. A. Jones, G. Beylkin, K. Sandberg, and P. Axelrad. Band-limited implicit Runge-Kutta integration for astrodynamics. *Celestial Mechanics and Dynamical Astronomy*, 119(2):143–168, 2014.

[41] B. K. Bradley, D. A. Vallado, A. Sibois, and P. Axelrad. Earth orientation parameter considerations for precise spacecraft operations. In *Proceedings of the 2011 AAS/AIAA Astrodynamics Specialist Conference*, Girdwood, AK, July 2011.

[42] D. Brouwer. Solution of the problem of artificial satellite theory without drag. *Astronomical Journal*, 64(1274):378–396, 1959.

[43] K. P. Burnham and D. R. Anderson. *Model Selection and Multimodel Inference*. Springer, New York, 2002.

[44] J. C. Butcher. *Numerical Methods for Ordinary Differential Equations*. John Wiley & Sons, West Sussex, England, 2008.

[45] N. Capitaine, P. T. Wallace, and J. Chapront. Expressions for IAU 2000 precession quantities. *Astronomy and Astrophysics*, 412:567–586, 2003.

[46] S. Casotto. Gaussian initial orbit determination in universal variables. In *Proceedings of the 25th AAS/AIAA Space Flight Mechanics Meeting*, Williamsburg, VA, 2015. Paper AAS 15-368.

[47] W. T. Cerven. Covariance error assessment, correction, and impact on probability of collision. In *Proceedings of the 2011 AAS/AIAA Space Flight Mechanics Meeting*, New Orleans, LA, February 2011.

[48] W. T. Cerven. Improved empirical covariance estimation. In *Proceedings of the 2013 AAS/AIAA Astrodynamics Specialist Conference*, Hilton Head, SC, August 2013.

[49] F. K. Chan. *Spacecraft Collision Probability*. Aerospace Press, El Segundo, CA, 2008.

[50] Y. T. Chan, A.G.C. Hu, and J. B. Plant. A Kalman filter based tracking scheme with input estimation. *Aerospace and Electronic Systems*, 15(2):237–244, 1979.

[51] Y. Cheng, K. J. DeMars, C. Fruh, and M. K. Jah. Gaussian mixture PHD filter for space object tracking. In *Proceedings of the 2013 AAS/AIAA Space Flight Mechanics Meeting*, Kauai, HI, February 2013.

[52] Y. Cheng, Y. Tian, and J. L. Crassidis. Extension of the sparse grid quadrature filter. In *17th International Conference on Information Fusion*, Salamanca, Spain, July 2014. Paper 372.

[53] J. Choi. Performance comparison of tropospheric propagation models: Ray-trace analysis results using worldwide tropospheric databases. Technical Report NRL/FR/8140–97-9857, Naval Research Laboratory, Washington, DC 20375-5320, September 1997.

[54] Committee. *Assessing the Reliability of Complex Models: Mathematical and Statistical Foundations of Verification, Validation, and Uncertainty Quantification*. National Academy of Sciences., THE NATIONAL ACADEMIES PRESS, 500 Fifth Street, NW Washington, DC 20001, 2012.

[55] J. L. Crassidis and J. L. Junkins. *Optimal Estimation of Dynamic Systems*. Applied Mathematics and Nonlinear Science Series. Chapman and Hall/CRC, 2nd edition, October 2010.

[56] D. Crisan and B. Rozovskii, editors. *The Oxford Handbook of Nonlinear Filtering*. Oxford Handbooks in Mathematics. Oxford University Press Inc., Oxford, February 2011.

[57] R. I. Cukier, H. B. Levine, and K. E. Shuler. Nonlinear sensitivity analysis of multiparameter model systems. *Journal of Computational Physics*, 26(1):1–42, 1978.

[58] R. D'Agostino and E. S. Pearson. Tests for departure from normality: empirical results for the distributions of b_2 and $(b_1)^{1/2}$. *Biometrika*, 60(3):613–622, 1973.

[59] R. B. D'Agostino and M. A. Stephens. *Goodness-of-Fit Techniques*. Marcel Dekker, New York, 1986.

[60] D. A. Darling. The Kolmogorov-Smirnov, Cramér-von Mises tests. *Annals of Mathematical Statistics*,

28(4):823–838, 1957.

[61] K. DeMars, R. Bishop, and M. K. Jah. An entropy-based approach for uncertainty propagation of non-linear dynamical systems. *Journal of Guidance, Control, and Dynamics*, 36(4):1047–1057, 2013.

[62] K. DeMars, M. K. Jah, D. Giza, and T. Kelecy. Orbit determination performance improvements for high area-to-mass ratio space object tracking using an adaptive Gaussian mixtures estimation algorithm. In *Proceedings of the 21st International Symposium on Space Flight Dynamics*, Toulouse, France, 2009.

[63] K. J. DeMars. *Nonlinear orbit uncertainty prediction and rectification for space situational awareness*. PhD thesis, University of Texas at Austin, 2010.

[64] K. J. DeMars, R. H. Bishop, and M. K. Jah. A splitting Gaussian mixture method for the propagation of uncertainty in orbital mechanics. In *Proceedings of the 21st AAS/AIAA Space Flight Mechanics Meeting*, New Orleans, LA, February 2011. Paper AAS-11-201.

[65] K. J. DeMars, Y. Cheng, and M. K. Jah. Collision probability with Gaussian mixture orbit uncertainty. *Journal of Guidance, Control and Dynamics*, 2014.

[66] K. J. DeMars, I. I. Hussein, M. K. Jah, and R. S. Erwin. The Cauchy-Schwarz divergence for assessing situational information gain. In *15th International Conference on Information Fusion*, Singapore, July 2012.

[67] K. J. DeMars, M. K. Jah, Y. Cheng, and R. H. Bishop. Methods for splitting Gaussian distributions and applications within the AEGIS filter. In *Proceedings of the 22nd AAS/AIAA Space Flight Mechanics Meeting*, Charleston, SC, February 2012. Paper AAS-12-261.

[68] K. J. DeMars, M. K. Jah, and P. W. Schumacher. The use of short-arc angle and angle rate data for deep-space initial orbit determination and track association. In *Proceedings of the Eighth US/Russian Space Surveillance Workshop*, Wailea, HI, October 2009.

[69] DoD. Verification, validation, and accreditation recommended practices guide. http://www.dmso.mil/docslib, 1996.

[70] A. Doostan and G. Iaccarino. A least-squares approximation of partial differential equations with high-dimensional random inputs. *Journal of Computational Physics*, 228(12):4332–4345, July 2009.

[71] A. Doostan and H. Owhadi. A non-adapted sparse approximation of PDEs with stochastic inputs. *Journal of Computational Physics*, 230(8):3015–3034, April 2011.

[72] A. Doostan, A. A. Validi, and G. Iaccarino. Non-intrusive low-rank separated approximation of high-dimensional stochastic models. *Computation Methods in Applied Mechanical Engineering*, 263:42–55, August 2013.

[73] A. Doucet, N.F. Freitas, N. Gordon, and A. Smith. Sequential Monte Carlo methods in practice. In *Statistics for Engineering and Information Sciences*. Springer, 2001.

[74] O. E. Drummond. Track covariance compensation for data misassociations: alternative data association algorithms. In O. E. Drummond, editor, *SPIE Signal and Data Processing of Small Targets 2008*,

volume 6969, Orlando, FL, 2008.

[75] O. E. Drummond, A. J. Perrella Jr., and S. Waugh. On target track covariance consistency. In *Proceedings of SPIE Conference on Signal and Data Processing of Small Targets*, volume 6236, 2006.

[76] O. E. Drummond, T. L. Ogle, and S. Waugh. Metrics for evaluating track covariance consistency. In O. E. Drummond and R. D. Teichgraeber, editors, *Signal and Data Processing of Small Targets 2007*, volume 6699, page 669916, San Diego, CA, 2007.

[77] O. E. Drummond, A. J. Perrella, Jr., and S. Waugh. On target track covariance consistency. In *SPIE Proceedings: Signal and Data Processing of Small Targets 2006*, volume 6236, page 623615, 2006.

[78] J. Durbin and M. Knott. Components of Cramér-von Mises statistics I. *Journal of the Royal Statistical Society Series B*, 34(2):290–307, 1972.

[79] A. El-Fallah, A. Zatezalo, R. Mahler, R. K. Mehra, and M. Alford. Unified Bayesian situation assessment sensor management. In *SPIE Proceedings*, volume 5809, pages 253–264, 2005.

[80] A. El-Fallah, A. Zatezalo, R. Mahler, R. K. Mehra, and J. Brown. Sensor management of space-based multiplatform EO/IR sensors for tracking geosynchronous satellites. In *SPIE Proceedings*, volume 7336, pages 73360H–73360H–12, 2009.

[81] A. El-Fallah, A. Zatezalo, R. Mahler, R. K. Mehra, and D. Donatelli. Dynamic sensor management of dispersed and disparate sensors for tracking resident space objects. In *SPIE Proceedings*, volume 6968, pages 69680P–69680P–11, 2008.

[82] A. I. El-Fallah, R. P. S. Mahler, T. Zajic, E. Sorensen, M. G. Alford, and R. K. Mehra. Scientific performance evaluation for sensor management. In *SPIE Proceedings*, volume 4052, pages 183–194, 2000.

[83] J. T. Emmert. Thermospheric mass density: A review. *Advances in Space Research*, 2015.

[84] John Emmert, Jeff Byers, Harry Warren, and Alan Segerman. Propagation of forecast errors from the sun to leo trajectories: How does drag uncertainty affect conjunction frequency? In *Proceedings of the 2014 Advanced Maui Optical and Space Surveillance Technologies Conference*, Wailea, HI, September 2014. AFRL.

[85] R. S. Erwin, P. Albuquerque, S. K. Jayaweera, and I. I. Hussein. Dynamic sensor tasking for space situational awareness. In *Proceedings of the 2010 American Control Conference*, pages 1153 – 1158, Baltimore, MD, June 2010.

[86] P. R. Escobal. *Methods of Orbit Determination*. John Wiley & Sons, 1965.

[87] D. Finkleman, K. Seidelmann, and J. Seago. The debate over UTC and leap seconds. In *Proceedings of the 2010 AAS/AIAA Astrodynamics Specialist Conference*, Toronto, Canada, August 2010. Paper AIAA 2010-8391.

[88] R. Fletcher. *Practical Methods of Optimization*. John Wiley & Sons, 1991.

[89] Z. J. Folcik, P. J. Cefola, and R. I. Abbot. GEO maneuver detection for space situational awareness.

Advances in Astronautical Sciences, 129, 2007.

[90] J. L. Foster. The analytic basis for debris avoidance operations for the international space station. In *Proceedings of the Third European Conference on Space Debris*, Darmstadt, Germany, March 2001.

[91] J. L. Foster and H. S. Estes. A parametric analysis of orbital debris collision probability and maneuver rate for space vehicles. Technical Report 25898, NASA/JSC, August 1992.

[92] J. L. Foster and J. H. Frisbee Jr. Position error covariance matrix scaling factors for early operational ISS debris avoidance. Technical Report DM33, Johnson Space Center, May 1998.

[93] P. Frazier, W. B. Powell, and S. Dayakin. A knowledge gradient policy for sequential information collection. *SIAM Journal of Control and Optimization*, 47:2410 – 2439, 2008.

[94] E. M. Gaposchkin. Calculation of satellite drag coefficients. Technical Report 998, MIT Lincoln Laboratory, Lexington, MA, 1994.

[95] S. Gehly, B. A. Jones, and P. Axelrad. Comparison of multitarget filtering methods as applied to space situational awareness. In *Proceedings of the 2013 AAS/AIAA Astrodynamics Specialist Conference*, Hilton Head, SC, August 2013. Paper AAS 13-765.

[96] A. Gelb. *Applied Optimal Estimation*. M.I.T. Press, London, 1974.

[97] R. G. Ghanem. Ingredients for a general purpose stochastic finite elements implementation. *Computer Methods in Applied Mechanics and Engineering*, 168(1-4):19–34, January 1999.

[98] R. G. Ghanem and P. D. Spanos. *Stochastic Finite Elements: A Spectral Approach*. Springer-Verlag, New York, 1991.

[99] R. W. Ghrist and D. Plakalovic. Impact of non-Gaussian error volumes on conjunction assessment risk analysis. In *Proceedings of the 2012 AAS/AIAA Astrodynamics Specialist Conference*, Minneapolis, MN, August 2012.

[100] D. R. Giza, P. Singla, J. L. Crassidis, R. Linares, P. J. Cefola, and K. Hill. Entropy-based space object data association using an adaptive Gaussian sum filter. In *Proceedings of the 2010 AIAA/AAS Astrodynamics Specialist Conference*, Toronto, Canada, August 2010. Paper AIAA-2010-7526.

[101] H. Goldstein, C. Poole, and J. Safko. *Classical Mechanics*. Addison Wesley, San Francisco, CA, 3rd edition, 2002.

[102] G. Golub and C. Van Loan. *Matrix Computations*. John Hopkins University Press, Baltimore, MD, 1996.

[103] R. H. Gooding. A new procedure for the solution for the classical problem of minimal orbit determination from three lines of sight. *Celestial Mechanics and Dynamical Astronomy*, 66(1):387–423, 1997.

[104] B. Grocholsky. *Information-Theoretic Control of Multiple Sensor Platforms*. PhD thesis, University of Sydney, Sydney, Australia, 2002.

[105] JMS Numerical Validation Working Group. JMS high accuracy catalog orbit determination (OD) and prediction numerical validation (NumVal) plan phase 1. Technical report, AFSPC, February 2013.

[106] P. Gurfil, editor. *Modern Astrodynamics*. Elsevier Astrodynamics Series, 2006.

[107] E. Hairer, S. P. Norsett, and G. Wanner. Solving ordinary differential equations I: Nonstiff problems. In *Springer Series in Computational Mathematics*. Springer, 2nd edition, 2009.

[108] E. Hairer and G. Wanner. Solving ordinary differential equations II: Stiff and differential-algebraic problems. In *Springer Series in Computational Mathematics*. Springer, 2nd edition, 2010.

[109] T. Hanselmann, M. Morelande, B. Moran, and P. Sarunic. Sensor scheduling for multiple target tracking and detection using passive measurements. In *Proceedings of the 11th International Conference on Information Fusion*, pages 1–8, June 2008.

[110] W. Hatch and C. Goad. Mathematical description of the oran error analysis program. Technical Report Planetary Sciences Department Report No. 009-73, Wolf Research and Development Corporation, 1973.

[111] M. D. Hejduk. Covariance calibration tool: Independent evaluation. NASA/GSFC Flight Dynamics Support Services Technical Report FDSS-21-0202, NASA Goddard Spaceflight Center, March 2014.

[112] S. M. Herman and A. B. Poore. Nonlinear least-squares estimation for sensor and navigation biases. In *SPIE Proceedings: Signal and Data Processing of Small Targets*, volume 6236, 2006.

[113] A. O. Hero, D. Castañón, D. Cochran, and K. Kastella. *Foundations and Applications of Sensor Management*. Springer, New York, 2008.

[114] K. Hill, K. T. Alfriend, and C. Sabol. Covariance-based uncorrelated track association. In *Proceedings of the 2008 AAS/AIAA Astrodynamics Conference*, Honolulu, HI, August 2008. Paper AIAA 2008-7211.

[115] K. Hill, C. Sabol, and K. T. Alfriend. Comparison of covariance-based track association approaches with simulated radar data. In *Proceedings of the 2010 AAS Kyle T. Alfriend Astrodynamics Symposium*, Monterey, CA, May 2010. Paper AAS-10-318.

[116] K. Hill, C. Sabol, and K. T. Alfriend. Nonlinear effects in the correlation of tracks and covariance propagation. *Acta Astronautica*, 84:69–80, 2013.

[117] K. Hill, P. Sydney, K. Hamada, R. Cortez, K. Luu, and M. K. Jah. Covariance based scheduling of a network of sensors. In *Proceedings of the 2010 AAS Kyle T. Alfriend Astrodynamics Symposium*, Monterey, CA, May 2010.

[118] D. Hitchings and D.A. Castañón. Receding horizon stochastic control algorithms for sensor management. In *Proceedings of the 2010 American Control Conference*, pages 6809–6815, June 2010.

[119] G.M. Hoffmann, S.L. Waslander, and C.J. Tomlin. Mutual information methods with particle filters for mobile sensor network control. In *Proceedings of the 45th IEEE Conference on Decision and Control*, pages 1019–1024, December 2006.

[120] M. J. Holzinger, D. J. Scheeres, and K. T. Alfriend. Object correlation, maneuver detection, and characterization using control distance metrics with uncertain systems. *Journal of Guidance, Control and Dynamics*, 35(4):1312–1325, July 2012.

[121] J. T. Horwood, N. D. Aragon, and A. B. Poore. A Gaussian sum filter framework for space surveillance. In *SPIE Proceedings: Signal and Data Processing of Small Targets*, volume 8137, 2011.

[122] J. T. Horwood, N. D. Aragon, and A. B. Poore. Gaussian sum filters for space surveillance: theory and simulations. *Journal of Guidance, Control, and Dynamics*, 34(6):1839–1851, 2011.

[123] J. T. Horwood, J. M. Aristoff, N. Singh, and A. B. Poore. A comparative study of new non-linear uncertainty propagation methods for space surveillance. In O. E. Drummond, editor, *SPIE Proceedings: Signal and Data Processing of Small Targets*, volume 9092, 2014.

[124] J. T. Horwood, J. M. Aristoff, N. Singh, A. B. Poore, and M. D. Hejduk. Beyond covariance realism: a new metric for uncertainty realism. In O. E. Drummond, editor, *SPIE Proceedings: Signal and Data Processing of Small Targets*, volume 9092, 2014.

[125] J. T. Horwood and A. B. Poore. Adaptive Gaussian sum filters for space surveillance. *IEEE Transactions on Automatic Control*, 56(8):1777–1790, 2011.

[126] J. T. Horwood and A. B. Poore. Orbital state uncertainty realism. In *Proceedings of the 2012 Advanced Maui Optical and Space Surveillance Technologies Conference*, Wailea, HI, September 2012.

[127] J. T. Horwood and A. B. Poore. Gauss von Mises distribution for improved uncertainty realism in space situational awareness. *SIAM Journal of Uncertainty Quantification*, 2:276–304, 2014.

[128] S. Hosder, R. W. Walters, and R. Perez. A non-intrusive polynomial chaos method for uncertainty propagation in CFD simulations. In *44th AIAA Aerospace Sciences Meeting and Exhibit*, Reno, NV, January 2006.

[129] J. M. Hudson and D. J. Scheeres. Orbital targeting using the reduced eccentric anomaly low-thrust coefficients. *Journal of Guidance, Control and Dynamics*, 34(3):820–831, 2011.

[130] J. M. Hudson and D. J. Scheeres. Fourier coefficient selection for low-thrust control shaping. *Journal of Guidance, Control and Dynamics*, 36(6):1783–1786, 2013.

[131] J. S. Hudson and D. J. Scheeres. Reduction of low thrust continuous controls for trajectory dynamics. *Journal of Guidance, Control, and Dynamics*, 32(3):780–787, 2009.

[132] J. Humpherys, P. Redd, and J. West. A fresh look at the Kalman filter. *SIAM Review*, 54(4):801–823, 2012.

[133] I. I. Hussein, K. J. DeMars, C. Fruh, R. S. Erwin, and M. K. Jah. An AEGIS-FISST integrated detection and tracking approach to space situational awareness. In *Proceedings of the 15th International Conference on Information Fusion*, pages 2065–2072, Singapore, July 2012.

[134] I. I. Hussein, C. Fruh, R. S. Erwin, and M. K. Jah. An AEGIS-FISST algorithm for joint detection, classification and tracking. In *Proceedings of the 2013 AAS/AIAA Space Flight Mechanics Meeting*, Kauai, HI, February 2013.

[135] I. I. Hussein, Z. Sunberg, S. Chakravorty, M. K. Jah, and R. S. Erwin. Stochastic optimization for sensor allocation using AEGIS-FISST. In *Proceedings of the 2014 AAS Space Flight Mechanics Conference*, Santa Fe, NM, January 2014.

[136] G. Iaccarino. YouQ: A self-guided tour of uncertainty quantification. http://web.stanford.edu/group/uq/uq_youq.html.

[137] A. Iserles. *A First Course in the Numerical Analysis of Differential Equations*. Cambridge University Press, Cambridge, 2004.

[138] K. Ito and K. Xiong. Gaussian filters for nonlinear filtering problems. *IEEE Transactions on Automatic Control*, 45(5):910–927, 2000.

[139] A. H. Jazwinski. *Stochastic Processes and Filtering Theory*. Dover, New York, 1998.

[140] B. Jia, M. M. Xin, and Y. Cheng. Sparse Gauss-Hermite quadrature filter with an application to spacecraft attitude estimation. *Journal of Guidance, Control, and Dynamics*, 34(2):367–379, 2011.

[141] B. Jia, M. M. Xin, and Y. Cheng. Anisotropic sparse Gauss-Hermite quadrature filter. *Journal of Guidance, Control, and Dynamics*, 35(3):1014–1023, 2012.

[142] B. Jia, M. M. Xin, and Y. Cheng. Sparse-grid quadrature nonlinear filtering. *Automatica*, 48(2):327–341, 2012.

[143] B. Jia, M. M. Xin, and Y. Cheng. High-degree cubature Kalman filter. *Automatica*, 49(2):510–518, 2013.

[144] B. Jia, M. M. Xin, and Y. Cheng. Relations between sparse-grid quadrature rule and spherical-radial cubature rule in nonlinear Gaussian estimation. *IEEE Transactions on Automatic Control*, 2015. (To Appear).

[145] B. A. Jones. Orbit propagation using Gauss-Legendre collocation. In *Proceedings of the 2012 AIAA/AAS Astrodynamics Specialist Conference*, Minneapolis, MN, August 2012. Paper AIAA-2012-4967.

[146] B. A. Jones and R. L. Anderson. A survey of symplectic and collocation integration methods for orbit propagation. In *Proceedings of the 22nd Annual AAS/AIAA Spaceflight Mechanics Meeting*, Charleston, SC, January 2012. Paper AAS 12-214.

[147] B. A. Jones, G. H. Born, and G. Beylkin. Comparisons of the cubed-sphere gravity model with the spherical harmonics. *Journal of Guidance, Control, and Dynamics*, 33(2), 2010.

[148] B. A. Jones and A. Doostan. Satellite collision probability estimation using polynomial chaos expansions. *Advances in Space Research*, 52(11):1860–1875, 2013.

[149] B. A. Jones, A. Doostan, and G. H. Born. Nonlinear propagation of orbit uncertainty using non-intrusive polynomial chaos. *Journal of Guidance, Control, and Dynamics*, 36(2):430–444, March 2013.

[150] B. A. Jones, S. Gehly, and P. Axelrad. Measurement-based birth model for a space object cardinalized probability hypothesis density filter. In *Proceedings of the 2014 AIAA/AAS Astrodynamics Specialist Conference*, San Diego, CA, August 2014. Paper AIAA 2014-4311.

[151] B. A. Jones, N. Parrish, M. S. Werner, and A. Doostan. Post-maneuver collision probability estimation using polynomial chaos. In *Proceedings of the 2013 AAS/AIAA Astrodynamics Specialist Conference*,

Hilton Head, SC, August 2013.

[152] B. A. Jones and B. N. Vo. A labeled multi-Bernoulli filter for space object tracking. In *Proceedings of the 2015 AAS/AIAA Spaceflight Mechanics Meeting*, Williamsburg, VA, January 2015. Paper AAS 15-413.

[153] J. H. Frisbee Jr. Delivery of scale factors to be used in the scaling of position error covariance matrices in orbital conjunction messages generated using the high accuracy satellite drag model (HASDM). Technical Report DM33, Johnson Space Center, December 2004.

[154] J. H. Frisbee Jr. High accuracy satellite drag model (HASDM) data analysis and position error covariance matrix scale factor determination. Technical Report DM33, Johnson Space Center, January 2005.

[155] J. H. Frisbee Jr. An empirical state error covariance matrix for weighted least squares estimation method. Technical Report NASA/TP-2014-217389, NASA, International Space Station Trajectory Operations, NASA/Johnson Space Center (United Space Alliance, LLC), May 2014.

[156] S. J. Julier and J. K. Uhlmann. Unscented filtering and nonlinear estimation. *Proceedings of the IEEE*, 92:401–422, 2004.

[157] S. J. Julier, J. K. Uhlmann, and H. F. Durant-Whyte. A new method for the nonlinear transformation of means and covariances in filters and estimators. *IEEE Transactions on Automatic Control*, 55:477–482, 2000.

[158] J. L. Junkins, M. R. Akella, and K. T. Alfriend. Non-Gaussian error propagation in orbit mechanics. *Journal of the Astronautical Sciences*, 44:541–563, 1996.

[159] L. P. Kaelbling and M. L. Littman. Planning and acting in partially observable stochastic domains. *Artificial Intelligence*, 101(1/2):99–134, May 1998.

[160] M. Kalandros and L. Y. Pao. Multisensor covariance control strategies for reducing bias effects in interacting target scenarios. *IEEE Transactions on Aerospace and Electronic Systems*, 41(1):153–173, 2005.

[161] C. Kalender and A. Schottl. Nonlinear filtering using sparse grids. In F. Holzapfel and S. Theil, editors, *Advances in Aerospace Guidance, Navigation and Control*, pages 359–371. Springer, 2011.

[162] G. H. Kaplan. The IAU resolutions on astronomical reference systems, time scales, and earth rotation models, explanation and implementation. Technical Report 179, US Naval Observatory Circular, 2005.

[163] P. E. Kloeden and E. Platen. *Numerical Solution of Stochastic Differential Equations*. Springer-Verlag, Berlin, 1992.

[164] H. S. Ko and D. J. Scheeres. Unobserved maneuver reconstruction and covariance propagation using the essential thrust Fourier coefficient. In *International Astronautical Congress*, Beijing, China, September 2013. Paper IAC-13-C1.4.2.

[165] H. S. Ko and D. J. Scheeres. Essential thrust Fourier coefficient set of averaged Gauss equations for

orbital mechanics. *Journal of Guidance, Control and Dynamics*, 2014.

[166] B. Kragel, S. Herman, and N. Roseveare. A comparison of methods for estimating track-to-track assignment probabilities. *IEEE Transactions on Aerospace and Electronic Systems*, 48(3):1870–1888, 2012.

[167] C. Kreucher, A. O. Hero III, and K. Kastella. A comparison of task driven and information driven sensor management for target tracking. In *Proceedings of the 44th IEEE Conf. Dec. Contr. & European Contr. Conf.*, pages 4004–4009, December 2005.

[168] C. Kreucher, K. Kastella, and A. O. Hero III. Information based sensor management for multitarget tracking. In O. E. Drummond, editor, *SPIE Proceedings: Signal and Data Processing of Small Targets*, volume 5204, Bellingham, WA, 2003.

[169] F. T. Krogh. Predictor-corrector methods of high order with improved stability characteristics. *Journal of the ACM*, 13(3):374–385, July 1966.

[170] F. T. Krogh. On testing a subroutine for the numerical integration of ordinary differential equations. *Journal of the ACM*, 20(4):545–562, October 1973.

[171] P. R. Kumar and P. P. Varaiya. *Stochastic Systems: Estimation, Identification and Adaptive Control*. Prentice-Hall, Englewood Cliffs, NJ, 1986.

[172] O. P. Le Maître and O. M. Knio. *Spectral Methods for Uncertainty Quantification with Applications to Computational Fluid Dynamics*. Springer, 2010, pp. 138-139.

[173] O. P. Le Maître, O. M. Knio, H. N. Najm, and R. G. Ghanem. A stochastic projection method for fluid flow I: Basic formulation. *Journal of Computational Physics*, 173:481–511, 2001.

[174] D. J. Lee and K.T. Alfriend. Sigma point filtering for sequential orbit estimation and prediction. *Journal of Spacecraft and Rockets*, 44(2):388–398, March 2007.

[175] S. Lemmens and H. Krag. Two-line-elements-based maneuver detection methods for satellites in low earth orbit. *Journal of Guidance, Control, and Dynamics*, 2014.

[176] J. M. Leonard, J. M. Forbes, and G. H. Born. Impact of tidal density variability on orbital and reentry predictions. *Space Weather*, 10, 2012.

[177] J. M. Leonard, F. G. Nievinski, and G. H. Born. Gravity error compensation using second-order Gauss-Markov processes. *Journal of Spacecraft and Rockets*, 50:217–229, 2013.

[178] X. R. Li and V. P. Jilkov. Survey of maneuvering target tracking – Part I: dynamic models. *IEEE Transactions on Aerospace and Electronic Systems*, 39(4):1333–1364, October 2003.

[179] X. Rong Li and Vesselin P. Jilkov. A survey of maneuvering target tracking—part iii: Measurement models. In Oliver E Drummond, editor, *Proceedings of SPIE Conference on Signal and Data Processing of Small Targets*, number 4473-41, San Diego, CA, July-August 2001. SPIE.

[180] P. Di Lizia, R. Armellin, F. Bernelli-Zazzera, K. Makino, and M. Berz. Validated integration of solar system dynamics. In *Proceedings of the 1st IAA Planetary Defense Conference: Protecting Earth from Asteroids*, Granada, Spain, April 2009.

[181] D. P. Lubev and D. J. Scheeres. Identifying and estimating mis-modeled dynamics via optimal control policies and distance metrics. *Journal of Guidance, Control and Dynamics*, 2014.

[182] D. P. Lubey and D. J. Scheeres. Identifying and quantifying mis-modeled dynamics via optimal control problem distance metrics. In *Proceedings of the 2012 AIAA/AAS Astrodynamics Specialist Meeting*, Minneapolis, MN, August 2012.

[183] R. H. Lyddane. Small eccentricities or inclinations in the Brouwer theory of the artificial satellite. *Astronomical Journal*, 68(8):555–558, 1963.

[184] P. C. Mahalanobis. On the generalised distance in statistics. *Proceedings of the National Institute of Sciences of India*, 2(1):49–55, 1936.

[185] R. P. S. Mahler. Multitarget Bayes filtering via first-order multitarget moments. *IEEE Transactions on Aerospace and Electronic Systems*, 39(4):1152–1178, October 2003.

[186] R. P. S. Mahler. PHD filters of higher order in target number. *IEEE Transactions on Aerospace and Electronic Systems*, 43(4):1523–1543, October 2007.

[187] R. P. S. Mahler. *Statistical Multisource-Multitarget Information Fusion*. Artech House, Boston, Massachusetts, 2007.

[188] R. P. S. Mahler. *Advances in Statistical Multisource-Multitarget Information Fusion*. Artech House, Boston, Massachusetts, 2014.

[189] M. Majji, R. M. Weisman, and K. T. Alfriend. Solution of the Liouville equation for Keplerian motion: Application to uncertainty calculations. In *Proceedings of the 2012 AAS/AIAA Spaceflight Mechanics Conference*, Charleston, SC, January 2012. Paper AAS 12-262.

[190] R. Mandankan, P. Singla, T. Singh, and P. D. Scott. Polynomial-chaos-based Bayesian approach for state and parameter estimations. *Journal of Guidance, Control, and Dynamics*, 36(4):1058–1074, 2013.

[191] H. B. Mann and A. Wald. On the choice of the number of class intervals in the application of the chi-square test. *Annals of Mathematical Statistics*, 13(3):306–317, 1942.

[192] K. V. Mardia and P. E. Jupp. *Directional Statistics*. John Wiley & Sons, New York, 2000.

[193] A. K. Mashiku, J. Garrison, and J. R. Carpenter. Statistical orbit determination using the particle filter for incorporating non-Gaussian uncertainties. In *Proceedings of the 2012 AIAA/AAS Astrodynamics Specialist Conference*, Minneapolis, MN, August 2012. Paper AIAA 2012-5063.

[194] J. S. McCabe and K. J. DeMars. Particle filter methods for space object tracking. In *Proceedings of the 2014 AIAA/AAS Astrodynamics Specialist Conference*, 2014. Paper AIAA 2014-4308.

[195] J. S. McCabe, K. J. DeMars, and C. Fruh. Integrated detection and tracking for multiple space objects. In *Proceedings of the 2015 AAS/AIAA Spaceflight Mechanics Meeting*, Paper AAS 15-361, Williamsburg, VA, January 2015.

[196] D. D. McCarthy. IERS conventions (1992). IERS Technical Note 13, U.S. Naval Observatory, 1992.

[197] D. D. McCarthy. IERS conventions (1996). IERS Technical Note 21, International Earth Rotation

and Reference Systems Service (IERS), Paris, France, July 1996.

[198] D. D. McCarthy and G. Petit. IERS conventions (2003). IERS Technical Note 32, U.S. Naval Observatory U.S. Naval Observatory, 2003.

[199] J. J. McCarthy. Operations manual for the oran multi-satellite error analysis program. Technical report, German Space Operations Center, December 1999.

[200] D. P. McKinley. Development of a nonlinear probability of collision tool for the earth observing system. In *Proceedings of the 2006 AAS/AIAA Astrodynamics Specialist Conference*, Keystone, CO, 2006.

[201] S. R. McReynolds. Editing data using sequential smoothing techniques for discrete systems. In *Proceedings of the 1984 AIAA/AAS Astrodynamics Conference*, Seattle, WA, 1984. Paper AIAA 1984-2053.

[202] J. G. Miller. A new sensor allocation algorithm for the space surveillance network. *Military Operations Research*, 12:57–70, 2007.

[203] G. H. Millman. Modern radar: Analysis, evaluation, and design. In R. S. Berkowitz, editor, *Atmospheric Effects on Radio Wave Propagation*, chapter 1, pages 317–378. John Wiley & Sons, New York, 1965.

[204] L. Mohamed, M. A. Christie, and V. Demyanov. Comparison of stochastic sampling algorithms for uncertainty quantification. *Society of Petroleum Engineers Journal*, 15(01), March 2010.

[205] A. D. Mont, C. P. Calderon, and A. B. Poore. A new computational method for ambiguity assessment of solutions to assignment problems arising in target tracking. In O. E. Drummond, editor, *SPIE Proceedings: Signal and Data Processing of Small Targets*, volume 9092, 2014.

[206] O. Montenbruck. Numerical integration methods for orbital motion. *Celestial Mechanics and Dynamical Astronomy*, 53:59–69, 1992.

[207] O. Montenbruck and E. Gill. *Satellite Orbits: Models, Methods, and Applications*. Springer, Berlin, 2nd edition, 2005.

[208] A. Morselli, R. Armellin, P. Di Lizia, and F. B. Zazzera. A high order method for orbital conjunctions analysis: Sensitivity to initial uncertainties. *Advances in Space Research*, 53:490–508, 2014.

[209] A. Morselli, R. Armellin, P. Di Lizia, and F. B. Zazzera. A high order method for orbital conjunctions analysis: Monte Carlo collision probability computation. *Advances in Space Research*, 55:311–333, 2015.

[210] M. D. Nevels, B. Jia, M. R. Turnowicz, M. Xin, and Y. Cheng. Sparse grid-based orbit uncertainty propagation. In *Proceedings of the 2011 AAS/AIAA Astrodynamics Specialist Conference*, Girdwood, AK, July 2011.

[211] G. W. Ng and K. H. Ng. Sensor management – what, why and how. *Information Fusion*, 1:67 – 75, 2000.

[212] M. Norgaardd, K. N. Poulsen, and O. Ravn. New developments in state estimation for nonlinear

systems. *Automatica*, 36(11):1627–1638, 2000.

[213] A. Nouy. Proper generalized decompositions and separated representations for the numerical solution of high dimensional stochastic problems. *Archives of Computational Methods in Engineering*, 17(4):403–434, 2010.

[214] R. Olfati-Saber. Distributed tracking for mobile sensor networks with information-driven mobility. In *Proceedings of the 2007 American Control Conference*, pages 4606–4612, July 2007.

[215] H. Owhadi, C. Scovel, T. J. Sullivan, M. McKerns, and M. Ortiz. Optimal uncertainty quantification. *SIAM Review*, 56(2):271—345, 2013.

[216] L. Y. Pao and M. Kalandros. The effects of delayed sensor requests on sensor manager systems. In *In Proceedings of the 1998 AIAA Guidance, Navigation, and Control Conference*, pages 1127–1135, 1998.

[217] A. Papoulis. *Probability, Random Variables, and Stochastic Processes*. McGraw-Hill, Boston, MA, 3rd edition, 1991.

[218] R. S. Park and D. J. Scheeres. Nonlinear mapping of Gaussian statistics: theory and applications to spacecraft trajectory design. *Journal of Guidance, Control, and Dynamics*, 29:1367–1375, 2006.

[219] R. P. Patera. General method for calculating satellite collision probability. *Journal of Guidance, Control, and Dynamics*, 24:716–722, 2001.

[220] R. P. Patera. Space event detection method. *Journal of Spacecraft and Rockets*, 45(3):554–559, 2008.

[221] N. K. Pavlis, S. A. Holmes, S. C. Kenyon, and J. K. Factor. The development and evaluation of the earth gravitational model 2008 (EGM2008). *Journal of Geophysical Research*, 117(B4), April 2012.

[222] M. R. Pearlman, J. J. Degnan, and J. M. Bosworth. The international laser ranging service. *Advances in Space Research*, 30(2):135–143, July 2002.

[223] G. Petit and B. Luzum. IERS conventions (2010). IERS Technical Note 36, International Earth Rotation and Reference Systems Service (IERS), Frankfurt, Germany, 2010.

[224] A. B. Poore. Multidimensional assignment formulation of data association problems arising from multitarget tracking and multisensor data fusion. *Computational Optimization and Applications*, 3:27–57, 1994.

[225] A. B. Poore, S. Danford, and M. J. Hilt. An assignment based distributed resource manager. In O. E. Drummond, editor, *SPIE Proceedings: Signal and Data Processing of Small Targets*, 2010.

[226] A. Renyi. On measures of entropy and information. In *Proceedings of the Fourth Berkeley Symposium on Mathematical Statistics and Probability, Volume 1: Contributions to the Theory of Statistics*, pages 547 – 561, Berkeley, CA, 1961. University of California Press.

[227] S. Reuter, B. T. Vo, B. N. Vo, and K. Dietmayer. The labeled multi-Bernoulli filter. *IEEE Transactions on Signal Processing*, 62(12):3246–3260, June 2014.

[228] B. Ristic, S. Arulampalam, and N. Gordon. *Beyond the Kalman Filter: Particle Filters for Tracking Applications*. Artech House Radar Library, 2004.

[229] C. J. Roy and W. L. Oberkampf. A comprehensive framework for verification, validation, and uncertainty quantification in scientific computing. *Computer Methods in Applied Mechanics and Engineering*, 200:2131–2144, June 2011.

[230] R. P. Russell and N. Arora. Global point Mascon models for simple, accurate, and parallel geopotential computation. *Journal of Guidance, Control, and Dynamics*, 35(5):1568–1581, 2012.

[231] C. Sabol, T. Sukut, K. Hill, K. T. Alfriend, B. Wright, Y. Li, and P. Schumacher. Linearized orbit covariance generation and propagation analysis via simple Monte Carlo simulations. In *Proceedings of the 20th AAS/AIAA Space Flight Mechanics Meeting*, San Diego, CA, February 2010. Paper AAS-10-134.

[232] S. Särkkä. On unscented Kalman filtering for state estimation of continuous-time nonlinear systems. *IEEE Transactions on Automatic Control*, 52:1631–1641, 2007.

[233] S. Särkkä. *Bayesian Filtering and Smoothing*, volume 3 of *IMS Textbooks*. Cambridge University Press, 2013.

[234] P. E. Schmid. Atmospheric tracking errors at S- and C-band frequencies. NASA Technical Note NASA TN D-3470, NASA Goddard Space Flight Center Greenbelt, MD, Washington, DC, August 1966.

[235] S. F. Schmidt. Applications of state-space methods to navigation problems. In C. T. Leondes, editor, *Advances in Control Systems*, volume 3, pages 293–340. Academic Press, New York, NY, 1966.

[236] K. Seidelmann. *Explanatory Supplement to the Astronomical Almanac*. University Science Books, California, 1992.

[237] L. F. Shampine. *Numerical solution of ordinary differential equations*. Chapman and Hall, 1994.

[238] L. F. Shampine. Error estimation and control for ODEs. *Journal of Scientific Computing*, 25:3–16, 2005.

[239] S. S. Shapiro and M. B. Wilk. An analysis of variance test for normality (complete samples). *Biometrika*, 52:591–611, 1965.

[240] J. Sharma, G. H. Stokes, C. von Braun, G. Zollinger, and A. J. Wiseman. Toward operational space-based space surveillance. *Lincoln Laboratory Journal*, 13(2):309 – 334, 2002.

[241] H. Shen, V. Vittaldev, C. D. Karlgaard, R. P. Russell, and E. Pellegrini. Parallel sigma point and particle filters for orbit determination. In *Proceedings of the 9th US/Russian Space Surveillance Workshop*, Krestovaya Pad, Listvyanka, Russia, 2012.

[242] H. Shen, V. Vittaldev, C. D. Karlgaard, R. P. Russell, and E. Pellegrini. Parallelized sigma point and particle filters for navigation problems. In *Proceedings of the 36th Annual AAS Guidance and Control Conference*, Breckenridge, CO, 2013. Paper AAS 13-034.

[243] A. T. Sinclair. Ilrs normal point algorithm. http://ilrs.gsfc.nasa.gov/data_and_products/data/npt/npt_algorithm.html, 1997.

[244] N. Singh, J. T. Horwood, J. M. Aristoff, A. B. Poore, C. Sheaff, and M. K. Jah. Multiple hypothesis

tracking (MHT) for space surveillance: results and simulation studies. In *Proceedings of the 2013 Advanced Maui Optical and Space Surveillance Technologies Conference*, Wailea, HI, September 2013.

[245] N. Singh, J. T. Horwood, and A. B. Poore. Space object maneuver detection via a joint optimal control and multiple hypothesis tracking approach. In *Proceedings of the 22nd AAS/AIAA Space Flight Mechanics Meeting*, Charleston, SC, January 2012. Paper AAS-12-159.

[246] R. C. Smith. *Uncertainty Quantification: Theory, Implementation, and Applications*. Computational Science and Engineering. SIAM, December 2013.

[247] G. W. Snedecor and W. G. Cochran. *Statistical Methods*. Iowa State University Press, 8th edition, 1989.

[248] J. Stauch, J. Baldwin, M. K. Jah, T. Kelecy, and K. Hill. Mutual application of joint probabilistic data association, filtering, and smoothing techniques for robust multiple space object tracking. In *Proceedings of the 2014 AAS/AIAA Astrodynamics Specialist Conference*, 2014. Paper AAS 2014-4365.

[249] J. Stauch and M. K. Jah. On the unscented Schmidt-Kalman filter algorithm. *Journal of Guidance, Control and Dynamics*, 38(1):117–123, 2015.

[250] M. A. Stephens. EDF statistics for goodness of fit and some comparisons. *Journal of the American Statistical Association*, 69(347):730–737, 1974.

[251] Z. Sunberg, S. Chakravorty, and R. S Erwin. Information space receding horizon control for multi-agent systems. In *Proceedings of the 2012 American Control Conference*, pages 5246 – 5251, Montreal, Canada, June 2012.

[252] Z. Sunberg, S. Chakravorty, and R. S. Erwin. Information space receding horizon control applied to a space situational awareness problem. In *Proceedings of the 2014 American Control Conference*, pages 79 – 84, Portland, OR, June 2014.

[253] L. P. Swiler, T. L. Paez, and R. L. Mayes. Epistemic uncertainty quantification tutorial. In *Proceedings of the IMAC-XXVII*, Orlando, FL, February 2009. Society for Experimental Mechanics, Inc.

[254] B. Tapley, B. Schutz, and G. Born. *Statistical Orbit Determination*. Elsevier Academic Press, 2004.

[255] G. Terejanu, P. Singla, T. Singh, and P. D. Scott. Uncertainty propagation for nonlinear dynamic systems using Gaussian mixture models. *Journal of Guidance, Control, and Dynamics*, 31(6):1623–1633, 2008.

[256] S. Truong. rbit determination error analysis system (odeas) user's guide. Technical report, 1993.

[257] M. R. Turnowicz, K. J. DeMars, B. Jia, M. Xin, Y. Cheng, and M. K. Jah. Quadrature methods for orbit uncertainty propagation under solar radiation pressure. In *Proceedings of the 2012 AAS/AIAA Space Flight Mechanics Meeting*, Charleston, South Carolina, January 2012.

[258] A. Urbina and S. Mahadevan. Quantification of aleatoric and epistemic uncertainty in computational models of complex systems. In *Proceedings of the IMAC-XXVIII*, Jacksonville, FL USA, February

2010. Society for Experimental Mechanics, Inc., Springer.

[259] D. A. Vallado. An analysis of state vector propagation for differing flight dynamics programs. In *Proceedings of the 2005 AAS/AIAA Space Flight Mechanics Conference*, Copper Mountain, CO, January 2005. Paper AAS 05-199.

[260] D. A. Vallado. An analysis of state vector prediction accuracy. In *US/Russian Workshop*, Monterey, CA, October 2007. Paper USR 07-S6.1.

[261] D. A. Vallado. *Orbital Mechanics Fundamentals, Encyclopedia of Aerospace Engineering*. Wiley Online Library, 2010.

[262] D. A. Vallado. *Fundamentals of Astrodynamics and Applications*. Microcosm, Hawthorne, CA, 2013.

[263] D. A. Vallado, R. S. Hujsak, T. M. Johnson, J. H. Seago, and J. W. Woodburn. Orbit determination using ODTK version 6. In *4th International Conference on Astrodynamics Tools and Techniques (ICATT) Conference*, Madrid, Spain, May 2010. Paper 10A08-1855538.

[264] D. A Vallado and T. S. Kelso. Earth orientation parameter and space weather data for flight operations. In *Proceedings of the 2013 AAS/AIAA Space Flight Mechanics Meeting*, Kauai, HI, February 2013. Paper AAS 13-373.

[265] D. A. Vallado and J. H. Seago. Covariance realism. In *Proceedings of the 2009 AAS/AIAA Astrodynamics Specialist Conference*, Pittsburgh, PA, August 2009. Paper AAS 09-304.

[266] M. Valli, R. Armellin, P. Di Lizia, and M. R. Lavagna. Nonlinear mapping of uncertainties in celestial mechanics. *Journal of Guidance, Control and Dynamics*, 36(1):48–63, 2013.

[267] M. Valli, R. Armellin, P. Di Lizia, and M. R. Lavagna. Nonlinear filtering methods for spacecraft navigation based on differential algebra. *Acta Astronautica*, 94:363–374, 2014.

[268] R. van der Merwe. *Sigma-Point Kalman Filters for Probabilistic Inference in Dynamic State-Space Models*. Phd thesis, University of Oregon, Electrical and Computer Engineering, April 2004.

[269] R. van der Merwe and E. A. Wan. The square-root unscented Kalman filter for state and parameter estimation. In *IEEE International Conference on Acoustics, Speech, and Signal Process (ICASSP)*, volume 6, pages 3461–3464, 2001.

[270] V. Vittaldev, R. Linares, H. Godinez, J. Koller, and R. Russell. Improved uncertainty quantification for physics-based atmospheric models via generalized polynomial chaos. In *AGU Fall Meeting Abstracts*, volume 1, 2013.

[271] V. Vittaldev, R. Linares, and R. P. Russell. Uncertainty propagation using Gaussian mixture models and polynomial chaos. In *Proceedings of the 2015 AAS/AIAA Space Flight Mechanics Meeting*, Williamsburg, VA, January 2015. Paper AAS 15-448.

[272] V. Vittaldev and R. P. Russell. Collision probability for resident space objects using Gaussian mixture models. In *Proceedings of the 23rd AAS/AIAA Spaceflight Mechanics Meeting*, Kauai, HI, 2013. Paper AAS 13-351.

[273] V. Vittaldev and R. P. Russell. Collision probability using multidirectional Gaussian mixture models.

In *Proceedings of the 25th AAS/AIAA Space Flight Mechanics Meeting*, Williamsburg, VA, 2015. Paper AAS 15-394.

[274] V. Vittaldev, R. P. Russell, N. Arora, and D. Gaylor. Second order Kalman filter using multicomplex step derivatives. In *Proceedings of the 22nd Annual AAS/AIAA Spaceflight Mechanics Meeting*, Charleston, SC, 2012. Paper AAS 12-204.

[275] B. N. Vo and W. K. Ma. The Gaussian mixture probability hypothesis density filter. *IEEE Transactions on Signal Processing*, 54(11):4091–4104, November 2006.

[276] B. N. Vo, S. Singh, and A. Doucet. Sequential Monte Carlo methods for multitarget filtering with random finite sets. *IEEE Transactions on Aerospace and Electronic Systems*, 41(4):1224–1245, October 2005.

[277] B. N. Vo, B. T. Vo, N. T. Pham, and D. Suter. Joint detection and estimation of multiple objects from image observations. *IEEE Transactions on Signal Processing*, 58(10):5129–5141, October 2010.

[278] B. T. Vo and B. N. Vo. Labeled random finite sets and multi-object conjugate priors. *IEEE Transactions on Signal Processing*, 61(13):3460–3475, July 2013.

[279] B. T. Vo, B. N. Vo, and A. Cantoni. The cardinalized probability hypothesis density filter for linear Gaussian multi-target models. In *40th Annual Conference on Information Sciences and Systems*, pages 681–686, Princeton, NJ, March 2006.

[280] P. T. Wallace and N. Capitaine. Precession-nutation procedures consistent with IAU 2006 resolutions. *Astronomy and Astrophysics*, 459:981–984, 2006.

[281] E. A. Wan and R. van der Merwe. The unscented Kalman filter for nonlinear estimation. In *Adaptive Systems for Signal Processing, Communications, and Control Symposium 2000*, pages 153–158. IEEE, October 2000.

[282] R. M. Weisman and M. K. Jah. Uncertainty quantification for angles-only initial orbit determination. In *Proceedings of the 2014 AAS/AIAA Spaceflight Mechanics Conference*, Santa Fe, NM, January 2014. Paper AAS 14-343.

[283] R. M. Weisman, M. Majji, and K. T. Alfriend. Analytic characterization of measurement uncertainty and initial orbit determination on orbital element representations. *Journal of Celestial Mechanics and Dynamical Astronomy*, 118(2), 2014. 165-195.

[284] R. M. Weisman, M. Majji, and K. T. Alfriend. Application of the transformation of variables technique for uncertainty mapping in nonlinear filtering. *Journal of Celestial Mechanics and Dynamical Astronomy*, 118(2):129–164, 2014.

[285] C. J. Wetterer, T. M. Kelecy, M. K. Ziebart, M. K. Jah, and P. J. Cefola. Refining space object radiation pressure modeling with bidirectional reflectance distribution functions. *Journal of Guidance, Control, and Dynamics*, 37(1):185–196, January 2014.

[286] N. Wiener. The homogeneous chaos. *American Journal of Mathematics*, 60(4):897–936, October 1938.

[287] Wikipedia. Uncertainty quantification. http://en.wikipedia.org/wiki/Uncertainty_quantification.

[288] P. S. Williams, D. S. Spencer, and R. S. Erwin. Coupling of nonlinear estimation and dynamic sensor tasking applied to space situational awareness. In *Proceedings of the 2011 AAS/AIAA Astrodynamics Specialist Conference*, pages 173 – 190, Girdwood, AK, July 2011.

[289] P. S. Williams, D. S. Spencer, and R. S. Erwin. Utilizing stability metrics to aid in sensor network management solutions for satellite tracking problems. In *Proceedings of the 22nd AAS/AIAA Space Flight Mechanics Meeting*, pages 155 – 172, Charleston, SC, January 2012.

[290] A. Wittig, C. Colombo, and R. Armellin. Density evolution of high area-to-mass objects using semi-analytical and differential algebra techniques. In *Proceedings of the 65th International Astronautical Congress*, Toronto, Canada, September 2014.

[291] A. Wittig, P. Di Lizia, R. Armellin, F. Bernelli-Zazzera, K. Makino, and M. Berz. An automatic domain splitting technique to propagate uncertainties in highly nonlinear orbital dynamics. In *24th AAS/AIAA Space Flight Mechanics Meeting*, pages 1923–1941, Santa Fe, NM, 2014. Paper AAS 14-344.

[292] J. Wright, J. Woodburn, S. Truong, and W. Chuba. Orbit gravity error covariance. In *Proceedings of the 2008 AAS/AIAA Spaceflight Mechanics Meeting*, Galveston, TX, January 2008. Paper AAS 08-157.

[293] J. R. Wright. Optimal orbit determination. Technical report, Analytical Graphics, Inc, 2002.

[294] D. Xiu. *Numerical Methods for Stochastic Computations: A Spectral Method Approach*. Princeton University Press, Princeton, NJ, 2010.

[295] D. Xiu and G. E. Karniadakis. The Wiener-Askey polynomial chaos for stochastic differential equations. *SIAM Journal of Scientific Computing*, 24(2):619–644, 2002.

[296] X. Yang, M. Choi, G. Lin, and G. E. Karniadakis. Adaptive ANOVA decomposition of stochastic incompressible and compressible flows. *Journal of Computational Physics*, 231(4):1587–1614, 2012.

[297] R. Zanetti and C. D'Souza. Recursive implementations of the consider filter. In *Proceedings of the 2012 AIAA/AAS Astrodynamics Specialist Conference*, Minneapolis, MN, 2012. Paper AAS 12-619.